

System-Size Dependence of Strangeness Production in Heavy-Ion Collisions at 158 AGeV

Dissertation
zur
Erlangung des Doktorgrades
der Naturwissenschaften
(Dr. rer. nat.)

dem
Fachbereich Physik
der Philipps-Universität Marburg
vorgelegt von

Claudia Höhne
aus Hüttental jetzt Siegen

Marburg/Lahn, 2003

Vom Fachbereich Physik der Philipps-Universität Marburg als Dissertation
angenommen am 23.07.2003.

Erstgutachter: Prof. Dr. F. Pühlhofer

Zweitgutachter: Prof. Dr. R. Stock, Johann Wolfgang Goethe-Universität
Frankfurt am Main

Tag der mündlichen Prüfung: 16.09.2003

Zusammenfassung

Hochenergetische Proton-Proton- und Kern-Kern-Kollisionen bieten die Möglichkeit, stark wechselwirkende Vielteilchensysteme bei hohen Energiedichten zu untersuchen. Werden bei diesen Stößen genügend hohe Temperaturen oder Baryonendichten erzeugt, so erwartet man einen Übergang in einen Materiezustand, in dem Quarks nicht mehr in Hadronen gebunden, sondern neben Gluonen als quasi-freie Teilchen vorliegen. Im Grenzfall großer Systeme im thermodynamischen Gleichgewicht bezeichnet man diese partonischen Systeme als Quark-Gluon-Plasma. Vor allem in zentralen Kollisionen schwerer Kerne wird erwartet, dass Energiedichte und Lebensdauer in der frühen Phase der Kollision hoch bzw. lang genug für einen Phasenübergang in das Quark-Gluon-Plasma sind. Eine mögliche Signatur dafür, dass im Verlauf dieser Kern-Kern-Stöße Quarkmaterie oder ein Quark-Gluon-Plasma entstehen, ist eine im Vergleich zu p-p-Stößen erhöhte Produktion Strangeness tragender Teilchen. Allerdings ist aber auch von einem Hadronengas im thermischen Gleichgewicht bekannt, dass darin vergleichsweise mehr Strangeness vorliegen kann. So ist der Rückschluss auf die Existenz einer partonischen Phase schwierig. Intensive Untersuchungen zentraler Pb-Pb- und Au-Au-Stöße mit etwa 360 partizipierenden Nukleonen bei unterschiedlichen Energien ergaben zwar eine im Vergleich zu p-p-Stößen erhöhte Strangeness-Produktion. Doch macht man auch bei zentralen S-S-Kollisionen mit nur 54 Partizipanten die gleiche Beobachtung. Die Suche nach dem Ursprung der Strangeness-Erhöhung ist deswegen nach wie vor eine zentrale Frage der Schwerionenphysik.

In dieser Arbeit wird die Produktion von Strangeness tragenden Teilchen in Abhängigkeit von der Größe des Stoßsystems in symmetrischen A-A-Kollisionen bei einer Strahlenergie von 158 GeV pro Nukleon untersucht. In minimum-bias p-p- sowie in p-p-Kollisionen mit Selektion von Wechselwirkungen verschiedener Inelastizität, zentralen C-C- und Si-Si-Stößen werden die Produktionsraten von Kaonen, $K^*(892)$ und ϕ -Mesonen analysiert. Die Häufigkeit von Pionen wird zur Normierung der Strangeness-Produktion ebenfalls bestimmt. Zusammen mit publizierten Werten für die Systeme S-S und Pb-Pb erhält man damit einen Datensatz mit systematischer Variation des Eingangskanals. Die Hoffnung ist, damit Aufschluss zu erhalten über die physikalisch relevanten Parameter, die zu der verstärkten Produktion von Strangeness führen.

Die Messungen wurden im Rahmen des NA49-Experiments am CERN-SPS mit einem Hadronenspektrometer großer Akzeptanz durchgeführt. Geladene Teilchen wurden in Spurdriktkammern nachgewiesen und anhand ihres Energieverlustes identifiziert, kurzlebige Resonanzen wurden mit der Methode der invarianten

Masse detektiert. Unter Berücksichtigung der Akzeptanz des Detektors, des Zerfalls der Kaonen im Detektor und der Beiträge von schwachen Zerfällen wurden für p-p-, zentrale C-C- und Si-Si-Kollisionen Rapiditäts- und Transversalimpuls-Spektren sowie die über den Phasenraum integrierte Häufigkeit von Pionen, Kaonen, $K^*(892)$ und ϕ -Mesonen bestimmt.

Die Transversalimpuls-Spektren zeigen eine mit der Systemgröße ansteigende kollektive Expansion der Reaktionszone. Die Produktion von Strangeness tragenden Teilchen relativ zu den Pionen ist gegenüber p-p schon in C-C und Si-Si deutlich erhöht. Sie steigt mit der Systemgröße zunächst rasch an, zusammen mit Daten für zentrale S-S- und Pb-Pb-Kollisionen zeigt sich jedoch eine Sättigung ab etwa 60 am Stoß partizipierenden Nukleonen.

Der Vergleich mit vorläufigen NA49-Resultaten für Pb-Pb-Kollisionen, bei denen die Systemgröße durch Wahl des Stoßparameters variiert wurde, weist jedoch auf einen starken Geometrieeffekt hin: Bei gleicher Anzahl von Partizipanten erhält man in zentralen Kollisionen leichter Kerne einen größeren Anteil von Strangeness tragenden Teilchen als bei peripheren Pb-Pb-Reaktionen.

Im Diskussionsteil dieser Arbeit werden anhand von Daten und Modellrechnungen verschiedene Gründe für den in Kern-Kern-Kollisionen beobachteten Überschuss von Strangeness tragenden Hadronen sowie für dessen Anstieg mit der Systemgröße untersucht: sekundäre Wechselwirkungen im hadronischen Endzustand der Reaktion, der Einfluss hoher Anregungsenergien als Folge von aufeinanderfolgenden N-N-Stößen, oder eine Art kohärenter Überlagerung von N-N-Reaktionen.

Experimentelle Hinweise wie der Geometrieeffekt, die im Vergleich zu zentralen Pb-Pb-Kollisionen schwache kollektive Expansion, die Häufigkeit von $K^*(892)$ -Mesonen, sowie UrQMD Simulationen deuten darauf hin, dass in C-C und Si-Si sekundäre Wechselwirkungen keine signifikante Rolle spielen. Es bleiben somit die primären N-N-Kollisionen und der Zerfall bzw. die Hadronisierung der resultierenden angeregten Resonanzen oder Strings als Quelle der erhöhten Strangeness-Produktion. In Kern-Kern-Stößen finden innerhalb von nur 1-2 fm/c im Ruhesystem der Reaktion etwa 2-5 Wechselwirkungen pro Nukleon statt; die Anzahl hängt vor allem von der Größe der kollidierenden Systeme ab. Bei einer unabhängigen Überlagerung von N-N-Stößen sollten sich die Energieüberträge addieren, Strings damit lediglich höher angeregt werden und unabhängig voneinander zerfallen. Dieses Szenario wird in p-p-Kollisionen durch eine Selektion von Stößen höherer Inelastizität untersucht, die über die Multiplizität und alternativ über das Feynman-x des verbliebenen Projektilprotons definiert wird. In FRITIOF-Simulationen wird der Zusammenhang zur Stringmasse, d. h. der für die Teilchenerzeugung zur Verfügung stehenden Energie, untersucht. Es wird kein Anstieg der relativen Strangeness-Produktion in diesen experimentell zugänglichen Unterklassen von p-p-Kollisionen, die aber den für die Fragestellung wesentlichen Bereich abdecken, beobachtet. Der leichte Anstieg der $K^*(892)$ - und ϕ -Produktion relativ zu den Pionen kann durch Schwelleneffekte erklärt werden.

Um einen Zugang zu den relevanten physikalischen Parametern zu erhalten, die die Erhöhung der Strangeness-Produktion bedingen, wird die beobachtete Geometrieabhängigkeit durch die Suche nach einer gemeinsamen Skalierungsvariablen

ausgenutzt. Die mittlere Dichte inelastischer Stöße in Raum und Zeit in der ersten Phase der Reaktion, in der die Kerne einander durchdringen, stellt eine solche Skalierungsgröße dar. Sie ist offensichtlich korreliert mit der Strangeness-Produktion und kann als Auslöser für die Bildung von kohärenten Systemen interpretiert werden. Diese Systeme würden mehrere Strings umfassen und als quantenmechanische Gesamtheit hadronisieren, aufgrund ihrer hohen Anregung wären sie und/oder ihr Zerfall statistisch beschreibbar. Damit sind die Erhöhung der Strangeness-Produktion und ihre Abhängigkeit von der Größe des Stoßsystems erklärbar: Aus thermodynamischen Modellen ist ein Volumeneffekt für erhaltene Quantenzahlen, hier der Strangeness, bekannt, wenn (mit dem Volumen) die Anzahl der Träger dieser Quantenzahl ansteigt und das System statt als kanonisches als großkanonisches Ensemble betrachtet werden kann.

Die stärkere Abhängigkeit der Häufigkeit von ϕ -Mesonen von der Systemgröße im Vergleich zu der von Kaonen deutet neben anderen Gründen darauf hin, dass die relative Häufigkeit von strange Quarks in einem partonischen System festgelegt wird.

Die Schlußfolgerung in dieser Arbeit ist daher, dass in A-A-Kollisionen bei genügend hoher Energie in Abhängigkeit von der Größe der Stoßsysteme, d. h. angenommen in Abhängigkeit von der Dichte der inelastischen Kollisionen in der Durchdringungsphase der Kerne, kohärente (partonische) Systeme bestehend aus mehreren angeregten Nukleonen oder Strings gebildet werden, die als quantenmechanische Gesamtheit zerfallen. Der damit verbundene Anstieg des Hadronisierungsvolumens bedingt die Aufhebung der durch die Forderung von Strangeness-Erhaltung entstandenen Einschränkung der Strangeness-Produktion in kleinen Volumina, und somit folgt eine erhöhte Strangeness-Produktion im Vergleich zum unabhängigen Zerfall einzelner Strings, d. h. zu p-p.

Abstract

Strangeness enhancement in A+A collisions relative to p+p interactions as a signal for the transition to a deconfined state of strongly interacting matter was recently searched for mostly in high-energy collisions of heavy nuclei such as central Pb+Pb or Au+Au. The expectation is that in these large systems with about 360 participating nucleons such a transition is more likely because of a longer lifetime and higher energy density. However, earlier studies with lighter beams had demonstrated that already in S+S with 54 participants strangeness is significantly enhanced.

In this work strange-particle production is studied as function of system size in symmetric central A+A collisions at 158 AGeV. Using the NA49 spectrometer at the CERN-SPS, yields and kinematic distributions of kaons, $K^*(892)$, the ϕ -meson and, for reference purposes, also of pions are measured in minimum-bias and inelasticity-selected p+p interactions, and in central C+C and Si+Si collisions. Together with earlier data for central S+S and Pb+Pb the results present a complete picture of the evolution of strangeness enhancement as function of system size.

The data show a continuous increase of the strange-particle abundances in dependence on system size, with a fast rise in small systems and a saturation already for about 60 participating nucleons if comparing central A+A collisions only.

On the basis of the present data and using microscopic models for A+A collisions an attempt is made to localize the origin of strangeness enhancement and to understand its evolution. For several reasons, rescattering is found to be an unlikely explanation, in particular for the lighter systems. The idea that the high string excitations – obtained in A+A collisions as a consequence of sequential N+N interactions – are responsible is dismissed on the basis of inelasticity-controlled p+p data. On the other hand, the geometry dependence indicated by a comparison of the central A+A data with those for peripheral Pb+Pb suggests that the density of the primary inelastic interactions in space-time plays a decisive role, because it is found to act as a scaling variable for the strangeness enhancement in all systems. The final conclusion of this work is that a high collision density leads to formation of coherent partonic (sub-)systems comprising several strings whose hadronization can be described statistically. Then, these systems and/or their hadronization must be subject to the phenomenon of canonical strangeness suppression respectively of grand-canonical strangeness enhancement. This would explain both the strangeness enhancement itself and its system-size dependence.

Contents

Zusammenfassung	ii
Abstract	vi
1 Introduction	1
1.1 Motivation	1
1.2 Basic concepts	4
1.3 Strongly interacting matter in experiments	8
1.3.1 e^+e^- annihilation into hadrons	8
1.3.2 Hadron-hadron collisions	9
1.3.3 Nucleus-nucleus collisions	11
1.3.4 Strangeness	14
1.4 Particle production in models	16
1.4.1 Overview	16
1.4.2 Schwinger mechanism	17
1.4.3 String models	18
1.4.4 Numerical codes for microscopic models	20
1.4.5 Thermodynamic models	28
2 The NA49 Experiment	33
2.1 Overview	33
2.2 Beamline	35
2.3 Time projection chambers and magnets	36
2.4 Time-of-flight detectors	40
2.5 Calorimeters	41
3 Methods for data analysis	43
3.1 Charged-particle identification by means of energy loss measurement	43
3.1.1 Basics of energy loss measurement	43
3.1.2 Raw spectra	45
3.1.3 Acceptance and feed-down corrections	49
3.1.4 Final spectra	54
3.1.5 Systematic errors	55
3.2 Identification of resonances	56
3.2.1 Invariant-mass method	56

3.2.2	Background	58
3.2.3	Extraction of yields	68
3.2.4	Simulation of the resonance	69
3.2.5	Acceptance and in-flight decay of kaons	70
3.2.6	Systematic errors	73
3.3	Particle identification with veto chambers and ring calorimeter	74
4	Event selection	77
4.1	Minimum-bias p+p interactions	77
4.1.1	The NA49 trigger cross section	77
4.1.2	Corrections for event losses	78
4.2	Inelasticity in p+p interactions	79
4.2.1	Introduction	79
4.2.2	Feynman-x of the leading proton	82
4.2.3	Multiplicity	87
4.2.4	Inelasticity in simulations with the FRITIOF model	87
4.3	Centrality in C+C and Si+Si collisions	92
4.3.1	Centrality determination via trigger cross section	94
4.3.2	Centrality determination via event multiplicity	100
4.3.3	Number of participants from zero-degree energy	101
4.3.4	Summary of results	103
5	p+p interactions	105
5.1	Kinematic distributions and yields in minimum-bias collisions	105
5.1.1	Pions	105
5.1.2	Kaons	109
5.1.3	ϕ -meson	112
5.1.4	$K^*(892)^0$ and $\bar{K}^*(892)^0$	119
5.1.5	Summary of minimum-bias results and comparison to other experiments	126
5.2	Inelasticity-selected p+p events	129
5.2.1	Multiplicity dependence	130
5.2.2	Correlation between yields and Feynman-x of the leading proton	133
5.2.3	Discussion of results and comparison to FRITIOF simulations	136
6	C+C and Si+Si collisions	143
6.1	Pions	143
6.2	Kaons	149
6.3	ϕ -meson	152
6.4	$K^*(892)^0$ and $\bar{K}^*(892)^0$	158
7	Discussion	163
7.1	Experimental results	164
7.2	Rescattering	171
7.3	Independent superposition of N+N interactions	178

7.4	Empirical scaling parameters	180
7.5	System-size dependence in the statistical model	186
7.6	Conclusion	191
A	Kinematic variables, cross sections and variable transformation	193
B	Clebsch-Gordan coefficients	197
C	Particle distributions: tables and figures	199
C.1	p+p collisions	202
C.2	C+C collisions	211
C.3	Si+Si collisions	214
D	System-size parameters	219
	Bibliography	225

Chapter 1

Introduction

1.1 Motivation

High-energy collisions between protons or nuclei offer the possibility to study the physics of strongly interacting multiparticle systems: At center-of-mass energies significantly higher than the nuclear rest mass and reaction times of only 10-20 fm/c in the rest frame of the collision up to thousands of particles are newly created. These multiplicities and reaction times imply the predominance of the strong interaction. For example, at center-of-mass energies of $\sqrt{s} = 17.3$ GeV per nucleon pair, 8 hadrons are produced on average in p+p interactions, about 200 in central Si+Si and 2200 in central Pb+Pb collisions. During the penetration time of the nuclei of 1-2 fm/c corresponding to $(3 - 7) \cdot 10^{-24}$ s, each of the 41 nucleons participating on average in a central Si+Si collision undergoes 2.5 sequential interactions. In Pb+Pb, the 360 participating nucleons interact 4-5 times on average. Secondary interactions of the produced hadrons last for some additional 10-20 fm/c.

Particle production by the strong interaction can best be studied in e^+e^- annihilation into a quark-antiquark pair with successive hadron production driven by the strong force. But in contrast to the electro-weak interaction these latter processes are not amenable to a quantitative calculation with perturbation theory. Production of secondary $q\bar{q}$ -pairs in the strong field and the hadronization have to be described by phenomenological models. These models can be adopted to p+p and A+A collisions, even if they are more complicated because protons are composite systems of valence quarks, sea-quarks and gluons, and in A+A interactions several N+N reactions are superimposed. In addition to phenomenological models based on a simulation of single interactions, the statistical description of multiparticle systems is a very successful concept for high-energy collisions. The average behavior of the system is described using only a few macroscopic parameters. In contrast to classical thermodynamics, the particle number is not constant; a relativistic calculation has to be applied. Conservation of, e. g., baryon number, electrical charge and flavor by the strong force have to be taken into account. Although the system is not in thermodynamic equilibrium since A+A collisions represent a dynamical process, certain phases of the interaction may be close to a local, i. e. momentary equilibrium state, because the strength of the strong force results in short equilibration times.

Strongly interacting multiparticle systems are of special interest, because a new phase of matter is expected at sufficiently high energy density; the so-called quark-gluon plasma (QGP) in the limit of a large system in thermal equilibrium. In this phase, deconfinement of quarks (and gluons) occurs in contrast to the confined states of quark matter, the hadrons as $q\bar{q}$, qqq or $\bar{q}q\bar{q}$ combinations. Such a deconfinement must have existed in the very early phase of the universe; its freeze-out into hadrons influenced the further development of our cosmos. Also the understanding of neutron stars might profit from knowledge about the QGP phase of matter because in the core of these stars the critical baryon density might be reached.

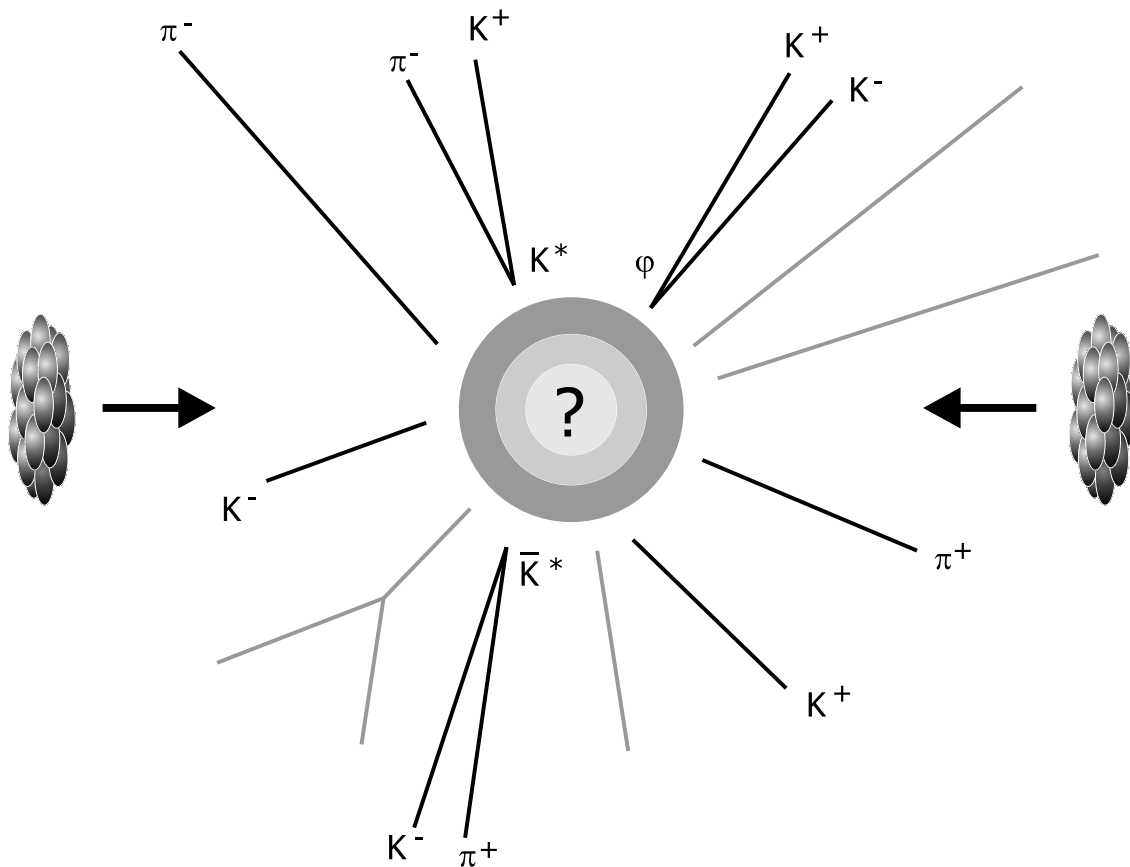


Figure 1.1: Schematic view of a nucleus-nucleus collision. Conclusions about the initial state of the collision may be drawn from the final state particles measured in the experiment.

In collision experiments only the produced particles are accessible for information. But the real interest lies in the mechanism of particle production, and, especially for large systems, in the space-time evolution of the colliding system and the potential proof of the existence of a quark-gluon plasma phase in the course of the interaction. The aim must therefore be to draw conclusions about the initial state and production processes via the study of the emitted particles, their yield, momentum distributions and correlations. Unfortunately there is no unambiguous

signal for QGP formation, but experiments can accumulate a set of data which support or eventually rule out this assumption. It is obvious that it is very important to measure a large variety of signals while systematically changing parameters as energy or the size of the collision system. As a reference, a good knowledge about p+p interactions is essential before new features in A+A reactions can be claimed.

The signal under investigation in this work is the content of strange mesons in the final hadronic state of p+p and A+A collisions. Strange quarks are newly produced, since they are not available from the valence quarks of the incoming nucleons. Their abundance relative to p+p is expected to be sensitive to the phase in which they are created, assuming that the large majority survives in the hadronic final state. To be specific, an enhancement compared to p+p is expected in case a QGP has been reached, however, a QGP would not be the only possible source. Charged kaons, $K^*(892)^0$, the ϕ -meson and, for reference purposes, charged pions are investigated: kaons, because they are the most abundant strange mesons and provide a measure of the total strangeness produced in the interactions; $K^*(892)^0$ since their abundance should be sensitive to the rescattering phase (the mean lifetime $\tau = 4 \text{ fm}/c$ is of the same order as that of the fireball); ϕ -mesons due to their multi-strange quark content as carrier of hidden strangeness ($s\bar{s}$).

A detailed analysis of p+p collisions at 158 GeV is made by investigating minimum-bias interactions for comparison with results in A+A, but also inelasticity-selected subsamples of p+p events. The fundamental question in the latter study was, whether already in p+p reactions a strangeness enhancement can be observed in more violent interactions. This way the higher excitation obtained in A+A by sequential N+N interactions can be simulated, assuming an independent accumulation of excitation energy and independent decay of the resulting strings.

The main focus of this work lies in the systematic investigation of strangeness production in dependence on the size of the collision system. Besides p+p interactions central C+C and Si+Si collisions were studied at 158 GeV beam energy per nucleon. The results will be discussed together with central S+S interactions at 200 AGeV and centrality-selected Pb+Pb reactions at 158 AGeV.

First, basic concepts, experimental observations and phenomenological models of importance for this work will be introduced in more detail (chapter 1) before the NA49 experiment is introduced (chapter 2) and methods for the analysis of the investigated particles are explained (chapter 3). After the definition (and study by FRITIOF simulations) of the inelasticity selection in p+p interactions by means of the charged-particle multiplicity or the Feynman-x of the leading proton, the centrality of the recorded C+C and Si+Si interactions is determined (chapter 4). Finally, results are presented for p+p (chapter 5), C+C and Si+Si collisions (chapter 6) and extensively discussed (chapter 7).

1.2 Basic concepts

Today, the so-called *Standard Model* of particle physics is widely accepted as an adequate or even the correct theory describing matter as being built up from fundamental particles interacting by four types of forces. To be more specific, only the strong and electro-weak interaction are included in the model, the latter being a unification of electromagnetic and weak force. Gravitation plays practically no role in the systems normally considered in particle physics. Some characteristic properties of the interactions and particles are given in tables 1.1 and 1.2.

force	typical range [m]	dimensionless coupling-constant α	carrier
gravitation	∞	10^{-38}	graviton
electromagnetic	∞	10^{-2}	photon
weak	10^{-18}	10^{-5}	W^\pm, Z^0
strong	$\leq 10^{-15}$	$\lesssim 1$	gluons

Table 1.1: Fundamental forces, their range and carriers [1].

The basic building blocks of matter are quarks and leptons, both spin $\frac{1}{2}$ fermions. For each particle an antiparticle exists with the same mass and spin, but with the inverse of electric charge and charge-like properties. Leptons take part in the electro-weak and quarks in the strong and the electro-weak interaction. So they both carry electric and weak charge. Quarks carry in addition the strong charge called *color*; it has three values, usually denoted as blue, green and red. Leptons are divided into three families, each consisting of an electrically charged (electron-type) and neutral (neutrino) lepton. The six known quarks differ in their flavor named *up*, *down*, *strange*, *charm*, *bottom*, and *top*, each flavor representing another mass eigenstate. In contrast to the strong force, the weak interaction allows transitions between the flavors.

The physics of the strong interaction is described by the theory of quantum chromodynamics (QCD). The corresponding field quanta – massless bosons named gluons – also carry color which leads to interactions among themselves. Thus, at larger distances, the spatial structure of the color field is different from that of the well known electromagnetic field: It does not spread isotropically into space, but

quarks	mass [MeV]	charge	leptons	mass [MeV]	charge
up (<i>u</i>)	1.5 - 4.5	$2/3 e$	electron (<i>e</i>)	0.511	$-1 e$
down (<i>d</i>)	5 - 8.5	$-1/3 e$	e-neutrino (ν_e)	$< 3 \cdot 10^{-6}$	$0 e$
charm (<i>c</i>)	1000 - 1400	$2/3 e$	myon (μ)	105.66	$-1 e$
strange (<i>s</i>)	80 - 155	$-1/3 e$	μ -neutrino (ν_μ)	< 0.19	$0 e$
top (<i>t</i>)	$(174.3 \pm 5.1) \cdot 10^3$	$2/3 e$	tau (τ)	$1776.99^{+0.29}_{-0.26}$	$-1 e$
bottom (<i>b</i>)	4000 - 4500	$-1/3 e$	τ -neutrino (ν_τ)	< 18.2	$0 e$

Table 1.2: Fundamental particles, their mass and charge [2].

the attraction of the gluons leads to the formation of flux tubes or *strings* (see illustration in fig. 1.2).

The special features of the strong interaction yield a coupling constant $\alpha_s(q^2)$ which increases with distance, or in other words decreases with momentum transfer q , because small distance scales correspond to large momentum transfers in interactions. In the limit of large q^2 the coupling constant α_s goes to 0 and quarks act as free particles (*asymptotic freedom*). In general, for small values of α_s , i. e. for so-called *hard* processes, a perturbative treatment of QCD is adequate. For large coupling constants this technique is not applicable. For all these *soft* processes, which unfortunately are the vast majority of the real interactions – also those of interest for this work – reactions cannot be calculated from first principles. To partially overcome this problem either phenomenological models are applied or the system is examined on a discrete lattice of space and time.

Phenomenological models were developed for a broad field of applications. The *confinement* of quarks in hadrons, which is probably connected with the behavior of α_s for small q^2 , is for example described by the bag model. Some phenomenological models for hadron-hadron reactions will be introduced in section 1.4.

In lattice QCD, quantum chromodynamics is formulated on a discrete lattice of space-time coordinates. This lattice provides a shortest distance scale and therefore a maximum momentum scale for the calculations. Integrals that diverge for large momenta are finite here. With the help of Monte-Carlo techniques calculations are performed for different numbers of lattice points, compared with expectations from perturbative QCD and extrapolated to the continuum case [3]. But since one aims at a high density of space-time points on the lattice, these calculations need large computer memory and speed. Although computational power has increased enormously during the last years, lattice QCD calculations are still restricted to closely defined topics and are mostly performed assuming massless particles or baryon number density zero.

Quarks form composite systems bound by the strong interaction. Only color-neutral states have been observed up to now: quark-antiquark pairs (mesons) and three-quark or three-antiquark systems (baryons). In particular, single quarks have never been isolated (*confinement*). From 2-jet events at the $p\bar{p}$ -collider (SPSC) at CERN (large q^2 , small r), from the linear increase of spin J with M^2 for hadronic resonances of mass M (small q^2 , larger r , see also formula 1.10, section 1.4.4), and

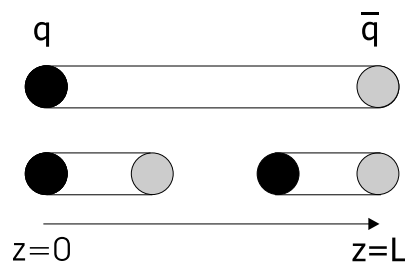


Figure 1.2: Illustration of the color flux tube (string) between a quark-antiquark pair and the creation of a new $q\bar{q}$ -pair.

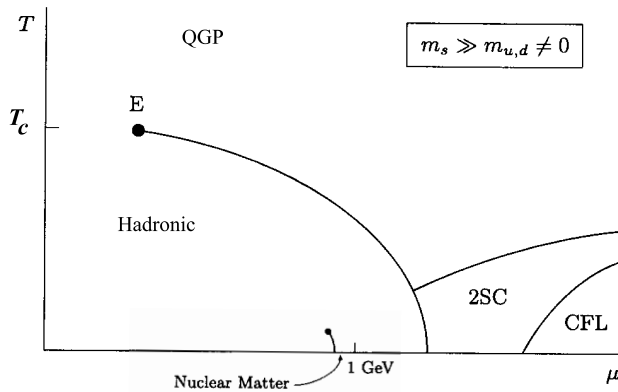


Figure 1.3: Qualitative phase diagram of strongly interacting matter. Here, the phase transition between hadronic matter and the quark-gluon plasma is of first order for large baryochemical potential μ up to the critical point E , at E of second order, and a crossover from E till $\mu = 0$. The critical temperature T_c is about 170 – 175 MeV. At large μ superconducting phases (2SC, CFL) are indicated, quarks are expected to form Cooper pairs there. (From [4].)

from the spectra of the *quarkonia* $c\bar{c}$ and $b\bar{b}$, a functional form

$$V(r) = -\frac{4}{3} \frac{\alpha_s}{r} + \kappa \cdot r \quad (1.1)$$

of the potential of the strong interaction between 2 quarks is derived [1]. The linear increase of the potential for larger r leads to an infinite separation energy of quarks ($\kappa \approx 1$ GeV/fm). Therefore new quark-antiquark pairs are produced when separating two quarks whenever this becomes energetically favorable (see illustration in fig. 1.2).

Protons and neutrons as the baryons with the lowest mass form nuclei. On the other hand, for high temperatures or large baryon densities a *deconfined phase* of quark matter is expected, the quark-gluon plasma (QGP) with quarks acting as quasi-free particles. A qualitative phase diagram of matter in dependence on these two variables, temperature T and baryochemical potential μ , is presented in figure 1.3. On the bottom, a phase transition from nuclear matter "liquid" to the hadron gas with a critical point at a temperature on the order of 10 MeV is indicated. This temperature is characteristic for the forces which bind nucleons into nuclei. The phase transition between the hadron gas and the QGP is presented above;

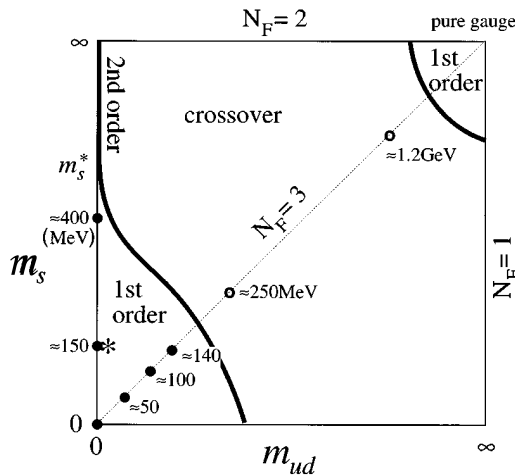


Figure 1.4: Order of the phase transition at $\mu = 0$ in dependence on the masses of up, down and strange quark. The phase transition is of first order in this calculation and marked with a star (*physics point*). (From [5].)

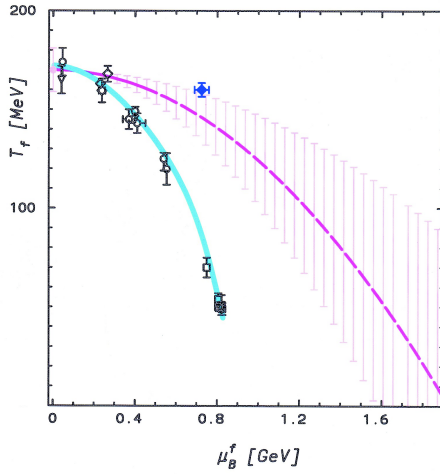


Figure 1.5: Phase diagram of hadronic matter with experimental data as open symbols and the common freeze-out condition (grey thick line) of $\langle E \rangle / \langle N \rangle = 1$ GeV. The endpoint of Fodor and Katz [8] is given as filled diamond (more details on next figure). Calculations of Allton et al. [9] are presented by the dashed line with vertical error bars. (From [10].)

depending on T , μ and the quark masses it may be of first or second order, or a crossover.

Within lattice QCD the critical temperature and the order of the phase transition at vanishing baryochemical potential ($\mu = 0$, i. e. also zero baryon density) can be calculated. Recent results give 170 MeV – 175 MeV as critical temperature [6], but the order of the phase transition is not clear yet. It depends on the number of quarks considered and their masses (fig. 1.4). Recent calculations seem to converge to a crossover (e. g. [7], [8]) at the so-called *physics point*, but a first-order phase transition (e. g. [5]) is not ruled out yet. A first-order phase transition is defined by a discontinuity in the first derivative of the free energy F which corresponds to a jump in the entropy. $\partial F / \partial T$ is related to the energy density ϵ , thus a first-order phase transition leads to a discontinuity of $\epsilon(T)$. For a second-order transition the entropy is continuous, but the second derivatives of the free energy are not, e. g. the specific heat. A crossover implies a fast but smooth change of physical variables.

Until recently such calculations could only be performed at vanishing baryochemical potential ($\mu = 0$), but new developments allow also for calculations at $\mu \neq 0$ [8, 9] (fig. 1.5 and 1.6). The calculated phase border of Fodor and Katz [8] is (starting from large μ) of first order till the end point E and a crossover from then

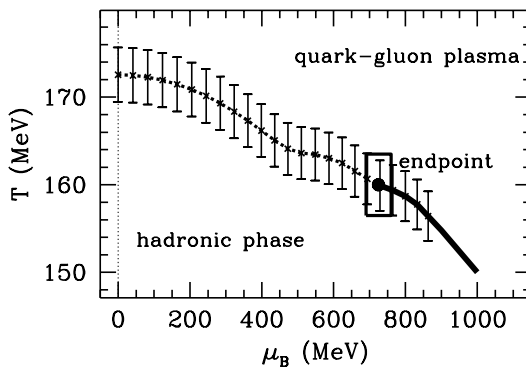


Figure 1.6: Phase diagram with calculated crossover (dotted) and first order phase transition (full line). The errors on the endpoint (critical point) are indicated by the box, the phase transition is of second order there. (From [8].)

on. At the critical point, whose location is sensitive to the strange quark mass, the phase transition is of second order.

These lattice calculations provide not only a critical temperature at which the phase transition to the quark-gluon plasma phase may occur, but also predict a critical energy density on the order of $\epsilon_c \approx 1 \text{ GeV}/\text{fm}^3$.

The phase diagram of matter is not only a theoretical exercise, but it is believed that in the very early universe the conditions were such that the baryon density was close to zero and the temperature extremely high. Therefore the universe would have been in the state of a quark-gluon plasma which was then transformed into a hadron gas while expanding and cooling. On the other hand the baryon density inside neutron stars might be high enough to also result in a state of deconfined matter.

As will be addressed in the next chapter and is already indicated by the grey thick line in fig. 1.5 a large region of the phase diagram of hadronic matter is accessible by heavy-ion collisions and can be explored by experiments. The question is whether a quark-gluon plasma can be achieved in the course of the collision and how this can be diagnosed.

1.3 Strongly interacting matter in experiments

The strong interaction and properties of matter can be investigated in high-energy collisions between leptons, hadrons or nuclei. e^+e^- annihilation into hadrons represents the cleanest tool to study particle production, because in contrast to proton-proton collisions no remnants from the input channel exist and the whole center-of-mass energy of the collision is used for the creation of new hadrons. Nucleus-nucleus collisions allow the investigation of dense, strongly interacting multiparticle systems. In particular, the creation of a quark-gluon plasma is searched for in these interactions. Proton-proton, or more general hadron-hadron collisions, are used to understand hadron production in a "simple" hadronic environment and as a comparison for nucleus-nucleus reactions.

1.3.1 e^+e^- annihilation into hadrons

Over many years, e^+e^- collisions were studied at the Stanford Linear Accelerator (SLAC), at DESY and the LEP collider at CERN. They represent a precise approach to study the electro-weak interaction and to compare experimental results with predictions and calculations from the Standard Model. No significant deviation has been found up to now. Also the production of a quark-antiquark pair in the e^+e^- annihilation process can be quantitatively calculated in this framework. The produced $q\bar{q}$ -pair starts the hadron production driven by the strong interaction.

From the investigations of these collisions the commonly accepted model for particle production by the strong interaction evolved (see fig. 1.2 and section 1.4). It is based on string formation and string fragmentation, the string representing

the color field between the quark-antiquark pair created in the e^+e^- annihilation process. The $q\bar{q}$ -pair is flying apart fast after production and expands the string until fragmentation into more $q\bar{q}$ -pairs. This concept can also be applied to hadron-hadron collisions, if one assumes that collision energy is partially stored in expanding color fields between the quarks forming the hadrons.

1.3.2 Hadron-hadron collisions

Hadron-hadron reactions have been studied over already a few decades in fixed-target or collider experiments; e.g. at Fermilab, Brookhaven National Lab (BNL), CERN or Dubna to mention a few facilities. Besides proton-proton interactions also pion-proton and kaon-proton or neutron-proton reactions were investigated in great detail. Therefore their global features are well known over a rather broad range of energy. Unless otherwise noted in this section, proton-proton interactions shall be taken as example for hadron-hadron collisions. Emphasis is put on the energy range and features of proton-proton reactions which are of interest for this work.

The total proton-proton interaction cross section is rather constant over a large range of energy (figure 1.7); it lies around 40 mb for laboratory beam momenta from 4 GeV to 2000 GeV, which corresponds to center-of-mass energies of 3 GeV to 60 GeV. From 60 GeV beam momentum on (~ 10 GeV center-of-mass energy), the elastic cross section is about 18 % of the total, but this fraction increases for lower momenta until below 1 GeV nearly all collisions are elastic. In inelastic

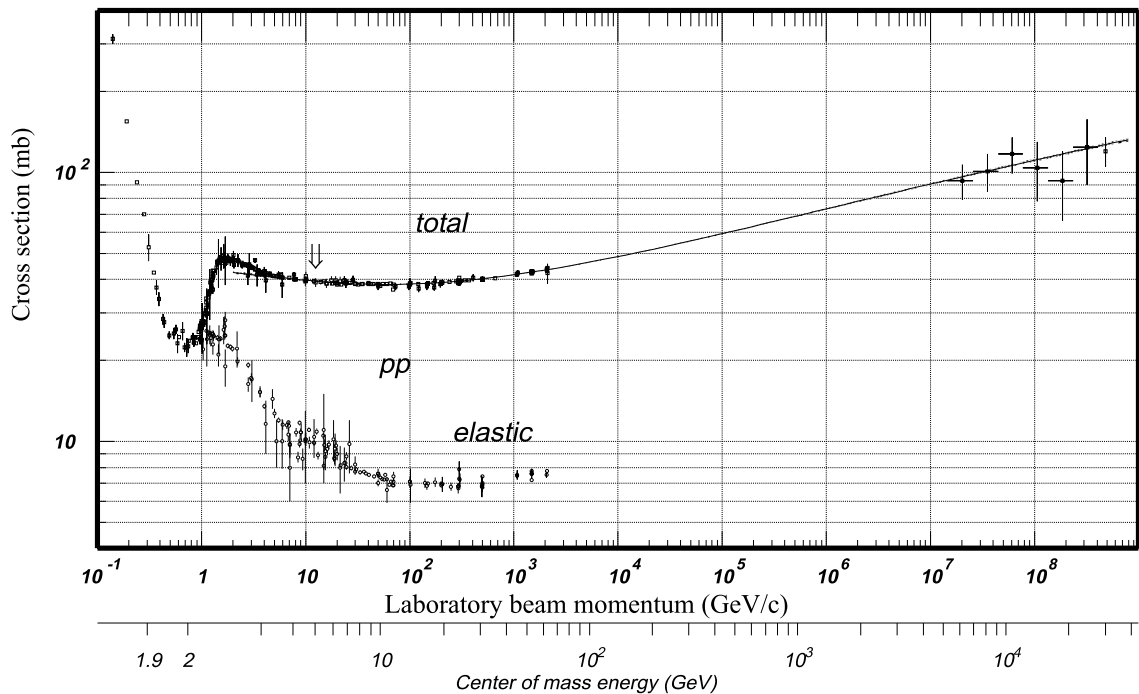


Figure 1.7: Total and elastic proton-proton cross section as function of beam momentum and center-of-mass energy. The line represents a parametrization suggested by Regge theory (for details see [2]). (From [2].)

interactions the interaction partners might lose a substantial fraction of their energy, which is used for particle production. One usually divides inelastic interactions into diffractive and non-diffractive ones. This classification is not exact and well defined; diffractive reactions account for roughly 10% of the inelastic events and essentially excite the projectile or target: The protons lose only a small fraction of their energy and basically only a few pions are produced by the decay of excited baryonic resonances.

Neutron-proton interactions have approximately the same cross section as proton-proton collisions whereas in pion-proton reactions the cross section is reduced to $\sim 2/3$ of the one in proton-proton; obviously this corresponds to the difference in the quark content. This is one of the observations that promoted the idea of the additive quark model where $\frac{1}{3}$ of the proton-proton cross section is assigned to the individual valence quarks of hadrons (chapter 1.4.4).

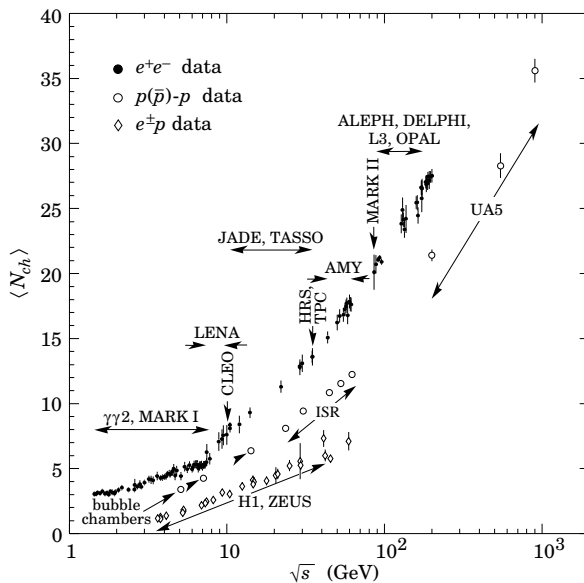


Figure 1.8: Charged-particle multiplicity in e^+e^- and inelastic $p+p$ reactions. (From [2].)

The charged-particle multiplicity of the produced particles is shown in figure 1.8, it is found to increase slowly with the center-of-mass energy (note the logarithmic x-axis). After the decay of short-lived resonances about 80-90 % of the produced particles are pions. In addition kaons, (anti)baryons, leptons and photons are found. The rapidity¹ distributions of most of the final hadrons are peaked around center-of-mass rapidity. For baryons, specifically for those with no or only one strange quark (e. g. protons, neutrons, Λ -baryons), there is a large probability of detecting them in the fragmentation regions, i. e. at large Feynman-x or rapidity. These *leading baryons* resemble the projectiles and very likely they still carry some of their valence quarks. Their energy and the energy available for particle production are closely correlated [11]. The Feynman-x distribution of *net-protons* for $p+p$ interactions in NA49 is presented in figure 1.9. Net-proton spectra are protons minus antiprotons. Assuming that protons and antiprotons are always created in pairs, or at least with

¹Definitions for kinematic variables like rapidity and Feynman-x can be found in appendix A.

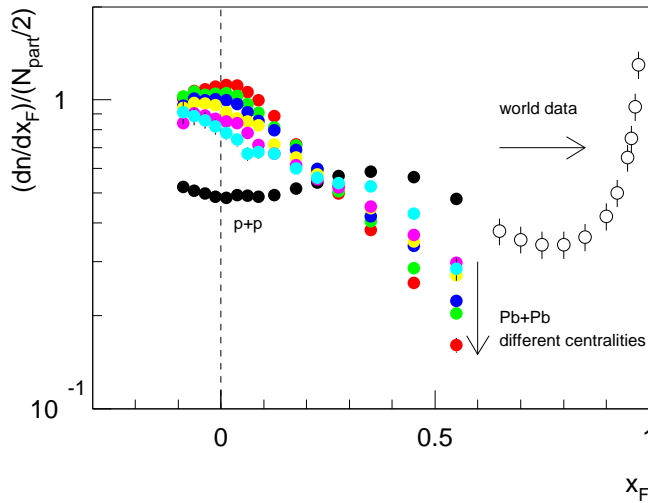


Figure 1.9: Feynman-x distribution of the net-protons in p+p and centrality-dependent Pb+Pb collisions. The centrality is increasing in direction of the arrow. Filled symbols present data from NA49 [12], open ones are a compilation of p+p data from other experiments [13].

the same yield and momentum distribution, this operation yields the distribution of protons originating from the projectile. Besides the diffractive peak near $x_F = \pm 1$ their Feynman-x distribution appears to be rather flat which holds for a broad range of energies [3]. The mean value of Feynman-x is about $\pm 1/2$ which indicates that on average in inelastic non-diffractive collisions the protons lose about half of their center-of-mass energy. This energy is available for particle production.

This assumption is supported by the observation that the charged-particle multiplicity in $e^+ + e^-$ collisions is larger than in p+p interactions at the same center-of-mass energy (see fig. 1.8). In contrast to p+p collisions in $e^+ + e^-$ the whole energy is available for particle production. Defining an effective center-of-mass energy for p+p collisions, i.e. extracting the energy in fact available for particle production, Basile et al. [11] demonstrated that average multiplicities of $e^+ + e^-$ and p+p data match. The same will be shown for the NA49 data in chapter 5.2.3.

1.3.3 Nucleus-nucleus collisions

The field of high-energy nucleus-nucleus collisions is the youngest of those discussed here. The recently active facilities ordered by increasing energy are SIS at GSI (Darmstadt, Germany), AGS at BNL (Brookhaven, USA), SPS at CERN (Geneva, Switzerland) and RHIC at BNL; a future project is LHC at CERN.

When nuclei traverse each other the nucleons undergo several sequential N+N collisions. This is a fundamental difference compared to hadron-hadron interactions as also is rescattering between the produced particles. Calculations taking into account the geometrical configuration and the known p+p and n+p cross sections (see section 1.4.4) yield about 2-5 collisions on average per participating nucleon. This number depends on the mass and impact parameter of the colliding nuclei. Considering the fact that in high-energy interactions the nuclei are longitudinally contracted, e.g. by a factor of about 9 in the center-of-mass system for collision energies of $\sqrt{s} = 17.3$ GeV, these multiple collisions occur within a very short time range, which is about 1-2 fm/c in the rest frame of the collision. The naive expecta-

tion that multiple N+N interactions in high-energy collisions might be regarded as simple superpositions of single ones is thus questionable. Particle production from the first collision is certainly not finished, when the second interaction takes place. It may not even have started.

In the course of these interactions each nucleon loses a large fraction of its kinetic energy which is deposited in a small reaction volume. The achieved energy density ϵ is estimated to be about $3 \text{ GeV}/\text{fm}^3$ for central Pb+Pb collisions at the SPS [14] and $\sim 5 \text{ GeV}/\text{fm}^3$ for central Au+Au collisions at RHIC [15, 16]. Both values are thus above the critical energy density calculated by lattice QCD for the creation of a deconfined phase. This energy loss of the nucleons is visible in the rapidity or Feynman-x spectra of the net-protons (fig. 1.9): Compared to proton-proton collisions a clear shift of the average Feynman-x towards the center of mass ($x_F = 0$) is observed, which is indicated by the increased steepness of the distribution. This so-called *stopping* is larger in systems where the mean number of collisions per nucleon is large, i. e. in the more central Pb+Pb interactions. It is expected that also the energy density created in the particle emitting system, the so-called *fireball*, increases with larger energy loss of the incoming nuclei.

In central Pb+Pb collisions at 158 AGeV about 1500 charged hadrons are produced on average, for p+p collisions at this energy the mean charged-particle multiplicity is 7.2. Therefore elastic and inelastic interactions between the produced particles (*rescattering*) are expected to be much more abundant in Pb+Pb. Such a rescattering phase may influence the rate of particles in the final state (see section 1.3.4).

At small collision energies the interacting nuclei are fully stopped leaving a baryon rich region in the center of mass of the interaction (Landau-picture, fig. 1.10(a)), e. g. in Au+Au collisions at AGS. On the other hand at very large energies as they are reached at RHIC, the nuclei are still fast enough to escape

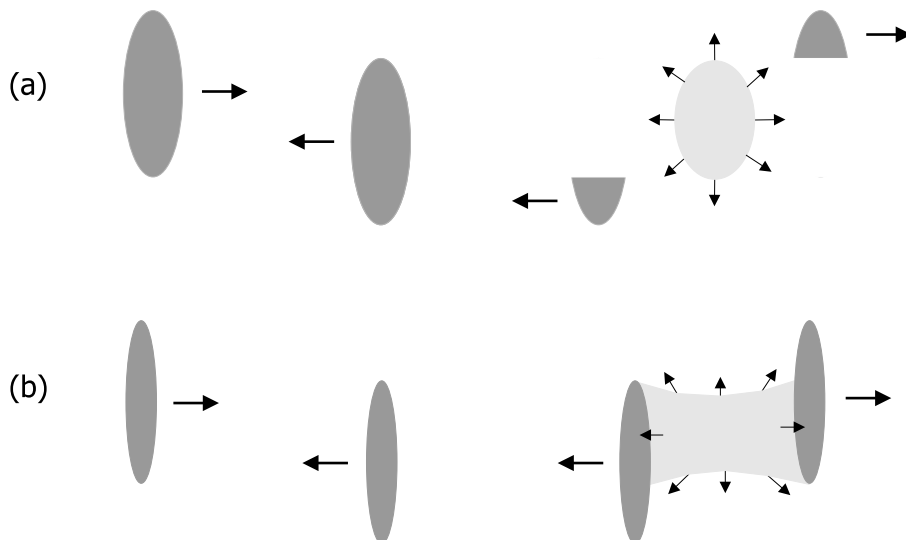


Figure 1.10: Illustration of the Landau (a) and Bjorken (b) picture of A+A collisions.

nearly completely from the interaction region even if they suffered a high energy loss. The result is an almost baryon-number free region in which a large amount of energy is deposited (Bjorken-picture, fig. 1.10(b)), much more than in the case of a baryon rich region at low collisions energies. Depending on temperature, baryon and energy density in the interaction region the phase boundary to the quark-gluon plasma might be crossed in the course of the reaction.

Bjorken [17] has given a simple estimate of the energy density reached in central A+A collisions. It depends on the radius R of the colliding nuclei, the hadron formation time τ (assumed to be 1 fm/c) and the rapidity density dN/dy and mean transverse masses of the produced particles:

$$\epsilon = \frac{m_t}{\tau \pi R^2} \cdot \frac{dN}{dy} \Big|_{y=y_{CM}} \quad (1.2)$$

The space-time evolution of a heavy-ion collision with or without formation of a quark-gluon plasma is illustrated in figure 1.11. In both cases first a formation time is needed before either a hadron gas or a quark-gluon plasma is created. It is still an open point whether the time scales are large enough for thermal and/or chemical equilibration either in the hadron gas or in the partonic phase. Characteristic for the hadron gas are frequent interactions (rescattering) which can change the kinetic

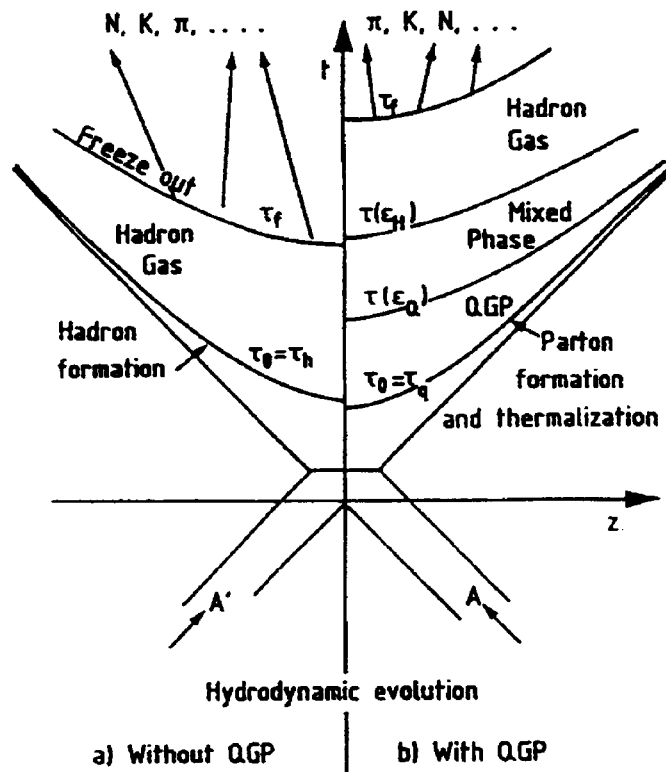


Figure 1.11: Space-time diagram of A+A collisions without (a), and with (b) formation of a quark-gluon plasma. (From [18].)

properties via elastic and the particle composition of the system via inelastic interactions. The *freeze-out* occurs if the particle density dropped enough that particles stop interacting. In this context *chemical* and *kinetic* freeze-out have to be distinguished: the first occurs when the particle composition is not changed anymore by inelastic collisions, the second when the kinematic distributions are fixed and elastic interactions fade out. Since at low energies elastic cross sections are larger than the inelastic ones, it is reasonable to assume that the chemical freeze-out occurs first. Indeed, this is supported by models (see section 1.4.5 for a more detailed discussion). Freeze-out times might be different for various particle species because of the different cross sections.

The difficult task is to conclude from the abundances of particles measured in the experiment, their momentum distributions and correlations, whether a quark-gluon plasma was formed or not. A variety of signatures which should survive the rescattering in the hadron gas were proposed (find a summary e.g. in [3, 19]). A few famous ones are: J/ψ suppression because of Debye screening, direct photons from the QGP which survived or have decayed into a lepton pair, or strangeness enhancement compared to proton-proton collisions. The latter will be discussed in more detail in the next section because of its relevance for this thesis. Besides those signatures HBT studies or the analysis of directed and elliptic flow of particles give information about size, lifetime and shape of their source.

1.3.4 Strangeness

Strangeness is not present in the valence quarks in the entrance channel of a N+N or A+A interaction, but is newly produced and shows up in the strange hadrons in the final state. Its production in string fragmentation is suppressed compared to that of new up and down quarks because of the higher mass of the strange quark (see e.g. the Schwinger formalism in section 1.4.2, equation 1.3). In p+p collisions at $\sqrt{s} = 17.3$ GeV the measured relative production rate expressed by the Wroblewski

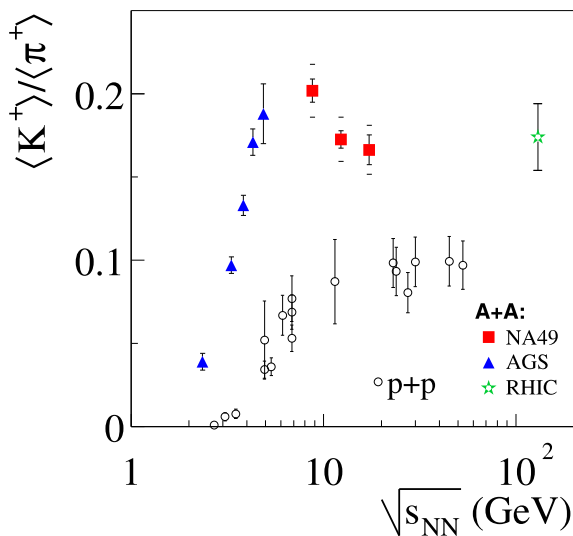


Figure 1.12: Energy dependence of $\langle K^+ \rangle / \langle \pi^+ \rangle$ ratio in p+p and central A+A collisions. At AGS and RHIC central collisions of Au+Au were investigated, the RHIC value is for midrapidity only. NA49 at SPS took data of central Pb+Pb interactions. (From [20].)

factor $\lambda_s = \frac{2\langle s\bar{s} \rangle}{\langle u\bar{u} + d\bar{d} \rangle}$ is about 0.2 [21].

In a hadron gas strangeness is produced (and destroyed in the reverse reactions) in processes like $\pi + \pi \rightarrow K + \bar{K}$ and $\pi + N \rightarrow \Lambda + K$, the reaction with the lowest threshold energy (~ 670 MeV) being the reaction $N + N \rightarrow \Lambda + K + N$. The equilibrium value of λ_s depends strongly on temperature and baryochemical potential μ_B , see e. g. [22, 23, 24], but is expected to be larger than in p+p collisions.

Still different is strangeness production in a QGP. Here $s\bar{s}$ -pairs are created via gluon fusion or $q\bar{q}$ annihilation. The required energy is reduced to $2m_s \approx 300$ MeV. The relative production rate in equilibrium compared to $u\bar{u}$ and $d\bar{d}$ depends on temperature and baryochemical potential, but also on the quark masses [22, 23, 24]. In addition, the number of degrees of freedom is larger in a QGP than in a hadron gas. Kapusta and Mekjian have shown that therefore the equilibrium strangeness per entropy is lower in a QGP compared to a hadron gas at the same temperature [24].

Besides the equilibrium rates, time constants for equilibration in both, the hadron gas and the QGP, in relation to the time span available in A+A collisions play an important role for any estimate of λ_s in the final state of a nucleus-nucleus interaction. In any case a strangeness enhancement in comparison to p+p collisions is expected. The amount depends on assumptions about the rescattering phase and whether a QGP is created.

Experimental data are available for a large range of energies and various particle species, see e. g. [26, 27, 28] for recent results. At all center-of-mass energies a strangeness enhancement is observed in A+A collisions relative to p+p. Two im-

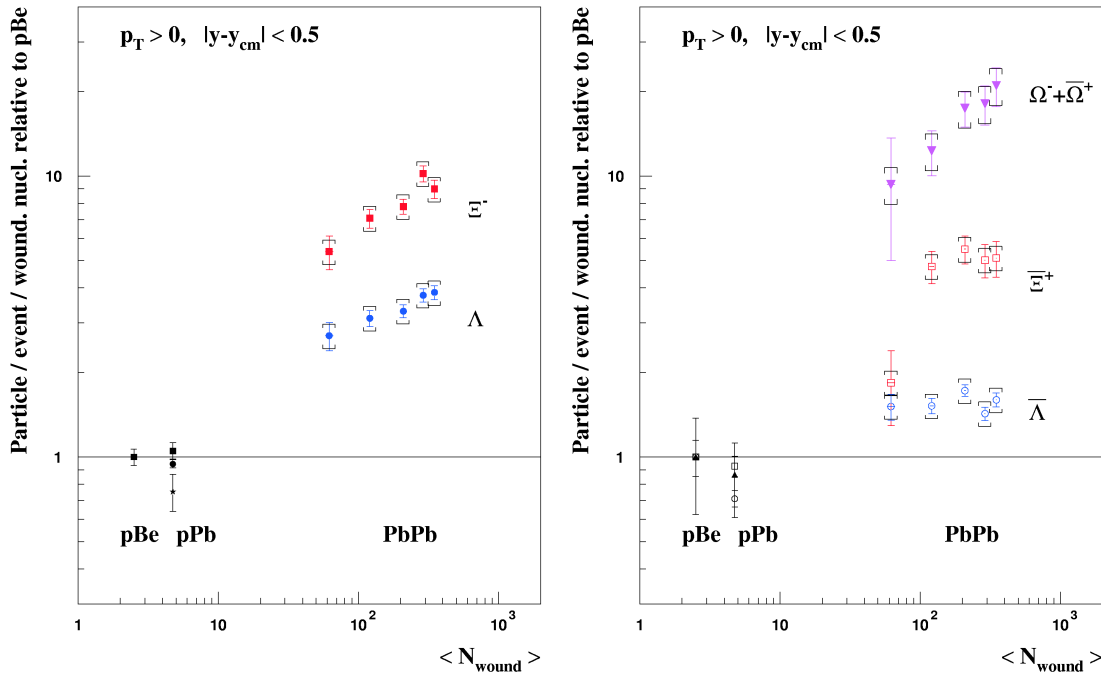


Figure 1.13: Centrality dependence of strange (anti-)baryons as measured by the NA57 experiment in Pb+Pb collisions at 158 AGeV at midrapidity. (From [25].)

portant experimental results are presented in figures 1.12 and 1.13. The $\langle K^+ \rangle / \langle \pi^+ \rangle$ ratio is, in a first approximation, proportional to λ_s . Its energy dependence shows a maximum at a center-of-mass energy around 7-9 GeV. This can be interpreted as the onset of deconfinement in A+A interactions [29]: The strangeness content increases significantly with energy in case of a hadronic mechanism ($\sqrt{s} \lesssim 5$ GeV), but it has a rather constant value in presence of a partonic phase ($\sqrt{s} > 15$ GeV). In the transition region ($\sqrt{s} \sim 9 - 15$ GeV) the $\langle K^+ \rangle / \langle \pi^+ \rangle$ ratio changes from the (higher) hadron gas value to the (lower) level from a partonic phase. The same data can also be parametrized on the basis of a pure hadron gas model (see section 1.4.5). In fig. 1.13 baryons with different strangeness content are compared; a hierarchy of strangeness enhancement is observed. In addition, an increase of strangeness enhancement with centrality is measured.

1.4 Particle production in models

1.4.1 Overview

As discussed in chapter 1.2 a large fraction of the produced particles stems from soft interactions which cannot be calculated from first principles of QCD. Therefore one tries to understand and describe these processes with phenomenological approaches. In general one has to distinguish between microscopic and statistical models. Both are successful in modelling many experimentally observed features.

Microscopic models propagate individual particles through a cascade of collisions and decays. Important input in these models are cross sections for all possible interaction types and assumptions on the resulting kinematic distributions.

The first step is the description of a "simple" nucleon-nucleon collision. Particle production is assumed to stem from string fragmentation, which is investigated in its pure form in e^+e^- interactions. In p+p collisions at the ISR jet structures similar to those already known from e^+e^- annihilation into hadrons were observed (see e.g. [30]). This leads to the important idea that the basic mechanism of hadron production is the same in both cases. Therefore, models for string fragmentation could be adopted from e^+e^- reactions. Additional assumptions concerning string formation and the behavior of the valence quarks are necessary for hadron-hadron interactions. All models are tuned to fit p+p data, especially the particle yields in dependence on energy [31, 32, 33, 34]. Momentum distributions do not always compare well to the data, see e.g. the proton x_F -distribution from the FRITIOF model in appendix C. As a second step, interactions of nuclei are implemented as superpositions of nucleon-nucleon reactions. Depending on the model additional string-string interactions in a region of high string density might be included.

Statistical models treat the collision system as a whole as statistical ensemble in local thermal equilibrium. This way information about all single processes is lost, but the final state of an A+A interaction can be described successfully with a small set of macroscopic parameters.

In this section, some of the main ideas and their implementation in models and computer codes are discussed. Special emphasis is put on those which are used later in the discussion and interpretation of the data analyzed in this work.

1.4.2 Schwinger mechanism

The Schwinger mechanism represents a basic concept for understanding particle-antiparticle production in fields of high strength due to electromagnetic or strong interactions. New particles are produced in a quantum-mechanical tunnelling process in a static field according to Dirac's particle-hole theory.

For larger distances, the potential in between two quarks can be described by a linear field with the string tension $\kappa \approx 1 \text{ GeV/fm}$ as proportionality constant (section 1.2, formula 1.1).

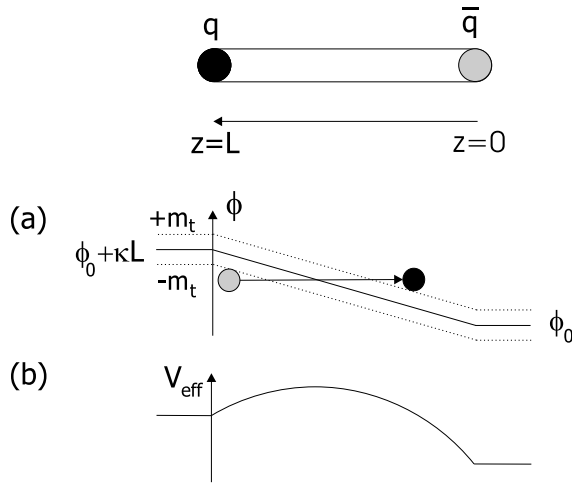


Figure 1.14: Schwinger mechanism: illustration of a quark-antiquark pair with a separation of length L . The static potential (a) $\phi = \kappa z$ of the Dirac equation, or (b) the effective potential V_{eff} of the Schrödinger equation is restricted to the color flux tube in between them. In (a) the tunnelling process yielding a new quark-antiquark pair is illustrated. (After [3].)

Separating the quarks results in a higher energy which is stored in the color flux tube. If the energy is large enough, production of new particles becomes possible and increasingly favorable. The tunnelling probability can be calculated, either with the Dirac equation or with the Schrödinger equation and an effective potential V_{eff} (figure 1.14). The resulting penetrability reads²

$$P = \exp\left(-\frac{\pi(m^2 + p_t^2)}{\kappa}\right). \quad (1.3)$$

The production probability rises for small masses and small transverse momenta. This leads to a Gaussian transverse momentum distribution of the quarks [3]:

$$\frac{dN}{dp_t} = \text{const} \cdot \exp\left(-\frac{\pi p_t^2}{\kappa}\right) \quad (1.4)$$

These findings correspond to the intuitive feeling that particles with higher energy in terms of mass or transverse momentum are less frequent. It is instructive and useful

²Note that $\hbar = c = 1$ is used in this formula. Including all units leads to $P = \exp\left(-\frac{\pi}{\hbar c \kappa} ((mc^2)^2 + (p_t c)^2)\right)$.

for the later discussion of the data to calculate the ratio of strange to up/down-quark production probabilities assuming the same p_i :

$$\frac{P_{s\bar{s}}}{P_{u\bar{u}/d\bar{d}}} = \exp\left(-\frac{\pi(m_s^2 - m_{u/d}^2)}{\kappa}\right) \quad (1.5)$$

In this approach the ratio of strange to non-strange particles depends on the mass differences between the quarks and the string tension κ . Both might change in an environment with high energy density, and might therefore be different in N+N and A+A collisions.

1.4.3 String models

In the modelling of high-energy collisions of hadrons or nuclei the static string picture of the Schwinger mechanism is not directly applicable, but a description of dynamical strings formed in interactions is needed. In a microscopic picture strings are stretched between quark-antiquark or quark-diquark pairs in the course of the interaction. Through formation of quark-antiquark or diquark-antidiquark pairs the fragmentation of these dynamic string segments results finally in new particles.

To describe hadron-hadron interactions one therefore basically needs mechanisms for string excitation (formation) and fragmentation. Both are treated differently in the various models. Modelling A+A collisions, nuclei are initialized with a proper nucleon density and multiple interactions between single nucleons are calculated. Additional rescattering of produced particles is also implemented in some models.

There exist two main concepts for understanding and modelling a soft hadron-hadron interaction resulting in an excited string (fig. 1.15). In the first, many small

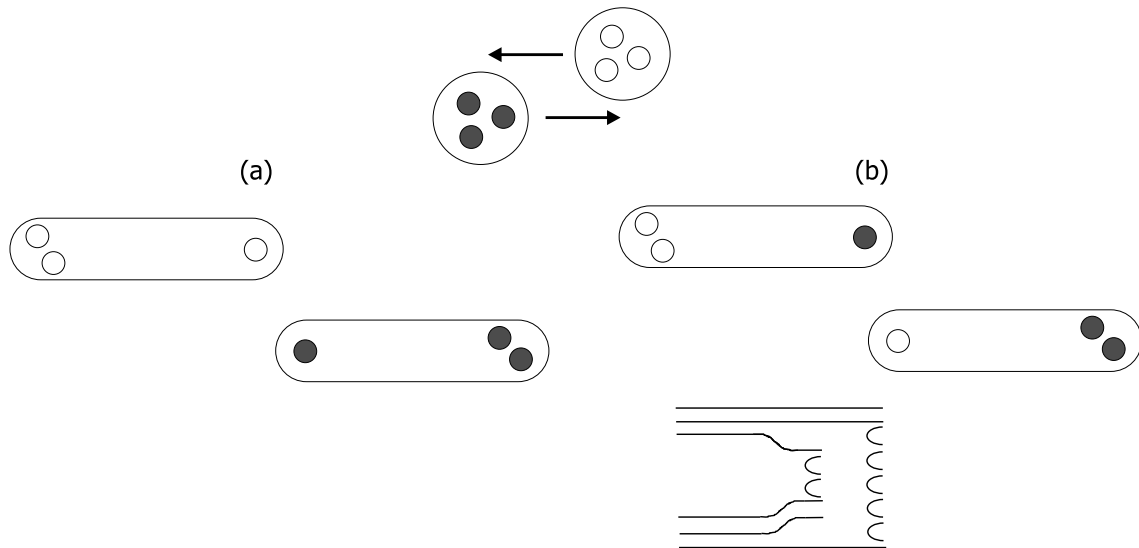


Figure 1.15: Illustration of a N+N collision: (a) strings after interaction via momentum exchange (e.g. FRITIOF), (b) after color exchange (e.g. VENUS). For (b) a typical visualization in a quark-line diagram is shown.

model	string excitation	fragmentation	A+B interaction	rescattering
VENUS	color exchange	AMOR	AGK	yes
FRITIOF	momentum exchange, long. excitation	LUND	Glauber	no
UrQMD	momentum exchange, long. excitation	Field-Feynman or LUND	transport theory	yes

Table 1.3: Comparison of microscopic models concerning some basic features, for further details see text. Note that the implementation of rescattering is different for VENUS and UrQMD.

momenta are transferred during the interaction, leaving the original hadrons intact but longitudinally excited. In the second, color is exchanged and strings are stretched between quark and diquark (antiquark) across the colliding baryons (mesons) thus reorganizing the original relations. In both cases the two generated strings fragment independently from each other. As a matter of principle they are indistinguishable from each other, the difference in the two concepts lies mainly in the realization of the string-excitation: In the first concept the size of the momentum transfer is needed. In the second concept the energy in the strings results from the momenta of the incoming quarks. Their momentum distributions can be taken from the results of deep inelastic scattering experiments of electrons and protons.

For large energy transfers hard processes are implemented. None of the models discussed in the following allow for string overlap and fusion which might happen if the string density in space and time is high. Such a string fusion is believed to increase the string tension κ which would result in an enhanced production of strange quarks compared to the fragmentation of a "normal" string (see equation 1.5).

The string fragmentation is implemented using various approaches. They will be discussed in context of the models in which they are implemented. But before,

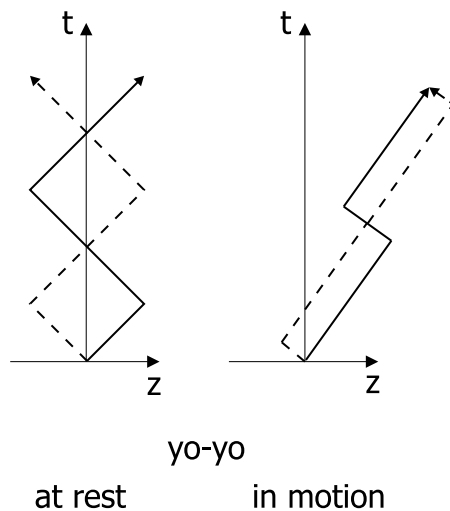


Figure 1.16: Space-time trajectories of quark (solid line) and antiquark (dashed line) of a stable meson with mass m within the yo-yo model of mesons. The area of the rectangle enclosed by the trajectories is the same at rest and in motion and equal to m^2/κ^2 .

the string picture of mesons and baryons shall be introduced because it is used for forming hadrons in the course of modelling the string fragmentation.

In the yo-yo model mesons and baryons are described by (massless) quarks at the endpoints of a string which represents the color field between them. This string is oscillating driven by the constant force $F = -\frac{dV}{dz} = -\kappa$ around its center, this also establishes an illustrative connection between mass and spin of a hadron (see below in context with the VENUS model). The elementary area enclosed by the space-time trajectories of the oscillating quark-antiquark (diquark) pair (fig. 1.16) is a Lorentz invariant and equal to the squared mass of the meson divided by κ^2 . New quarks are created when a string with a large invariant mass breaks up into smaller fragments which have masses of stable particles (fig. 1.18).

1.4.4 Numerical codes for microscopic models

Glauber Model

The Glauber model (see e. g. the description in [3]) is a simplified geometrical model of nucleus-nucleus collisions and serves as basis for most of the advanced microscopic models, e. g. for FRITIOF or VENUS. It is based on the assumption that nucleons inside a nucleus are independent, and that a nucleus-nucleus collision can be regarded as a superposition of independent sequential nucleon-nucleon interactions. Each nucleon is traversing the other nucleus on a straight line and is interacting with the nucleons on its way (fig. 1.17). Cross sections are interpreted as geometric areas and if two nucleons overlap, they interact. Not considered is the possibility that after a nucleon has suffered a collision it might have been excited or destroyed and the remaining baryon might have a cross section differing from that of the original proton or neutron.

In the additive quark model (AQM) cross sections are assigned to the individ-

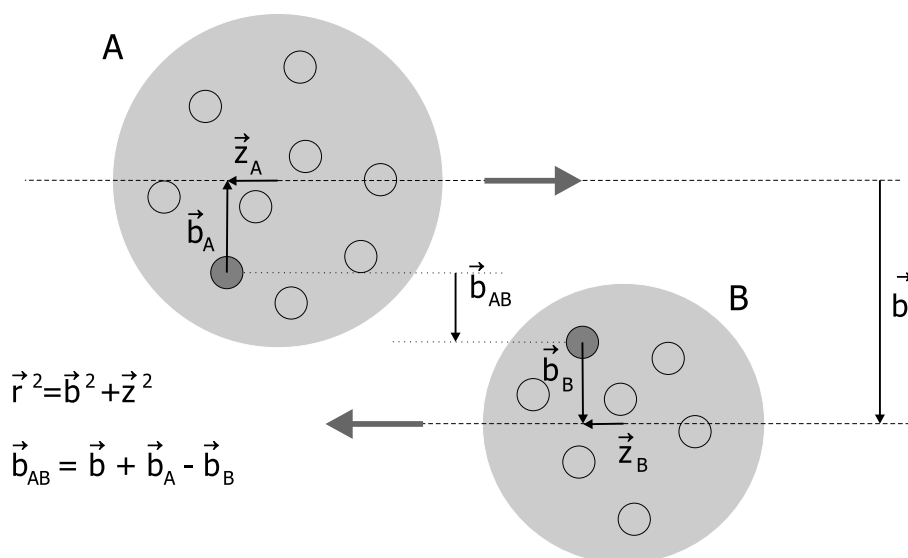


Figure 1.17: Illustration of an A+B collision within the Glauber picture.

ual quarks, thus the cross section for an interaction depends on the valence quark content of the hadrons alone. This can be used to extend the Glauber model providing modified cross sections in sequential nucleon-nucleon collisions. Each valence quark of a nucleon is given a cross section of $\frac{1}{3} \cdot \sigma_{NN}$. Every interaction is assumed to involve one valence quark only which is not available for reactions afterwards anymore, i. e. after one interaction the remaining baryon is left with a cross section of $\frac{2}{3}\sigma_{NN}$ and so on.

The Glauber model can be calculated analytically, or numerically in computer codes as for example in FRITIOF or VENUS. $t(\vec{b})d\vec{b}$ is defined as the probability of a collision between two nucleons at impact parameter \vec{b} (for definitions see also fig. 1.17). The nucleons are distributed in a nucleus according to a density function $\rho(r)$, usually the Fermi distribution is taken:

$$\rho(r) = \frac{\rho_0}{1 + \exp\left(\frac{r-R_{1/2}}{d}\right)} \quad (1.6)$$

$R_{1/2}$ is the half-density radius and d the diffuseness. Both values are tabulated, e. g. in Landolt-Börnstein [35]. The probability of finding a nucleon in the volume element $dbdz$ is $\rho(b, z)dbdz$. The probability dP of a nucleon-nucleon interaction while the nuclei A and B are penetrating each other is written as

$$dP = \rho_A(b_A, z_A)db_Adz_A \cdot \rho_B(b_B, z_B)db_Bdz_B \cdot t(b + b_A - b_B) \cdot \sigma_{NN}. \quad (1.7)$$

Continuing these considerations quantities as the total inelastic cross section σ_{in}^{AB} , the number of wounded nucleons N_{wound} , or the mean number of collisions ν per wounded nucleon can be calculated with only requiring b , $\rho(r)$ and σ_{NN} as input.

FRITIOF

FRITIOF [34] is a Monte Carlo simulation of hadron-hadron, hadron-nucleus, and nucleus-nucleus interactions with string formation via momentum exchange and a string fragmentation according to the LUND model [36] which is based on the ideas discussed before. The exchange of many momenta in a collision between hadrons leaves them longitudinally excited after the interaction. The transverse momentum exchange is considered to be uncorrelated and follows a Gaussian distribution. If the exchanged transverse momenta are large enough, hard processes are taken into account. Gluons may radiate from strings and fragment in a separate chain.

The longitudinally excited hadrons are regarded as strings with the valence quarks attached to the end points (quark-antiquark for mesons, quark-diquark for baryons). Usually the diquark in case of baryons remains fast and ends up in an energetic baryon after fragmentation; this leads to a leading particle effect. The diquark might also be dispersed resulting in larger stopping, because the middle quark usually happens to become a baryon. Strings of projectile and target fragment independently, the fragmentation is modelled within the framework of the LUND model. The basic assumption is here that the vertices of the newly produced quark-antiquark pairs (or diquark-antidiquark pairs to allow for baryon production) lie

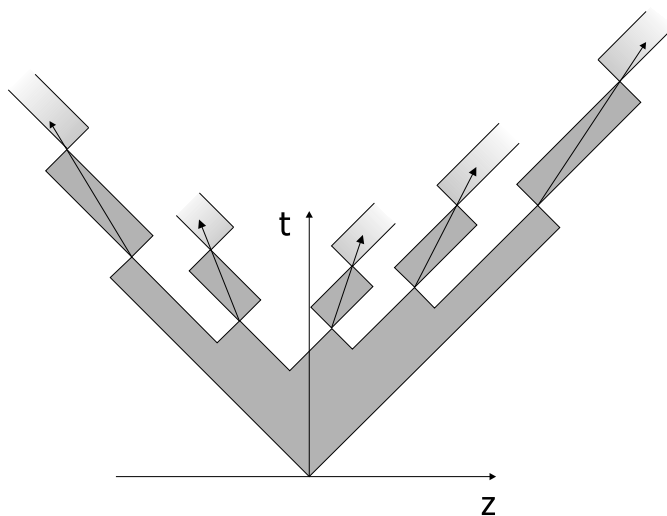


Figure 1.18: Space-time trajectories of quarks and antiquarks in a string fragmentation. Stable mesons are formed in an inside-outside cascade (see text), grey areas illustrate the color field of the strong interaction.

approximately on a curve of constant proper time τ . This time of the order of 1 fm/c is understood as a kind of formation time. As result the particles are produced in a so-called "inside-outside-cascade" in time: the first particles produced are the slowest ones, the last contain the leading quarks. The probability for breakup at a given point is given by Fermi's Golden rule

$$dP = |\mathcal{M}|^2 dn. \quad (1.8)$$

\mathcal{M} is a quantum mechanical transition matrix element and dn the density of the states available. For the simple Lund model one assumes that \mathcal{M} is a constant and $dn \sim dM^2$ (M stands for mass). The generated quarks of neighboring vertices form hadrons in yo-yo states, therefore the hadron mass fixes the area and consequential the distance to nearby vertices (fig. 1.18). Requiring left-right symmetry of the fragmenting string, the scaling function $f_{\alpha\beta}(z, m_t^2)$ can be written as

$$f_{\alpha\beta}(z, m_t^2) = N_{\alpha\beta} \frac{1}{z} (1-z)^a \exp(-bm_t^2/z), \quad (1.9)$$

assuming that the parameter a is the same for each flavor. It describes the probability for a quark with flavor α to combine with an antiquark of flavor β to form a meson with transverse mass m_t and energy-momentum fraction z . The a variable is fixed together with b to best fit the experimental data, both are strongly correlated. $N_{\alpha\beta}$ is a normalization constant. In addition, assumptions about $u : d : s$ quark ratios from parametrizations of e^+e^- data, the scalar to vector meson ratio, and the probability of diquark production enter the fragmentation.

Hadron-hadron collisions are straightforward generalized to nucleus-nucleus interactions. Collisions between nuclei are described in the framework of the Glauber

model. Each of the ν collisions per nucleon is treated in the way as described above for single N+N interactions. The various momentum transfers are simply added while the nucleons continue traversing the nucleus as baryonic state or excited string. Fragmentation into hadrons of these ν times excited string states is performed in the very end, eventually after radiation of associated bremsstrahlung. This implies the assumption that no string fragmentation and therefore also no hadronization takes place in between two collisions. This is justified at high energies because due to time dilatation the string-fragmentation time is expected to be much longer than the time the nucleon needs to pass the nucleus. As improvement of the simple Glauber model the nucleon-nucleon cross sections are implemented energy dependent here. No rescattering of produced particles is realized.

An important input for nuclei is the nuclear density function. In FRITIOF, for nuclei with atomic number $A > 16$ a Woods-Saxon potential is used (see equation 1.6). For nuclei with $A \leq 16$ a harmonic oscillator shell model density is implemented. Fermi-motion for all nucleons is included.

VENUS

The VENUS model (Very ENergetic NUclear Scattering) [33] is based on Gribov-Regge theory (GRT). GRT is a phenomenological model to obtain cross sections of the various processes for soft and semihard hadron-hadron scattering. The concept of Reggeon and Pomeron exchange is used which can be linked to special QCD diagrams. This is an important concept developed from π +N and N+N scattering and resonances observed therein. In principle the VENUS model does not require any free parameters and is completely obtained from model concepts of hadron-hadron interactions.

Basic assumption of GRT is, that hadrons interact either through the formation of intermediate states/resonances (s-channel scattering process) or through the exchange of particles (t-channel scattering process); with $s = (p_1 + p_2)^2 = p_j^2$ and $t = (p_1 - p_3)^2 = p_j^2$ being the usual Mandelstam variables (fig. 1.19). In fact it can be shown that the two descriptions are equivalent.

In N+N and π +N scattering experiments (see [3]) a linear relationship between

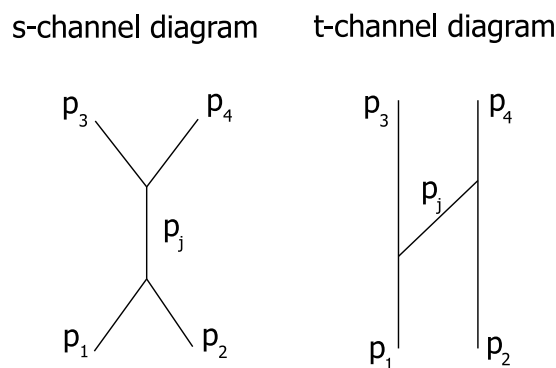


Figure 1.19: s- and t-channel diagram for elastic scattering.

the spin J of the exchanged or created intermediate resonance state and its mass squared M^2 ($= s$) was observed:

$$J(M) = \alpha(0) + \alpha' M^2 \quad (1.10)$$

The straight lines in the corresponding histograms are called Regge trajectories and the set of particles belonging to one intercept and slope is usually referred to as *Reggeon*. The slope parameter is approximately a universal constant with a value of $\alpha' = 1 \text{ GeV}^{-2}$, at least for the trajectories with resonances like N^* , Δ , or ρ , ω .

As a side-remark it might be noted that there is an illustrative connection between spin J and mass M of the discussed resonances. If the hadron is described as a string of length $2L$ rotating around its center with massless quarks at the endpoints, its total energy is $M = \pi\kappa L$ with κ being the string tension coefficient introduced above. On the other hand the angular momentum of the rotating string is $J = \kappa L^2 \pi / 2$ which gives the relation $J = \frac{1}{2\pi\kappa} M^2$. Besides the intercept this is the experimentally observed equation.

At high energies experimental results hint to the exchange of colorless objects with $\alpha(0) = 1$ and $\alpha' \sim 0.4 \text{ GeV}^{-2}$ called *Pomeron*. Up to now these Pomerons could not be observed as isolated resonances but it is speculated that they are connected to glueballs (e. g. [37]).

Amplitudes and thus cross sections for the Feynman-diagrams with Reggeons (fig. 1.19) can be calculated with standard procedures whereas Pomerons are related to more complex diagrams. These are not planar anymore but have a non-planar topology with cylindrical objects representing an exchange of closed strings (fig. 1.20). Cutting such diagrams provides two fragmenting string chains. In the full Gribov-Regge theory much more complex QCD-ladder diagrams are considered. Therefore the model offers a combination of perturbative QCD and classical relativistic string dynamics.

The two string chains (fig. 1.20 and 1.21) are stretched between quark and diquark (antiquark) in between the colliding baryons (mesons) thus reorganizing the original relations which implies an exchange of color in between the interacting hadrons. In VENUS, the momenta of the incoming quarks, which are known from deep inelastic scattering of electrons on protons, determine the energy stored in the string. The diquark remains usually fast providing a leading particle effect. The following string fragmentation is performed using the AMOR fragmentation model (Artru-Menessier Off-shell Resonance model) which does not require each fragment to be a hadron with a discrete mass as the LUND model does. Here a "tree-structure" is applied: a string decays in substrings and so on. If the substring mass is small enough either stable hadrons with discrete masses are formed or resonances which might be off-mass-shell. As for LUND, probabilities for $u : d : s$ quark production as well as for creation of diquark-pairs enter the model.

The extrapolation to collisions of nuclei is again straightforward. A Woods-Saxon potential for the density distribution of the nucleons is used here from atomic

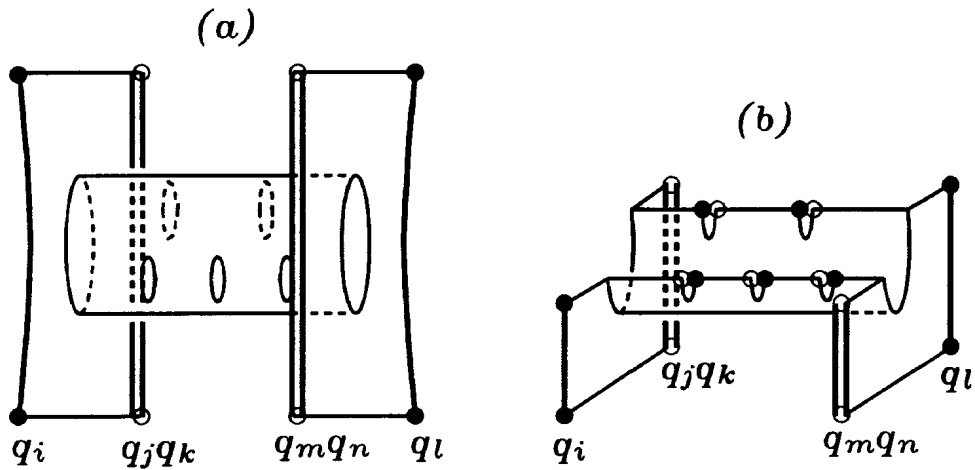


Figure 1.20: (a) Non-planar diagram for elastic nucleon-nucleon scattering. (b) Cutting the diagram represents an inelastic process with two fragmenting string chains and resulting particle production. (From [3].)

mass number 8 on, for smaller nuclei a different description is performed. Fermi motion of the nucleons inside the nuclei is included.

With a Monte Carlo implementation of the Glauber model the number of collisions and collision partners for each nucleon are determined. After the first collision the nucleons continue traversing the nucleus without a change of their cross section. Similar as in FRITIOF string fragmentation is performed only in the end after all nucleon-nucleon collisions have been modelled. Usually the leading diquark continues to interact with new nucleons on the way, but there is also a probability that it might break up (fig. 1.21). As a result the incoming nucleons lose more energy leading to the experimentally observed stopping.

In contrast to FRITIOF rescattering of string fragments with each other or with spectator nucleons is implemented. Spectators are those nucleons which did not take part in the primary interactions, but they might interact in a second step with particles stemming from a string fragmentation. This rescattering is added to

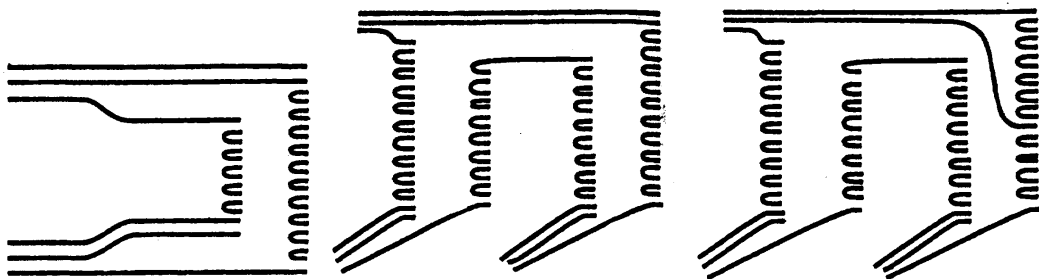


Figure 1.21: Quark-line diagram for a nucleon-nucleon collision (left), multiple collisions (middle), and multiple collisions with diquark breakup (right). (From [38].)

the model by implementing particle trajectories and a space time structure of the collision. Particles interact whenever they come close enough in phase space, in the model they form a cluster which decays after a certain lifetime.

As a result the number of wounded nucleons N_{wound} , i. e. the number of nucleons hit according to the Glauber model, is slightly smaller than the number of participating nucleons N_{part} . For the latter also those are counted which were involved in further interactions because of rescattering.

UrQMD

UrQMD (Ultra-relativistic Quantum Molecular Dynamics) [31, 32] is a microscopic model based on a phase space description of the reaction with transport theory. This is a different ansatz from the models discussed above because a full relativistic calculation of the whole reaction is performed in four dimensions. A consistent formulation of the reaction dynamics of heavy-ion collisions at low and high energies is given. Therefore different reaction mechanisms are included depending on the collision energy reaching from compound nucleus formation and deep inelastic scattering at the Coulomb barrier over particle and resonance production at intermediate energies up to string-excitation and fragmentation or parton scattering at relativistic energies (fig. 1.22). Particle production takes place via excitation, coalescence, resonance decay or string fragmentation.

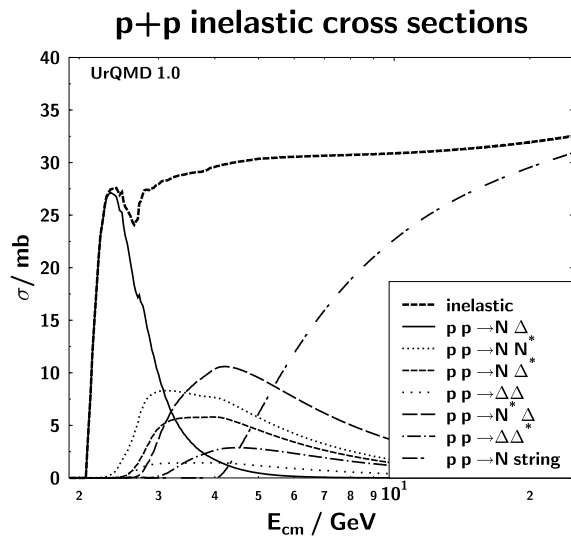


Figure 1.22: Inelastic p+p cross sections implemented into the UrQMD model, subdivided into various p+p \rightarrow B+B processes. For center-of-mass energies from ~ 7 GeV on string excitation is dominant. (From [31].)

The propagation of all particles is simulated numerically according to equations of motion. Cross sections are interpreted geometrically providing an interaction if two particles come close enough to each other. Therefore rescattering of particles is included by construction of the model. Besides cross sections essential input are two body potentials and decay widths, no in-medium properties different from those in vacuum are assumed.

If available, cross sections are used from experimental measurements either in tabulated or parametrized form. Still missing ones are derived via general principles

like the additive quark model or detailed balance. The main idea of the latter is based on the time-reversal invariance of the matrix element of the reaction. This principle has a large influence on particle production in UrQMD: Up to center-of-mass energies of 6-7 GeV meson-baryon and meson-meson interactions are dominantly modelled by resonance scattering. Especially the cross section of the frequent πN and $\pi\pi$ collisions are extracted this way.

From center-of-mass energies of ~ 7 GeV on string excitation and fragmentation becomes the most important particle production mechanism. No color but only momenta are exchanged when hadrons collide inelastically. In standard settings FRITIOF is used to model the exchange of momenta, as alternatives the QGSM ansatz or a simple $1/M$ excitation are implemented: For the latter the transverse momentum exchange is simulated according to a Gaussian distribution

$$f(p_t) \approx \frac{1}{\sqrt{\pi}\sigma^2} \exp\left(-\frac{p_t^2}{\sigma^2}\right) \quad (1.11)$$

where $\sigma=1.6$ GeV/c. The excited strings get a mass M from the continuous distribution $f(M) \approx 1/M^2$ limited by the total collision energy. What is still left from the collision energy is then distributed equally between the longitudinal momenta.

The string is stretched between diquark (antiquark) and quark from the same baryon (meson) and fragments in an inside-outside-cascade according either to the LUND, to the QGSM or as default setting according to the Field-Feynman fragmentation function

$$f(x)_{\text{prod}} = (1-x)^2 \quad (1.12)$$

for produced particles. For leading nucleons a different fragmentation function

$$f(x)_{\text{nuc}} = \exp\left(-\frac{(x-B)^2}{2A^2}\right) \quad (1.13)$$

is used with $A = 0.275$ and $B = 0.42$. The $u : d : s$ quark ratios are defined by the Schwinger formula, in addition a probability for diquark-antidiquark pairs is included. Similar to FRITIOF the vertices lie on a constant proper time but here not only final momenta of the produced hadrons are needed but also their creation point in space and time. As formation point of newly created hadrons not the string break up point (constituent formation point) is taken but the point where the quark trajectories meet for the first time (yo-yo formation point, see figure 1.23). This gives each hadron a formation time $t_f = \frac{1}{2}(t_{n-1} + t_n + z_{n-1} - z_n)$ of 1 - 2 fm/c in which the interaction cross section is zero if no leading quark is involved. If they do consist of leading constituent quarks the cross section is reduced to their relative contribution since prior to the formation of the hadron only the constituent part of the cross section is present.

Nuclei are initialized according to the Fermi-gas ansatz with a radius that follows the mass dependence $R(A) \approx r_0 \cdot A^{\frac{1}{3}}$ and has a reasonable surface-thickness. Fermi-motion of the nucleons is implemented in addition.

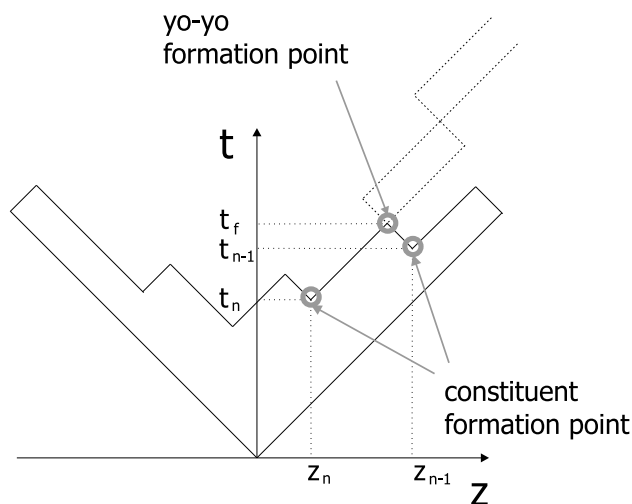


Figure 1.23: Space-time trajectories of quarks and antiquarks in a string fragmentation. Yo-yo and constituent formation points are indicated.

1.4.5 Thermodynamic models

Statistical models successfully describe the final state of high-energy collisions with a small set of macroscopic parameters. Basis of these models is a thermodynamic characterization of the final state as hadron gas, or a primary phase as partonic state, in thermal and chemical equilibrium. This way, information on single particles, their phase-space trajectories and individual interactions is lost, but the system is described as a whole.

An important observation for the development of these models was the universal behavior of m_t -distributions in p+p collisions. For all produced particles (mass m_0), the spectra can be described with one common inverse slope or temperature, $T \approx 160$ MeV, by the ansatz:

$$\frac{dN}{m_t \cdot dm_t} \propto \exp\left(-\frac{m_t - m_0}{T}\right) \quad (1.14)$$

Hagedorn [39] first interpreted this feature by assuming a thermodynamic fireball close to equilibrium or a highly excited resonance as thermal source for all emitted hadrons. With increasing energy of the fireball the available phase space, but also the number of particle species rises. This leads to a maximum temperature from which on free energy is spent for new particles only but not for higher kinetic energies.

The application of this model to A+A collisions is not straightforward, because there the inverse slope parameters rise with the particle mass [40]. This can be understood by a superposition of thermal motion as in p+p interactions and, in addition, a common transverse flow of all particles of the source [41]. With a common transverse velocity distribution of the collectively expanding source, heavier particles gain higher transverse momenta resulting in higher effective temperatures. For the development of such a common kinetic behavior thermal equilibrium has to

be required. A radial flow fit according to Schnedermann, Sollfrank and Heinz [41] to NA49 data yields a common thermal, i. e. kinetic freeze-out temperature of about 120-130 MeV for central Pb+Pb collisions at 40 AGeV, 80 AGeV and 158 AGeV. Mean transverse velocities are on the order of 0.4c to 0.5c.

If the common thermal source for the emitted particles is also in chemical equilibrium the relative production rates of the various particle species can be calculated in the framework of statistical thermodynamics. However, a chemical equilibrium is a stronger requirement than the kinetic equilibrium suggested by the m_t -spectra.

For small systems as e^+e^- and p+p collisions, or for particles with small production rates, the canonical ensemble with exact quantum number conservation is the appropriate description. The one body partition function of noninteracting particles is [42]

$$Z_1(T, V) = V \int \frac{d^3p}{(2\pi)^3} \exp \left[-\frac{\sqrt{p^2 + m^2}}{T} \right]. \quad (1.15)$$

Several authors pointed out (e. g. Rafelski and Danos [42], Hagedorn and Redlich [43], Hamieh et al. [44], Cleymans et al. [45], Rafelski and Letessier [46]) that in small volumes or for a small number of carriers of a conserved quantum number, e. g. strangeness, the abundance of these carriers is suppressed due to the restrictions imposed by the conservation: The accessible phase space is reduced by particle-antiparticle correlation [46]. The relative strangeness content of the final state is therefore volume-dependent, the stronger, the more strange valence quarks a hadron has (fig. 1.24). A hierarchy of strangeness enhancement as observed in the data (fig. 1.13) is the result.

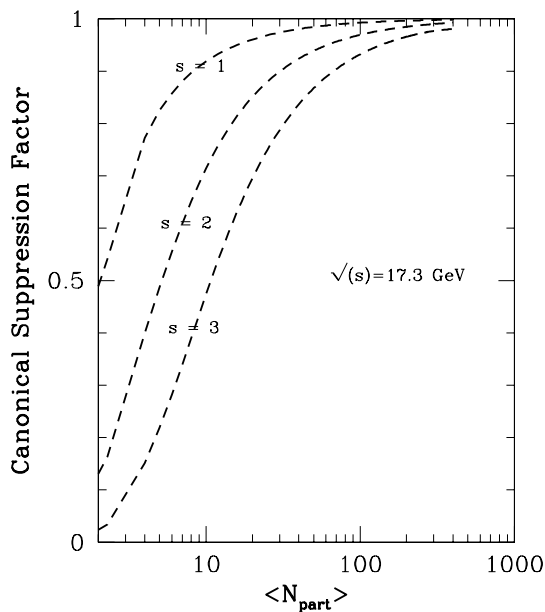


Figure 1.24: Strangeness suppression factor for collisions at 158 AGeV laboratory momentum in dependence on the strange quark content of the particles ($s = 1, 2, \text{ or } 3$). The number of participants is calculated from the volume by $V \simeq \frac{V_0}{2} N_{part}$ with $V_0 \approx 7 \text{ fm}^3$. (From [47].)

For high multiplicities or large volumes, e. g. as in central A+A interactions, a grand-canonical description is applicable. In this case quantum number conservation is required only on average which is expressed by the introduction of corresponding chemical potentials. The system is then described by a volume term V , a temperature T and chemical potentials (μ_Q, μ_S, μ_B) for all conserved quantum numbers q_i : electric charge, flavor (i. e. only strangeness here), baryon number. Average multiplicities for hadrons and hadronic resonances i are given by an integral over a statistical distribution [21]

$$\langle n_i \rangle = (2J_i + 1) \frac{V}{(2\pi)^3} \int d^3p \frac{1}{\gamma_s^{-S_i} \exp[(E_i - \mu_{q_i})/T] \pm 1}. \quad (1.16)$$

For final particle numbers the contribution from decays of unstable resonances is included. A phenomenological factor $\gamma_s^{-S_i}$ might be introduced in case strangeness is not in full chemical equilibrium. S_i is the total number of strange quarks in hadron species i , γ_s is often referred to as the strangeness suppression factor. This factor is not used by all models: it is implemented in the models by Becattini et al. [21, 48] and in new publications of Kämpfer, Cleymans and others [49, 50], but not by Braun-Munzinger et al. [51, 52, 53] and Redlich et al. [44, 47]. Rafelski [54] recently introduced a similar factor for light quarks, γ_q , in addition to γ_s .

Various groups performed fits to available experimental data of central Au+Au and Pb+Pb interactions. For these collision systems a grand-canonical description is applicable and (surprisingly) successful in describing particle yields over several decades [20, 21]. Either an infinite volume or the large volume of a Pb or Au nucleus is assumed. γ_s turns out to be rather constant, at least for SPS energies [20, 21]. The extracted parameters T and μ_B show a systematic energy dependence: The baryochemical potential μ_B is decreasing with energy while the chemical freeze-out temperature T_{chem} is increasing [21, 53]. All derived freeze-out conditions happen to lie on a common freeze-out curve which is defined by the condition $\langle E \rangle / \langle N \rangle \approx 1$ GeV [21] (see also fig. 1.5). The combined variation of T and μ_B causes a maximum of the Wroblewski factor at about 30 AGeV beam energy [53]. The main contribution stems from strange baryons, Braun-Munzinger et al. [53] consider the associated production of kaons together with hyperons, which dominates at low \sqrt{s} , as reason.

With the models described above, chemical freeze-out temperatures are always found to be larger than thermal freeze-out temperatures. This means that chemical freeze-out takes place first and fixes the hadron abundances followed by a kinetic decoupling when elastic interactions fade out (fig. 1.25). This was already discussed in context of section 1.3.3 and can be understood because of the energy dependence of inelastic and elastic cross sections.

Common of these models is the assumption of a hadron gas at least close to chemical equilibrium. The success of thermal models in describing particle abundances supports this idea. But the question arises how this equilibrium can be reached, if it is reached. Basically, there are two possibilities:

Either the created hadron gas lives long enough to thermalize. But according to microscopic model calculations rather long equilibration times are expected,

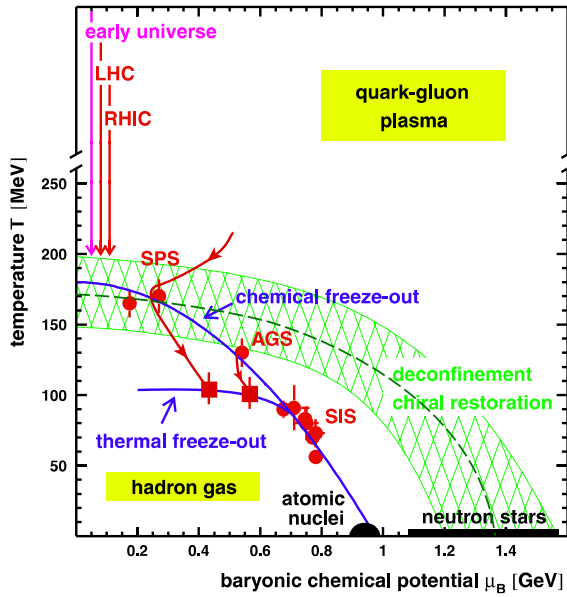


Figure 1.25: Phase diagram of hadronic matter with data from experiments analyzed in thermal models. The difference of thermal and chemical freeze-out curves is pointed out here. (From [55].)

depending on the model from 10 fm/c to more than 40 fm/c concerning, for example, kaons [24, 56]. Recently it was proposed [56] that reactions of the type $n_1\pi + n_2K \rightarrow B\bar{B}$ should take place rather frequently. This would reduce equilibration times enormously.

Another solution is offered by, e.g. [29, 57, 58]. Each of the authors has a different main emphasis, but common of all of them is the assumption of a partonic phase which freezes out into the equilibrated hadron gas. Special for the model of Rafelski and Letessier [58] is the scenario of a supercooled quark-gluon plasma, thermal and chemical freeze-out take place at the same time. The main point of Stock [57] is, that the observed yields and ratios allow the interpretation of a parton to hadron phase transition filling phase space according to the statistical weights, i. e. Fermi's Golden Rule. The partonic phase hadronizes into the maximum entropy state and the equilibrated hadron gas is the outcome of this transition.

Chapter 2

The NA49 Experiment

2.1 Overview

NA49 is a fixed-target experiment designed for the investigation of high-energy heavy-ion collisions, specifically for the high-multiplicity environment of central Pb+Pb reactions. In 1994, data taking started at the H2 beamline in the North Area of the SPS accelerator with the first Pb-beam period at CERN. The experiment was aimed at studying matter under extreme conditions, the ultimate goal being to provide an experimental proof of the existence of a QGP in nucleus-nucleus collisions.

New features occurring in Pb+Pb interactions can only be detected and understood in relation to other data. In particular, p+p reactions are needed for comparison. Of importance are variations of system size and beam energy in order to localize the onset of possible new phenomena. Therefore, NA49 took data for a series of beam-target combinations with well defined centrality selections (see table 2.1). In this work p+p, C+C, and Si+Si interactions are analyzed.

NA49 concentrates on the hadronic observables, the detector system (fig. 2.1

target	projectile	energy	thickness	interaction probability
Pb	^{208}Pb	158 AGeV	200 μm	0.5%
Pb	^{208}Pb	158 AGeV	800 μm	2%
Pb	^{208}Pb	80 AGeV	200 μm	0.5%
Pb	^{208}Pb	40 AGeV	200 μm	0.5%
Si	^{28}Si	158 AGeV	5.02 mm	4.4%
C	^{12}C	158 AGeV	3.05 mm	2.4%
C	^{12}C	158 AGeV	10 mm	7.9%
Pb	$\pi^+, \text{K}^+, \text{p}$	158 GeV	0.5 mm	0.29% for p as projectile
Al	p	158 GeV	1.25 mm	0.32%
LH ₂	p	158 GeV	14 cm	1.9%
LH ₂	p	158 GeV	20 cm	2.8%

Table 2.1: Target, beam and energies for data taken by the NA49 Collaboration.

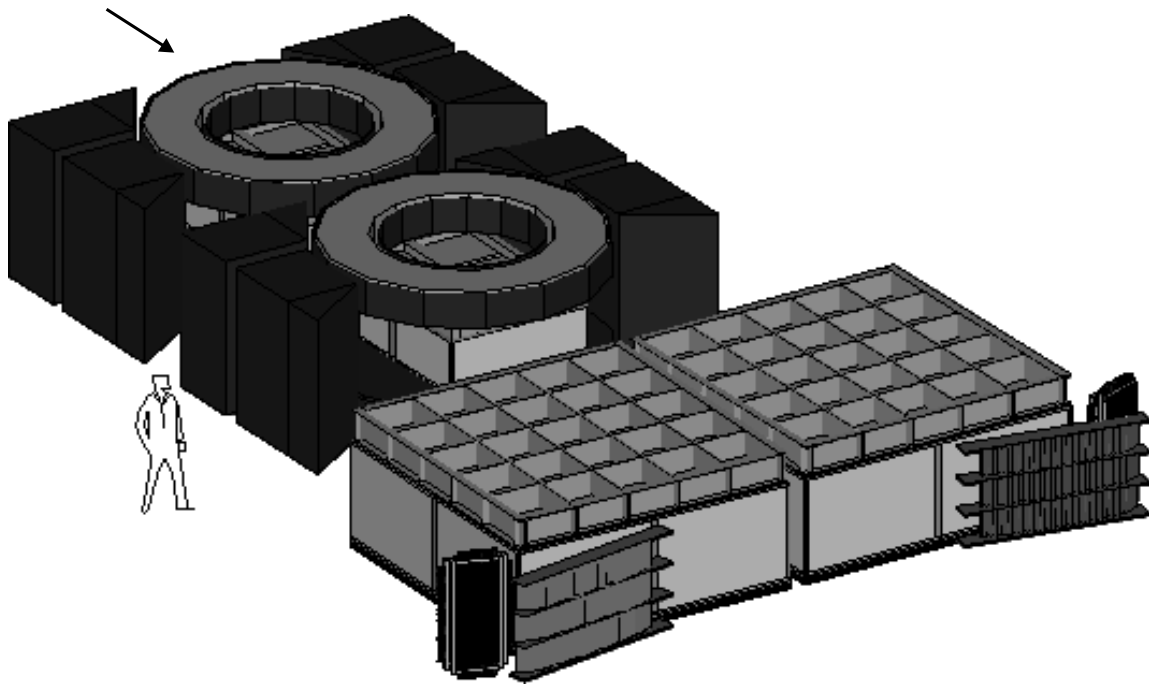


Figure 2.1: The NA49 experiment seen from the downstream side. As indicated by the arrow, the beam enters from the upper right edge in this figure.

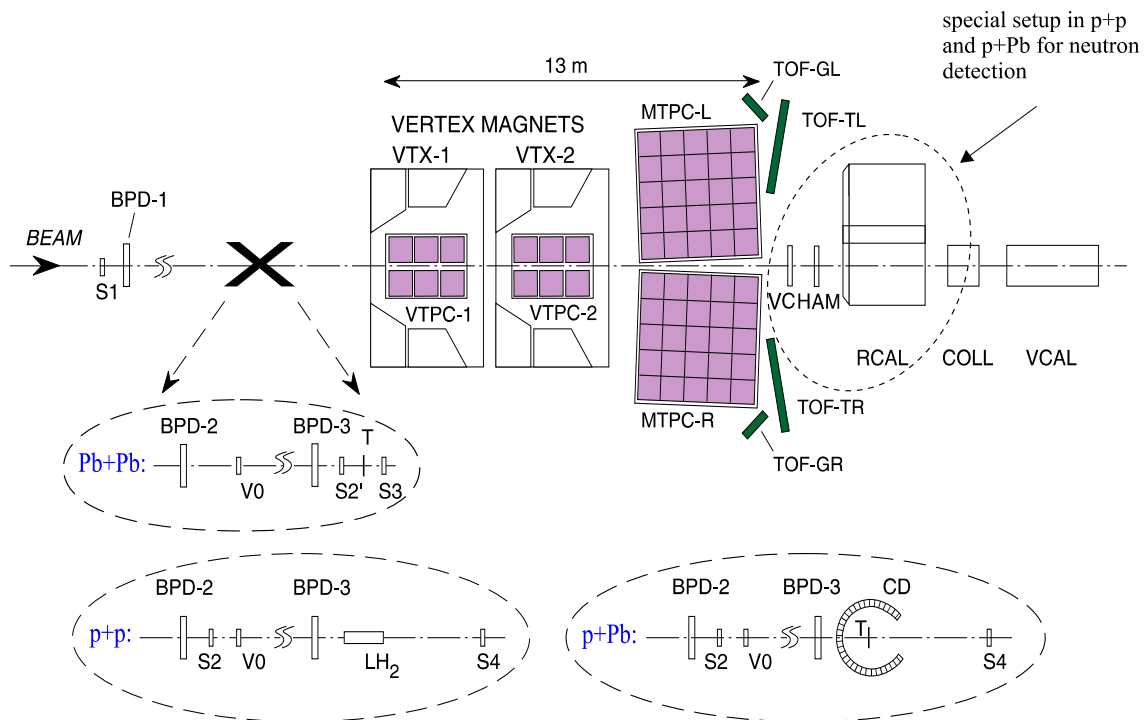


Figure 2.2: Layout of the NA49 experiment with different target settings and the special arrangement for neutron detection in p+p and p+Pb interactions. Otherwise the veto chambers (VCHAM) are missing and the ring calorimeter (RCAL) is centered around the beam axis.

and 2.2) was designed to measure charged hadrons emitted from the collisions over a large fraction of their phase space. The main components are four large-volume time projection chambers (TPCs), two of which are positioned inside superconducting magnets. The magnets allow for momentum measurement and reduce the track density in the TPCs by bending the particle tracks. The two chambers outside of the magnetic field significantly increase the resolution of the energy loss measurement. The system is backed up by four time-of-flight (TOF) walls which improve particle identification near midrapidity. Further downstream, calorimeters are installed, which determine the centrality of the collision by measuring the energy of the spectators. In case of hadron beams the ring calorimeter is moved sideways such that fast hadrons emitted close to the beam axis are measured. Two proportional chambers in front of it distinguish neutral from charged particles, e. g. neutrons from protons.

The various detector components will be introduced below with special emphasis on those whose information is used in this analysis. Detailed information can be found in [59].

2.2 Beamline

At CERN, protons and Pb-ions are pre-accelerated in a LINAC, then injected into the PS Booster (PSB) and the PS (Proton Synchrotron) and finally into the SPS (Super Proton Synchrotron). The Pb-ions are fully ionized in several steps while passing this chain. The variety of beams used in NA49 requires different detectors in the beamline after the extraction of the beam from the SPS.

In case of a hadron beams 400 GeV protons from the SPS are sent to a production target (T2 target, usually Be) just after extraction from the SPS. Positive or negative hadrons at 158 GeV are selected by a proper setting of the magnets in the H2 beamline. Approximately 20 meters upstream of the NA49 target a Cherenkov counter is installed to distinguish protons, kaons and pions. When selecting protons, contamination by pions and kaons is suppressed to a level below 10^{-3} . Beam position detectors (BPD, proportional counters) serve to center the beam on the nominal beam axis and to focus the beam on the target. Scintillation counters (S1) start the detector or veto the start (V0) if the beam particle is too far off the center of the beamline. A valid projectile is defined by a coincidence of the hadron selection via the Cherenkov counter, S1, $\bar{V}0$ and S2. The S2 scintillator is positioned close to the target and proves whether the beam particle is still existent. A further scintillation counter behind the target (S4) measures if the beam particle is still close to the center of the beamline. If not, an interaction has taken place. The S4 counter thus excludes elastic and most of the diffractive collisions [60, 61] (for more details see section 4.1).

If a Pb foil is used as target, it is surrounded by a proportional counter (centrality detector CD) measuring the so-called grey protons which are connected to the number of collisions the projectile undergoes during the reaction. This defines a centrality for hadron+Pb interactions.

Pb ions are delivered fully ionized with 158 GeV per nucleon from the SPS. For S1 a quartz wafer coupled to a photomultiplier is used due to the higher beam charge. A fast start signal is derived from the Cherenkov light in the quartz. S2 and S4 are replaced by helium gas Cherenkov counters S2' and S3. The beam is defined by $S1 \times \overline{V0} \times S2'$. The position is again controlled with help of the BPDs. The S3 detector behind the target excludes very peripheral collisions; with an upper threshold on the energy of the veto calorimeter the requirement of central collisions can be included into the trigger.

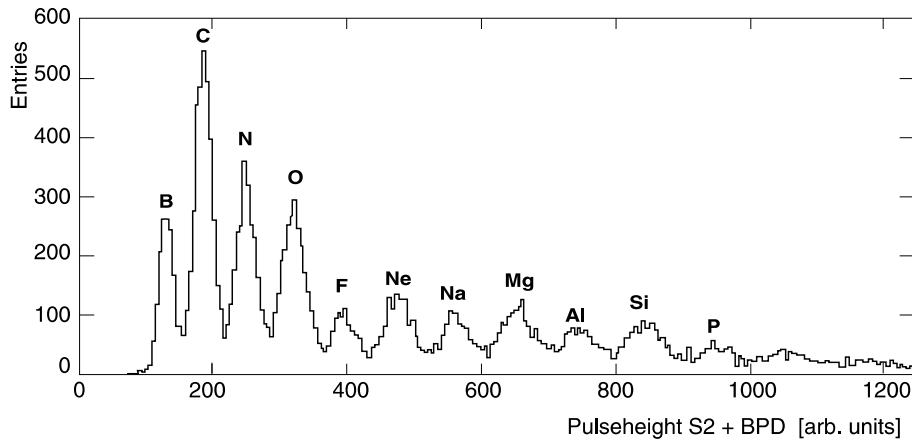


Figure 2.3: Spectrum of lead fragments for 158 AGeV beam momentum combining the charge sum signal of the BPDs with the information from S2. Only nuclei with $Z/A=0.5$ are selected by the setting of the beam line. (From [59].)

The Pb ions from the SPS can be fragmented by directing the beam to a conversion target (10 mm carbon) immediately after extraction from the SPS. A special *rigidity* (Z/A) of the fragments at the target is chosen by the setting of the beamline momentum (fig. 2.3). The BPDs deliver not only the position of the beam but also its energy loss which allows to distinguish different masses at the same momentum. The pulse height of the signal in the beam counters S1 or S2' gives information about the charge. Combining both measurements therefore allows for a clean selection of one specific nucleus.

In practice, a window on the S2 pulse height is set, which limits the spectrum of nuclei to be recorded online (fig. 4.13). Offline, the BPD information can be used to select only one type of nuclei. For C and Si beams the S1, S2' and S4 detectors were used for the beam definition.

2.3 Time projection chambers and magnets

In central Pb+Pb collisions about 1500 charged hadrons are produced. Since NA49 is a fixed-target experiment all particles are emitted in a small cone around the beam. Therefore, one task of the magnets is to reduce the track density. The maximum combined bending power of the two magnets is 9 Tm over 7 m length with

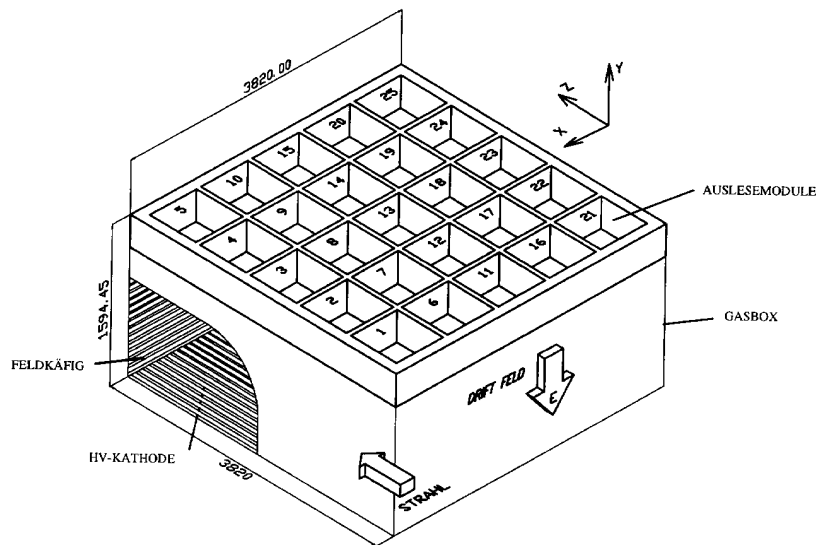


Figure 2.4: Design of the Main-TPCs. (From [59].)

a magnetic field of 1.5 T each. In standard operation the downstream magnet is operated with a reduced magnetic field of 1.1 T. Then, the two magnets provide a combined transverse momentum kick of 1.5 GeV/c. STD− setting of the field bends positive particles into the right hemisphere of the experiment, STD+ setting negative ones. The inner volume and the downstream opening angle of the magnets determine to a large extent the acceptance of the detector.

The time projection chambers (TPCs) are large gas boxes (for the scale see fig. 2.2, the size is also specified below). They serve as tracking devices by recording the ionization trail left by charged particles in the gas. Applying an electrostatic field causes the electrons around the particle track to drift to the top surface of the TPC. Amplification and measurement of the electrons on a segmented readout plane provides two-dimensional information of the track (fig. 2.4, 2.5). The vertical dimension is obtained by recording the drift time of the electrons.

The two so-called Vertex-TPCs located inside of the magnets cover a $2 \text{ m} \times 2.5 \text{ m}$ plane with a drift length of 666 mm. The larger Main-TPCs outside the

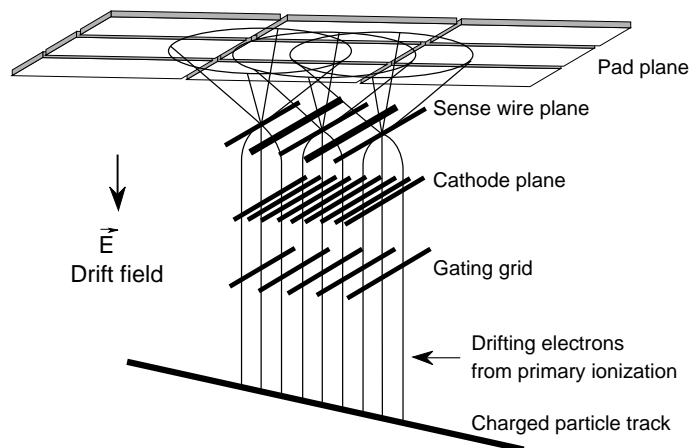


Figure 2.5: Schematic layout and operation of the TPC readout. (From [59].)

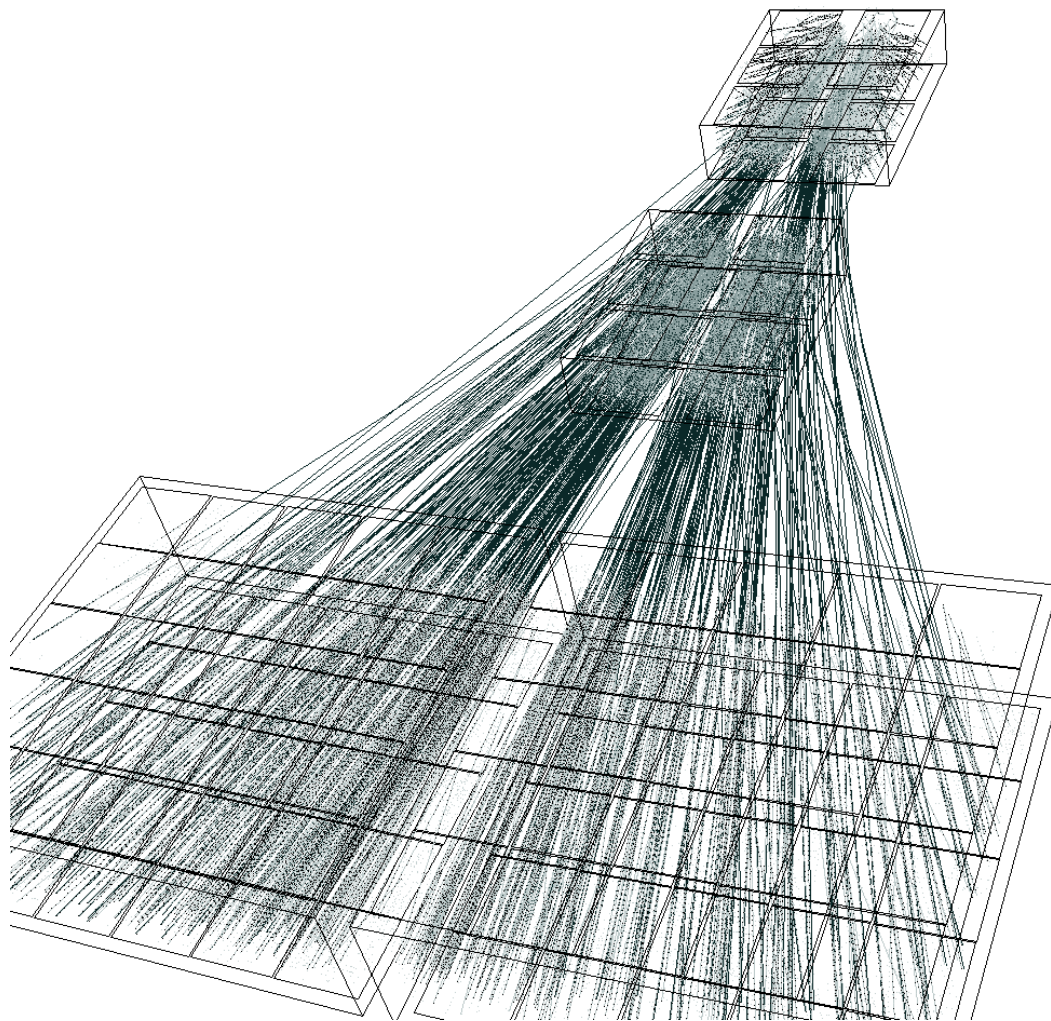


Figure 2.6: Three-dimensional tracking in the TPCs. (From [62].)

magnetic field have a drift length of 1117 mm and a plane of $3.9 \text{ m} \times 3.9 \text{ m}$. The gas is chosen to best fulfill the requirements of low diffusion, low mass, low electron attachment and moderate drift velocities. The selection for the VTPCs is a gas mixture of Ne/CO₂ (90/10) and for the MTPCs of Ar/CH₄/CO₂ (90/5/5). Drift fields of 200 V/cm and 175 V/cm are applied and result in drift velocities of 1.4 cm/ μ s and 2.4 cm/ μ s, respectively. The homogeneous drift fields are realized with drift cages built of aluminized mylar strips, which are wound around ceramic rods standing on each edge of the rectangular gas box.

The TPCs are read out via proportional chambers consisting of three planes of wires (fig. 2.5). The lowest plane is the gating grid which is followed by the cathode plane. Charge amplification is then performed towards the sense wire plane. It consists of an alternating pattern of sense wires at high voltage and field wires at zero potential. The signals induced on the segmented pad plane above the wires are read out in 512 time slices. The copper pads have widths of 3.5 mm to 5.5 mm and lengths of 16 mm to 40 mm depending on track density and track angles. They are

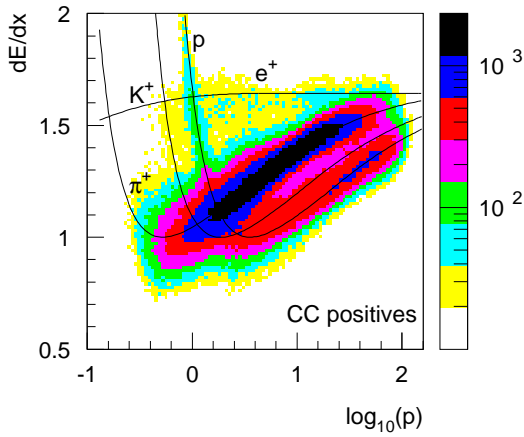


Figure 2.7: Particle identification by dE/dx for positive particles in C+C collisions at 158 AGeV. The lines present the Bethe-Bloch formula adjusted to match the NA49 data.

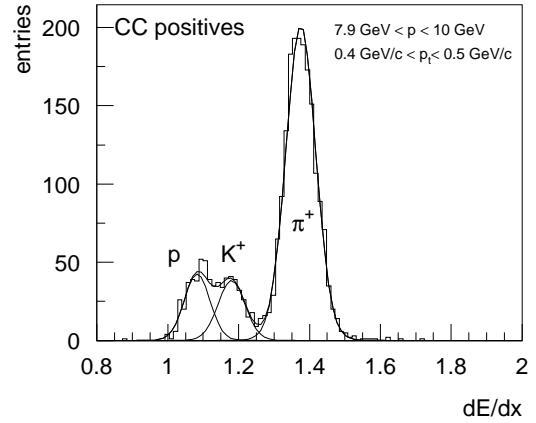


Figure 2.8: Energy loss distribution in a small (p, p_t) bin. Even though the single distributions are overlapping particle yields can be extracted on a statistical basis.

aligned such that the longer pad direction is approximately parallel to the tracks which requires pad angles of 0° to 55° . A track crossing the full length of the VTPCs leaves charged signals on 72 pads in each, in the MTPCs on 90 pads.

Offline the measured charges of neighboring pads are combined to charge clusters which are joined to tracks, first for each TPC separately. Afterwards the tracks of all TPCs are merged together (*global tracking*) yielding track lengths up to 14 m. Three dimensional tracking with high precision and good two track resolution of about 1 cm is achieved (fig. 2.6).

The TPCs provide not only tracking, they also serve for particle identification. The momentum of each track can be calculated from its curvature inside the magnetic field recorded by the two Vertex-TPCs. Secondly, not only the location of the clusters are measured but also their integrated charge which depends on the

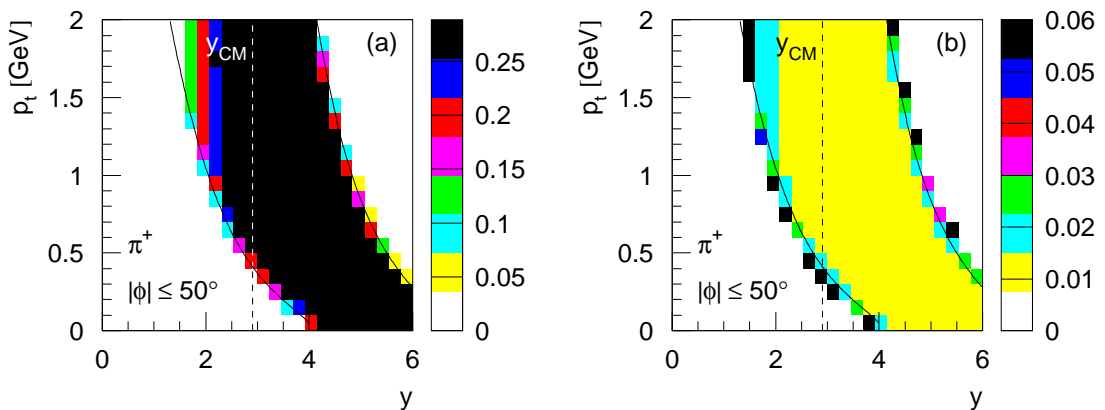


Figure 2.9: Acceptance (a) and statistical error (b) in (y, p_t) for π^+ . Here $n \geq 30$ and $|\Phi| \leq 50^\circ$ is required, the lines give typical borders for identification of $p = 4$ GeV and $p = 63$ GeV. Midrapidity is indicated by the dashed line, for other details see caption of figure 3.6.

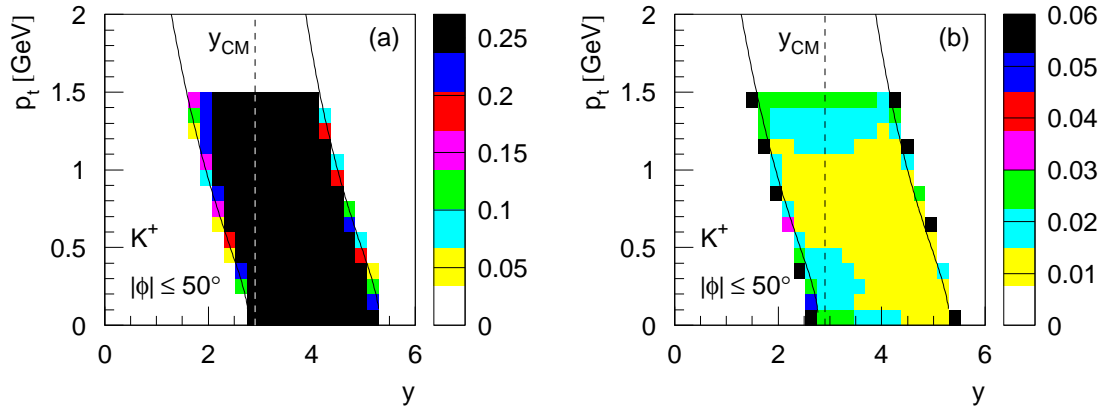


Figure 2.10: Acceptance including correction for kaon decay (a), and statistical error (b) in (y, p_t) for K^+ . $n \geq 30$ and $|\Phi| \leq 50^\circ$ is required, the lines give typical borders for identification of $p = 4$ GeV and $p = 50$ GeV.

velocity of the particle; the functional form describing this is the Bethe-Bloch formula (section 3.1.1). Therefore the energy loss is different for protons, kaons and pions at the same momentum (fig. 2.7) allowing to distinguish amongst them. Unfortunately the difference is small, this requires a good energy loss resolution for clean particle identification (fig. 2.8).

With the four TPCs described above NA49 covers nearly the full forward hemisphere for most of the particles under investigation, see, e. g., fig. 2.9 and 2.10 for kaons and pions, more acceptance plots can be found in chapter 3.1.3. Definitions of the kinematic variables used in this work and the assignment of momenta to "midrapidity" are summarized in appendix A.

2.4 Time-of-flight detectors

Particle identification by energy loss measurement alone fails in the region of minimum ionization (fig. 2.7). Unfortunately e. g. kaons in this region are close to midrapidity and therefore of interest. Even with a good energy loss resolution they are difficult to distinguish from protons, especially no identification track by track is possible. To overcome these handicaps time-of-flight detectors are added for particle identification in selected regions of phase space.

In NA49 two sets of time-of-flight (TOF) systems are integrated, each having a detector on both sides of the beam. The pixel detectors TOF-TR/TL consisting of 891 single scintillation counters were developed in Marburg (fig. 2.11). The time-of-flight measurement is started by the detector S1 in the beam (fig. 2.2), and individually stopped by particles traversing one of the scintillators. Together with the momentum and track length information from the TPCs the mass of the particles can be obtained from

$$m_0 c^2 = \frac{pc}{\beta\gamma} \quad \Leftrightarrow \quad (m_0 c^2)^2 = (pc)^2 \left(\frac{(ct)^2}{s^2} - 1 \right) \quad (2.1)$$

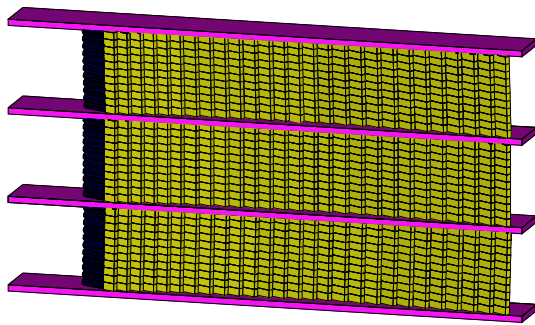


Figure 2.11: Design of the pixel TOF detectors TOF-TR/TL in NA49. (From [63].)

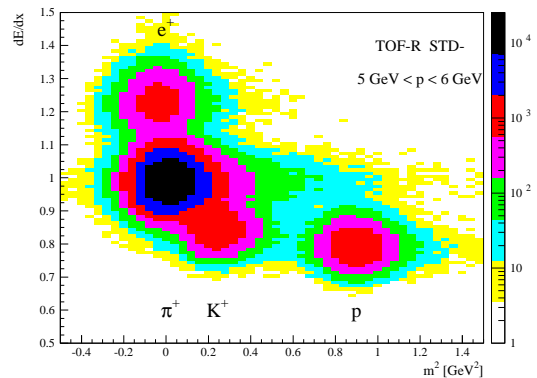


Figure 2.12: Particle identification with dE/dx and time-of-flight. Data from TOF-TR in central Pb+Pb collisions are shown here in a small slice of total momentum. (From [64].)

where t is the flight time between target and scintillator (obtained after subtracting the constant delay between S1 and target, and after corrections for differing cable lengths), s is the flight path between target and scintillator and $\beta = \frac{v}{c}$. Combining energy loss and mass measurements good particle identification is achieved also for kaons at midrapidity (fig. 2.12).

The smaller TOF-system TOF-GR/GL consists of long scintillator rods in a grid design. This is adequate for the lower particle densities at their positions farther away from the beam.

In this work the TOF detectors could not be used for particle identification as statistics is not sufficient for an analysis due to the limited acceptance, small particle yields and event numbers recorded for p+p, C+C and Si+Si interactions.

2.5 Calorimeters

Downstream of the TPCs and TOF walls a set of calorimeters is employed for classifying the inelasticity or the centrality of the collision. They serve for measuring the history of the projectiles for a study of their correlation with particle production. In p+p collisions the fastest baryon is very likely connected to the incoming projectile. In nucleus-nucleus collisions the interesting parameter is the number of participants. This can be obtained (see section 4.3) from the energy that is carried by the spectators and measured in the zero-degree calorimeter (VCAL).

In case of hadron beams veto chamber (VCHAM) and ring calorimeter (RCAL) are used. The setup allows the detection of fast hadrons distinguishing between charged and neutral ones. The two veto chambers are double-layered proportional chambers with strip readout. The two strip layers build a grid running diagonal in the readout plane. The rectangular surface of each ($0.8 \text{ m} \times 1.6 \text{ m}$) covers the gap in between the TPCs and therefore detects charged hadrons with high momenta outside of the TPC acceptance. The multiplicity of fast hadrons in hadron+p or hadron+Pb

collisions is low enough that the probability of double hits on the strips is small. The particle energy is measured independently of charge in the ring calorimeter standing behind the veto chambers. In order to accept the fast hadrons crossing the veto chambers the calorimeter is moved sideways (fig. 2.2) from its usual position where the beam runs through the inner bore of 56 cm diameter.

The calorimeter RCAL is constructed as a cylinder with an outer radius of 151 cm, its sensitive area is subdivided into 240 cells by 10 radial rings and 24 azimuthal sectors. In the front it has an electromagnetic part consisting of a lead/scintillator sandwich of 16 radiation lengths and in the back a hadronic part with an iron/scintillator sandwich of 6 radiation lengths. The sectors are read out with photomultipliers in the back via wavelength shifter bars to distinguish between the two parts.

The more participants take part in a nucleus-nucleus collision the fewer is the energy carried by the spectators along the beam. Measuring this energy is therefore a good tool to determine the centrality of A+A reactions. About 20 m downstream of the target a veto calorimeter (VCAL) is positioned behind a collimator (COLL). The collimator allows only beam particles, projectile fragments and spectator protons and neutrons to reach the sensitive area of the veto calorimeter. The veto calorimeter is separated into 4 quarters each consisting of an electromagnetic part in the front and a hadronic part in the back. The first is a lead/scintillator sandwich of 16 radiation lengths, the latter an iron/scintillator section of 7.5 interaction lengths. Readout is provided by 8 photomultipliers, each for one of the sections. To enhance the recorded event sample of central events an upper threshold of the energy measured in the calorimeter can be included in the trigger.

Chapter 3

Methods for data analysis

In this work, data recorded by NA49 for the collision systems p+p, C+C, and Si+Si at 158 AGeV beam energy are analyzed in order to determine the relative strangeness content in their final hadronic state. In this chapter, the methods applied in the data analysis, particularly the particle identification procedures and quality criteria for the track selection are introduced. Simulations and corrections for the extraction of particle yields are discussed. Both, identification and corrections are used in the same way for the various datasets. Solutions of special problems are addressed where necessary in chapters 5 and 6 when presenting the results. Event cuts for cleaning up the recorded data samples are reported in chapter 4, where cross sections and the centrality of the various interactions are discussed.

3.1 Charged-particle identification by means of energy loss measurement

Charged particles living long enough to traverse the TPCs are identified by the combined measurement of their momenta and their specific energy loss. After a more detailed introduction into the energy loss measurement and the resulting particle identification capabilities the determination of particle spectra will be explained. More details on the dE/dx measurement and calibration procedures are given in notes by G. Veres and F. Sikler [65, 66, 67].

3.1.1 Basics of energy loss measurement

Charged particles passing through matter lose energy by electromagnetic interactions with the atoms of the medium. In case of a dense medium, e. g. in the calorimeters, the particles are fully stopped providing a direct measurement of their energy. In case of gases as used in the TPCs of NA49, the particles ionize gas atoms along their path. As explained in chapter 2.3 these ionization trails are recorded allowing for a three-dimensional tracking in the TPCs. The amount of ionization is measured by the pulse height of the signal on the pads and is proportional to the energy loss of the particles.

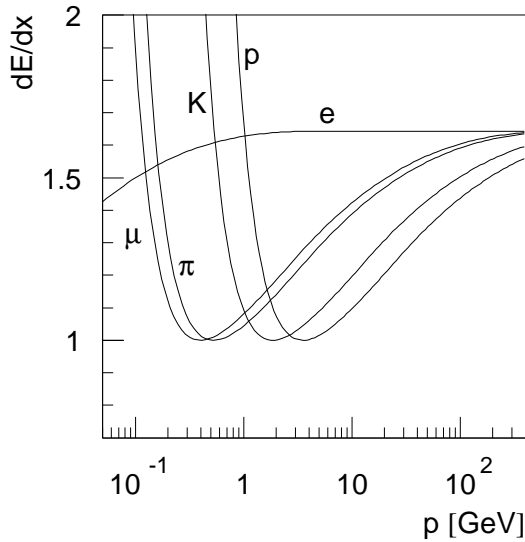


Figure 3.1: Bethe-Bloch curves for various particles.

For each particle the amount of the mean energy loss per unit path length dE/dx depends on its velocity $\beta = \frac{p}{E}$ and is thus different for various masses at the same momentum (fig. 3.1). The mean energy loss per path length of a particle with charge z passing through a medium with atomic number Z and atomic mass A is described by the Bethe-Bloch formula

$$\left\langle -\frac{dE}{dx} \right\rangle = Kz^2 \frac{Z}{A} \frac{1}{\beta^2} \left[\frac{1}{2} \ln \frac{2m_e c^2 \beta^2 \gamma^2 T_{max}}{I^2} - \beta^2 - \frac{\delta}{2} \right], \quad (3.1)$$

where $K = 4\pi N_A r_e^2 m_e c^2$ and $\gamma = (1 - \beta^2)^{-1/2}$ [2]. I is the mean excitation energy and T_{max} is the maximum kinetic energy which can be imparted to a free electron in a single collision. δ is the density effect correction introduced by Fermi.

The NA49 detector measures particles in the momentum range from a few GeV up to nearly 100 GeV therefore covering the relativistic rise of the Bethe-Bloch formula (fig. 2.7). Combination of momentum and energy loss measurement in this range allows a separation of electrons, pions, kaons and protons on a statistical basis (fig. 2.8). Obviously, a lower limit for particle identification is given by the crossing region of the Bethe-Bloch curves, a higher by the *Fermi plateau* in which all the curves converge. This usable span corresponds to the forward hemisphere in the center of mass of the collision in case of NA49 as a fixed-target experiment with 158 AGeV beam momentum. Since symmetric systems are studied here, particle yields in both hemispheres are the same on average. This symmetry might be violated in some special cases where selection criteria are imposed on one hemisphere only (see section 4.2.2).

Particle identification is limited by the uncertainty of the dE/dx measurement which, besides detector effects, depends on the total charge in each cluster and the number of clusters on a track. The probability of the energy loss in a single collision, and therefore also a sampling of the energy loss in a small portion of the flight path (cluster), follows an asymmetric distribution called Landau distribution (fig. 3.2). It has a tail reaching out to high energies representing the energy loss

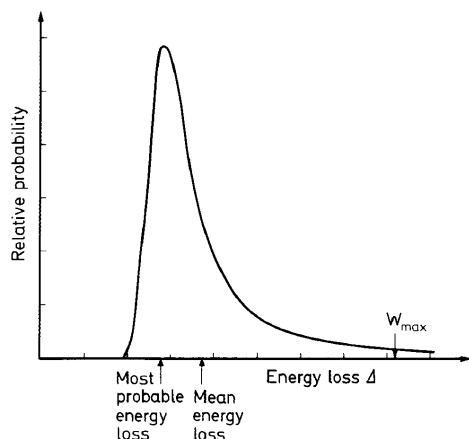


Figure 3.2: Schematically form of Landau distribution with indication of most probable and mean energy loss. (From [68].)

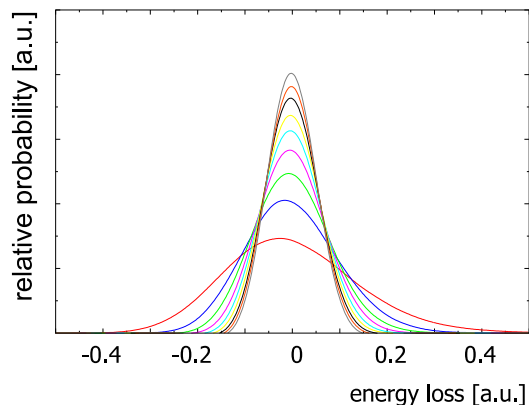


Figure 3.3: Parametrization of truncated mean distributions for tracks with different numbers of clusters (10, 20, ..., 90 clusters from broad to narrow distribution). (From [65].)

in the rare nuclear collisions. If the particle track is long, i. e. if many clusters are measured, the energy loss distribution becomes nearly Gaussian. But for a few clusters per track the fluctuation is large leading to a discrepancy between most probable and mean energy loss. The *truncated mean method* represents a proper way of calculating a measurement of the mean energy loss by rejecting a fixed percentage of the smallest and highest energy loss measurements of all clusters on a track. Still a small asymmetry remains which is more pronounced for tracks with a small number of clusters (fig. 3.3). But for tracks with at least 30 clusters the resulting distribution approaches a Gaussian shape, mean and most probable energy loss coincide. For p+p, C+C and Si+Si data in NA49, best results are obtained by cutting off the upper 50 % of the distribution [67] (for Pb+Pb the upper 35 % are cut off [69]). The resulting resolution σ_{abs} depends only on the material (α) and the total number of clusters (N_{points}):

$$\sigma_{abs} = \frac{a}{\sqrt{N_{points}}} \left(\frac{dE}{dx} \right)^\alpha \quad (3.2)$$

α is 0.5 for the VTPCs and 0.7 for the MTPCs, combining the energy loss measurement of both TPCs it is 0.625 [65, 66]. The resolution a is about 0.4 resulting for example in a relative sigma of 3.7 % for typical track lengths of 100 points and a dE/dx (normalized to minimum ionization) of 1.2.

3.1.2 Raw spectra

For all data analyzed in this work *global tracking* and global energy loss are used, i. e. the track and dE/dx information of Vertex and Main-TPCs are combined. This slightly broadens the dE/dx distribution compared to the situation where only data

of the MTPC are used but enlarges the acceptance. The resolution of the VTPCs is slightly worse compared to the MTPCs because of a different gas mixture and larger angles between tracks and pads. Track cuts are applied to ensure a good quality of the analyzed track sample. They will be listed before the determination of the raw spectra is explained.

Track selection

- Only tracks stemming from the main vertex and having a reasonable momentum fit are accepted [66] in the analyzed track sample (for the exact requirements on the DST-level see appendix C).
- A minimum of 30 points on the track is required giving nearly Gaussian dE/dx distributions (see fig. 3.3) which are assumed for the extraction of the yields in this work.
- During calibration of the pulse height (energy loss) its vertical drift length dependence is taken into account. However, remnants of this dependence are still present in the data and appear in the tails of the spectra (fig. 3.4). To circumvent this problem to a large extent, a cut in the azimuthal angle Φ is imposed: $\Phi = \arctan\left(\frac{p_y}{p_x}\right) \leq \pm 30^\circ$ if enough events are available (p+p minimum-bias) or $\pm 50^\circ$ for the low statistics samples (inelasticity selected p+p, C+C, and Si+Si events). The acceptance in the selected Φ -wedge is flat and close to 1 (see acceptance plots in section 2.3 and 3.1.3).

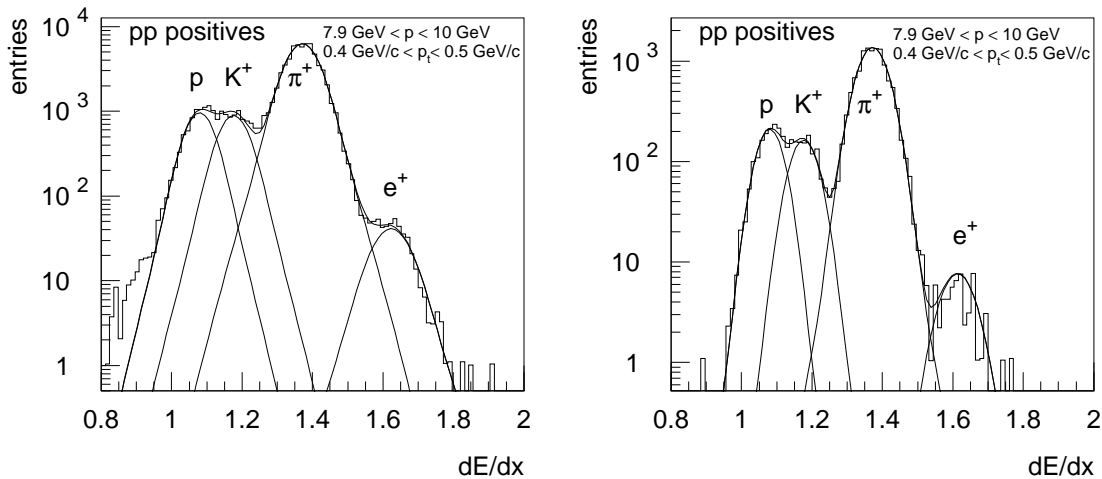


Figure 3.4: Energy loss distribution in a small p and p_t -bin for p+p collisions. For better visibility of the tails a logarithmic presentation is chosen. Left, no Φ -cut is imposed, right, $|\Phi| \leq 30^\circ$ and right-side type is required which suppresses the tail on the left side of the protons.

- Depending on p_x and charge tracks are divided into so-called *wrong-side* and *right-side* tracks. Right-side tracks are all their way in the same hemisphere of the detector, wrong-side tracks start into one side of the detector, but are bent over to the other side by the magnets. Their energy loss resolution suffers from

the large crossing angles with respect to the pad directions. In addition, tracking is more complicated and more frequently track segments are not combined leaving *split tracks* in the sample. To clean up the track sample of such contributions wrong-side tracks are rejected, although the combined Φ -wedge and right-side cut reduces the track sample for analysis by a factor 6 at maximum (for $|\Phi| \leq 30^\circ$, acceptance of 1 without any cuts).

Fitting procedure

Tracks with 30 clusters in the TPCs show a relative dE/dx resolution of about 6-7 %, typical track lengths are longer resulting in σ_{rel} of ~ 4 %. The pion to kaon to proton separation according to formula 3.1 is of the same order resulting in overlapping dE/dx distributions for the particles of interest (see fig. 2.8 and 3.4). A track by track identification is thus not achievable; particle yields can only be extracted on a statistical basis.

The energy loss of all particles from the available event samples is therefore accumulated into histograms in small bins of total momentum p and transverse momentum p_t . Here, bins of $\Delta \log(p) = 0.1$ and $\Delta p_t = 0.1$ GeV are used. These variables are chosen because p is directly measurable and the "natural variable" for the energy loss and p_t is needed to obtain transverse spectra. Later, a transformation into the variables of interest (y, p_t) or (x_F, p_t) is performed (for the method see appendix A). In p+p collisions the entry of each particle is weighted with a multiplicity-dependent correction factor $C1 \cdot C2(N_{ch})$ for vertex reconstruction inefficiencies (see chapter 4.1.2, table 4.2). The dE/dx spectra are fitted with the strategy explained below and yields N_i for each particle species i and (p, p_t) -bin are extracted: $\frac{N_i}{\Delta p \cdot \Delta p_t}$.

In principle, the mean energy loss $\left(\frac{dE}{dx}\right)_{i, \text{Bethe-Bloch}}$ in dependence on the total momentum p is given for each particle species i by the Bethe-Bloch formula for which parameters are derived during calibration of the pulse height. But in reality there are deviations from this functional form, however, the relative positions of the particles to each other should not change. Thus a common scaling parameter b for the particle mean positions $\left(\frac{dE}{dx}\right)_{i, \text{mean}}$ is introduced:

$$\left(\frac{dE}{dx}\right)_{i, \text{mean}} = b \cdot \left(\frac{dE}{dx}\right)_{i, \text{Bethe-Bloch}} \quad (3.3)$$

As a result of the calibration procedure of the pulse height this relative scaling might not be completely correct. It was found that the electrons especially at low momenta do not follow the common scaling. A possible reason is the fact that a large fraction of the electrons is not coming from the vertex but stems from conversions elsewhere in the detector material resulting in wrongly assigned momenta. Therefore for lower momenta their mean was allowed to shift independently from the others. An effect of deviations from the common scaling on kaons is investigated in chapters 5 and 6.

The absolute sigma $\sigma_{n,i}$ of each particle energy loss follows equation 3.2 with α fixed to 0.625. n is the number of points and a the resolution which is independent of particle type:

$$\sigma_{n,i} = \frac{a}{\sqrt{n}} \left(\frac{dE}{dx} \right)_{i,mean}^{\alpha} \quad (3.4)$$

For each (p, p_t) -bin the distribution of the number of points is extracted from data. The relative fraction $g_n = \frac{N_n}{\sum_{i=1}^{n_{max}} N_i}$ of tracks with n points per (p, p_t) -bin is calculated; N_n is the number of tracks with n points in a (p, p_t) -bin. The energy loss distribution for each particle species i corresponds to the sum of Gaussians with widths according to these fractions¹.

The following formula is fitted to the data: Free parameters are the resolution a , the scaling parameter b , and c_i ($i = 1, \dots, 4$,) which is proportional to the particle yield N_i in the specific bin, $N_i = \frac{c_i}{\Delta(dE/dx)}$ where $\Delta(dE/dx)$ is the bin size of the dE/dx histograms.

$$f \left(\frac{dE}{dx} \right) = \sum_{i=1}^4 c_i \sum_{n=1}^{n_{max}} g_n \frac{1}{\sqrt{2\pi} \cdot \sigma_{n,i}} \exp \left(- \frac{\left[\frac{dE}{dx} - \left(\frac{dE}{dx} \right)_{i,mean} \right]^2}{2\sigma_{n,i}^2} \right) \quad (3.5)$$

A minimum of usually 500 entries per fitted (p, p_t) -bin is required. This turned out to be necessary to secure reliable fits; a higher minimum would reduce the number of fitted bins too much leading to larger uncertainties in the final p_t and rapidity-spectra. As fitting procedure the minimization of

$$\chi^2 = \sum_{j=k_{low}}^{k_{high}} \left(\frac{f \left(\left(\frac{dE}{dx} \right)_j \right) - N_{exp} \left(\left(\frac{dE}{dx} \right)_j \right)}{\sqrt{N_{exp} \left(\left(\frac{dE}{dx} \right)_j \right)}} \right)^2 \quad (3.6)$$

is chosen; the sum runs over bin-numbers k_{low} to k_{high} of the histogram in which the energy loss $N_{exp} \left(\left(\frac{dE}{dx} \right)_j \right)$ from data is accumulated. The difference of function 3.5 and data relative to the expected variation is optimized with this method. The (statistic) error of each bin is the square root of the number of entries. Neighboring bins should result in similar values for the shift of the mean and the resolution because their tracks lie close in the TPCs. Regions where this is not the case lie far out in p and p_t and are excluded in the final results.

¹As discussed before, the Gaussian shape is only an approximation which holds for tracks with a large number of points. M.v. Leeuwen [70] suggested to use asymmetric Gaussians to account for the remnants of the asymmetric Landau-distribution:

$$f(x) = \frac{c}{\sigma\sqrt{2\pi}} \cdot \exp \left(- \frac{1}{2} \frac{(x-x_0)^2}{((1\pm\delta)\sigma)^2} \right)$$

The asymmetry parameter δ was found to be rather independent on p for central Pb+Pb interactions at 158 AGeV, typical values vary between 0.06 - 0.09. Its influence on particle yields is small, more important is the α parameter for scaling the width (equation 3.4). For the study of systematic uncertainties of the analysis presented in this thesis, asymmetric Gaussians with $\delta = 0.07$ will also be used to extract the yields. However, the effect is only about 1-2 % (see section 6.1 and 6.2).

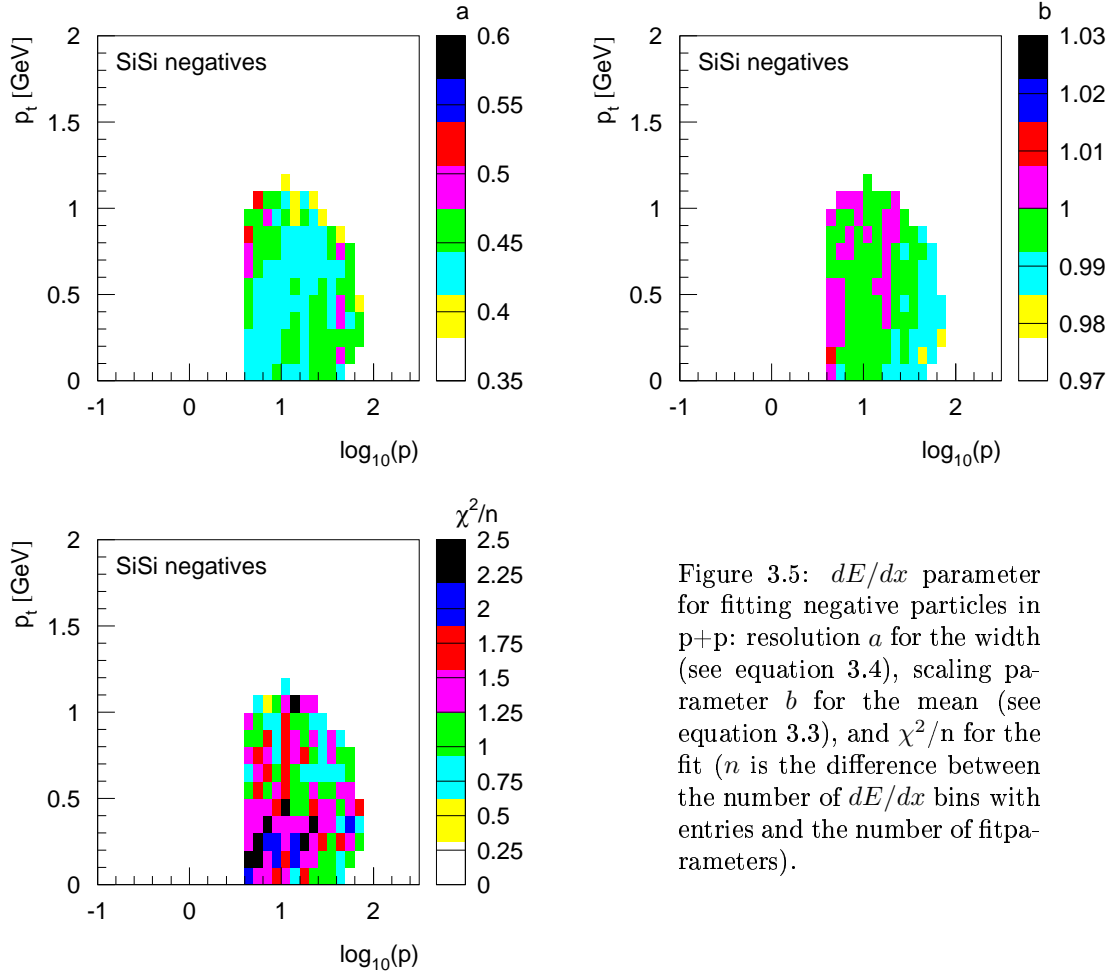


Figure 3.5: dE/dx parameter for fitting negative particles in p+p: resolution a for the width (see equation 3.4), scaling parameter b for the mean (see equation 3.3), and χ^2/n for the fit (n is the difference between the number of dE/dx bins with entries and the number of fitparameters).

Examples for the agreement of data and fit are already presented in figure 3.4, more examples can be found in appendix C. Typical values for the shift of the mean, resolution and fit quality are shown in figure 3.5. Reasonable fits were usually obtained from $\log(p) = 0.6$ ($p = 4$ GeV) to $\log(p) = 1.7/1.8/1.9$ ($p = 50/63/79$ GeV) depending on particle species and available statistics. The fitted p_t -range depends on statistics only.

The determined parameters for width and mean position are also used for kaon and pion selection for the invariant-mass spectra of the $K^*(892)$ and ϕ -meson.

3.1.3 Acceptance and feed-down corrections

After normalization to the number of events the raw yields for pions and kaons² obtained from the dE/dx distributions have to be corrected for the geometrical acceptance of the detector, in-flight decay (kaons), tracking inefficiencies, and back-

²Yields of protons and antiprotons are not extracted in this work. Identified protons are only used for triggering on different inelasticity classes in p+p collisions. The acceptance tables needed for simulations of these selections are extracted in the same way as those for pions.

ground from weak decays of long-lived hadrons (pions). Only then they represent the spectra of the particles as they are emitted from the target.

Within the small collision systems studied in this work the track density is relatively low. In central Pb+Pb collisions at 158 AGeV with track densities about a factor 10 higher than in Si+Si, tracking losses were found to be rather independent of y and p_t and on the order of 5 % only, [70, 71]. Due to the much lower multiplicity in p+p, C+C, and Si+Si collisions, losses of at most 1 % are expected: 100 % efficiency are assumed for this work. This assumption is supported by studies in context of the determination of feed-down corrections for pions (see below).

Geometrical acceptance and in-flight decay of kaons

Geometrical acceptance corrections are differently performed for pions and kaons. For the latter in-flight decay is included in the acceptance tables.

The pion acceptance is determined using a routine provided by F. Sikler [72]: Three-dimensional acceptance tables have been calculated using measured points from data. Therefore $\vec{E} \times \vec{B}$ effects in the VTPCs and the real sensitive volume of the TPCs is taken into account. The tables contain for each (charge, p_x, p_y, p_z) the expected number of points the track should leave in the TPCs, the accuracy of this number of *potential points* is within 1-2 points³.

With a simple Monte Carlo simulation a flat distribution of pions in (y, p_t, Φ) is generated with more than 10000 entries (C_{sim}) per (y, p_t) -bin. In case of an acceptance of 1 % the statistical error is thus still below 10 %. The number of pions per (y, p_t) -bin or (p, p_t) -bin which fulfills the track criteria as explained in section 3.1 are counted (C_{acc}): more than 30 points on the track (number of points is taken from the table introduced above), right-side track, $|\Phi| \leq 30^\circ(50^\circ)$, and a momentum range as introduced by quality requirements from the determination of the raw yields: $0.6 \leq \log_{10}(p) < 1.7/1.8/1.9$. The geometrical acceptance is the ratio of both, $\frac{C_{acc}}{C_{sim}}$ (fig. 3.6 and 2.9); as seen in the figures the statistical errors are small. For discussion the presentation in bins of (y, p_t) is more appropriate, for the analysis (p, p_t) -bins are used.

For the determination of the kaon acceptance, kaons are simulated in bins of (y, p_t, Φ) and tracked through the NA49 detector with help of the GEANT package [73]. GEANT provides a simulation of the detector including physical processes like multiple scattering, hadronic interactions and also the decay of unstable particles. The GEANT output is taken as input to the reconstruction chain of the NA49 experiment. First MTSIM [74] transforms the GEANT points on the track into realistic charge clusters as they are generated by real particles traversing the TPC and ionizing the gas. These simulated clusters are used as input into the track reconstruction software instead of real data. This full event simulation and its data

³This acceptance table is also used for the calculation of the proton acceptance in the TPCs in section 4.2.2. In addition, the table provides information about the geometrical acceptance for neutrons in the combined VCHAM and RCAL setup.

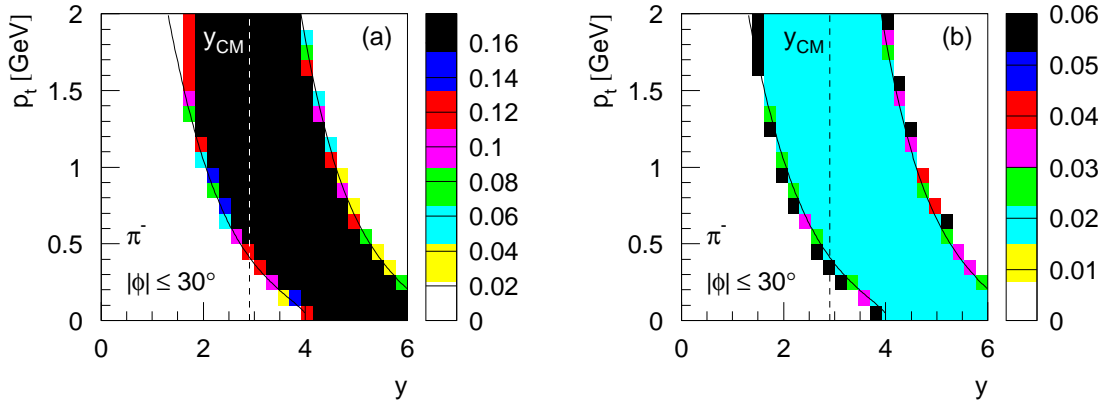


Figure 3.6: Acceptance (a) and statistical error (b) in (y, p_t) for π^- . Here $|\Phi| \leq 30^\circ$ is required, the lines give typical borders for identification of $p = 4$ GeV and $p = 50$ GeV. Center-of-mass rapidity is indicated by the dashed line, because of the Φ -cut the acceptance is flat. Unfortunately π ad midrapidity and low p_t are not accepted due to the lower momentum cut. The bins outside the lines are not used for the analysis.

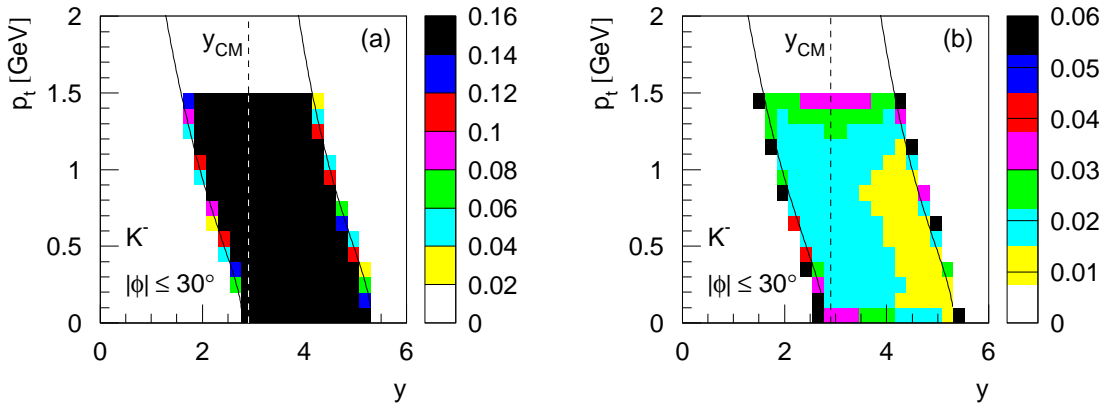


Figure 3.7: Acceptance for kaons including their in-flight decay (a) and statistical error (b) in (y, p_t) for K^- . Here $|\Phi| \leq 30^\circ$ is required, the lines give typical borders for identification of $p = 4$ GeV and $p = 50$ GeV. As for the pions the edge bins of the acceptance are not used.

output are time and space consuming, thus kaons were generated and investigated in context with the ϕ -meson: acceptance criteria for kaons, specifically for those decaying in the detector, are discussed in detail in section 3.2.5. In addition, the tracks are required to be of right-side type and to lie in the azimuth range of $|\Phi| \leq 30^\circ$ (50°). The ratio of accepted to generated kaons is presented in figures 3.7 and 2.10 together with the statistical error of the calculation. Besides the geometrical acceptance also the in-flight decay of kaons is included.

π feed-down from weak decays

Hadrons decaying by the weak interaction have decay lengths of several μm (mesons and baryons containing charm or bottom quarks) or cm (mesons and baryons containing strange quarks) in their rest frame. This corresponds to a distance of centimeters or meters in the laboratory frame the hadrons may still fly before they decay in the TPCs of NA49. Depending on the distance of this decay vertex to the main vertex of the collision, decay products are reconstructed in NA49 as stemming from the main vertex. But these decay products from weak decays bias, e. g., the strangeness measurement. Therefore their contribution is calculated from simulations and subtracted.

At collisions with 158 AGeV beam energy only weak decays of strange hadrons give a significant contribution, those considered in this work are summarized in table 3.1. Their main charged decay products are protons and pions, thus for both a correction is needed for final yields⁴. The contribution of K_L^0 -mesons can be neglected because they are decaying far outside of the NA49 detector ($c\tau = 15.51$ m). Additional Λ -baryons from the immediate decay of $\Sigma^0 \rightarrow \Lambda\gamma$ with a branching ratio of 100 % are included in the calculation of correction factors.

The VENUS model [33] is employed for the generation of p+p and central Si+Si ($b_{max}=2.6$ fm) events at 158 AGeV⁵. The generated particles are tracked through the simulation chain GEANT \rightarrow MTSIM \rightarrow reconstruction, which allows to follow up the production vertex for each particle and to prove whether a generated track points back to the main vertex and gets a reasonable momentum assigned.

From the VENUS input, yields and kinematic distributions of the simulated particles are known, also those of pions stemming from the main vertex, N_π . After reconstruction the distribution of main vertex pions includes the original pions plus those from weak decays as explained above. For p+p events there is one more important source of pions: slow pions are originating from secondary interactions in the extended proton target. The sum of these pions $N_{\pi+decay+2nd}$ corresponds to what is extracted as pion yield from data, $N_{measured}$. The relative feed-down correction factor is given by $C_{corr}^\pi = \frac{N_{\pi+decay+2nd}-N_\pi}{N_{\pi+decay+2nd}}$, presented in fig. 3.8 for π^- in p+p and Si+Si and collisions (see appendix C for more results). This contribution is subtracted from the acceptance corrected pion yields.

In this feed-down correction procedure it has to be ensured that the relative yields of pions and the weakly decaying hadrons are the same as in data, fig. 3.9 shows that the agreement is satisfactory for rapidity distributions in Si+Si collisions, the same holds for p_t -spectra. For C+C interactions pions, kaons and Λ -baryons from the Si+Si simulation are rescaled, also in p+p reactions yields from VENUS are adjusted to data.

⁴Corrections for pions are determined from VENUS simulations as described below. The feed-down correction for protons needed for simulation of inelasticity selected p+p events is provided by M. Kreps [75].

⁵Generated and reconstructed events were provided by T. Susa for p+p and M. Mitrovski for Si+Si collisions.

particle	charged decay modes	branching ratio [%]	$c\tau$ [cm]
K_S^0	$\longrightarrow \pi^+\pi^-$	68.61 ± 0.28	2.6762
Λ	$\longrightarrow p\pi^-$	63.9 ± 0.5	7.89
Σ^+	$\longrightarrow p\pi^0$	51.57 ± 0.30	2.396
	$\longrightarrow n\pi^+$	48.31 ± 0.30	
Σ^-	$\longrightarrow n\pi^-$	99.848 ± 0.005	4.434
Ξ^-	$\longrightarrow \Lambda\pi^-$	99.887 ± 0.035	4.91
Ω^-	$\longrightarrow \Lambda K^-$	67.8 ± 0.7	2.46
	$\longrightarrow \Xi^0\pi^-$	23.6 ± 0.7	

Table 3.1: Particles decaying by the weak interaction in the detector, antiparticles are not listed but included in the calculation. Only the charged decay modes relevant for the feed-down corrections are given [2].

Unfortunately, 260k p+p and 1.6k Si+Si events provide not enough statistics to apply this correction in (y, p_t) -bins, therefore y -integrated correction factors in dependence on p_t and p_t -integrated correction factors in dependence on y are calculated. The latter show only a weak dependence on y , only for p+p interactions the contribution of slow pions from secondary interactions in the extended proton target increases for lower rapidities. For these correction factors the acceptance of pions, in particular the missing measurement of midrapidity pions at low- p_t is considered. This is necessary since the p_t -dependent correction factors (see appendix C) are only rather constant for medium p_t values and increase strongly for low- p_t .

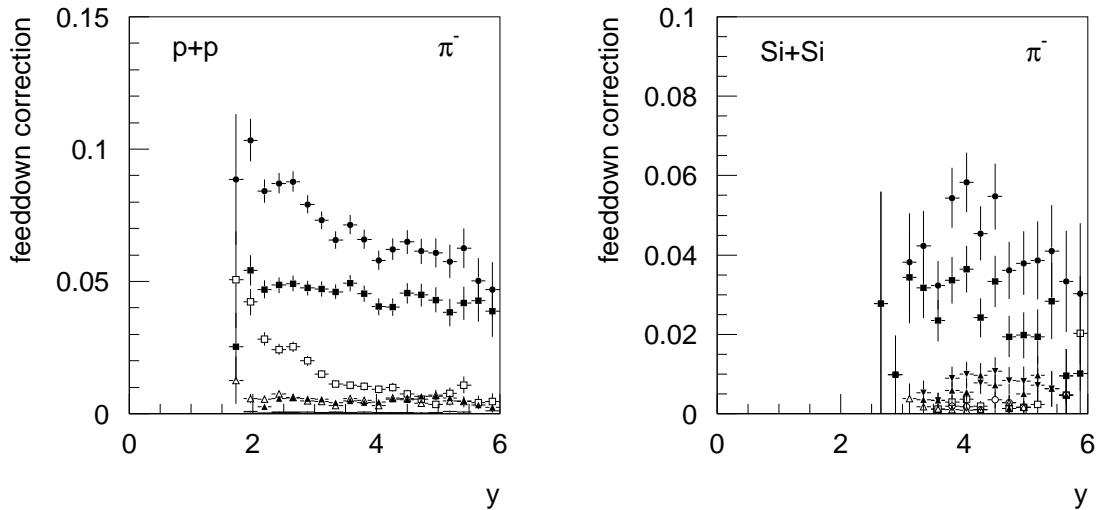


Figure 3.8: Relative feed-down correction for π^- in p+p and Si+Si in dependence on y (p_t -integrated, note the different scales). \bullet is the total feed-down correction. Contributions from the different sources are indicated as follows: \blacksquare π from K_S^0 , \blacktriangle π from Λ , \circ π from Ξ , \blacktriangledown π from Σ , \square π from secondary interactions (in particular important for p+p due to the extended proton target), and \triangle π from split tracks and similar sources.

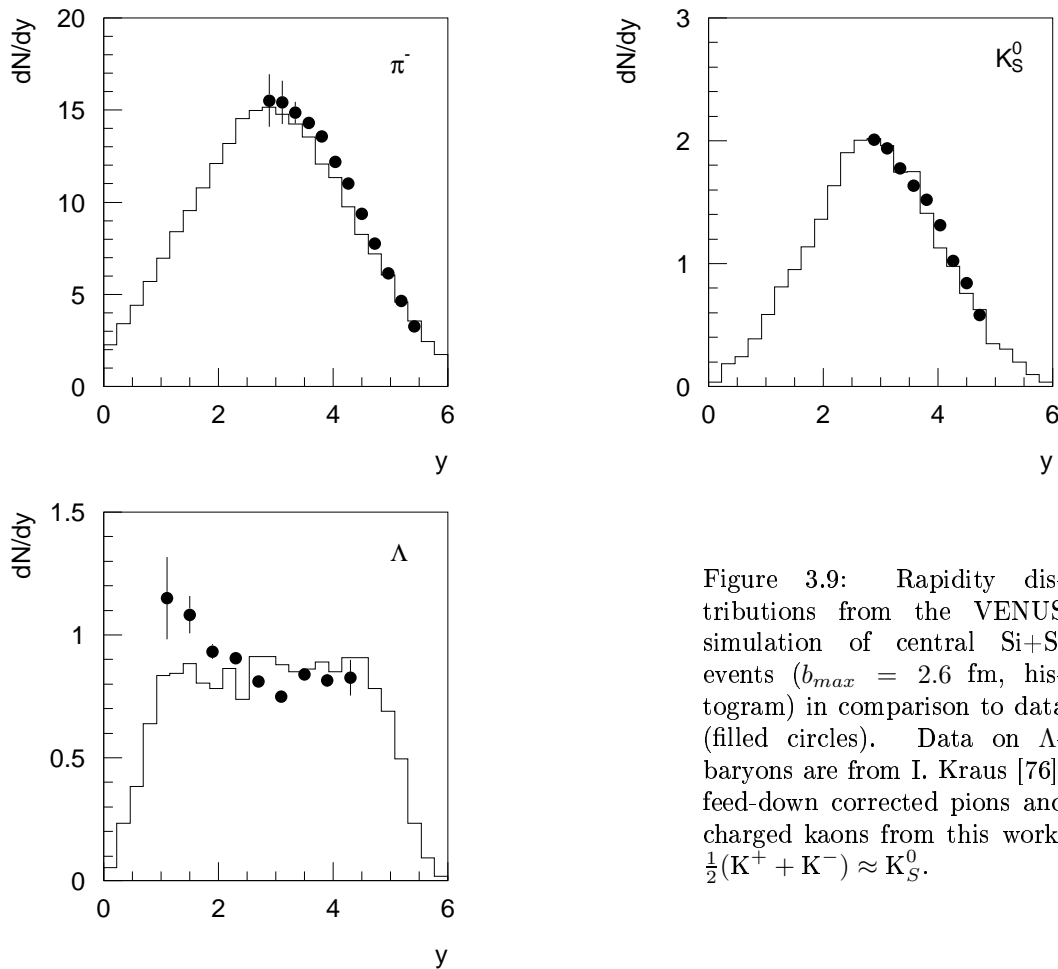


Figure 3.9: Rapidity distributions from the VENUS simulation of central Si+Si events ($b_{max} = 2.6$ fm, histogram) in comparison to data (filled circles). Data on Λ -baryons are from I. Kraus [76], feed-down corrected pions and charged kaons from this work, $\frac{1}{2}(K^+ + K^-) \approx K_S^0$.

As a side-product of this study tracking efficiency and other inefficiencies can be investigated since a full simulation of the detector and the reconstruction software is performed. Losses are found to be at or below a 1 % level. Furthermore, in the p+p simulation the effect of the extended proton target on the acceptance can be studied: no significant systematic change is found. Thus all acceptance tables which are extracted assuming a fixed z -position of the vertex are also valid for the extended proton target.

3.1.4 Final spectra

The raw spectra, extracted in bins of (p, p_t) from the data, are normalized to the number of events and corrected for geometrical acceptance and in-flight decay of kaons by dividing each bin by the corresponding acceptance determined in the previous section (also in (p, p_t) bins). Then, yields in the (p, p_t) bins are transformed to the variables of interest, here (y, p_t) (see appendix A).

From this two-dimensional distribution transverse momentum spectra $\frac{dN}{dp_t}$ are

derived in the various rapidity bins. They are either fitted by the function

$$\frac{dN}{dp_t} = c \cdot p_t \cdot e^{-\frac{m_t}{T}} \quad (3.7)$$

or transformed to transverse mass spectra $\frac{dN}{m_t \cdot dm_t}$. If the bins are small no recalculation is necessary because $\frac{dN}{m_t \cdot dm_t} = \frac{dN}{p_t \cdot dp_t}$. But especially for higher p_t the corresponding m_t -bins get large, in these cases a recalculation according to the upper relation is performed. Transverse mass spectra are usually presented versus $(m_t - m_0)$ and described by

$$\frac{dN}{m_t \cdot dm_t} = c \cdot e^{-\frac{m_t - m_0}{T}}. \quad (3.8)$$

The temperature parameter is independent of whether p_t or m_t -distributions are fitted. For particle yields in rapidity bins $\frac{dN}{dy}$, available data in the transverse momentum bins are summed and extrapolated for the missing part using the introduced thermal distribution. Errors are also calculated this way. For pions the feed-down correction is applied (see tables in appendix C). The shape of the resulting p_t -integrated rapidity spectra is either approximated by a double Gaussian (pions) centered around midrapidity

$$\frac{dN}{dy} = c \cdot \left(e^{-\frac{(y-y_\Delta)^2}{2\sigma_y^2}} + e^{-\frac{(y+y_\Delta)^2}{2\sigma_y^2}} \right) \quad (3.9)$$

or by a simple Gaussian (kaons, but also $K^*(892)$ and ϕ)

$$\frac{dN}{dy} = c \cdot e^{-\frac{y^2}{2\sigma_y^2}} \quad (3.10)$$

for y in the center-of-mass frame. For total yields the y -distributions are integrated.

3.1.5 Systematic errors

Several sources for errors originate from the introduced determination of yields and kinematic distributions for pions and kaons. The respective size of the errors will be estimated in the analysis chapters 5 and 6. Here, only the main sources and the order of magnitude are summarized.

All data presented in this analysis were taken with the STD+ configuration of the magnets, i. e. positive particles were deflected into the left hemisphere of NA49. For other collision systems data on both polarizations of the magnets were recorded and it was shown that the results agree within 5 % [71].

The unfolding of dE/dx -spectra is accompanied by several uncertainties. The position of the peaks is mainly fixed by pions; kaons and protons are shifted relative to them. But as a result of the dE/dx calibration the relative scaling of the mean dE/dx values may not be completely correct. A reasonable variation of the kaon position gives an error of 8 % for kaon yields. The stability of the results also on the track selection criteria is examined as well. Results scatter within 3-5 %.

Since Gaussian dE/dx distributions are used for the fitting procedure the slight asymmetry showing up in a larger tail at the high side of the energy loss spectra is neglected. Using an asymmetric Gaussian as suggested by M.v. Leeuwen [70] changes yields by $\sim 2\%$.

The extrapolation in p_t for integrated yields in bins of rapidity is usually on the order of 5-10 %, apart from the midrapidity yields of pions. Due to the missing acceptance at low- p_t extrapolation factors up to 3 are needed, which results in additional errors of $\sim 10\%$ for the central rapidity bins of pions. The large range of rapidity covered with measurements leads to a small extrapolation for yields in the forward hemisphere, about 5-8 % only. The uncertainty of the acceptance tables is about 1-2 %.

To summarize, systematic errors on the order of 5-7 % for integrated yields of pions and 10 % for kaons are realistic.

3.2 Identification of resonances

In NA49 not only long-lived charged particles traversing the TPCs are accessible for investigation, but also short-lived neutral resonances and strange hadrons decaying into charged particles either directly at the target or somewhere in the TPCs. Their reconstruction is based on the identification of their charged decay products in the TPCs. In case of weak decays ($\Lambda, \Xi, \Omega, K_S^0$) characteristic V^0 decay patterns with vertices outside the target can be observed in the TPCs (e.g. [77, 78]). For the strongly decaying resonances, as e.g. for ϕ -mesons and $K^*(892)$, the vertex lies inside the target and the decay particles cannot be separated from directly produced hadrons. The measurement of these resonances is based on the invariant-mass method.

3.2.1 Invariant-mass method

Short-lived resonances decaying at the main vertex into two charged particles are reconstructed by the invariant-mass m_{inv} of their daughters identified via the combined momentum and energy loss measurement in the TPCs:

$$m_{inv} = \sqrt{(E_1 + E_2)^2 - (\vec{p}_1 + \vec{p}_2)^2} \quad (3.11)$$

E_1, E_2 are the energies and \vec{p}_1, \vec{p}_2 the momenta of the decay products, e.g. in the laboratory system. Energy and momentum are conserved in the decay, thus $E_0 = E_1 + E_2$ and $\vec{p}_0 = \vec{p}_1 + \vec{p}_2$ are the corresponding quantities of the parent particle. Its mass $m_0 = \sqrt{E_0^2 - \vec{p}_0^2}$ as the modulus of the energy-momentum four-vector

particle	mass [MeV]	width [MeV]	lifetime τ [s]	$c\tau$ [fm]
$K^*(892)^0$	896.10 ± 0.28	50.5 ± 0.6	$0.1303 \cdot 10^{-22}$	3.91
ϕ	1019.413 ± 0.008	4.43 ± 0.05	$1.4858 \cdot 10^{-22}$	44.54

Table 3.2: Properties of $K^*(892)^0$ and ϕ -meson [2].

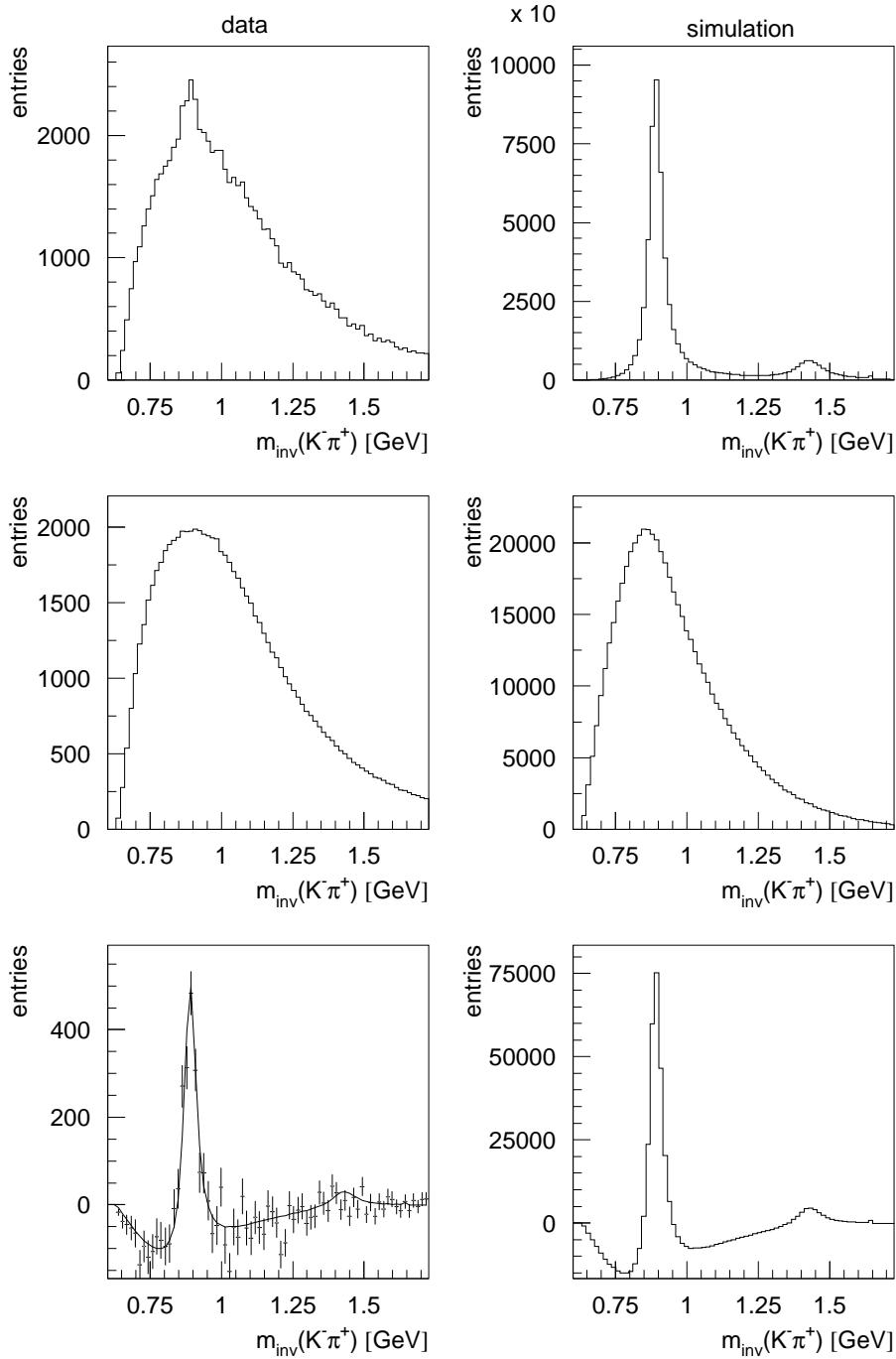


Figure 3.10: Illustration of the invariant-mass method with the $\overline{K}^*(892)^0$ as example. The presented $\overline{K}^*(892)^0$ is extracted from p+p data in the range $3.3 \leq y < 3.5$ and $p_t < 1.5$ GeV. In the left column data are shown, in the right a simulated invariant-mass spectrum of $K^-\pi^+$ pairs including the $\overline{K}^*(892)^0$ and $\overline{K}_2^*(1430)^0$ resonances (for details see section 3.2.2). Original spectrum (upper row), background from event-mix (middle), and background subtracted signal (lower row) are presented. The properly scaled simulated signal from the simulation (lower right) is overlaid as a line in the data (lower left).

is Lorentz invariant, therefore it also represents the rest mass in the rest frame of the resonance.

In this work $K^*(892)^0$, $\overline{K}^*(892)^0$ and the ϕ -meson are studied. The first two decay with a branching fraction of $2/3$ (see appendix B) into $K^+\pi^-$ and $K^-\pi^+$, respectively. $(49.1 \pm 0.8)\%$ of the ϕ -mesons decay into a K^+K^- pair [2]. The short lifetime of these resonances (see table 3.2) makes the daughter particles indistinguishable from the other main vertex particles.

In each event the invariant-mass is calculated for every identified $K^\pm\pi^\mp$ or K^+K^- pair and accumulated in histograms. In p+p collisions the entry of each pair is weighted with a multiplicity dependent correction factor $C1 \cdot C2(N_{ch})$ for vertex reconstruction inefficiencies (see chapter 4.1.2). However, most of the charged kaons and pions in an event do not stem from the decay of $K^*(892)$ or ϕ . Pairs of these uncorrelated particles generate a broad distribution of invariant-masses (fig. 3.10). Its shape is determined by the kinematic spectrum of these particles. Combinations originating from a $K^*(892)$ or ϕ form a peak at the mass of the resonance.

The extraction of the number of resonances in this signal requires a reliable method for background subtraction. Here the *event-mixing* method is used: Under the assumption that the background is produced by uncorrelated particles, pairs of particles taken from different events should result in a distribution of the same shape, because particles of different events are truly uncorrelated. Every kaon or pion is combined with several kaons or pions from other events. The multiple usage reduces the scatter of the calculated background. The event-mix spectrum is normalized to the same area, i. e. the same number of entries as in the original spectrum. Subtraction of this background yields a clear resonance signal (see fig. 3.10). Misidentified particles do not harm the extraction of the resonance as long as they are uncorrelated.

The applied method of histogram normalization produces an undershoot around the signal. Simulations for the ϕ -meson [64] have shown that pairs of uncorrelated kaons are subtracted to zero. But with the event-mixing technique also kaons (and pions) originating from ϕ -mesons (and $K^*(892)$) in different events are combined. Their origin constrains their energy and momentum which introduces a remaining correlation also between those kaons and pions, respectively. Simulating the event-mix with kaons and pions stemming from ϕ and $K^*(892)$ decays and subtracting this spectrum from a mass distribution of pure ϕ and $K^*(892)$ mesons results in the same undershoot structure as observed in data (see fig. 3.10) [79].

3.2.2 Background

The introduced methods works only if the resonance is the sole source of correlation between pairs entering the spectrum. In fact, not all kaons and pions in one event not originating from the $K^*(892)^0$, $\overline{K}^*(892)^0$ or ϕ are uncorrelated and therefore correctly subtracted (see e. g. $K^*(892)^0$ and $\overline{K}^*(892)^0$ in C+C and Si+Si, chapter 6).

First, there are contributions from resonances also decaying into $K^\pm\pi^\mp$ or K^+K^- pairs resulting in a distortion of the background. Second, decay products

of other resonances might be misidentified as kaons or pions and contribute to the spectra under investigation ("reflection"), e. g. a proton from the decay $\Delta \rightarrow p\pi^-$ might be declared as a kaon and combined with the π^- . Third, kaons or pions correlated in their q_{inv} because of Coulomb attraction have invariant-masses near threshold. Further, the shape of the background depends on kinematic correlations between the contributing pairs and therefore also on the multiplicity of the event.

These possible contributions to distortions in the background subtracted spectra are discussed in the following.

Higher excited resonances

In table 3.3, ϕ and $K^*(892)^0$ are listed together with resonances also decaying into K^+K^- or $K\pi$ (all final $K\pi$ states, no distinction according to Clebsch-Gordan coefficients is made here for the branching ratio).

Several experiments (e. g. [80, 81]) observed an exponential dependence of yield and mass of resonances from one family (see fig. 3.12). Besides mass the spin plays also a role in the relative abundance of single states; therefore about a factor 5 more $K_2^*(1430)$ than $K_0^*(1430)$ should exist. Yields of excited kaons can be approximately read off from fig. 3.12. For the ϕ -meson the same slope but an intercept scaled to the ϕ -yield is assumed for an estimate of the f_2 -yield. The f_2 -meson belongs to the excited pion trajectory [82], thus the same should hold for the a_2 . Therefore their multiplicities are estimated to be higher by a factor 6.7 compared to the ϕ -meson.

Invariant-mass spectra of $K^\pm\pi^\mp$ and K^+K^- pairs including the most abundant four resonances were simulated taking into account the given branching ratios and, for simplicity, assuming the same kinematic distributions for the whole spectrum of resonances.

Figure 3.11 (left) shows that the sharp ϕ -resonance overwhelms all other con-

particle	mass [MeV]	width [MeV]	branching ratio [%]
$K^*(892)^0$	896.10 ± 0.28	50.5 ± 0.6	100
$K^*(1410)$	1414 ± 15	232 ± 21	6.6 ± 1.3
$K_0^*(1430)$	1429 ± 6	287 ± 23	93 ± 10
$K_2^*(1430)^0$	1432.4 ± 1.3	109 ± 5	49.9 ± 1.2
$K^*(1680)$	1717 ± 27	322 ± 110	38.7 ± 2.5
$K_3^*(1780)$	1776 ± 7	159 ± 21	18.8 ± 1.0
f_0	980 ± 10	40 to 100	seen
a_0	983.4 ± 0.9	50 to 100	seen
ϕ	1019.413 ± 0.008	4.43 ± 0.05	49.1 ± 0.8
f_2	1275.0 ± 1.2	$185.5^{+3.8}_{-2.7}$	4.6 ± 0.4
a_2	1318.1 ± 0.6	107 ± 5	4.9 ± 0.8
f_2'	1525 ± 5	76 ± 10	88.8 ± 3.1

Table 3.3: Resonances decaying into $K\pi$ (upper part) and K^+K^- (lower part). The quoted branching ratio is for these decay channels. In case of $K\pi$ no distinction between the various charged decay modes according to Clebsch-Gordan coefficients is made. [2]

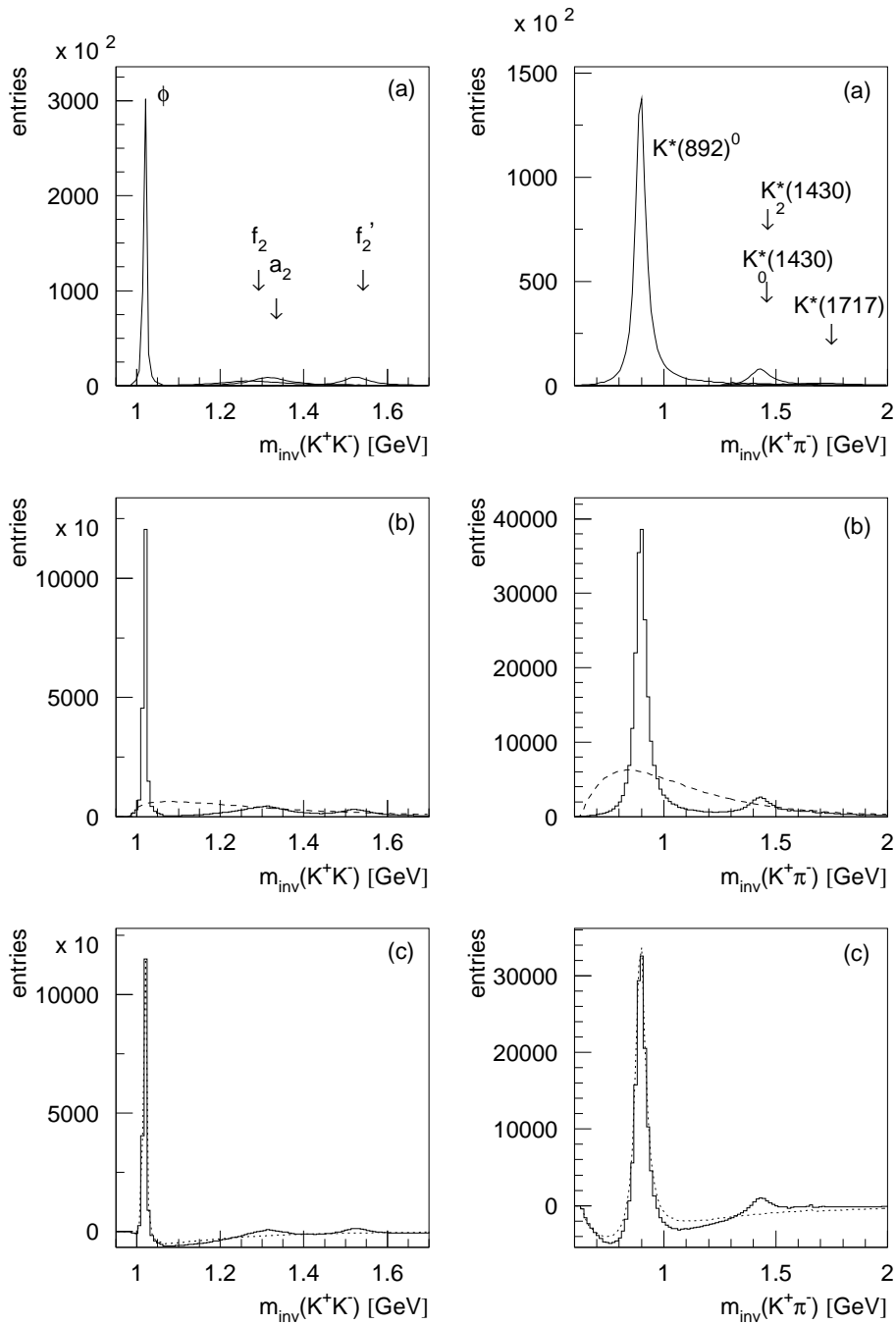


Figure 3.11: Simulation of the ϕ , f_2 , a_2 , and f_2' -mesons with relative yields of 1 : 6.7 : 6.7 : 0.14 (left) and the $K^*(892)^0$, $K_0^*(1430)$, $K_2^*(1430)$, and $K^*(1717)$ with relative yields of 1 : 0.047 : 0.24 : 0.14 (right). All resonances decay into K^+K^- and $K^+\pi^-$ pairs respectively according to their branching ratios. The figures presented in each column contain: (a) mass distributions of the simulated resonances indicated by separate lines; (b) sum of resonances within the acceptance with the event-mix background as dashed line; (c) event-mix subtracted spectrum. An event-mix subtracted spectrum with the simulation of the ϕ -meson or $K^*(892)^0$ alone is indicated by the dotted line. The clear peak in the $K^+\pi^-$ invariant-mass spectrum at $m_{inv} \approx 1.43$ GeV stems from the $K_2^*(1430)$.

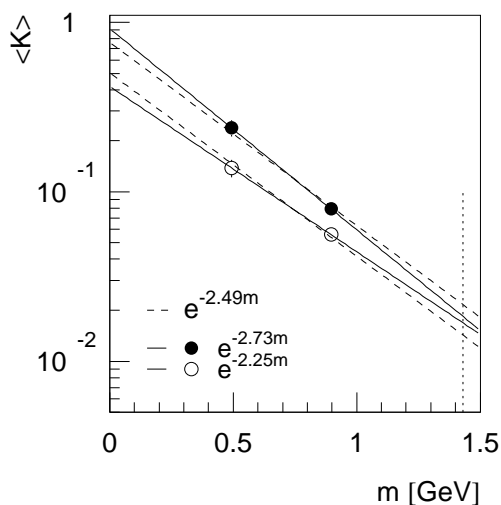


Figure 3.12: Yields for K^\pm , $K^*(892)^0$ and $\bar{K}^*(892)^0$ as extracted from data in dependence on their mass. Particles are plotted with filled, antiparticles with open symbols. The mass of the $K_2^*(1430)$ is indicated by the vertical short-dashed line. A fit assuming an exponential dependence of the yield on the mass is shown ($\langle K \rangle \propto \exp(-c \cdot m)$); for all kaons together (dashed line) and separately for particles and antiparticles (solid line). Extracted slopes agree well with results published in [80, 81].

tributions; no resonances besides the ϕ -meson have to be taken into account as also in the data no indication of other resonances is seen.

But in the invariant-mass spectrum of the $K^*(892)^0$ (fig. 3.11, right) higher resonances, specifically the $K_2^*(1430)^0$ show a clear effect. Both, $K_0^*(1430)^0$ and $K^*(1717)^0$ are too broad and seldom for any significant contribution. The $K_2^*(1430)^0$ also pulls down the baseline around the $K^*(892)^0$ compared to a simulation in which only the $K^*(892)^0$ is considered. Indeed, there is a slight indication for a similar behavior in the data (see e. g. fig. 3.10 or fig. 5.19). For a better description of the $K^\pm\pi^\mp$ invariant-mass spectrum, $K^*(892)^0$ and $K_2^*(1430)^0$ are taken into account. The slight effect on the yield will be discussed in chapter 5.1.4.

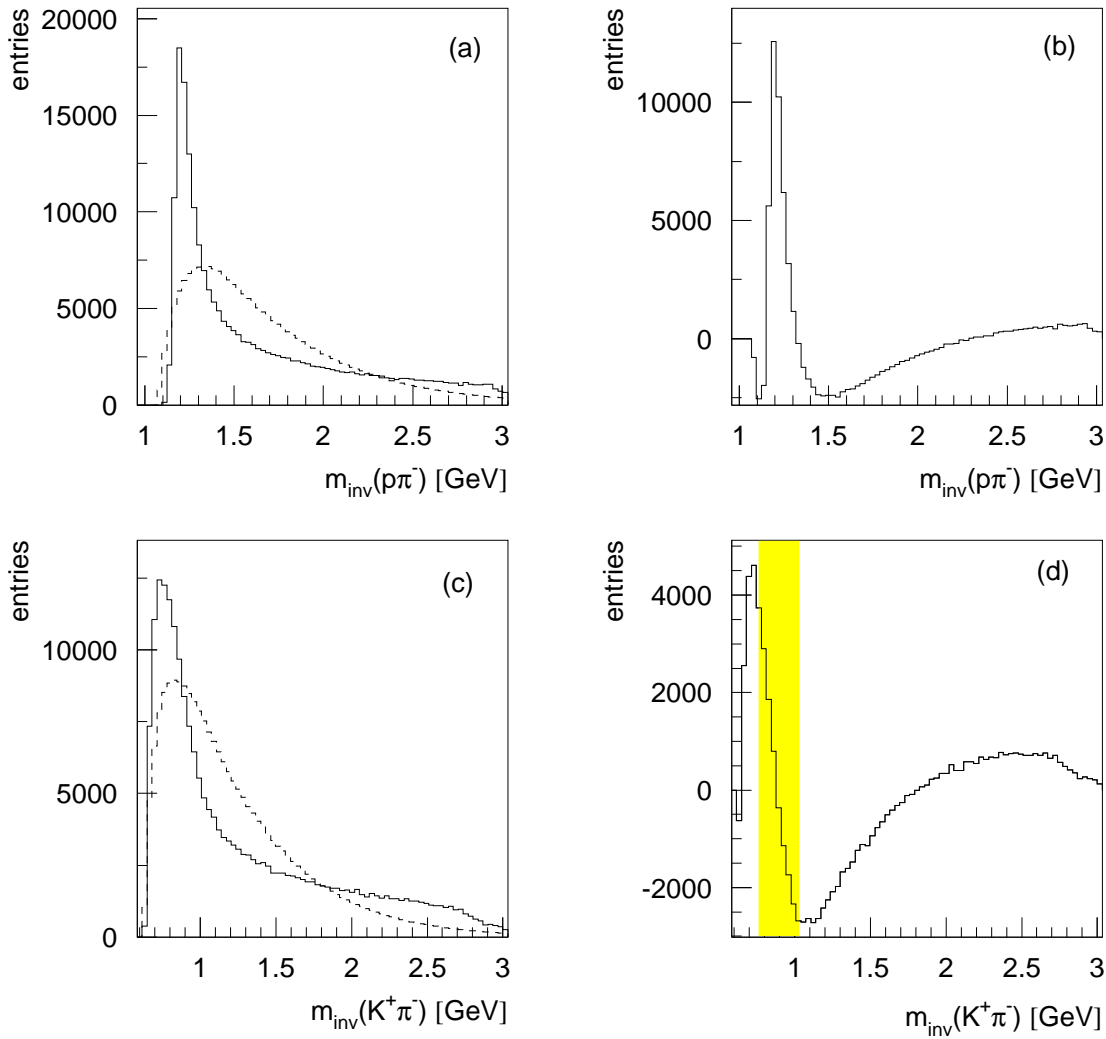


Figure 3.13: Simulation of the $\Delta(1232)$ resonance (solid line in (a)). The event-mix background (dotted line in (a)) is subtracted in (b). (c) and (d) show the same distributions but with assigning the kaon mass to the decay proton of the $\Delta(1232)$. In (d) the mass range of the $K^*(892)^0$ is indicated by the grey band. An enlargement of this histogram can be found in fig. 3.14.

Reflections of other resonances

A large variety of resonances is produced in the collisions under investigation, most of them decaying in a two body decay into kaons, pions and protons. Besides weak decays of strange baryons like Λ , Ξ and Ω or the neutral kaons K_S^0 and K_L^0 , nearly all resonances decay via the strong interaction at the main vertex, and the decay particles are reconstructed as stemming from there. Because of the uncertainty of the energy loss measurement particles cannot be identified track-by-track. A selection of kaons or pions by a window around their mean dE/dx value⁶ implies therefore a contribution of pions and protons into the kaon sample and kaons into the pion

⁶The selection method for kaon and pion pairs entering the invariant-mass spectra is explained in the next section. For simplicity and precision of the description the knowledge of the method is presupposed already here.

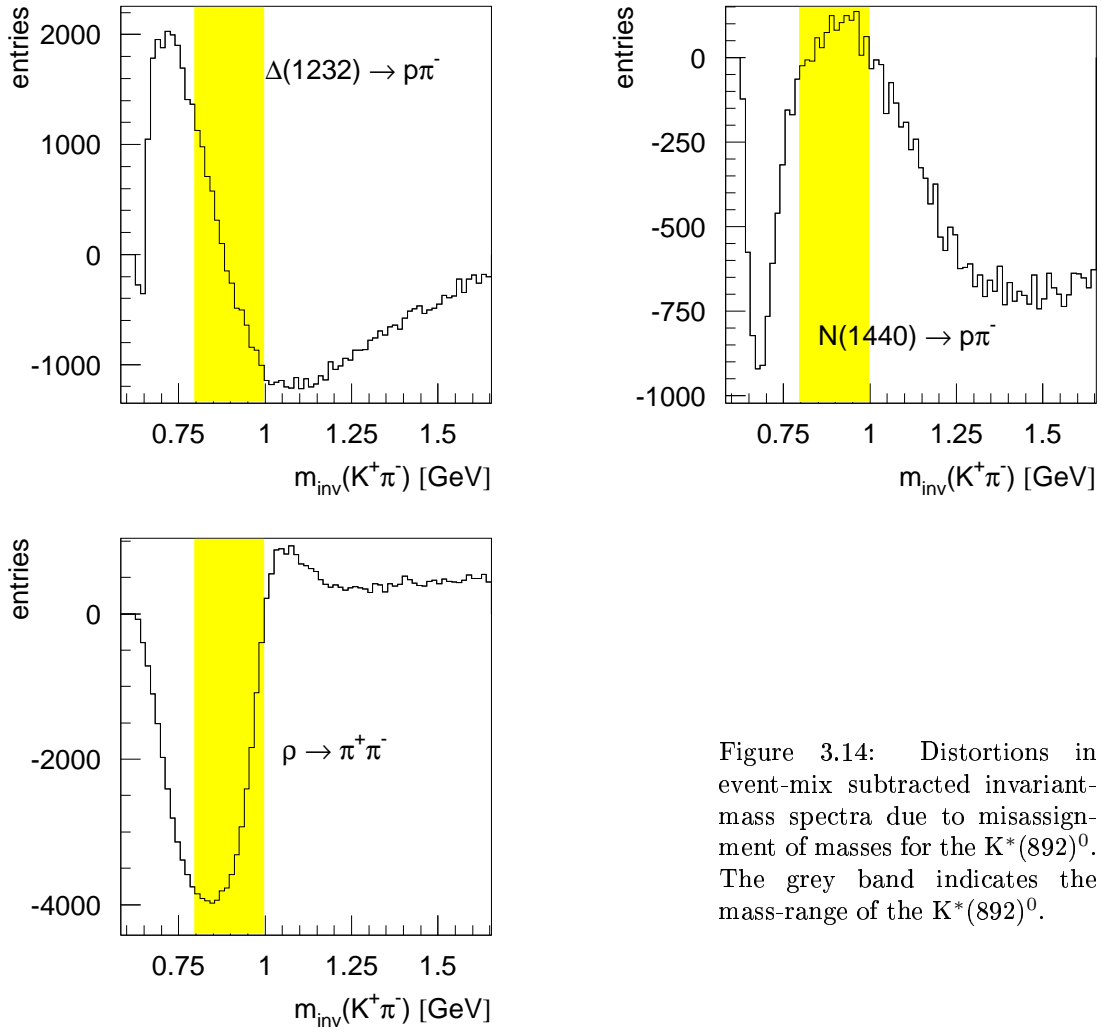


Figure 3.14: Distortions in event-mix subtracted invariant-mass spectra due to misassignment of masses for the $K^*(892)^0$. The grey band indicates the mass-range of the $K^*(892)^0$.

sample. These misidentified particles contribute to the invariant-mass spectrum. This leads to distortions in the background subtracted spectra, because, e. g., pion and proton stemming from a N^* or Δ resonance are correlated and thus not described by the event-mix spectrum (fig. 3.13, 3.14, 3.15).

The deformations from misidentification of decay products were investigated by simulations, only very abundant resonances should contribute. The resonances

particle	mass [MeV]	width [MeV]	decay channel	branching ratio [%]
N^*	1430 to 1470 (≈ 1440)	250 to 450 (≈ 350)	$N\pi$	60-70
Δ	1230 to 1234 (≈ 1232)	115 to 125 (≈ 120)	$N\pi$	> 99
ρ	770.0 ± 0.8	150.7 ± 1.1	$\pi\pi$	~ 100
$K^*(892)^0$	896.1	50.5	$K\pi$	~ 100

Table 3.4: Main resonances contributing to the distortions in the invariant-mass spectra of $K^*(892)^0$ and ϕ by misidentification of their decay products. [2]

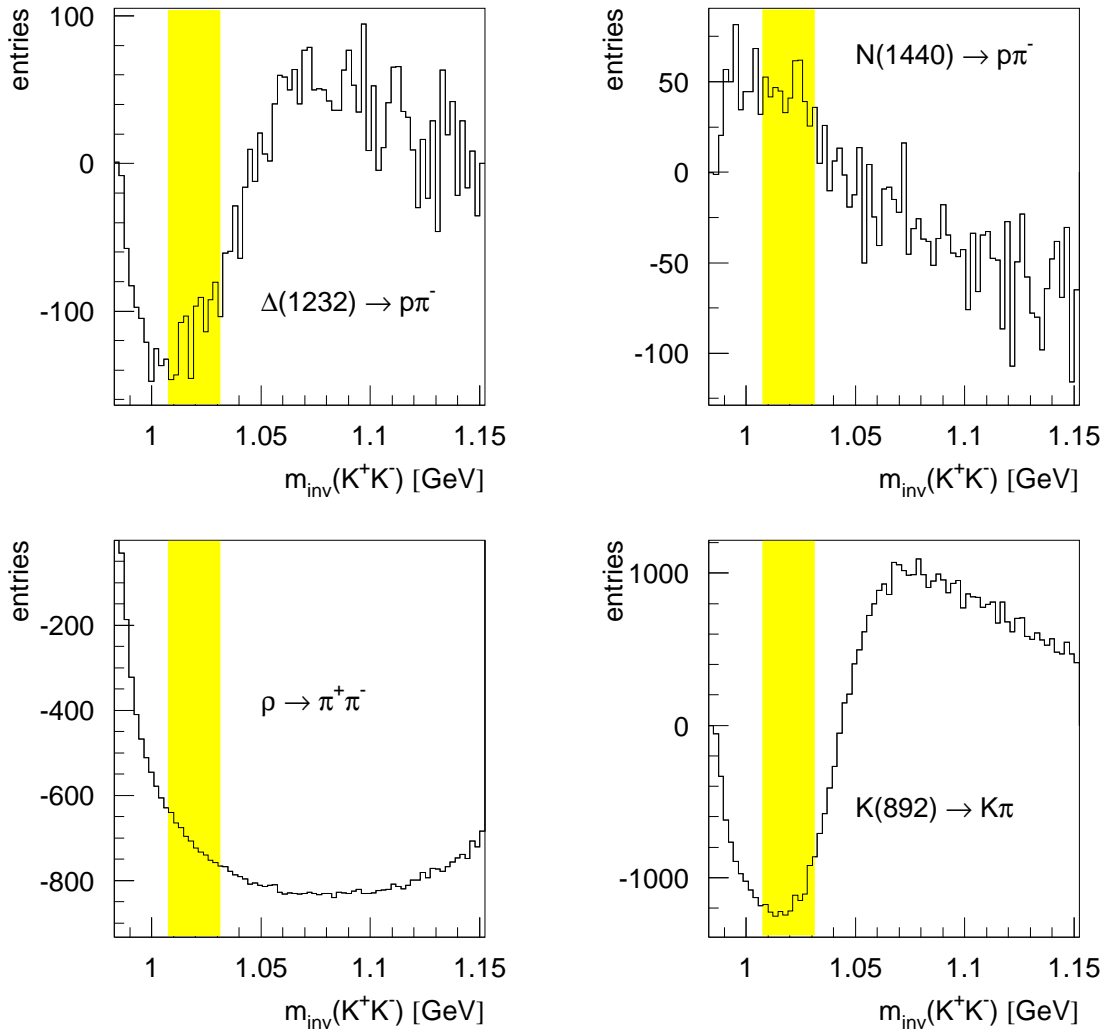


Figure 3.15: Distortions in event-mix subtracted invariant-mass spectra due to misassignment of masses for the ϕ -meson. Grey bands indicate the mass-range of the ϕ -meson (see also [64]).

from table 3.4 were generated with mass and width according to the particle data book [2] and reasonable kinematic distributions. Fig. 3.13 shows the Δ -baryon as example. The isotropic decay into, here, $p\pi^-$ was performed and the invariant-mass with incorrectly assigned masses of the decay products was reconstructed for the hypothesis of a $K^+\pi^-$ pair (fig. 3.13 (c)), the event-mix background is also calculated with misassigned masses. Background subtracted spectra for other relevant resonances with misidentification of their decay products are shown in figures 3.14 and 3.15. The mass-range of ϕ -meson and $K^*(892)^0$ is indicated.

The misidentification introduces large structures in the spectra which indeed might be the origin of the ones observed in real data (see e.g. fig. 3.16 or the figures in chapter 6.4). However, in fig. 3.14 and 3.15 ideal cases are presented; in reality all these contributions mix according to the relative abundances of the resonances and the misidentified hadrons.

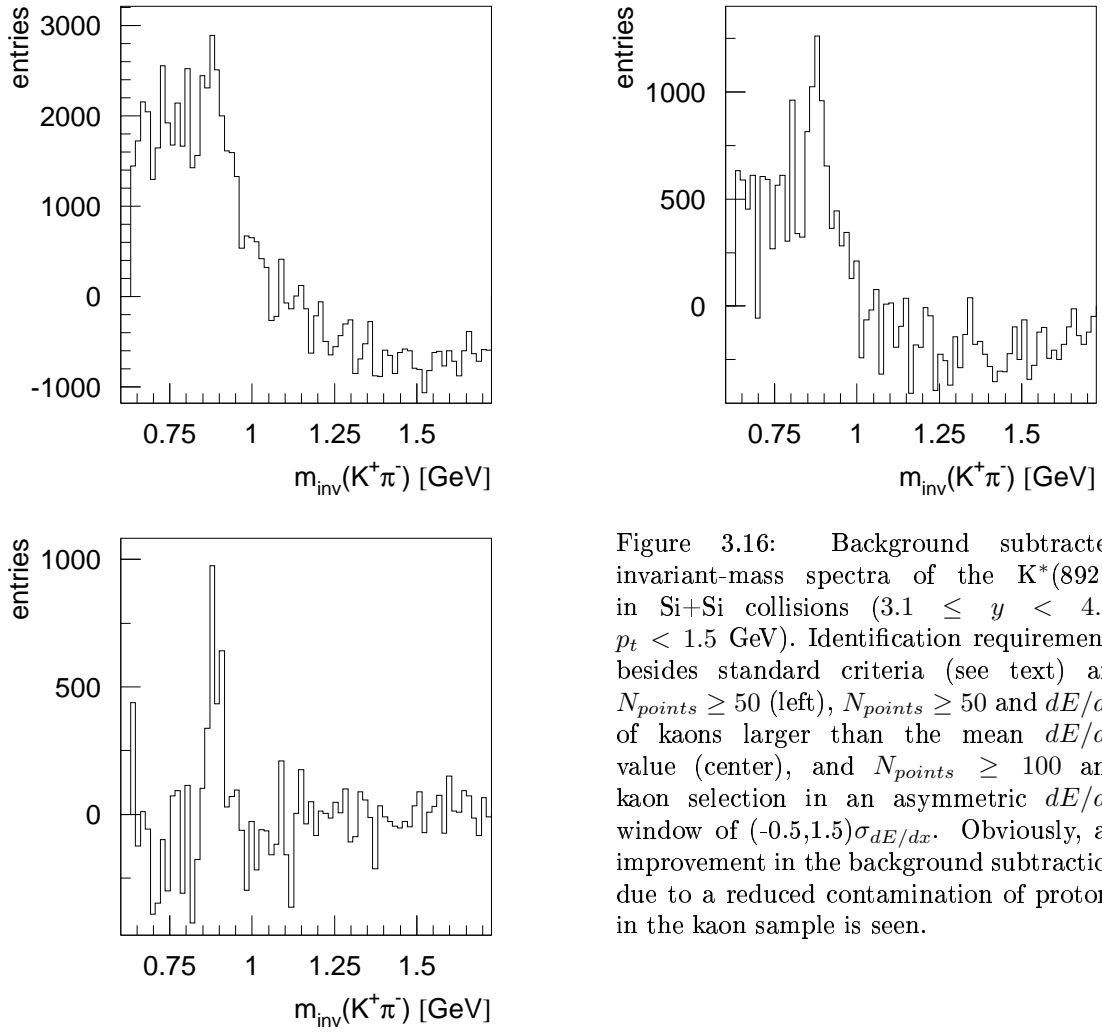


Figure 3.16: Background subtracted invariant-mass spectra of the $K^*(892)^0$ in Si+Si collisions ($3.1 \leq y < 4.7$, $p_t < 1.5$ GeV). Identification requirements besides standard criteria (see text) are $N_{points} \geq 50$ (left), $N_{points} \geq 50$ and dE/dx of kaons larger than the mean dE/dx value (center), and $N_{points} \geq 100$ and kaon selection in an asymmetric dE/dx window of $(-0.5, 1.5)\sigma_{dE/dx}$. Obviously, an improvement in the background subtraction due to a reduced contamination of protons in the kaon sample is seen.

Whether the structures in data are really correlated to misidentification can be investigated by changing the selection criteria for kaons and pions: Excluding protons in the kaon sample by certain quality cuts significantly improves the background subtracted spectrum of the $K^*(892)^0$ (see fig. 3.16). A similar behavior is observed for $\bar{K}^*(892)^0$ and ϕ -mesons especially in C+C and Si+Si interactions, however, the effect is largest for the $K^*(892)^0$.

The different shape of the background subtracted spectra of $K^*(892)^0$ and $\bar{K}^*(892)^0$ can also be understood by this effect because $\Delta(1232)$ and $N(1440)$ are much more abundant than their antiparticles (see section 5.1.4).

Bose-Einstein correlation of charged kaons

From the investigation of Bose-Einstein correlations it is known that unlike sign kaons close in phase space, i. e. with a small

$$q_{inv} = \sqrt{(\vec{p}_1 - \vec{p}_2)^2 - (E_1 - E_2)^2}, \quad (3.12)$$

show a strong correlation (fig. 3.17) due to Coulomb attraction. This should also reflect into a correlation in the invariant-mass, as on the other hand the ϕ -meson results in a wiggle of the K^+K^- correlation function [83].

The momentum difference of the decay kaons in the rest frame of the ϕ -meson is two times their decay momentum $|\vec{p}|$ and can be calculated from equation 3.17:

$$|\vec{p}| = \sqrt{\left(\frac{m_\phi^2}{4}\right) - m_K^2} \quad (3.13)$$

This yields 250 MeV which is the position of the slight peak in the correlation function (fig. 3.17). The other way round kaons with zero momentum difference show up at threshold in the invariant-mass spectrum, i. e. at $m_{inv} = 2 \cdot m_K = 0.987$ GeV. The correlation function C_2 reaches out to values of 50 MeV which transforms to an invariant-mass of $m_{inv} = 2 \cdot \sqrt{\left(\frac{0.05\text{GeV}}{2}\right)^2 + m_K^2} \approx 0.989$ GeV for a decay into two particles with equal mass. Therefore, the Coulomb correlation observed for unlike charged kaons influences the invariant-mass spectrum only in the very first bin (e. g. for a binsize of 2 MeV).

In the data, very often a small peak at threshold is observed, however, usually with a width of a few MeV. Recently it was discussed that a stronger and longer reaching effect might come from strong interactions in the final state [84], investigations are still going on. On the other hand, the invariant-mass spectrum as well as the event-mix background are steeply rising at threshold, which might result in this peak because of uncertainties in the shape of the spectra.

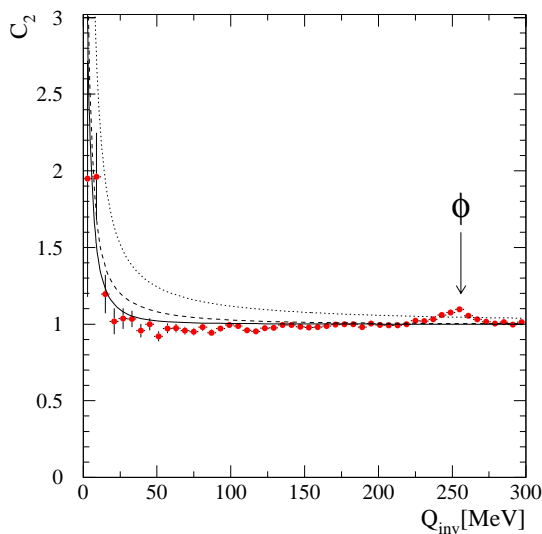


Figure 3.17: Q_{inv} -distribution of K^+K^- pairs for central Pb+Pb collisions at 158 AGeV. (From [83].)

Multiplicity

Kinematic constraints of events reflect in the momenta of the produced particles and thus also enter the invariant-mass spectra. Especially p+p collisions with a large relative change of multiplicity result in different kinematic distributions (e. g. [85, 86] and references therein, see also chapter 5.2.1). For example pions show a broader rapidity distribution in events with lower multiplicity. An effect of these correlations is seen in figure 3.18 where the event-mix background is compared for events with two kaons or one kaon at minimum. Since for a ϕ -meson at least two kaons are required for events entering the original spectrum, the event-mix background is also calculated from this class of events.

A similar effect was observed in A+A collisions by C. Markert [87]: An event-mix in event classes depending on multiplicity significantly improved the background subtraction. However, in the event samples available for this analysis no significant improvement is found. The variation in multiplicity and thus in kinematic correlations might be not large enough for this effect. Still, an event-mix in multiplicity bins was performed.

Naturally, the same holds for the $K^*(892)^0$ and the same treatment of the event-mix is performed there.

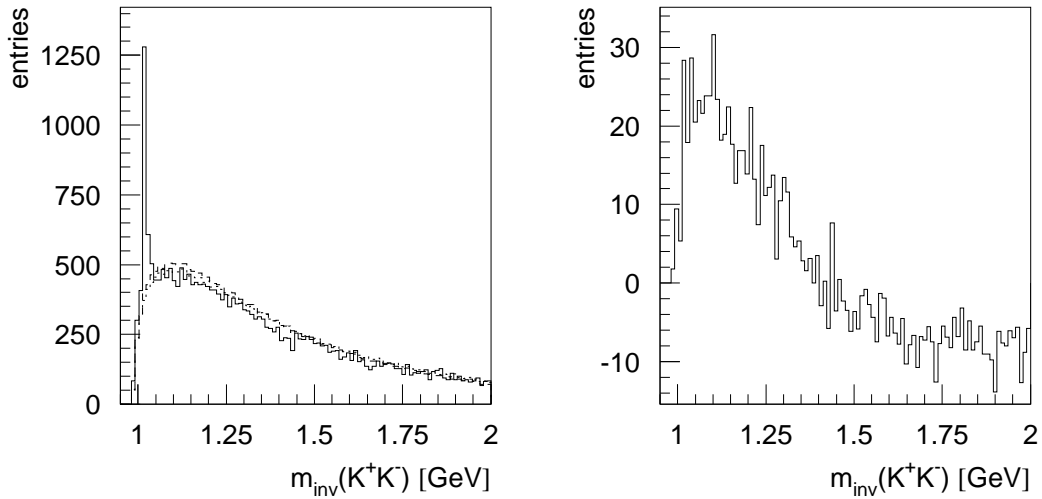


Figure 3.18: Invariant-mass spectrum of the ϕ -meson in p+p collisions (left), $2.9 \leq y < 4$, $0.4 \leq p_t < 0.6$ GeV, standard selection criteria. Two types of event-mix background are calculated and superposed (hardly visible): the first (1) using all identified kaons (dotted) and the second (2) using only kaons from events where at minimum one K^+K^- pair was found (dashed). The difference of these two types of event-mix background is presented in the right figure, strictly speaking (2) - (1) is shown.

3.2.3 Extraction of yields

Invariant-mass spectra of the $K^*(892)^0$, $\bar{K}^*(892)^0$ and ϕ -mesons are accumulated in bins of rapidity $y = y_1 + y_2$ or transverse momentum $p_t = p_{t,1} + p_{t,2}$ of the $K^\pm\pi^\mp$ and K^+K^- pairs; 1 and 2 denote the two contributing hadrons. All cuts applied for the original spectrum are also used for the event-mix spectrum, otherwise no proper description of the background would be achieved because of the strong kinematic constraints.

Kaons and pions are identified or rather enhanced in the track sample used for calculating the invariant-mass by setting a fix $c \cdot \sigma_{dE/dx}$ window around the mean dE/dx position; as standard criterion $c = 1.5$ is chosen. This selects 86.64 % of all pions or kaons which corresponds to $(86.64)^2$ % = 75.06 % of all $K^*(892)$ or ϕ -mesons. Mean positions and absolute widths are calculated according to formula 3.3 and 3.4 with parameters b and a as extracted from the fits of the dE/dx -spectra (see section 3.1.2). Special fits were performed without a Φ -cut and rejection of wrong-side tracks in order to determine a and b for the same track sample as used for the invariant-mass method.

Only a minimum of quality cuts is applied for the selected kaons and pions not to reduce the statistics more than necessary. As discussed above, a clean track sample is not as important as for the dE/dx spectra because "bad" tracks only contribute to the background which is subtracted.

Each track is required to have at least 30 points. A cut in the azimuth Φ is not performed, because the angles of the decay products are strongly correlated and a large coverage in Φ significantly increases the acceptance of the resonance. A lower and higher limit of total momenta, $\log_{10}(p) = 0.6$ ($p = 4$ GeV) and $\log_{10}(p) = 1.7$ ($p = 50$ GeV), is used to minimize distortions in the invariant-mass spectrum due to misidentified particles. Their fraction increases in the crossing or converging region of the Bethe-Bloch curves. In addition an upper limit in p_t is required (1.5 GeV for p+p, 1 GeV for C+C and Si+Si collisions) because of the limited range in which $\sigma_{dE/dx}$ and mean positions of dE/dx were available from dE/dx fits.

The background is calculated with the event-mixing technique and subtracted. Yields are extracted by adjusting a simulation which includes corrections for geometrical acceptance and in-flight decay of kaons by minimizing the χ^2 [79]. Scaling factor d and number of simulated resonances N_{sim} provide the content of the signal: $N_{signal} = d \cdot N_{sim}$. The number of resonances in a (y, p_t) bin is thus given by

$$N_{resonance}(y, p_t) = \frac{d \cdot N_{sim}(y, p_t)}{N_{events} p_{pid} F \Delta y \Delta p_t}, \quad (3.14)$$

where F denotes the branching ratio and p_{pid} the particle identification probability according to the $c \cdot \sigma_{dE/dx}$ cut. For p+p collisions the number of events N_{events} is corrected for losses as explained in chapter 4.1. Unfortunately, statistics allow only for p_t -integrated y -bins and p_t -bins in a wider y -range. For the extraction of rapidity spectra, $\frac{1}{\Delta p_t}$ in equation 3.14 is therefore replaced by a factor f_{p_t} which extrapolates the used p_t -range to infinity. If the signal is extracted in close to the full acceptance, i. e. in a large y and p_t -bin, also $\frac{1}{\Delta y}$ has to be replaced by a factor

f_y which extrapolates the used rapidity range to the full one. Both extrapolation factors are sensitive to the assumed kinematic distributions.

For the validity of the method one has to take great care that the background is subtracted such that data and simulation fit. Problems and solutions of this fact will be discussed separately for the various cases in chapters 5 and 6.

3.2.4 Simulation of the resonance

In the previous section the extraction of the yield in the resonance signal of the invariant-mass distribution was reduced to the adjustment of a simulation: The mass distribution of the resonance is simulated according to a relativistic Breit-Wigner function [88] with width Γ_0 and mass m_0 according to the particle data book [2] (see also table 3.2):

$$\frac{dN}{dm} \propto \frac{m}{q} \frac{\Gamma(m)}{(m_0^2 - m^2)^2 + m_0^2 \Gamma^2(m)} \quad (3.15)$$

with

$$\Gamma(m) = \Gamma_0 \left(\frac{q}{q_0} \right)^3 \frac{m_0}{m} \quad (3.16)$$

and decay momentum

$$q_0 = \frac{1}{2m_0} \sqrt{[m_0^2 - (m_1 + m_2)^2] \cdot [m_0^2 - (m_1 - m_2)^2]}. \quad (3.17)$$

q in the equations above is calculated as in 3.17 but with mass m instead of m_0 . m_1 and m_2 denote the masses of the decay products, i. e. m_K and m_π .

Kinematic distributions of the resonances are generated as introduced in equation 3.10 for rapidity and 3.7 for the transverse momenta, the azimuth Φ is populated isotropically.

The resonances decay isotropically in their rest frame into the decay products 1 and 2. Both get the same absolute momentum according to equation 3.17, $|\vec{p}_1| = |\vec{p}_2|$. After transformation of the momenta into the center-of-mass system the acceptance of both particles is proved, the corresponding acceptance tables are achieved in the next section.

The invariant-mass of the pair is accumulated in histograms in the same bins of y and p_t as in the data. To account for the momentum resolution of the detector the invariant-mass is additionally broadened by a Gaussian centered at m_0 and with a width σ_m .

The event-mix subtracted spectrum is adjusted to data (see e. g. fig. 3.10): In a first step mass m_0 and width σ_m for the Breit-Wigner mass distribution and the Gaussian broadening are determined and fixed for the rest of the analysis. In an iterative process the parameters T and σ_y entering the kinematic distributions are extracted afterwards, if starting with reasonable parameters only 2 to 3 iterative steps are needed.

3.2.5 Acceptance and in-flight decay of kaons

ϕ - meson

Acceptance tables for the ϕ -meson including in-flight decay of kaons are calculated starting with the generation of ϕ -mesons with a Breit-Wigner mass distribution. Momenta are equally distributed, i.e. isotropically in the azimuth and with flat distributions in (x_F, p_t) with binsizes of $\Delta x_F = 0.05$ and $\Delta p_t = 0.1$ GeV in a range of $-0.6 \leq x_F < 1$ and $0 \text{ GeV} \leq p_t < 2.5$ GeV. For each bin 10000 ϕ -mesons are simulated resulting in a statistical error of 10 % in case the acceptance is only 1 %. For an acceptance table in (y, p_t) the kinematic variables are recalculated.

The decay kaons of the ϕ -meson are used as input to the simulation chain GEANT \rightarrow MTSIM \rightarrow reconstruction. The decay length of charged kaons is $c\tau = 3.7$ m in their rest frame, this corresponds to several meters in the laboratory frame so that about 30 % of the kaons decay inside the detector. This fraction depends on the momentum but also on the track-length of the kaons (fig. 3.19).

A ϕ -meson is accepted if both decay kaons fulfill the acceptance criteria described below. The ratio of accepted to generated ϕ -mesons per (x_F, p_t) or (y, p_t) bin gives the relative acceptance in phase space presented in figure 3.20.

As explained briefly in section 3.1.3 the simulation chain GEANT \rightarrow MTSIM \rightarrow reconstruction allows to follow whether a simulated track is reconstructed with a reasonable momentum. Here, a kaon is accepted if it is reconstructed with a minimum of 30 points per track and a momentum unequal to zero.

Furthermore it is proved whether a kaon has decayed in GEANT, and whether this decay took place inside the TPCs. $K^\pm \rightarrow \mu^\pm \nu_\mu$ is the most dominant decay mode of charged kaons with a branching ratio of 63.5 %, the next frequent are decays into pions. Since the neutrino takes away only a small part of the kaon energy and is not seen in the detector, the track of the decay- μ can only be distinguished from the kaon by a small kink at the decay vertex (see fig. 3.21). In the reconstruction this kink is not always found thus kaon and μ might be *matched* to one track.

If the kink is recognized and the kaon is reconstructed with more than 30

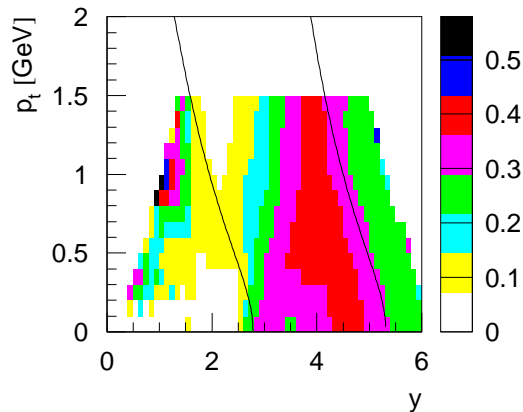


Figure 3.19: Kaons decaying in the detector relative to reconstructed ones in dependence on (y, p_t) . The lines indicate typical momentum borders for the identification of kaons of 4 GeV and 50 GeV.

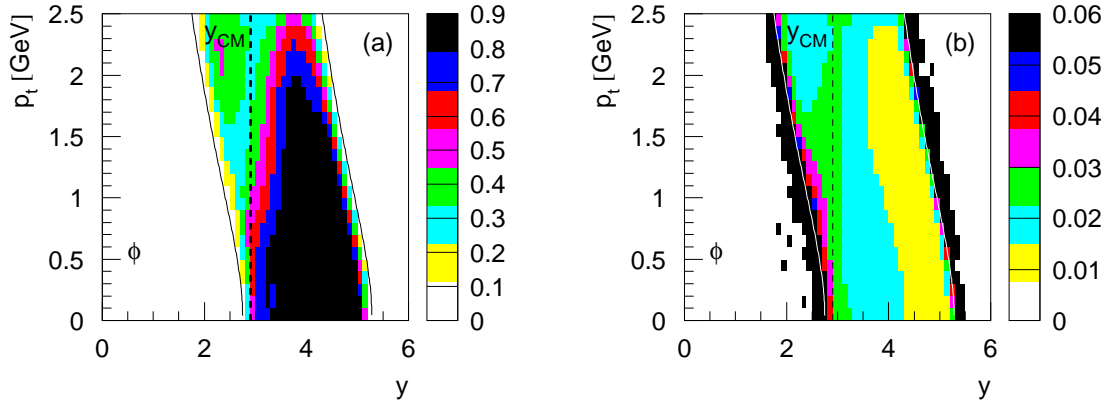


Figure 3.20: Acceptance (a) and statistical error (b) in (y, p_t) for ϕ mesons. The kaon acceptance is defined as described in the text, only kaons with $p_t < 1.5$ GeV are used here. The lines present the identification borders stemming from the momentum cut for kaons of 4 GeV and 50 GeV. Bins outside of these bands are not used for analysis.

points on the track, it is accepted. If kaon and μ have very similar momenta, the kink might not be found by the software and kaon and μ are matched to one track which has only a slightly different momentum compared to the kaon. But the μ has a different energy loss in the TPCs compared to the kaon (see fig. 3.1). If the myonic part of the track is too long the "kaon" is not anymore identified as such because the combined dE/dx is shifted below the pion peak.

At maximum 25 % of all kaons decaying in the TPCs are matched to their daughter, this reduces to 9 % of the reconstructed ones (fig. 3.22). Figure 3.23 shows that for a large majority of these kaons only a few points are matched to the original track. In real data these kaons are still identified, thus for the acceptance calculation not all these matched tracks have to be excluded. As indicated by the line in figure 3.23, as acceptance criterion it is required that not more than 30 % of points are matched to the kaon track. Matched tracks rejected by this cut are located at backward rapidities which corresponds to low momenta in the laboratory system (fig. 3.24).

The following estimation might justify the 30 % limit: The difference in mean energy loss of kaons and pions is about 15-10 % in the momentum range of interest, for kaons and μ it is 20-10 % (see fig. 3.1). Even in case of 10 % separation a combined dE/dx value of K and μ leaves a difference in the energy loss of K and π of at least 6-7 %. This should still allow to identify the matched track as kaon.

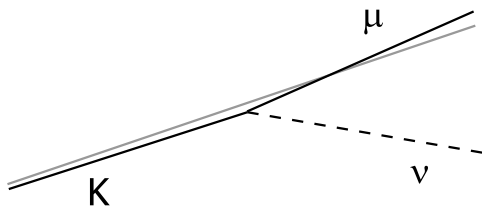


Figure 3.21: Illustration of a kaon decaying into $\mu\nu$; the grey line indicates the problem of matching tracks of kaon and muon to one track.

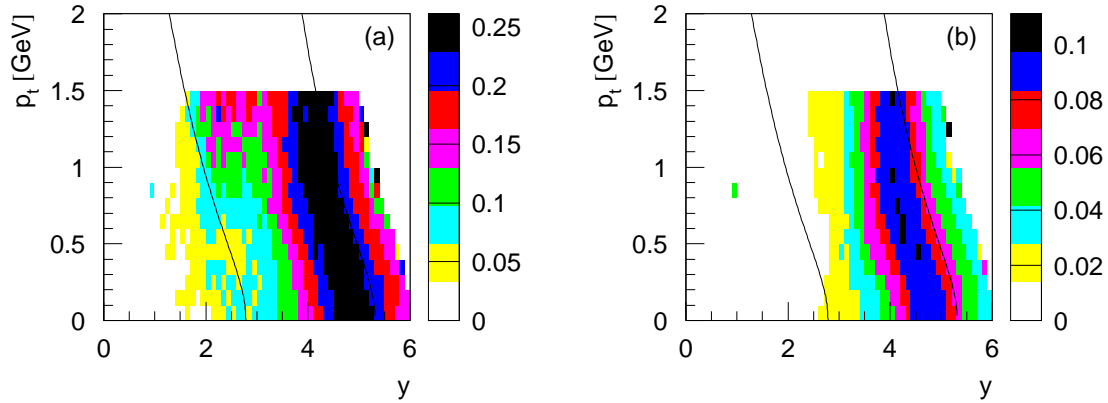


Figure 3.22: Kaon tracks matched with their decay daughter track relative to all decayed kaons (a) and relative to all reconstructed kaons (b). Lines indicate typical identification borders for kaons of 4 GeV and 50 GeV in total momentum.

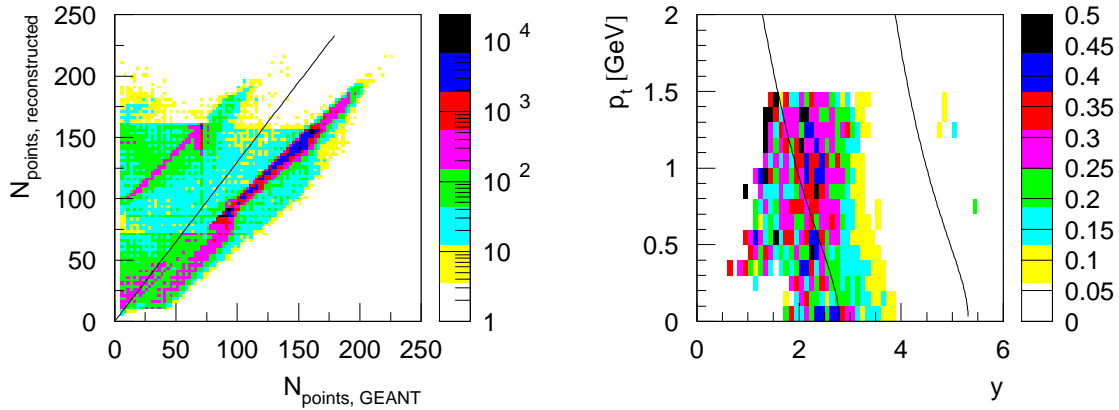


Figure 3.23: Number of reconstructed points versus number of points in GEANT for tracks where kaon and decay daughter are matched. The line shows the limit of 30 % points matched to the kaon track.

Figure 3.24: Kaon tracks with more than 30 % matched points relative to all matched kaon tracks. Lines indicate typical identification borders for kaons of 4 GeV and 50 GeV in total momentum.

$K^*(892)^0$ and $\bar{K}^*(892)^0$

For $K^*(892)^0$ and $\bar{K}^*(892)^0$ no independent acceptance calculation was performed, instead results computed for kaons and pions were used. Three-dimensional acceptance tables of both were extracted from the information for pions, provided by the tables of F. Sikler [72], and from the acceptance calculation for kaons (for both see section 3.1). The resulting precision of the acceptance for $K^*(892)^0$ is the weakest therefore compared to the other particles investigated in this thesis, statistical errors are about 5 %. Fig. 3.25 presents the acceptance of $K^*(892)^0$, the small values at midrapidity result from the missing acceptance for pions in this region (see fig. 3.6).

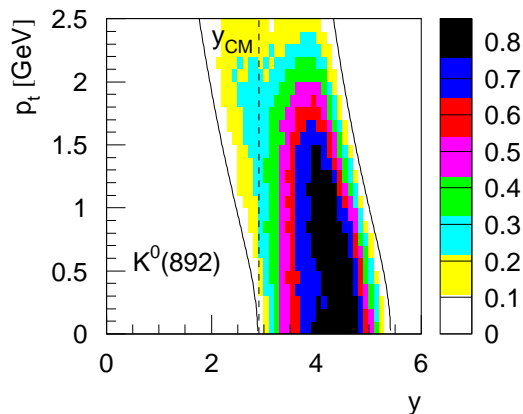


Figure 3.25: Acceptance in (y, p_t) for the $K^*(892)^0$, the one for $\overline{K}^*(892)^0$ is the same besides small variations on a 1 % level. Kaons and pions are accepted as explained in the text, the lines present the identification borders stemming from the total momentum range of kaons and pions of 4 GeV to 50 GeV.

3.2.6 Systematic errors

Systematic errors of the extraction of resonances identified by means of their invariant-mass will be estimated in the corresponding analysis chapters 5 and 6. Here only main sources and the order of magnitude are summarized.

As already mentioned in section 3.1.5, data analyzed in this work were taken with the STD+ configuration of the magnets in NA49, which was shown to agree within 5 % to the data taken at STD- configuration [71].

The main systematic error for yields analyzed with the invariant-mass method lies in the subtraction of the background. Especially if statistics are weak and remaining distortions are large the uncertainty can be rather large, e. g. up to 30 % for the $K^*(892)$ in C+C and Si+Si collisions. But in normal conditions the systematic uncertainty is on the order of 10 % for the ϕ -meson and a bit less for $K^*(892)$ (8 %).

Another source of errors lies in the precision of the assumed mean dE/dx and $\sigma_{dE/dx}$ for particle identification which introduces an uncertainty of about 3-4 %. Systematic errors from other selection criteria are of the same order. Assuming that all matched kaons are lost increases the yield by about 5-6 %. Only 1-2 % errors are introduced by the extrapolation of the p_t and y -spectra.

The acceptance is calculated with a precision of 1-2 % and 5 % for ϕ and $K^*(892)$, respectively.

To summarize, systematic errors on the order of 8-10 % are realistic for total yields of $K^*(892)^0$, $\overline{K}^*(892)^0$ and ϕ . For C+C and Si+Si collisions the systematic errors are larger because of the weak statistics available so far and increased uncertainties in the background determination.

3.3 Particle identification with veto chambers and ring calorimeter

For hadron+p and hadron+Pb collisions from the year 1999 on the Ring Calorimeter (RCAL, fig. 2.2) was shifted perpendicular to the beam axis in order to detect fast hadrons emitted close to the beam axis. A set of proportional counters (VCHAM) in front of the active area acts as charged-particle detector. This way, fast protons and neutrons going through the central gap of the TPCs are measured (see fig. 3.26). This feature is relevant for the selection of p+p interactions in dependence on inelasticity as discussed in chapter 4.2.

The particles are fully stopped in the calorimeter, which provides a direct measurement of their energy. The hit positions give p_x and p_y , p_z is then also calculable. Since the single cells of the calorimeter are rather large (fig. 3.26), the measurement of p_x and p_y has large uncertainties. The data sets were analyzed by D. Varga [89], the provided information (charge, p_x , p_y , p_z) is obtained assuming that all hadrons are neutrons. He also discussed the quality of the detection method, the results will be summarized briefly in the remaining part of this section.

The energy resolution of the calorimeter is only on the order of 20-30 % with an additional error on the absolute energy scale of about 5 %. The calorimeter distinguishes between hadrons and photons using the different response of the hadronic

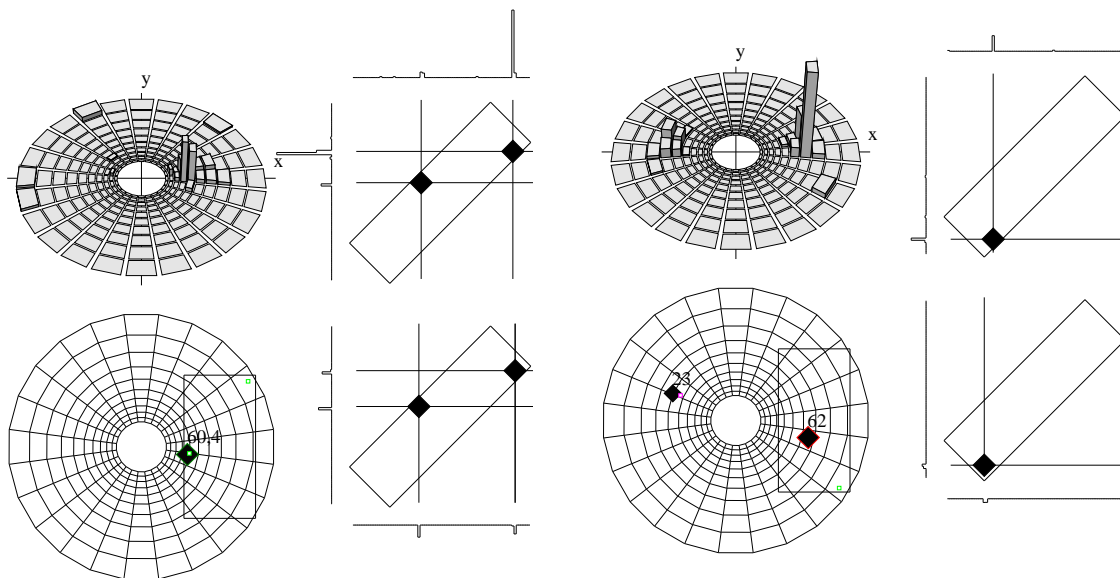


Figure 3.26: Example for the detection of a proton (left) and neutron (right) with the combined VCHAM and RCAL setup. On the right side of each example the veto chambers are turned such that the strips are running horizontal and vertical in this demonstration. This allows the inclusion of the signals recorded on the strips in the picture. On the left side of each example the superposition of VCHAM and RCAL gives a realistic illustration of the overlapping area. For protons the hit in the VCHAM and corresponding energy deposit in the RCAL is clearly seen, for neutrons the veto chambers show no signal. Both examples have a less energetic charged particle in the upper right (p example) and lower right (n example) edge. (From [89].)

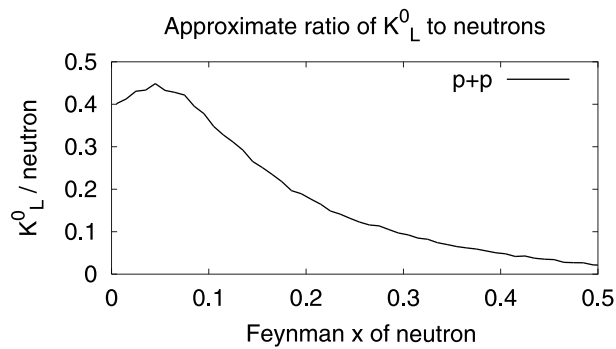


Figure 3.27: Fraction of K_L^0 relative to all neutrons in p+p collisions detected with the combined VCHAM and RCAL setup. (From [89].)

and electromagnetic section. Hadrons are selected in the analysis by requiring less than 60 % of their energy in the electromagnetic part. This introduces losses of 5 (10) % for neutrons with an energy of 120 (40) GeV. Losses due to overlapping clusters account for a few percent only. The efficiency for both veto chambers for the detection of charged particles is 97-99 %. Losses due to many hits in the chambers which reduces the capability of resolving single particle hits is about 8 (11) % for neutrons with an energy of 120 (40) GeV. The matching efficiency between veto chambers and calorimeter is nearly 100 %. Summarizing these losses, the total probability to detect a fast neutron in the combined VCHAM and RCAL setup adds to 85 (78) % for an energy of 120 (40) GeV. It is assumed in this work that the probability for proton detection is the same.

The quality of the neutron detection suffers also from the fact that with the combination of VCHAM and RCAL only neutral particles are measured, i. e. a mixture of neutrons, antineutrons but also K_L^0 . Especially at low x_F their contribution to the neutral particles is sizeable (fig. 3.27).

Chapter 4

Event selection

4.1 Minimum-bias p+p interactions

The total cross section for p+p collisions (fig. 1.7) includes elastic as well as inelastic interactions, only the latter contributing to particle production. Values are available from tables or parametrizations [2]. The term "minimum-bias" is specific for an experiment and given by the trigger condition. In NA49, the minimum-bias trigger includes most of the inelastic interactions, but also some elastic scattering events.

In this section a short overview over the determination of the NA49 trigger cross section is given. Corrections for event losses, which have been determined by O. Chvala [60] and will be applied in the analysis, are introduced.

4.1.1 The NA49 trigger cross section

The NA49 minimum-bias trigger uses the beam counters S1, V0, S2, and S4 as described in section 2.2. They define a trigger cross section of about 28.5 mb (tab. 4.1) including 27.4 mb inelastic interactions of the nominally 31.6 mb, 4.2 mb presumably mostly diffractive events are rejected. Still contained in the trigger are about 1.1 mb of the 7.1 mb elastic scattering events [60, 61].

The trigger rate $\frac{dN_{trig}}{dt}$ in a fixed-target experiment is given by the beam particle current $\frac{dN_{beam}}{dt}$, the number of target nuclei per area $\frac{N}{S}$ and the trigger cross section σ_{trig} :

$$\frac{dN_{trig}}{dt} = \frac{dN_{beam}}{dt} \cdot \frac{N}{S} \sigma_{trig} \quad (4.1)$$

With $\frac{N}{S} = \rho \frac{N_A}{M} d$ (ρ density of the target, d its thickness, M the molar mass and N_A the Avogadro number) the trigger cross section reads:

$$\sigma_{trig} = \frac{1}{\rho \frac{N_A}{M} \cdot d} \cdot \frac{N_{trig}/dt}{N_{beam}/dt} \quad (4.2)$$

Experimentally, the number of interactions accepted by the trigger N_{trig} and the number of beam particles N_{beam} are measured by the counting rates in the beam

dataset	year	target length	σ_{trig} [mb]	N_{events}	efficiency [%]
00A	1996	14 cm	27.75 ± 0.5	417708	76.5
00D	1999	20 cm	28.28 ± 0.1	653982	73.7
00R	2000	20 cm	28.48 ± 0.1	1469613	74.5
combined			28.31 ± 0.1	2541303	74.6

Table 4.1: Trigger cross sections and the analyzed number of events for the various datasets of p+p interactions in NA49. In the last column the overall efficiency is given with which minimum-bias p+p events are reconstructed and analyzed (for details see section 4.1.2). (From [60].)

detectors $S1 \times \overline{V0} \times S2$ and $S1 \times \overline{V0} \times S2 \times \overline{S4}$, requiring proton identification via the Cherenkov signal in addition.

The proton target consists of a Mylar¹ cylinder filled with liquid hydrogen in a vacuum vessel for thermal insulation. Therefore not only p+p interactions are selected by the trigger definition, but also p+Mylar events of beam and target windows and even a few with the entrance or exit window of the vacuum tube. The contribution of these events can be determined when taking data with an empty target tube. The difference $\left[\left(\frac{N_{trig}}{N_{beam}} \right)_{full\ target} - \left(\frac{N_{trig}}{N_{beam}} \right)_{empty\ target} \right]$ is the ratio $\frac{N_{trig}}{N_{beam}}$ used in formula 4.2.

4.1.2 Corrections for event losses

In order to obtain a clean sample of p+p collisions and to reduce background events like p+Mylar interactions below a 1 % level, several event cuts are applied: Events with a reconstructed vertex z -position outside the central 18 cm (11 cm) of the 20 cm (14 cm) long target are rejected. In addition, a cut in the plane perpendicular to the beam axis is performed; only events inside a circle with 1 cm radius are used. This area is large compared to the beam spot at the target, which is approximately of Gaussian shape with a σ of about 1.4 mm in x and 0.9 mm in y . Therefore, losses due to this cut are negligible.

In inelastic p+p events the mean charged-particle multiplicity is 7.2 for a center-of-mass energy of 17.3 GeV. Since the NA49 detector geometry accepts on average about 60 % of all tracks (with certain quality criteria, see next section), the number of tracks in the spectrometer might be very small in some events. The vertex is reconstructed combining the beam position known from the BPDs and the extrapolation of the measured tracks back to the target. Therefore, the uncertainty of the vertex position increases the fewer particles an event has leading to a rising fraction of p+p events rejected by the vertex z -position cut. Correction factors (C1) for these losses are calculated by O. Chvala [60] and included in the analysis.

A second multiplicity dependent correction factor (C2) is necessary, because the reconstruction for interactions with only a few particles in the detector fails sometimes. In the analysis events are weighted with the product of both. A third overall correction factor (C0) is applied to account for events in which no track was

¹Polyethylene terephthlate, monomer: $C_5H_4O_2$ [2].

	00A	00D	00R
C0	1.0665 ± 0.0017	1.0775 ± 0.0009	1.0758 ± 0.0007
multiplicity	C1 · C2	C1 · C2	C1 · C2
1	4.150 ± 0.090	3.648 ± 0.038	3.308 ± 0.026
2	1.879 ± 0.032	1.906 ± 0.015	1.797 ± 0.012
3	1.500 ± 0.019	1.567 ± 0.010	1.532 ± 0.007
4	1.259 ± 0.015	1.304 ± 0.008	1.281 ± 0.005
5	1.159 ± 0.013	1.204 ± 0.007	1.195 ± 0.005
6	1.090 ± 0.012	1.138 ± 0.006	1.138 ± 0.005
7	1.057 ± 0.012	1.102 ± 0.006	1.102 ± 0.005
8	1.046 ± 0.013	1.073 ± 0.007	1.073 ± 0.005
9	1.038 ± 0.015	1.061 ± 0.007	1.061 ± 0.005
10	1.031 ± 0.016	1.050 ± 0.008	1.050 ± 0.006
11	1.025 ± 0.019	1.040 ± 0.010	1.040 ± 0.007
12	1.020 ± 0.023	1.033 ± 0.011	1.033 ± 0.009
13	1.015 ± 0.029	1.027 ± 0.014	1.027 ± 0.011
14	1.011 ± 0.035	1.016 ± 0.018	1.016 ± 0.013
15	1.008 ± 0.047	1.010 ± 0.023	1.010 ± 0.017
16	1.004 ± 0.063	1.005 ± 0.029	1.005 ± 0.024
17	1.002 ± 0.085	1.001 ± 0.039	1.001 ± 0.033
18 - ∞	1.0	1.0	1.0

Table 4.2: Multiplicity dependent correction factors for the losses due to the vertex cut and vertex reconstruction inefficiencies (C1 · C2) as well as for events with no tracks reconstructed in the detector (C0). (From [60].)

accepted in the detector as coming from the main vertex. Such events are for example diffractive interactions, where the fast proton is not accepted in the TPCs, reactions with only neutral particles passing the detector or other low multiplicity events. The correction factors and their errors are given in table 4.2. Their use for the extraction of particle spectra has been explained in chapter 3. The overall efficiency in table 4.1 is the ratio of the number of analyzed events and the number of events corrected for the described inefficiencies: each event is weighted with $C1 \cdot C2(N_{ch})$ and the sum is multiplied with C0.

4.2 Inelasticity in p+p interactions

4.2.1 Introduction

In e^+e^- annihilation into hadrons all center-of-mass energy is spent for the production of new particles. In p+p collisions the energy used for the creation of new hadrons is not as well defined, because due to baryon number conservation two baryons have to re-appear after the interaction. Obviously, only the difference of

the center-of-mass energy and their energy is available for particle production:

$$\sqrt{s_{\text{eff}}} = \sqrt{s} - E_{B1} - E_{B2} \quad (4.3)$$

This effective center-of-mass energy covers a range from zero to $(\sqrt{s} - 2m_p)$ at the most. Experimentally, it is correlated to the multiplicity as known from the hadron production in e^+e^- interactions in dependence on \sqrt{s} . On the other hand, it could be calculated if the energy of the re-appearing baryons would be known.

In diffractive interactions the protons are excited into resonances; after de-excitation they are observed as protons, neutrons or Λ -baryons at large Feynman-x (leading baryons). Since they are kinematically separated from the newly produced $B\bar{B}$ pairs which are concentrated at midrapidity, they can be identified experimentally. Applying this observation also to more inelastic collisions, the leading baryon can be identified with the fastest baryon in an event. This picture may lose its validity in very violent interactions, but there it does not have much influence whether the leading baryon is "correctly" identified or mixed up with a newly produced one, as both have small energy.

In p+p collisions at the ISR, Basile et al. [11] have defined leading protons within a certain Feynman-x range as the fastest protons in an event and measured the associated charged-particle multiplicity in the same hemisphere. Assuming a symmetric behavior of both hemispheres on average, they doubled the multiplicity, and calculated the effective center-of-mass energy as $\sqrt{s_{\text{eff}}} = \sqrt{s} - 2E_{\text{lead}}$, (E_{lead} leading-proton energy). Indeed, the multiplicity in dependence of $\sqrt{s_{\text{eff}}}$ agrees well with results from e^+e^- interactions.

Charged-particle multiplicity and the energy of the leading proton – measured, e. g., by Feynman-x – allow therefore to define a kind of "centrality" or degree of inelasticity in minimum-bias p+p collisions. It is evident, that both variables are correlated (fig. 4.1), however, the correlation is not sharp because even at a fixed inelasticity there are fluctuations in the multiplicity and Feynman-x of the leading proton. The influence of the effective center-of-mass energy on particle production

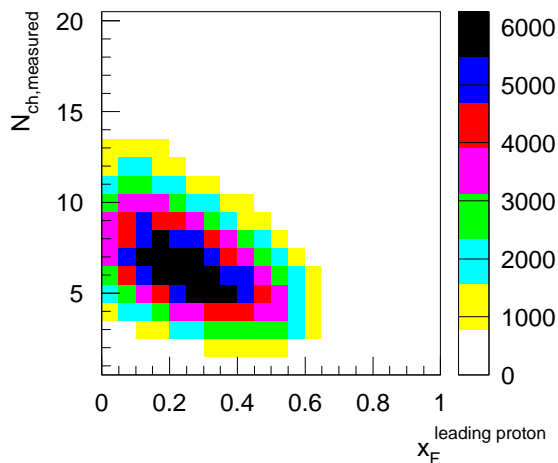


Figure 4.1: Correlation of measured multiplicity within the NA49 acceptance and Feynman-x of the leading proton in p+p collisions (for definition see section 4.2.2).

and particle abundances is of particular interest for the understanding of A+A collisions, because there the energy loss of the incident nucleons is larger compared to minimum-bias p+p interactions ("stopping", see fig. 1.9).

Experimentally, only charged particles in the forward hemisphere are accessible in the TPCs of NA49. Therefore, only leading *protons* in this hemisphere can be observed, also produced hadrons are studied only there.

The first of this twofold restriction, the selection of one exit channel of leading baryons only, is assumed not to bias the representativeness of this class of interactions, because the mass difference between p, n , and Λ is small. Only the different strangeness content has an effect on, in particular, relative kaon production in low multiplicity events. However, overall the influence of the latter events is small. This subject will be discussed in more detail in context with the FRITIOF simulations in section 4.2.4 and 5.2.3.

The restriction to one hemisphere only for the inelasticity definition and the measurement of its consequences is more involved, because one assumes that the observations in one hemisphere are representative for a certain inelasticity and no bias is introduced by the other (unobserved) hemisphere. It is plausible, and was shown by Basile et al. [11, 90], that energy loss of the leading baryon and particle production in the same hemisphere are correlated. The correlation of multiplicity and particle yields in one hemisphere is trivial. The comparison of the results of Basile et al. with charged-particle multiplicities from e^+e^- annihilation demonstrates, that the measured correlation of E_{lead} and multiplicity in one hemisphere is representative for the inelasticity of the whole interaction.

However, they assumed that both hemispheres show the same charged-particle multiplicity and energy loss of the incident proton on average. Whereas measurements of Bøggild et al. [91] indicate an approximate independence of the charged-particle multiplicity in both hemispheres for p+p collisions at 19 GeV: If selecting a leading proton in the forward hemisphere, the forward multiplicity increases for lower x_F -values, as it is observed in this work. However, multiplicities in the backward hemisphere are hardly affected. The NA22 collaboration [92] (and references therein) studied in detail forward-backward multiplicity correlations and found that for higher energies reality lies in between: The charged-particle multiplicity in the backward hemisphere is proportional to the forward one, but with a proportionality factor smaller than 1 (~ 0.17 for p+p collisions at 250 GeV). This correlation strength increases with \sqrt{s} . They also showed that the correlation is basically restricted to the central region $|y| \lesssim 1$. In general, the FRITIOF model provides a good description of these correlations.

In section 5.2.3 it is shown that neither assumption is crucial, because for both extreme cases a rather good agreement with results from e^+e^- interactions is achieved. The same should hold if using the event multiplicity in one hemisphere as inelasticity criterion since it is correlated to Feynman-x of the leading proton.

The question is, whether this representativeness also holds for event-characteristics besides the charged-particle multiplicity, as e. g. the strangeness content in the final state. A simple illustration of the two extreme cases of either

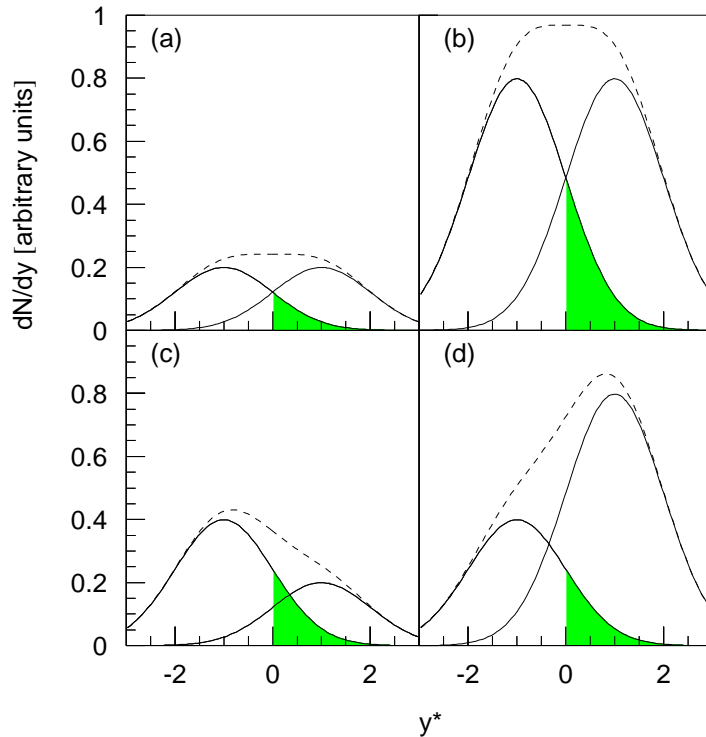


Figure 4.2: The influence from forward and backward hemisphere on particle production for the measurement of particle yields at $y^* > 0$ is illustrated within a simple picture. In (a) and (b) a symmetry of both hemispheres on average is assumed, in (c) and (d) they are assumed to be independent, i.e. the backward hemisphere stays the same even if the forward hemisphere changes. (a) and (c) illustrate a subclass of p+p events with low multiplicity, e.g. for a selected leading proton with high Feynman- x ; (b) and (d) show the same for larger multiplicity.

equality on average [(a), (b)], or independency [(c), (d)] of backward and forward hemisphere helps to argue qualitatively that the effect of the not-accessible backward hemisphere is small (fig. 4.2): In the first case, the feed-over of particles from backward increases in the same way as the forward multiplicity thus only strengthens an observed trend. Assuming that both hemispheres are the same on average also implies that this feed-over has the same characteristics, e.g. the same $\langle K \rangle / \langle \pi \rangle$ ratio, as the forward part. Therefore effects and developments observed in the forward hemisphere would be representative for the inelasticity. In the second case, the contribution from backward remains unchanged, independently on characteristics in the forward part. Therefore relative changes observed forward by requiring different event selections would also not be biased by the backward hemisphere.

In the next subsections, the experimental selection procedure of the leading proton, its uncertainties, and the measurement of the charged-particle multiplicity are introduced. Consequences of the experimental restrictions and the correlation to the energy in fact available for particle production are investigated with FRITIOF simulations.

4.2.2 Feynman- x of the leading proton

Leading proton selection

In NA49 no track-by-track particle identification by means of dE/dx measurement is achievable due to the overlapping energy loss distributions. The aim must therefore be to establish a procedure with which a leading proton sample as clean as possible

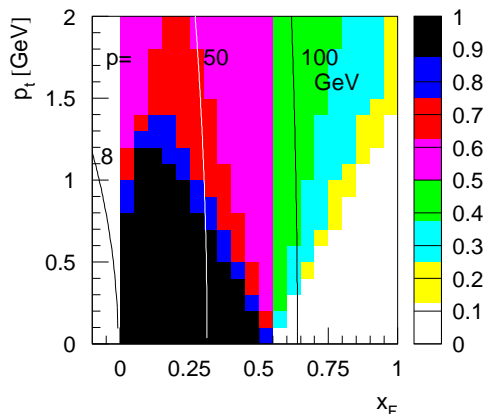


Figure 4.3: Acceptance of protons in the TPCs in (x_F, p_t) . Only the forward hemisphere is presented. More than 30 number of points are required for each track, no Φ -wedge cut is applied. Lines of constant momenta are included in the figure.

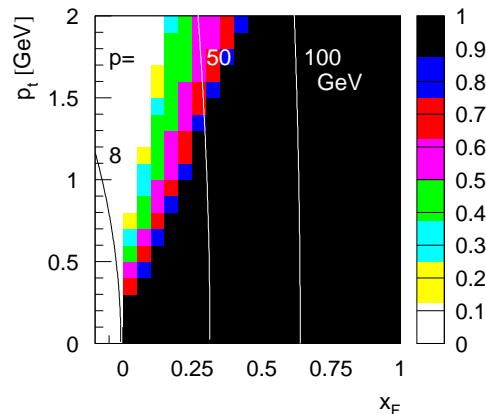


Figure 4.4: Acceptance of neutrons in the combined VCHAM and RCAL setup in (x_F, p_t) , only the forward hemisphere is presented. Lines of constant momenta are included.

can be derived. In the following the standard method used for this analysis will be described. Variations and their effect are checked in chapter 5.

In the first step all positive particles in a $3\sigma_{dE/dx}$ range below the mean proton dE/dx position are defined as being a proton; mean values and widths were taken from the Bethe-Bloch curve obtained during the energy loss calibration [66]. The Feynman-x of the selected particles is required to be above 0 since the interest lies in the forward hemisphere. Unfortunately, due to the sharp dE/dx criterion one rejects 50% of all protons, the advantage being that the kaon contamination remains small (see fig. 4.6 and table 4.3). In each event only the fastest proton is selected in case there are more. However, the TPC acceptance for protons² fades out around $x_F > 0.6$ depending on p_t (fig. 4.3). For an identified proton with $x_F > 0.5$ the appearance of an even faster baryon is forbidden by energy conservation, but at lower x_F values baryons with larger x_F become increasingly more likely. It is therefore necessary to veto the leading proton candidates with $x_F < 0.5$ selected in this first step.

In the next step, information from veto chamber and ring calorimeter becomes essential (see sections 2.5 and 3.3, note that only the datasets 00D and 00R have information on neutrons and can be used). Their acceptance for protons and neutrons covers the part of the forward hemisphere missing in the TPCs (fig. 4.4). Leading proton candidates are rejected, if a faster proton or neutron occurs (fig. 4.5). However, one should keep in mind that protons and neutrons cannot be identified unambiguously, but only a detection of fast positive, negative or neutral hadrons is possible. Previous studies by D. Varga [89] have shown that below $x_F = 0.2$ a large fraction of K_L^0 is contained in the neutrals (fig. 3.27). The strangeness measurement in the selected events might be biased if K_L^0 mesons are used as veto. Thus, neutral

²Acceptances are extracted as for pions, a description can be found in chapter 3.1.3.

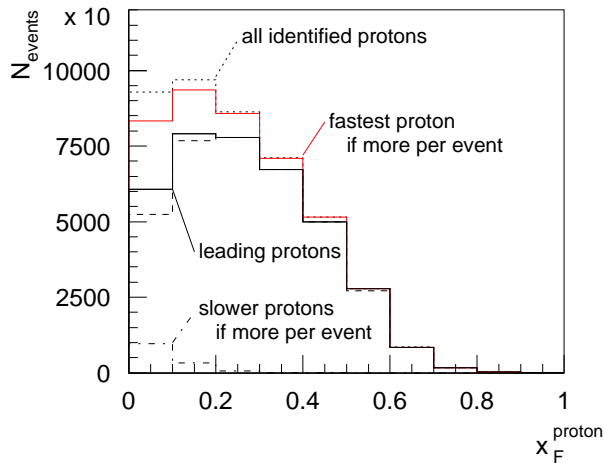


Figure 4.5: Number of events in x_F -bins of the leading proton candidates after the various steps in the selection procedure (for description see text). The dashed line close to the one for final leading protons shows the result if also neutral particles with $x_F < 0.2$ are used as veto, and if protons identified by means of dE/dx with $x_F > 0.5$ are allowed to be vetoed by the occurrence of still faster positives or neutrals in the VCHAM + RCAL setup.

hadrons are used only from $x_F = 0.2$ on to veto the leading proton candidates. For fast positive hadrons this restriction is not necessary, all identified ones are used.

A further handicap is the bad energy resolution of the ring calorimeter. Therefore fast positive or neutral hadrons cannot be positively selected as leading baryons but only used for rejection purposes of protons from the TPC. Of course also the veto suffers from the energy resolution. But since the veto is more important for slow leading protons, the harm of a bad energy resolution for fast hadrons is acceptable because of the large difference in energy. Indeed, although fast protons and neutrons are not measured with maximum cleanliness, results show that about 40 % of the leading proton candidates in the lowest x_F -bin ($0 < x_F < 0.1$) are rejected because of the appearance of faster positives or neutrals and nearly none at $x_F \approx 0.5$ (fig. 4.5).

Due to the introduced selection criteria the event sample available for analysis is significantly reduced. In fact only about 17 % of all minimum-bias p+p data are left. This can be roughly understood when considering first, that about 40 % of the protons appear as neutron after the interaction, and second, that only protons with $x_F < 0.6$ are considered within a restricted acceptance. Third, 50 % of the protons are rejected due to the dE/dx selection criterion. These reduction factors are confirmed by simulation (18.8 % events left in total, see section 4.2.4).

Kaon contamination

The fraction of kaons remaining in the proton sample after the selection by means of dE/dx can be determined using results from the extraction of particle yields from dE/dx spectra (chapter 3.1). For each particle species, the extracted parameters allow to calculate the dE/dx distribution in bins of (p, p_t) according to formula 3.5. This also provides the K^+ to proton ratio for tracks with an energy loss below the mean proton dE/dx position. Figure 4.6 shows this ratio, but transformed to (x_F, p_t) -bins of the proton. Protons at $x_F = 0$ have already rather large momenta (about 8-10 GeV), thus protons and kaons are well separated in dE/dx (see

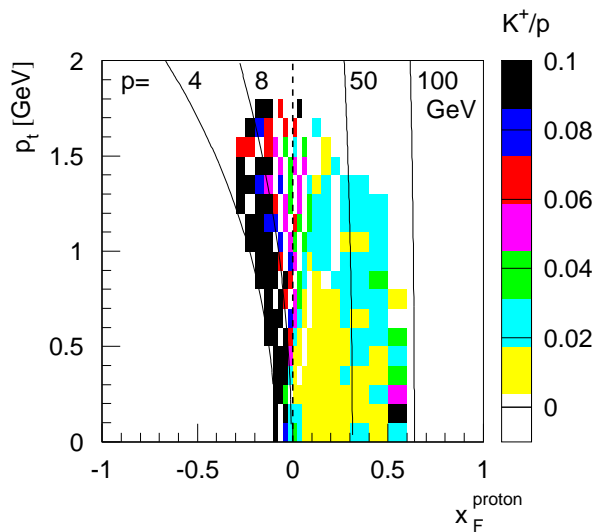


Figure 4.6: K^+/p ratio in bins of (x_F, p_t) of the proton after the first selection step for leading protons, i. e. for the selection of all positive tracks with an energy loss below the mean dE/dx position of protons. The dashed line indicates $x_F = 0$, leading proton candidates are only selected in the forward hemisphere. Lines of constant momenta are also shown.

x_F	K^+ contamination [%]
0.0 - 0.1	1.9 ± 0.03
0.1 - 0.2	1.3 ± 0.03
0.2 - 0.3	1.6 ± 0.03
0.3 - 0.4	2.0 ± 0.05
0.4 - 0.5	2.0 ± 0.05
0.5 - 0.6	4.1 ± 0.05

Table 4.3: Kaon contamination in the selected proton sample in bins of x_F of the protons. The values are integrated over p_t , errors are statistical only.

e. g. fig. 3.4). Only for large momenta the overlap increases, yielding a larger contamination of kaons in the proton sample. Assuming thermal p_t -distributions for protons with a temperature of 160 MeV (formula 3.7), integrated values are obtained in bins of x_F of the proton (table 4.3). The resulting kaon contamination after the first selection step of the leading protons is already small, it will be even further diminished when using the veto with faster neutrons or protons.

Tagging uncertainties

A fraction of fast protons and neutrons with no experimental access remains: On the one hand, the combined detection efficiency of veto chamber and ring calorimeter is about 85 (78) % for a neutron with an energy of 120 (40) GeV (see section 3.3); protons are assumed to have the same detection efficiency. On the other hand, protons accepted in the TPCs, and thus not in the combined setup of veto chamber and ring calorimeter, but with an energy loss above the mean dE/dx value for protons are not included in the described selection procedure. Their influence can only be estimated by simulation (see section 4.2.4, table 4.4). In addition, leading baryons appearing as Λ -baryons are not considered in this work. The introduced bias is also studied by simulation. The effect of these uncertainties is found to be small, at least from $x_F = 0.1$ on (see section 4.2.4).

Checks

The definition and experimental selection of the leading proton is afflicted with rather large uncertainties. The kaon contamination in the proton sample can be checked by data, but the determination of other error sources has to rely on simulation. Therefore experimental checks of the introduced selection method are necessary. A small compilation is given here to underline the validity of the selection procedure, the corresponding analysis is mainly described in chapter 5.

Figure 4.1 already presented one confirmation. As discussed, a correlation of both variables is expected and, indeed, it is observed. One step further, the same exercise as suggested by Basile et al. [11] can be performed for the NA49 p+p data (see chapter 5.2.3, fig. 5.36). A good agreement of multiplicity in p+p in bins of the effective center-of-mass energy defined by x_F of the leading proton and multiplicity in e^+e^- is found.

The selection of protons with rather large x_F is fairly safe, problematic are leading protons with small x_F since other high energetic baryons might have been missed. In this case the total energy of the event should be significantly smaller than 158 GeV. Without particle identification only the sum of all momenta is accessible within the NA49 acceptance. Fig. 4.7 shows a smooth correlation of $x_F^{\text{leading proton}}$ and p_{tot} , no fraction of events with a sizeable amount of missing energy is separated. The slight drop of p_{tot} for small $x_F^{\text{leading proton}}$ can be understood, because only 60 % of all particles are measured on average, and the energy is dissipated more equally among the hadrons for low $x_F^{\text{leading proton}}$, because the identified leading proton carries a less significant fraction of energy there.

Another hint for the validity of the selection method can be taken from results presented in chapter 5.2.2, e. g. in fig. 5.33. The selection method of leading protons is varied there, e. g. also positives and neutrals from the VCHAM+RCAL setup are used as leading baryons. Since their energy resolution is weaker one expects a softening of the correlation, which is indeed observed.

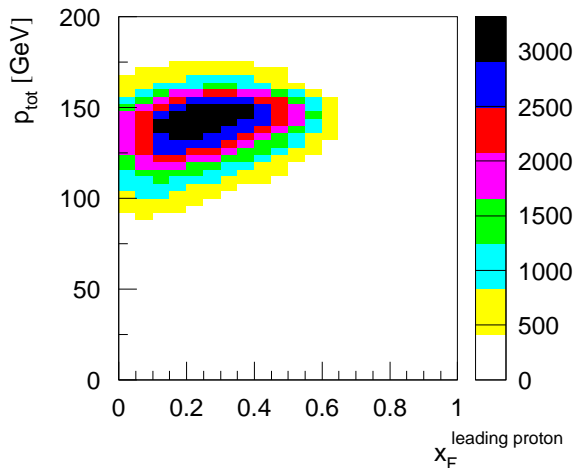


Figure 4.7: Correlation of the sum of all momenta measured within the NA49 acceptance including positives and neutrals from the VCHAM and RCAL setup and Feynman-x of the leading proton in p+p collisions.

4.2.3 Multiplicity

The NA49 detector is designed to measure mainly the forward hemisphere of the reaction in the center-of-mass system. Therefore not the *total* charged-particle multiplicity is detected, but only about 60 %. This fraction is proportional to the total charged-particle multiplicity (see fig. 4.8) and can also be used to define inelasticity in p+p collisions.

For determination of the measured charged-particle multiplicity a minimum of 30 points per track is required to reduce fake or split tracks and to increase the quality of the track sample. The sum of all these charged tracks in one event is called $N_{ch,measured}$. However, there is on principle no way to correct for the missing tracks on an event-by-event basis. This can only be done on average with help of simulations.

4.2.4 Inelasticity in simulations with the FRITIOF model

In the preceding sections several problems were mentioned concerning the restriction to one hemisphere of the experiment, the reduction to one exit channel of leading baryons only, and uncertainties in the selection method of the proton. To study these restrictions and efficiencies, simulations with the FRITIOF model were performed³. Model simulations also open the possibility to investigate the correlation between particle multiplicities and the energy available for their production, which corresponds to the string mass in FRITIOF. This correlation is of interest, because this energy is one difference between minimum-bias p+p and A+A collisions due to the larger energy loss of protons and neutrons in the latter system. The correlation of string mass and Feynman-x of the leading proton or the charged-particle multiplicity is also investigated in order to learn about the sensitivity of these experimentally accessible parameters to the energy of interest.

The FRITIOF event generator (version 7.02, in each case 1 million events are generated) is used to deliver p+p events at a center-of-mass energy of 17.3 GeV; the weak decay of, e. g., Λ , Σ , their antiparticles and K_S^0 is allowed. For final state particles the acceptance of each track is proved with the same acceptance tables as used for the data analysis. In addition, for pions and protons stemming from the mentioned weak decays the probability for a reconstruction at the main-vertex is taken into account (tables with probabilities from M. Kreps [75], the resulting size of the correction is in agreement with the one extracted in chapter 3.1.3). As in data, $N_{ch,accepted}$ is the sum of the accepted particles including pions and protons from weak decays. Particle yields from FRITIOF in bins of $x_F^{leading\ proton}$ or $N_{ch,accepted}$ contain also pions and protons from the discussed feed-down channels. This way, an inelasticity-dependent feed-down correction of the data is avoided (for results in comparison to data see chapter 5.2.3). The total or total charged multiplicity and the ideal leading proton or baryon are of course calculated without considering these

³For a short introduction of the model see section 1.4.4 and references therein.

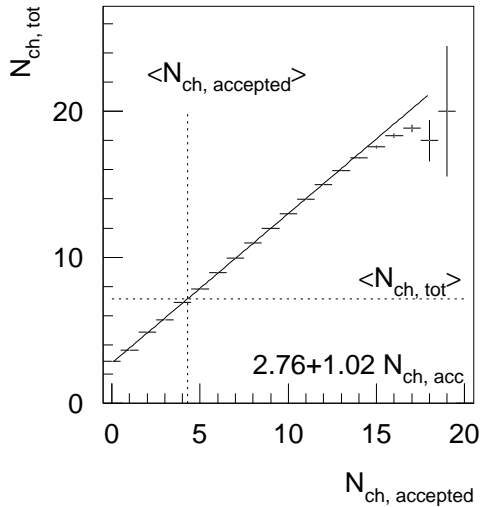


Figure 4.8: Correlation of total charged and measured charged multiplicity for p+p collisions at $\sqrt{s} = 17.3$ GeV in FRITIOF. The solid line presents a linear fit to the data, parameters are given in the figure. Mean multiplicities are indicated by the dotted lines, on average about 60 % of all tracks are accepted in the detector.

experimental restrictions. The extracted proportionality between total charged and measured charged multiplicity is presented in fig. 4.8.

Within the simulation caveats of the experimental selection procedure of leading protons can be studied, because the full information of the event is accessible: A clean selection of the leading proton, neutron or Λ is performed. The leading proton is also extracted including the experimental restrictions of TPC acceptance, feeddown of protons from Λ and Σ , the dE/dx window by which half of the protons accepted in the TPCs are rejected, as well as acceptance and efficiency of the VCHAM+RCAL setup.

The resulting efficiency of the selection procedure of the leading proton, i. e. the probability to correctly choose the fastest proton in the event, is given in table 4.4. Especially in the first x_F -bin the chance is large to miss the "real" leading proton: The effect of rejecting half of the protons in the TPC due to the dE/dx cut is clearly visible (15.8 %). The large fraction of events in which a faster neutron is not detected

x_F	efficiency of lead. p sel. [%]	faster p in TPC [%]	faster p in V+R [%]	faster n in V+R [%]	leading Λ [%]
0.0 - 0.1	66.2	15.8	5	13	4
0.1 - 0.2	92.4	4	1.2	2.4	1
0.2 - 0.3	98.6	0.9	0.3	0.2	0.2
0.3 - 0.4	99.7				
0.4 - 0.5	> 99.9				
0.5 - 0.6	> 99.9				

Table 4.4: Efficiency (left) of the leading proton selection procedure in dependence on x_F of the leading proton (FRITIOF simulation). The reasons might be (middle part of table), that either a fast proton in the TPCs, or a fast proton or a neutron in the VCHAM+RCAL (=V+R) setup are not detected. In the most right column the relative fraction of events is given, in which a Λ is the leading baryon and the decay proton is not selected as leading proton; this is mainly due to the inefficiencies reported in the middle part of the table.

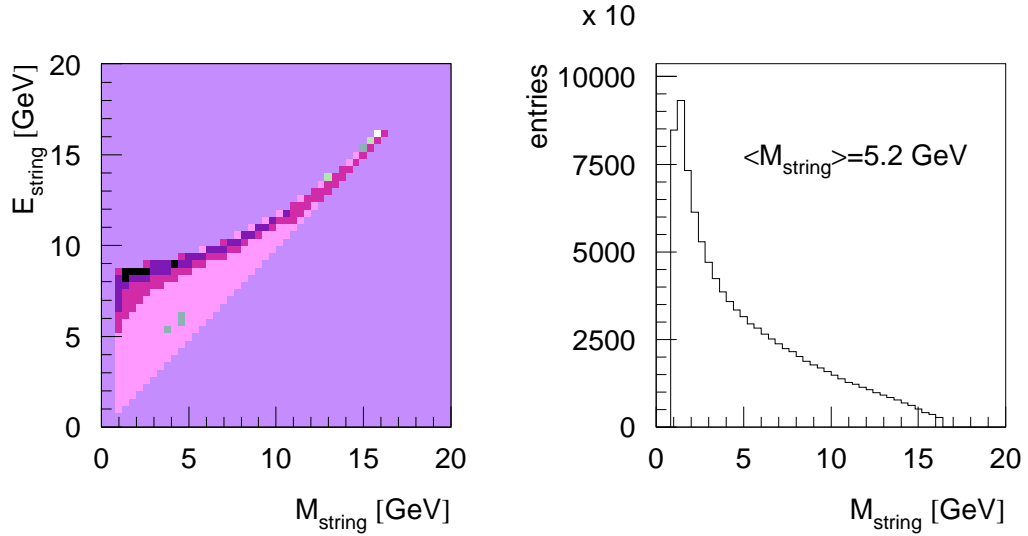


Figure 4.9: Correlation of string mass and energy for p+p collisions at $\sqrt{s} = 17.3$ GeV in FRITIOF (left), for better visibility of the tails a logarithmic color scale is chosen. Right, the distribution for M_{string} is shown, the mean string mass is 5.2 GeV.

(13 %) results from the exclusion of neutrals with $x_F < 0.2$ as veto. However, by this cut the contamination with K_L^0 is kept small in data. Consequently, the fastest baryon in these events is a neutron with $x_F < 0.2$, which is still a rather inelastic p+p event. Therefore this inefficiency does not harm the inelasticity selection.

In FRITIOF, 58 % of the p+p events yield a leading proton, in 32 % the fastest baryon is a neutron, in 7 % it is a Λ . However, after the decay of the Λ , the decay proton or neutron appears in less than 1 % of the events *not* as the leading proton

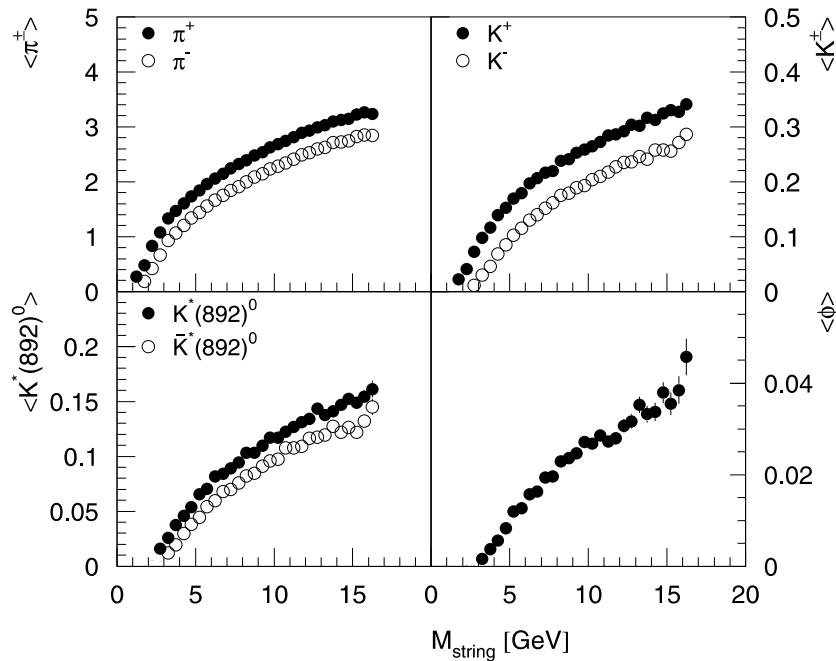


Figure 4.10: Particle production in dependence on M_{string} in FRITIOF simulations for p+p interactions at $\sqrt{s} = 17.3$ GeV.

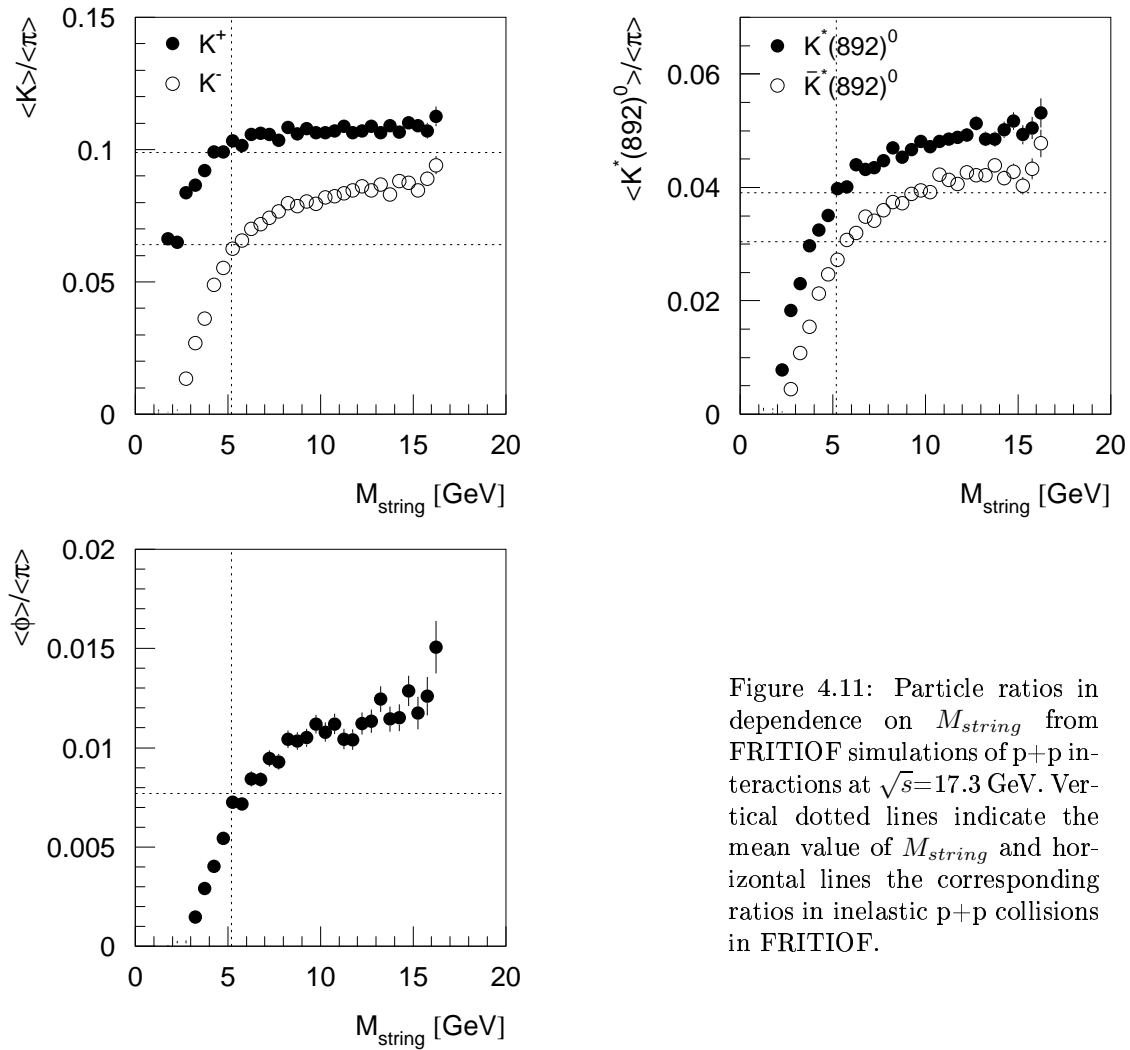


Figure 4.11: Particle ratios in dependence on M_{string} from FRITIOF simulations of p+p interactions at $\sqrt{s}=17.3$ GeV. Vertical dotted lines indicate the mean value of M_{string} and horizontal lines the corresponding ratios in inelastic p+p collisions in FRITIOF.

or neutron. Including protons and neutrons from the Λ decay, 63 % of all events provide a leading proton, 34.7 % a leading neutron. The inefficiency of finding the fastest baryon in data, especially in the first x_F -bin, results in a fraction of 4 % of events in which a Λ was the leading baryon and its decay proton was not selected as leading particle.

These numbers all show that the class of interactions with a proton in the final state is representative for all. In addition, it is demonstrated in section 5.2.3, that the overall behavior of relative particle yields is not biased by the selection of protons.

The second aim of the simulation was to study the correlation between energy available for particle production and multiplicity of different particle species, and between this energy and $x_F^{\text{leading proton}}$ or N_{ch} . In the string picture, the string mass M_{string} defines the energy used for the creation of new hadrons, whereas the string momentum is distributed in between the produced particles considering momentum conservation. Figure 4.9 presents the string mass and its correlation to the string energy in FRITIOF. The string mass can be $(\sqrt{s} - m_p)$ at most, the sum of target

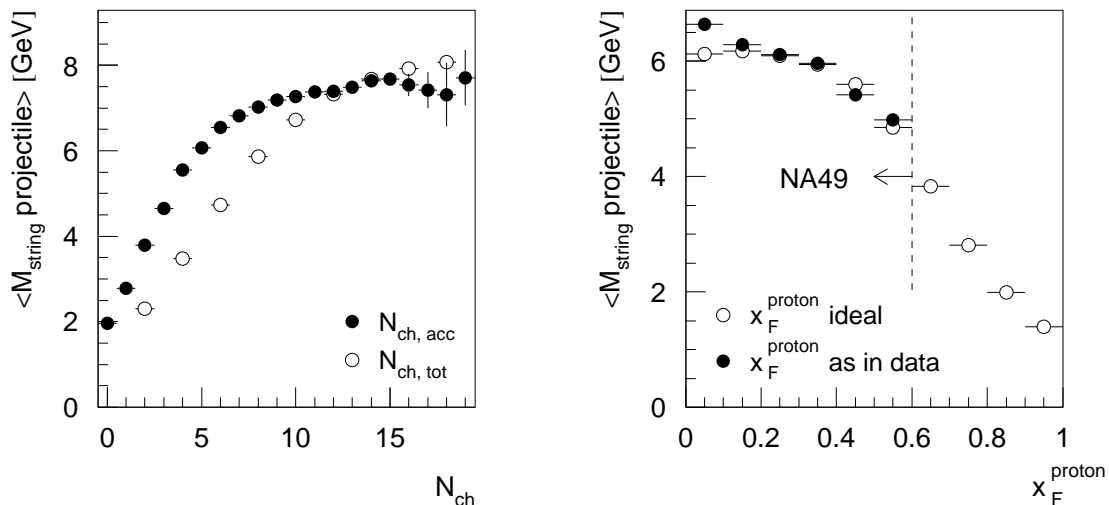


Figure 4.12: Correlation of M_{string} and multiplicity (left) respectively $x_F^{\text{leading proton}}$ (right) in FRITIOF for p+p collisions at $\sqrt{s} = 17.3$ GeV. Right, the dashed line indicates the x_F -range accessible in NA49.

string energy and projectile string energy is of course \sqrt{s} . Both strings can be identified separately in the model and the produced particles can be correlated to the string they are stemming from. The mean value of the string mass supports the general statement that, at least in FRITIOF, on average about half of the center-of-mass energy is used for particle production ($5.2 \text{ GeV} - m_p = 4.26 \text{ GeV}$, $\sqrt{s}/4 = 4.32 \text{ GeV}$).

Fig. 4.10 presents particle yields for the mesons under study in dependence on the string mass M_{string} . The higher the particle mass is, and the more particles are required to go along with it to fulfill, e. g., strangeness conservation, the higher is the threshold in string mass for this specific particle. This results from energy conservation and naturally generates a threshold effect in the ratios (fig. 4.11). After threshold all ratios saturate, however, not all until string masses of 5.2 GeV, i. e. at the value for inelastic p+p interactions in FRITIOF.

M_{string} and $x_F^{\text{leading proton}}$ or N_{ch} show a broad correlation (fig. 4.12), but the mean string-mass increases significantly with N_{ch} and $x_F^{\text{leading proton}}$. However, for the latter the rise in the measurable range of NA49 is a 30 % effect only. Using both figures it can be argued, that a correlation of particle production with M_{string} would be measurable in $x_F^{\text{leading proton}}$ and even better in N_{ch} : Assuming a test-correlation $f(M_{string}) = c \cdot M_{string}$ the response of this dependence visible in N_{ch} and $x_F^{\text{leading proton}}$ is of interest. The case $c = 1$ is already presented in fig. 4.12. Experimental restrictions do not significantly limit the effect. The investigation of particle yields in dependence on multiplicity allows to scan a string-mass range of 2 GeV to 7.5 GeV. The available range using Feynman-x is much smaller (5 GeV to 6.5 GeV).

In section 5.2.3 experimental results and results from FRITIOF will be compared in detail for minimum-bias and inelasticity-dependent p+p interactions.

4.3 Centrality in C+C and Si+Si collisions

Two beam types and targets were selected for data taking with the fragmentation beam (fig. 2.3) in 1998: a spectrum of nuclei centered around carbon and silicon (fig. 4.13) and a carbon and silicon target, respectively. C+C interactions were recorded for two target thicknesses, 3.05 mm and 10.0 mm, the corresponding interaction probabilities are 2.4 % and 7.9 %. By mistake, two different settings of the vertex TPC currents were used for the thick target. This gives 3 different datasets of C+C events for which the dE/dx has to be calibrated independently. Unfortunately, up to now a calibration is available only for the data recorded with the thin target. For Si+Si interactions only one target thickness (5.02 mm, 4.4 % interaction probability) and one setting of currents for the vertex TPCs was used, but also here not for all data the energy loss is calculated yet. This leaves only a subset of the full amount of data which could be used for the analysis presented in this work (tab. 4.5).

Fig. 4.13 demonstrates that the trigger selected not only carbon and silicon projectiles, but also nuclei with similar atomic mass and the same Z/A . Offline the charge is precisely calculated allowing for a clean identification from then on (see section 2.2). Requiring only carbon or silicon projectiles would reduce the event sample for analysis by 30 % (C+C) or 70 % (Si+Si). To avoid this strong reduction of the event sample, in this analysis carbon and nitrogen nuclei were accepted as beam particles for the C-target providing a dataset of 46k events. Aluminum, silicon and phosphor nuclei were accepted in case of the Si-target (43k events). To simplify matters, the combined C+N (Al+Si+P) beam will be called C (Si) in this work, exceptions are explicitly mentioned.

The following cuts on the vertex position were applied in order to ensure that only beam+target events are analyzed: The z -position of the event vertex is required to be within a ± 5 cm range of the nominal target position (fig. 4.14). As for p+p events a cut on the vertex position in the plane perpendicular to the beam axis is performed; only events inside a circle with 1 cm radius are used. Only a few C+C and Si+Si events are rejected by these cuts, because the σ of a Gaussian fitted to the beam spot is about 2.2 mm in x and 3.4 mm in y , and the z -position of the vertex is well known.

target	d [mm]	events recorded	events after cuts and with dE/dx	beam	N_{events}
C	3.05	104500	46254	C	31553
				C,N	45532
	10.0	224100	to do	C	78k expected
	10.0	256900	to do	C	89k expected
Si	5.02	94000	53682	Si	17053
				Al,Si,P	43466
	5.02	325400	to do	Si	59k expected

Table 4.5: Datasets for central C+C and Si+Si events.

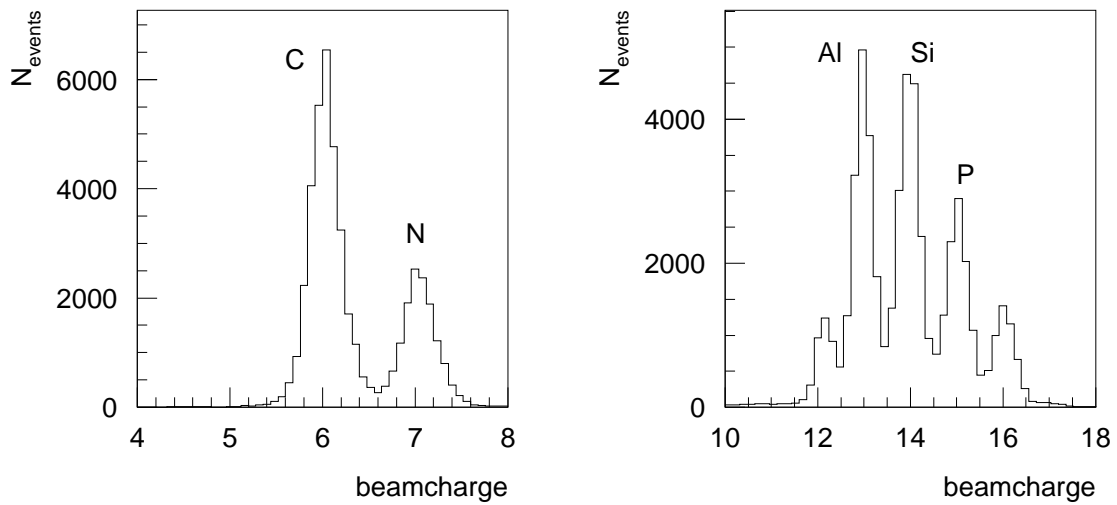


Figure 4.13: Spectrum of beam particles in the triggered carbon and silicon events. The fraction of C in the beam is 68%, for Si it is 32%.

For both, C+C and Si+Si interactions, only central collisions were recorded by setting an upper threshold on the spectator energy in the veto calorimeter (see chapter 2.5). This is also an event selection in one hemisphere only, but much less restrictive than the inelasticity selection in p+p. From geometrical considerations as in the Glauber model one expects the same number of participating nucleons in both nuclei on average. Therefore, the measurement of the spectator-energy in one hemisphere is characteristic for the centrality of the A+A interaction.

In the following, the number of participants and other parameters character-

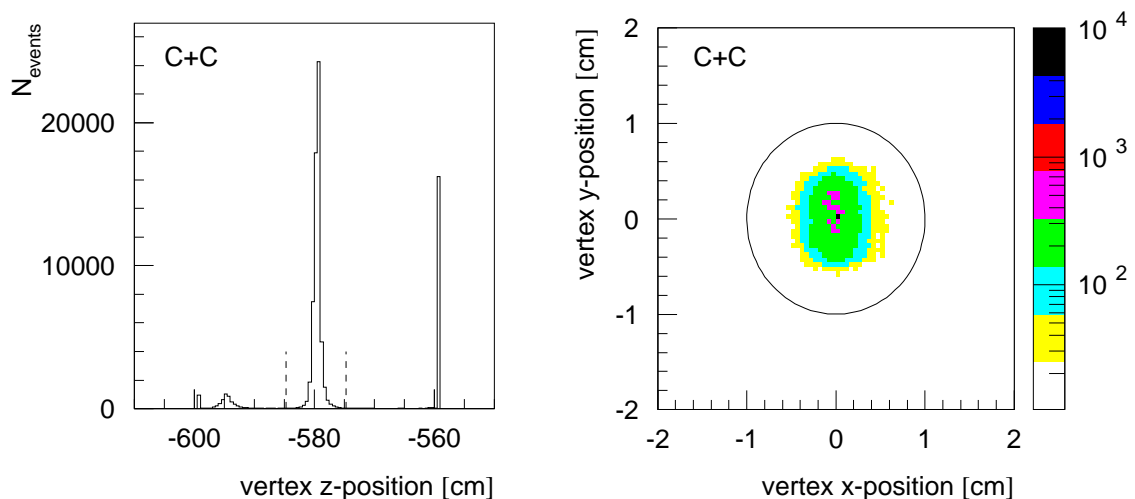


Figure 4.14: Vertex- z and (x, y) -position for C+C interactions. The accepted range of the z -position is indicated by the dashed lines, for the (x, y) -position all events within the circle are selected.

izing the centrality are determined with three methods: First, using the selected percentage of central events as input for model calculations and second, using the multiplicity instead. Third, the approximate number of spectators can be calculated directly from the measured energy in the veto calorimeter.

4.3.1 Centrality determination via trigger cross section

The method for extracting the event centrality and corresponding parameters introduced in this section uses the experimentally selected fraction of the total inelastic cross section by the threshold setting of the veto calorimeter. To determine this fraction, trigger cross section from data and total inelastic cross section from literature are needed. Their ratio is used as input to the VENUS or FRITIOF model (for a short introduction to the models see chapter 1.4.4 and references therein). Impact parameter, number of wounded nucleons and participants, and mean number of collisions per nucleon are extracted from these simulations.

Trigger cross section in the experiment

The calculation of a trigger cross section for an experiment with certain trigger conditions was already reported for p+p collisions.

$$\sigma_{trig} = \rho_{trig} \cdot \left(\rho \cdot d \cdot \frac{N_A}{M} \right)^{-1} \quad (4.4)$$

Thickness d , density ρ and material of the target (molar mass M) are known (table 4.6). The interaction probability in experiment $\rho_{trig} = \frac{N_{trig}}{N_{beam}}$ is extracted from the recorded beam and trigger rates.

For the number of triggered events N_{trig} all events are counted for which the fitted vertex position meets the requirements chosen for analysis (see above for the introduction of the event cuts). The number of valid beams (B_{gated}) is defined by a coincidence of the beam counters $S1 \times \overline{V0} \times S2$, whereby the S2 pulse height is required to lie in a certain window limiting the spectrum of all fragments to the ones presented in fig. 4.13. B_{gated} is recorded in experiment, in this number the *deadtime* of the detector is taken into account, i. e. valid beams are not counted when the detector is not ready to record them. The interaction probability ρ_{trig} is then extracted as the slope from mapping N_{trig} versus B_{gated} . Note, that by

target	d	ρ	ρ_{trig}	σ_{trig} [mb]
C	3.05 mm	$1.84 \text{ g/cm}^3 \pm 0.5\%$	$4.116 \cdot 10^{-3}$	146
C _{with target out}			$3.676 \cdot 10^{-3}$	131 ± 15
Si	5.02 mm	2.33 g/cm^3	$5.445 \cdot 10^{-3}$	216 ± 24

Table 4.6: Target properties and trigger cross section for the recorded C+C and Si+Si interactions. For carbon beam a few data without target exist, which are included in the calculation for the second value reported (for error estimation see text). The impurity of the carbon target is below 100 ppm (class N).

this procedure, the trigger cross section is given for interactions of the whole beam spectrum from fig. 4.13 with the carbon and silicon target, respectively.

As for p+p collisions, interactions with, e. g., beam foils can take place. Due to the sharp cut on the z -position of the vertex their contribution is expected to be small, but the vertex position itself could be calculated incorrectly. This contribution can be tested by data taking without a target. Unfortunately, just a few events have been recorded with this condition for carbon beam only. Therefore, for C+C collisions an interaction probability $\rho_{trig} = \left[\left(\frac{N_{trig}}{B_{gated}} \right)_{\text{target in}} - \left(\frac{N_{trig}}{B_{gated}} \right)_{\text{target out}} \right]$ taking into account this effect is calculated. The difference to the uncorrected value is regarded as error estimate (11 %). For silicon beam the effect is expected to be of the same order. Since no events without target are recorded, the interaction probability without an empty-target correction has to be used, 11 % is taken as error estimate (table 4.6).

Total inelastic cross section of A+A collisions

The cross section of p+p and p+n collisions is well measured over a broad range of energies (fig. 1.7) and either tables or parametrizations are available to allow their calculation at each energy needed. In nucleus-nucleus collisions the situation is not that clear. Most of the existing measurements are performed at low energies [93, 94, 95], that is below 5 GeV incident beam energy per nucleon, and for a selected variety of nuclei only. For higher energies (60, 158 and 200 GeV per nucleon) very few data exist [74, 96, 97].

The cross section in p+p collisions appears to be approximately independent on beam momentum over a rather broad range of energies, i. e. from about 4 GeV to 2000 GeV beam energy. Regarding it as constant, simple models can describe nuclear inelastic cross sections by geometrical considerations. In the hard sphere model of colliding billiard balls the total cross section reads $\sigma_{inel} = \pi R_0^2 (A_p^{1/3} + A_t^{1/3})^2$ with A_p and A_t being projectile and target mass number, respectively, and R_0 being a unique parameter which has to be determined from experiments. A much better description of the data is given by $\sigma_{inel} = \pi R_0^2 (A_p^{1/3} + A_t^{1/3} - b)^2$. However, difficulties arise to assign a unique value to the overlap parameter b from comparison with data. The slightly modified formula

$$\sigma_{inel} = \pi R_0^2 (A_p^{1/3} + A_t^{1/3} - \beta (A_p^{-1/3} + A_t^{-1/3}))^2 \quad (4.5)$$

provides rather stable values for R_0 and β extracted from interactions of several nuclei. Cross sections calculated for C+C and Si+Si interactions using three different sets of parameters [93, 94, 95] are presented in table 4.7.

Taking into account the diffuseness of nuclei and energy dependent cross sections of p+p and n+p interactions, Karol derived a simple analytical expression for the nuclear reaction cross section based on the semiclassical optical model, the so-called soft spheres model [98]. Input are the energy dependent inelastic p+p and p+n cross sections, the surface skin thickness parameter $t = 2.4$ fm for nuclei

			σ_{inel} [mb]	
			$^{12}\text{C}+\text{C}$	$^{28}\text{Si}+\text{Si}$
R_0 [fm]	β			
1.3	0.93	[93]	753	1585
1.33 ± 0.04	0.85 ± 0.1	[94]	818 ± 62	1692 ± 109
1.36	1.11 ± 0.05	[95]	757	1661
R_{rms} [fm]				
2.42		[35]	860	
3.04		[35]		1838

Table 4.7: Total inelastic cross sections calculated from a modification of the hard sphere model (upper part) and the soft spheres model [98] (lower part), respectively. Parameters were taken from the indicated sources. In [94] errors on the extracted parameters are given. The resulting errors in the cross section are calculated, their size is approximately of the same order as the differences in between the various parameter sets. For the soft spheres model inelastic cross sections for p+p (n+p) of 31.7 mb (32.1 mb) were used [2].

with $A > 40$, and R_{rms} as measured in experiments and tabulated, e. g., in Landolt-Börnstein [35] for nuclei with $A \leq 40$. Calculations for C+C and Si+Si collisions are also presented in table 4.7.

Results of the different models vary considerably, and a comparison to experiments at higher energies is needed to test the extrapolation from low energy. In table 4.8 the models are compared to results at 158 and 200 AGeV beam energy. The experiments NA35 [96] and NA36 [97] measured also cross sections at 60 AGeV, no significant energy dependence was found. NA36 always measured about 20 % higher cross sections than NA35, both experiments provide cross sections larger than those from extrapolations of the parametrized hard sphere model [93, 94, 95]. Depending on the size of the nuclei, parameters from [94] or [98] seem to provide an approximate description of data. Therefore, for the inelastic cross section of C+C and Si+Si interactions the mean of both will be taken, but an error including also the extrapolations of [93, 95] is assigned.

However, up to now the fact has been neglected, that for the number of valid

	σ_{inel} [mb]			σ_{inel} [mb]	σ_{inel} [mb]
	hard sphere: R_0, β from				
	[93]	[94]	[95]	[98]	
$^{16}\text{O}+\text{Al}$	1244	1334	1289	1450	1610 ± 270 [97]
$^{16}\text{O}+\text{Cu}$	1853	1973	1948	2145	1960 ± 71 [96]
$^{16}\text{O}+\text{Au}$	3238	3429	3452	3451	3610 ± 154 [96]
$^{16}\text{O}+\text{Pb}$	3323	3518	3544	3528	4720 ± 390 [97]
$^{207}\text{Pb}+\text{Pb}$	7044	7408	7628	7118	7150 [74]

Table 4.8: Total inelastic cross sections calculated from a modification of the hard sphere model and the soft spheres model in comparison to data for beam momenta of 158 AGeV [74] and 200 AGeV [96, 97]. If available, errors are quoted for data.

projectile	target	σ_{inel} [mb]	fraction [%]	$\sigma_{inel}^{combined}$ [mb]
^{12}C	C	839	68	856 ± 88
^{14}N	C	894	30	
^{24}Mg	Si	1665	9	1768 ± 180
^{27}Al	Si	1725	28	
^{28}Si	Si	1765	32	
^{31}P	Si	1827	19	
^{32}S	Si	1880	10	

Table 4.9: Total inelastic cross sections for the various projectile+target combinations. For σ_{inel} the mean of values calculated according to [94] and [98] is taken. The combined cross section takes the relative composition of the beam into account; extrapolations from [93, 95] are included in the error.

beams B_{gated} and triggered interactions N_{trig} all nuclei according to the spectrum in figure 4.5 are included. Therefore also the trigger cross section is calculated for this beam composition. This has to be taken into account for the correct determination of the total inelastic cross section. The fractions of the beam nuclei are summarized in table 4.9 and for each relevant combination the cross section is given. The last column contains the combined value.

Centrality

Finally, the centrality of the recorded event sample is derived from the ratio $\sigma_{trig}/\sigma_{inel}$. Results are presented in table 4.10.

centrality	
C+C	$(15.3 \pm 2.4) \%$
Si+Si	$(12.2 \pm 1.8) \%$

Table 4.10: Centrality of the recorded C+C and Si+Si events.

In the following simulations, only pure carbon and silicon beams will be investigated, neglecting the mixture of nuclei in the real beam. This is justified because, within the errors quoted in table 4.10, the centrality is the same for all combinations.

Parameters for the centrality from the VENUS and FRITIOF model

Parameters for the centrality as impact parameter, mean number of participants or wounded nucleons, and number of collisions per participant can be derived from model calculations once knowing the centrality. The framework used here is basically the Glauber Model as it is implemented in the VENUS and FRITIOF computer codes.

The FRITIOF and VENUS models provide the energy carried along by the spectators E_{spec} . As spectators (or *first spectators* in the VENUS terminology) all nucleons are counted which have had no direct collision with the nucleons from the other nucleus. Correspondingly, the number of *wounded nucleons* is $N_{wound} =$

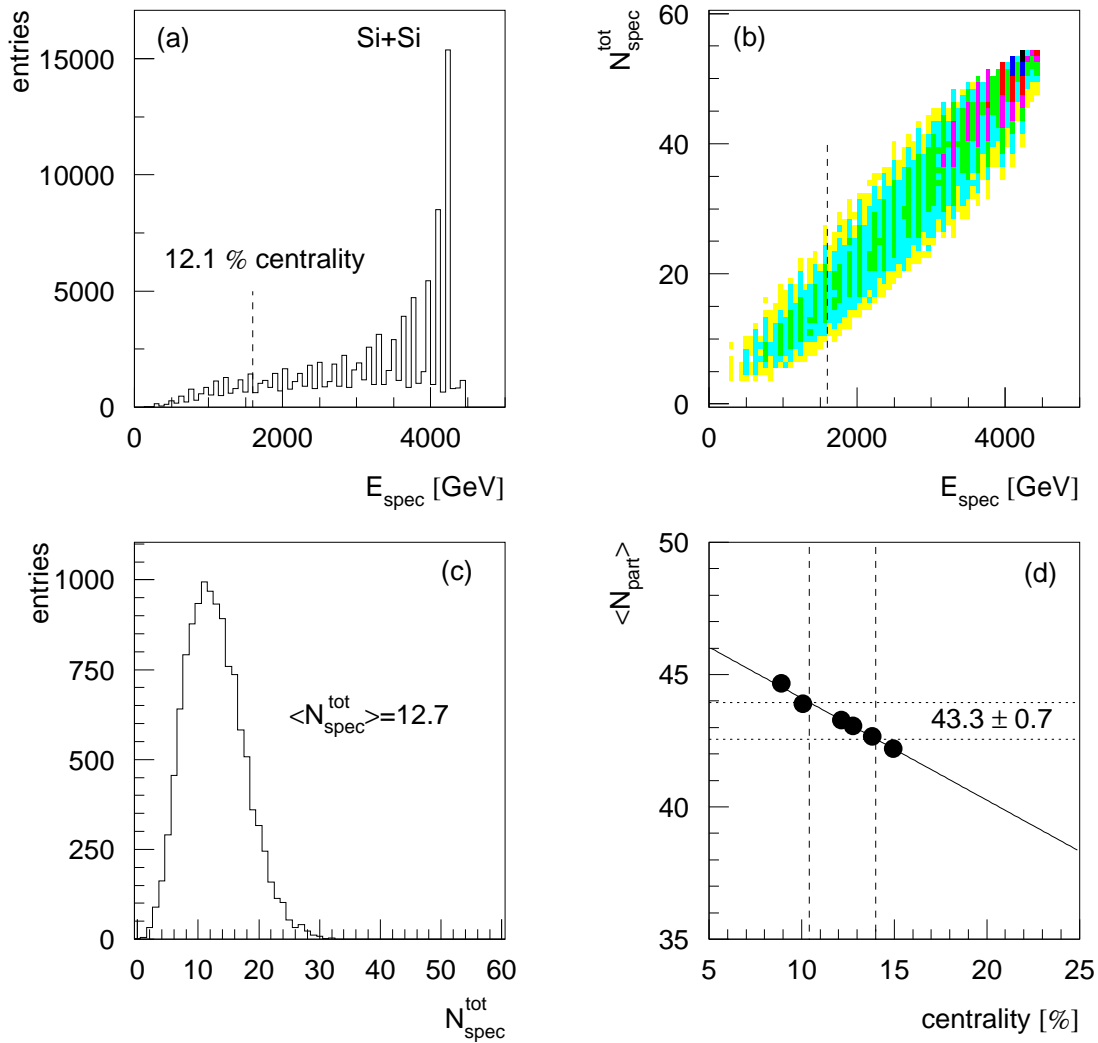


Figure 4.15: Example for the extraction of parameters for the centrality from VENUS. In (a) the energy spectrum of fast hadrons approximately in the acceptance of the veto calorimeter is presented, the dashed line indicates the cut for the 12 % most central events. The 2-dimensional correlation of E_{spec} and N_{spec}^{tot} within VENUS is presented in (b), again the cut for the central part is shown. In (c) the N_{spec}^{tot} distribution for the selected central events providing the mean value $\langle N_{spec}^{tot} \rangle$ is presented. Finally, (d) shows mean values for N_{part} for several centralities; $\langle N_{part} \rangle = A - \langle N_{spec}^{tot} \rangle$. A linear extrapolation allows for the extraction of $\langle N_{part} \rangle$ in the centrality range of NA49. The dashed lines give the borders of the (12.2 ± 1.8) % centrality selection and provide an estimate of the uncertainty of $\langle N_{part} \rangle$.

$A - N_{spec}^{first}$. In VENUS, rescattering of nucleons inside the nucleus is implemented which involves further nucleons in the collision. The final number of nucleons having participated is called N_{part} ($> N_{wound}$), the spectators still left are named *total spectators* N_{spec}^{tot} . However, since secondary participants might lose only a small fraction of their energy, some of them will be measured experimentally in the veto calorimeter.

The centrality of an interaction in the models is defined according to the mea-

	VENUS		FRITIOF	
	C+C	Si+Si	C+C	Si+Si
centrality [%]	15.3 ± 2.4	12.2 ± 1.8	15.3 ± 2.4	12.2 ± 1.8
$\langle N_{wound} \rangle$	13.9 ± 0.4	37.0 ± 0.8	15.9 ± 0.4	39.9 ± 1
$\langle N_{part} \rangle$	16.6 ± 0.4	43.3 ± 0.7		
$\langle \nu \rangle$	1.71 ± 0.01	2.16 ± 0.01	1.8 ± 0.01	2.25 ± 0.01
$\langle b \rangle$	1.88 ± 0.07	2.0 ± 0.1	1.51 ± 0.08	1.81 ± 0.12
b_{max}	2.02 ± 0.16	2.6 ± 0.2	1.95 ± 0.16	2.54 ± 0.18

Table 4.11: Centrality parameters calculated with the FRITIOF and VENUS model. In FRITIOF no rescattering of nucleons is implemented, only N_{wound} is available. Consequently $\langle \nu \rangle$ is calculated for wounded nucleons only, in contrast to the values reported for VENUS. The slight variation of the results between VENUS and FRITIOF is mainly due to the different initialization of the nuclei (see chapter 1.4.4).

surement in NA49. Events in which the energy of the spectators E_{spec} is below a certain threshold are selected as central events. In FRITIOF, E_{spec} as supplied by the model is used. In VENUS, the energy of the (total) spectators does not contain secondary participants which have lost few energy only. Therefore, fast hadrons approximately in the acceptance of the veto calorimeter are also included into E_{spec} . For the selected central event sample mean numbers of wounded nucleons N_{wound} , participants N_{part} , collisions per participant or wounded nucleon ν , and impact parameter b are extracted (as example for the procedure see fig. 4.15, results are summarized in table 4.11). The experimental uncertainty of the centrality allows for a certain range of parameters. A linear relationship is always observed in the range of interest, the resulting error of the mean values can directly be calculated

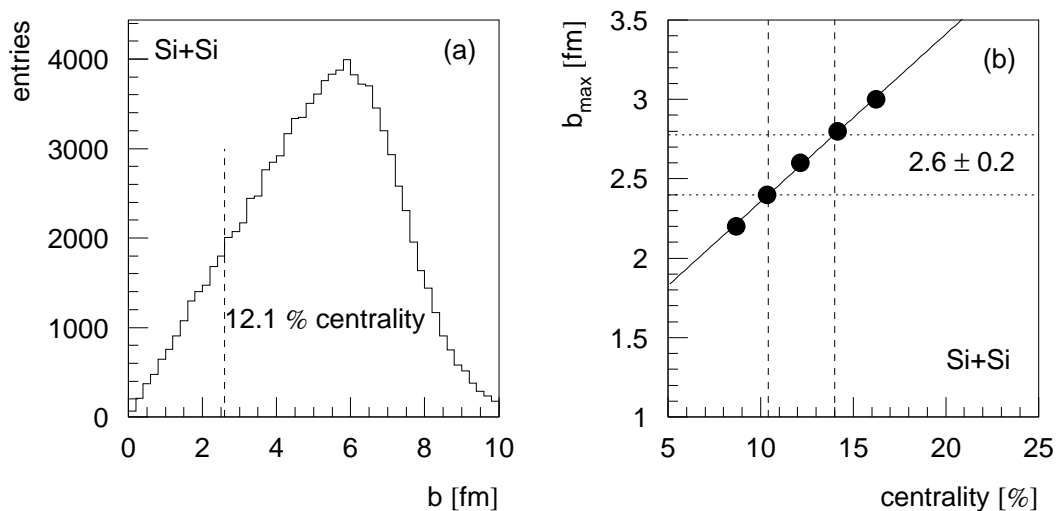


Figure 4.16: The maximum impact parameter belonging to a certain centrality is extracted by defining a central event sample with a cut in b , see (a). A linear extrapolation of values for b_{max} at different centralities allows to extract the maximum impact parameter for a centrality range as in the experiment (b).

from this proportionality (fig. 4.15).

Sometimes not only mean values but the impact parameter range with maximum impact parameter b_{max} belonging to a certain centrality is needed. The same procedure as introduced above is applied, with the exception that central events are defined by a cut in b instead of E_{spec} (fig. 4.16). Also here, the uncertainty about the experimental centrality determines the error of b_{max} , results are also presented in table 4.11.

4.3.2 Centrality determination via event multiplicity

More central events show not only less energy deposited in the veto calorimeter but also a higher multiplicity (fig. 4.17): The zero-degree energy E_0 and the accepted charged-particle multiplicity N_{ch} in the NA49 TPCs (more than 30 points are required for each track) exhibit approximately a linear relationship. Mean charged-particle multiplicity for all and the most central collisions ($E_0 = 0$ GeV) are presented in table 4.12.

A simulation using the FRITIOF event generator with additional proof of the acceptance for each generated particle yields the same mean multiplicity for the most central events as in the data (for a detailed description of this simulation chain see section 4.2.4). Of course, for the most peripheral events at $E_{spec} = E_0 = A \cdot 158$ GeV the mean multiplicity is zero in the data and in simulation. Therefore, for both cases the same linear correlation exists between E_{spec} or E_0 and the accepted charged-particle multiplicity. In simulation also multiplicity and the number of wounded nucleons N_{wound} are proportional which allows to calculate the mean number of wounded nucleons from the mean charged-particle multiplicity as measured in the data (see fig. 4.18 and table 4.12).

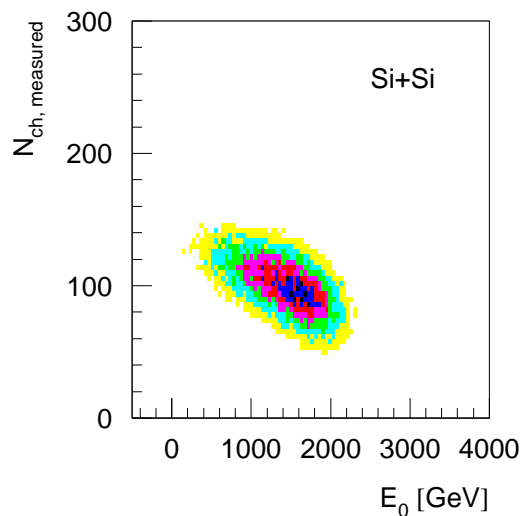


Figure 4.17: Correlation of charged-particle multiplicity as measured in the NA49 detector and zero-degree energy for central Si+Si collisions. Besides for the most central events at $E_0 \simeq 0$ GeV the correlation is linear.

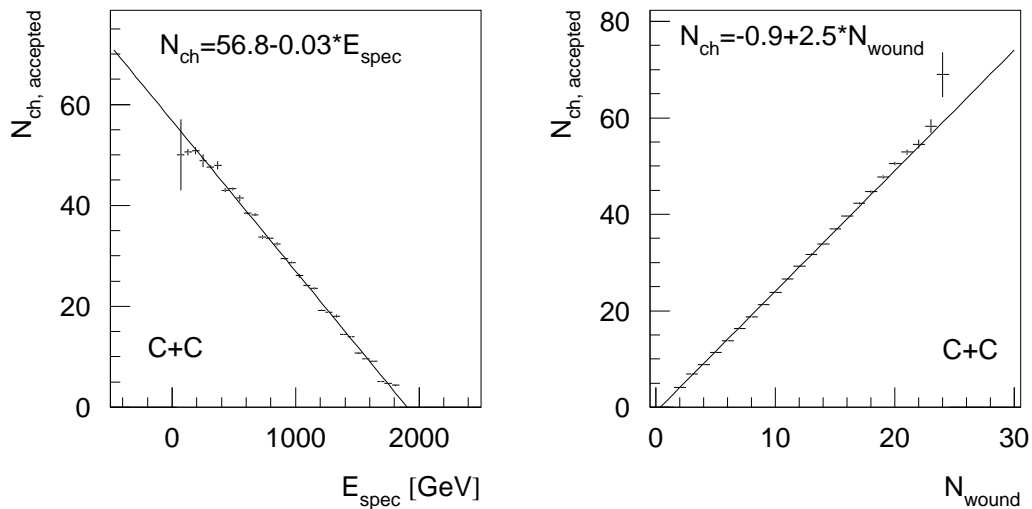


Figure 4.18: Correlation between accepted charged-particle multiplicity $N_{ch,accepted}$ and E_{spec} , and between $N_{ch,accepted}$ and N_{wound} , respectively, from FRITIOF simulations of minimum-bias C+C collisions at 158 AGeV. The linear relationship for both cases allows to extract the number of wounded nucleons from the mean charged-particle multiplicity.

	data		FRITIOF	
	$\langle N_{ch} \rangle_{data}$	$\langle N_{ch}^{E_0=0} \rangle$	$\langle N_{ch}^{E_{spec}=0} \rangle$	$N_{wound} (\langle N_{ch} \rangle_{data})$
C+C	38.6	56.3	56.8	15.8
Si+Si	100.9	139	137.4	40.5

Table 4.12: Mean multiplicity of all, and the most central events in the data (left). In FRITIOF, the accepted mean multiplicity for most central events is the same. The number of wounded nucleons is calculated from the linear relationship of $N_{ch,accepted}$ and N_{wound} in FRITIOF (fig. 4.18) using the mean multiplicity measured in data $\langle N_{ch} \rangle_{data}$ as input.

4.3.3 Number of participants from zero-degree energy

The zero-degree energy E_0 measured in the veto calorimeter is calibrated such that the beam energy yields $E_0 = A \cdot 158$ GeV. The mean energy measured in the calorimeter is therefore proportional to the mean number of projectile spectators N_{spec} . Assuming symmetry between projectile and target hemisphere on average, the number of participants can be calculated as

$$N_{part} = 2 \left(A - \frac{\langle E_0 \rangle}{158 \text{ GeV}} \right) \quad (4.6)$$

Figure 4.19 presents the zero-degree energy spectrum as measured in experiment, results for mean values and the corresponding number of participants are summarized in table 4.13.

However, this estimation assumes first, that there is no (or very few) contamination by additional energy from produced particles in E_0 , second that all secondary participants are not accepted in the veto calorimeter, and third that the collisions

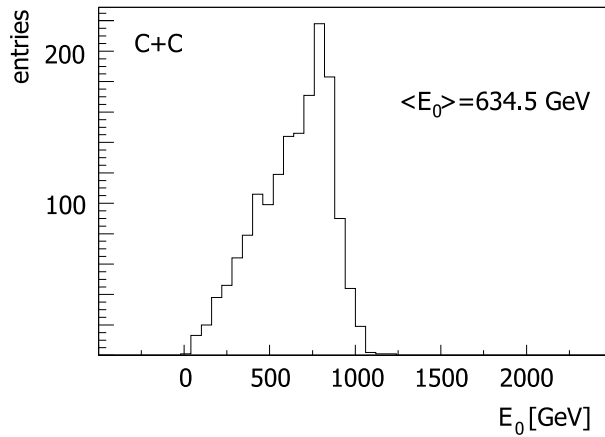


Figure 4.19: Spectrum of the zero-degree energy in central C+C collisions.

are symmetric on average. The last point is especially not true for N+C interactions, but as seen from the previous investigations the difference is small and well within uncertainties from other sources. Participants accepted in the veto calorimeter have lost only very few energy, therefore they did not contribute much to particle production and can as well be counted as spectators. As in the data, also in VENUS simulations the energy of these fast participants was considered for the centrality determination. Therefore, the second assumption has a negligible influence. The first assumption approximately holds as seen from the rapidity spectra of produced mesons in chapter 6. Only neutral particles which are not swept out of the beam trajectory by the magnets contribute as neutrons or K_L^0 .

In addition, the calorimeter is assumed to provide a linear relationship of spectator energy and E_0 between E_{beam} and zero. As known from Pb+Pb interactions [74] this is not true for the whole range of energy, but holds approximately for central collisions.

	$\langle E_0 \rangle$ [GeV]	$N_{spec} = \frac{\langle E_0 \rangle}{158 \text{ GeV}}$	N_{part}
C+C	634.5	4.0	16
Si+Si	1318	8.3	39.4

Table 4.13: Number of participants derived from the zero-degree energy measured in the veto calorimeter.

4.3.4 Summary of results

The number of participants and other variables for the centrality extracted in the previous sections are compared in table 4.14. Overall the three methods show a good agreement. Especially FRITIOF results for N_{wound} coincide well within the methods. However, FRITIOF always yields more wounded nucleons, more collisions per wounded nucleon, and a lower impact parameter compared to VENUS. This is mainly due to the different initialization of the nuclei. The values derived from VENUS simulations are taken as final numbers, since nuclei are initialized with a Woods-Saxon density profile there. In the error estimate FRITIOF results are considered. For the number of participants the average of VENUS and the measurement using the veto energy is taken.

	σ_{trig}^{VENUS}	$\sigma_{trig}^{FRITIOF}$	N_{ch}^{data}	E_0	combined
C+C	$\langle N_{part} \rangle$	16.6 ± 0.4		16	16.3 ± 1
	$\langle N_{wound} \rangle$	13.9 ± 0.4	15.9 ± 0.4	15.8	14 ± 2
	$\langle \nu \rangle$	1.71 ± 0.01	1.80 ± 0.01		1.75 ± 0.05
	$\langle b \rangle$	1.88 ± 0.07	1.51 ± 0.08		1.9 ± 0.2
	b_{max}	2.02 ± 0.16	1.95 ± 0.16		2 ± 0.2
Si+Si	$\langle N_{part} \rangle$	43.3 ± 0.7		39.4	41.4 ± 2
	$\langle N_{wound} \rangle$	37.0 ± 0.8	39.9 ± 1	40.5	37 ± 3
	$\langle \nu \rangle$	2.16 ± 0.01	2.25 ± 0.01		2.2 ± 0.05
	$\langle b \rangle$	2.0 ± 0.1	1.81 ± 0.12		2 ± 0.2
	b_{max}	2.6 ± 0.2	2.54 ± 0.18		2.6 ± 0.2

Table 4.14: Summary of the various measurements of variables characterizing the centrality. The last column contains values finally used.

Chapter 5

p+p interactions

5.1 Kinematic distributions and yields in minimum-bias collisions

In this section results for p+p interactions within the NA49 minimum-bias trigger are presented for 158 GeV beam energy. This means, experimental multiplicities for particle production are not corrected for the difference of the NA49 trigger cross section and the expected value for σ_{inel} (see section 4.1), the reason being uncertainties in the scaling (see more detailed discussion in section 5.1.5).

Tables with numerical values of the results and additional figures can be found in appendix C.

5.1.1 Pions

Yields for pions and kaons were extracted from the dE/dx fits as described in chapter 3.1. As standard parameters were required: a minimum of 30 points per track, and right-side tracks in a Φ -wedge of $|\Phi| \leq 30^\circ$. Only dE/dx spectra with more than 500 entries were fitted. A momentum range of $0.6 < \log_{10}(p) \leq 1.7$ was used for π^- , of $0.6 < \log_{10}(p) \leq 1.9$ for π^+ . Sufficient statistics was available for measurements of transverse-momenta up to 1.5 GeV at most.

Transverse-momentum distributions

Transverse-momentum distributions were extracted in rapidity bins; a presentation in the form of m_t -spectra can be found in figure 5.1, see appendix C for some p_t -spectra. Statistical errors are smaller than the symbol size, m_t -distributions according to equation 3.8 are fitted to the data. The temperature parameter T as tabulated in appendix C was determined in two steps. First, p_t -spectra are fitted with a free parameter T (formula 3.7). Then, the dependence of T on y is approximated with a parabola and a new fit is performed using this smoothed temperature development as constraint (see fig. 5.3(b)). Motivation and usefulness of this procedure become more clear for pions in C+C and Si+Si collisions, for a detailed discussion see section 6.1. For consistency of the results in p+p, C+C, and Si+Si the same strategy

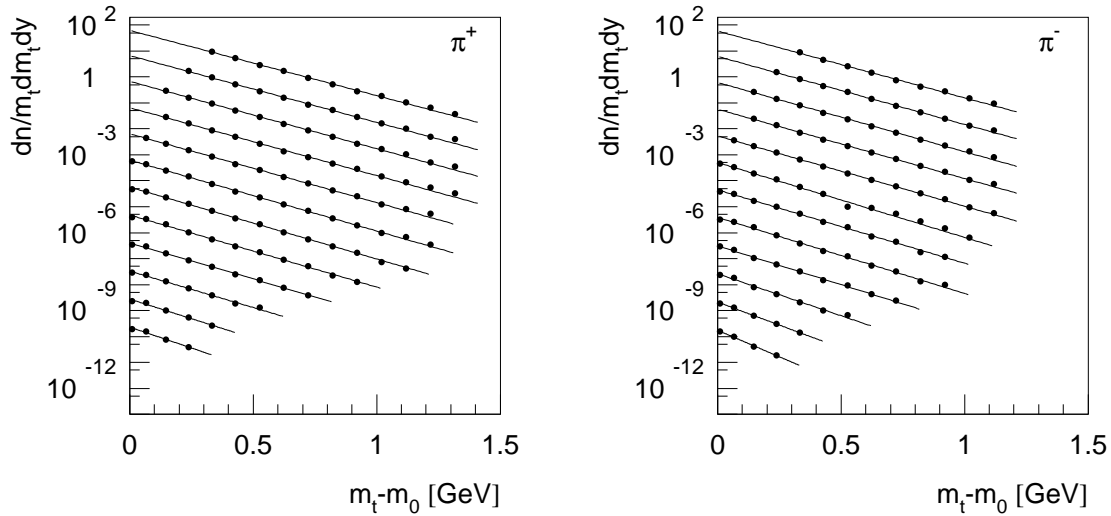


Figure 5.1: Transverse-mass distributions for pions in minimum-bias p+p collisions in bins of rapidity. The upper curve is at midrapidity ($2.77 < y \leq 3$), the other spectra are successively scaled down by a factor of 10 for better visibility. The lowest spectrum corresponds to $5.31 < y \leq 5.54$. No feed-down correction for pions is applied yet. Lines correspond to fits assuming a thermal m_t -distribution (formula 3.8). Statistical errors which are smaller than the symbol size are calculated as the square root of the number of pions in each (y, p_t) bin.

was used here. However, the the difference of the constraint-temperature fit and the free-temperature fit are minor in p+p (see open and close circles in fig. 5.2).

Rapidity distribution and integrated yield

The p_t -integrated rapidity distributions presented in figure 5.2 are obtained by summing yields in transverse momentum where available, and extrapolating for the missing part using the fitted transverse-momentum distributions with smoothed temperatures. Integration of the analytical distributions gives the same results within $\sim 2\%$. Errors included in the figures are statistical only, for the extrapolation an uncertainty of ± 10 MeV in the temperatures is assumed. The feed-down correction was applied as described in chapter 3.1.3 (see fig. 3.8); it reduces total measured yields by about 4%. The resulting rapidity distribution is better described by a double Gaussian (equation 3.9) than by a simple one. Integrated yields of both differ by about 4% for π^+ and 1% for π^- (Gaussian: $\langle \pi^+ \rangle = 3.20 \pm 0.01$, $\sigma_y = 1.58$ and $\langle \pi^- \rangle = 2.36 \pm 0.01$, $\sigma_y = 1.33$). In case of the double-Gaussian fit the width is characterized by the FWHM, which is 3.87 for π^+ and 3.34 for π^- .

Final results are listed in table 5.1. The systematic errors will be discussed in the next paragraph.

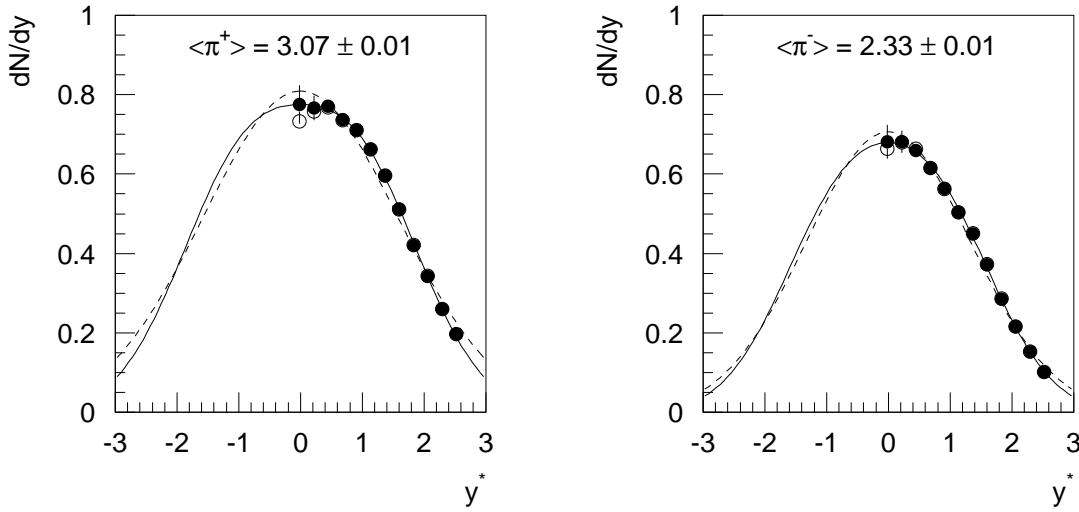


Figure 5.2: Feed-down corrected rapidity distributions for pions in minimum-bias p+p interactions. A double Gaussian (solid line) gives an improved fit compared to a simple one (dashed line). The integrated yield is given in the figure. For comparison, p_t -integrated values using temperatures from a free fit are shown as open symbols (see fig. 5.3). Only at midrapidity the difference is significant.

	π^+	π^-
$T _{y_{CMS}}$	$167 \pm 1 \pm 10$	$166 \pm 1.5 \pm 10$
σ_y	1.04 ± 0.01	0.984 ± 0.008
y_Δ	0.949 ± 0.005	0.799 ± 0.007
$dN/dy _{y_{CMS}}$	$0.771 \pm 0.029 \pm 0.062$	$0.681 \pm 0.026 \pm 0.054$
$\langle \pi \rangle$	$3.07 \pm 0.01 \pm 0.15$	$2.33 \pm 0.01 \pm 0.12$

Table 5.1: Final feed-down corrected results of pions in minimum-bias p+p collisions at 158 GeV. The first error is statistical, the second, if available, systematic. For values at midrapidity the mean of the first two bins ($2.77 < y \leq 3.23$) is taken.

Systematic errors

The extracted transverse-mass and rapidity distributions show small statistical errors. Indeed, the analysis is dominated by systematic errors. The main uncertainties stem from unfolding the dE/dx spectra and the extrapolation to low p_t at midrapidity. By systematically varying selection parameters and settings of the fitting routine, their impact on the results was investigated. The scaling of mean position and width in the dE/dx spectra is mainly determined by pions, thus the resulting uncertainty should be small. Some trouble comes in from the electrons, but setting them to zero does change results by 1 % at most. The influence of the kaon position is checked in the context of systematic studies of the kaon yield. There, the kaon position is shifted by ± 1 %, which changes pions by less than 1 %.

Integrated yields are very stable against a variation of selection parameters of pions, see left part of fig. 5.3(c). As will be shown in section 6.1 also the assumption of slightly asymmetric dE/dx distributions changes yields by 1-2 % only. However,

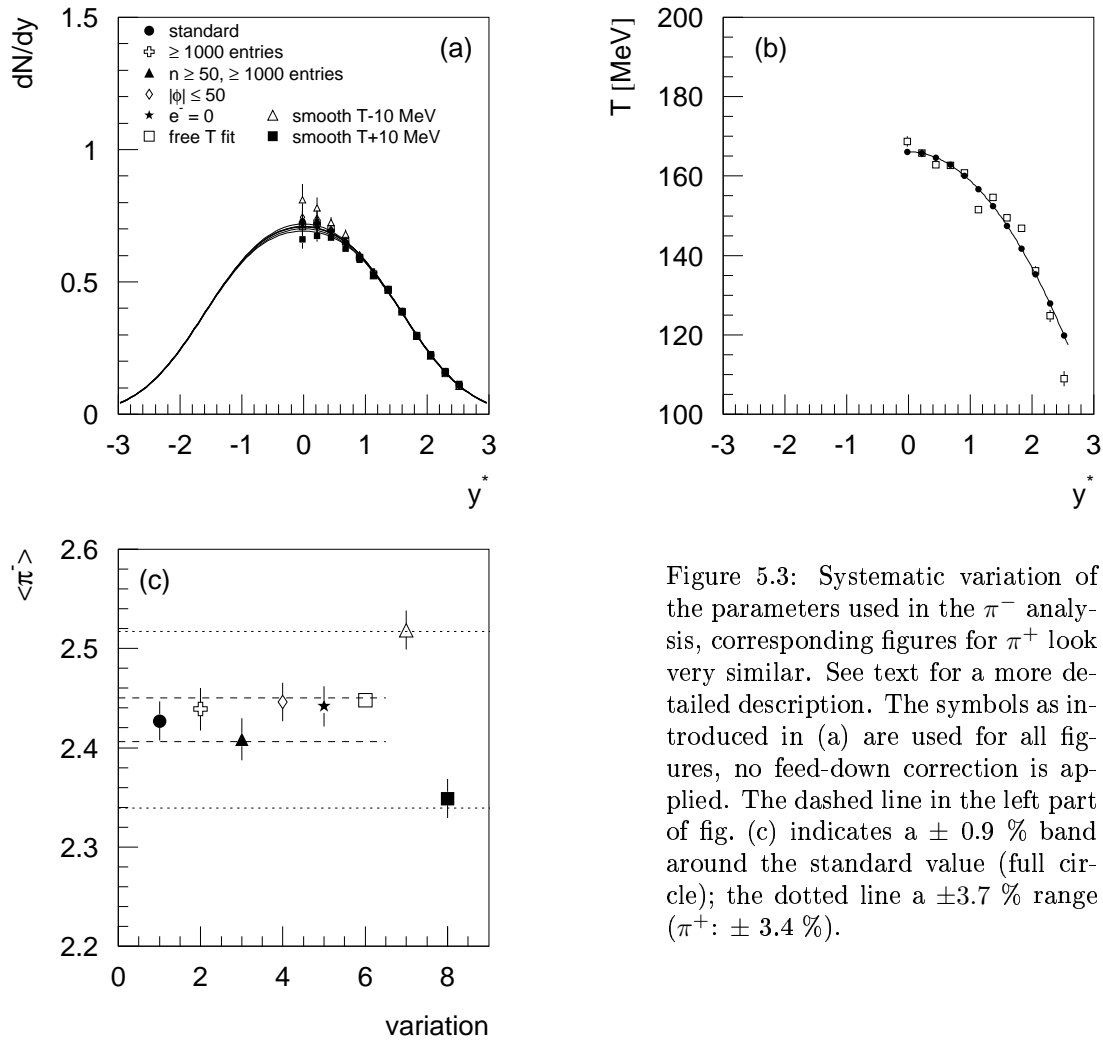


Figure 5.3: Systematic variation of the parameters used in the π^- analysis, corresponding figures for π^+ look very similar. See text for a more detailed description. The symbols as introduced in (a) are used for all figures, no feed-down correction is applied. The dashed line in the left part of fig. (c) indicates a $\pm 0.9\%$ band around the standard value (full circle); the dotted line a $\pm 3.7\%$ range (π^+ : $\pm 3.4\%$).

a variation of T by ± 10 MeV moves the dN/dy at midrapidity by $\pm 10\%$, and by $\pm 7.5\%$ and $\pm 4.5\%$ in the next two bins. Reason is the rather large extrapolation in these bins due to the missing measurement at low p_t . A systematic error of $\pm 4\%$ on the total yield results from the uncertainty at midrapidity.

To further constrain the midrapidity yield a preliminary analysis of negative hadrons was performed. Contributions of K^- and \bar{p} were subtracted with help of VENUS simulations. Midrapidity yields agree within 4% and integrated yields within 3% . Also p_t -extrapolations taking into account a low- p_t enhancement due to resonance decays were tested [99]. They lead to variations of the same order as reported above. Both crosschecks are introduced in more detail in section 6.1, for figures see appendix C.

Taking into account also statistical uncertainties in the feed-down correction and the acceptance a systematic error of 5% seems to be reasonable.

5.1.2 Kaons

Kaons were extracted in the same way as pions, however spectra are better defined because of the more convenient acceptance. The momentum range used is $0.6 < \log_{10}(p) \leq 1.7$ for both, K^+ and K^- . Otherwise, the standard parameters for the fits are already reported above.

Transverse-momentum distributions

Transverse-mass spectra in bins of rapidity are presented in fig. 5.4. Statistical errors are smaller than the symbol size, the extraction of yields is governed by systematic uncertainties. Temperatures obtained from the spectra by fitting thermal distributions scatter as shown in fig. 5.6 for K^+ , for K^- the variation is less. Compensating for the scatter by a parabola fit does not change yields significantly, because the extrapolation is small due to the large p_t coverage of the measured yields. Integrating spectra gives the same results within 1 % compared to using the sum of the bins and an extrapolation for the missing p_t -range. K^- temperatures vary with rapidity in a systematically different way compared to the ones of K^+ . This might be due to a proton contamination in the K^+ spectra, or an intrinsic difference between the two charged kaons. However, assuming that the parameter T of K^- holds also for K^+ does not change the total yield of K^+ because of the, already mentioned, small range of extrapolation: Integrated yield and σ_y would be reduced by 2 %.

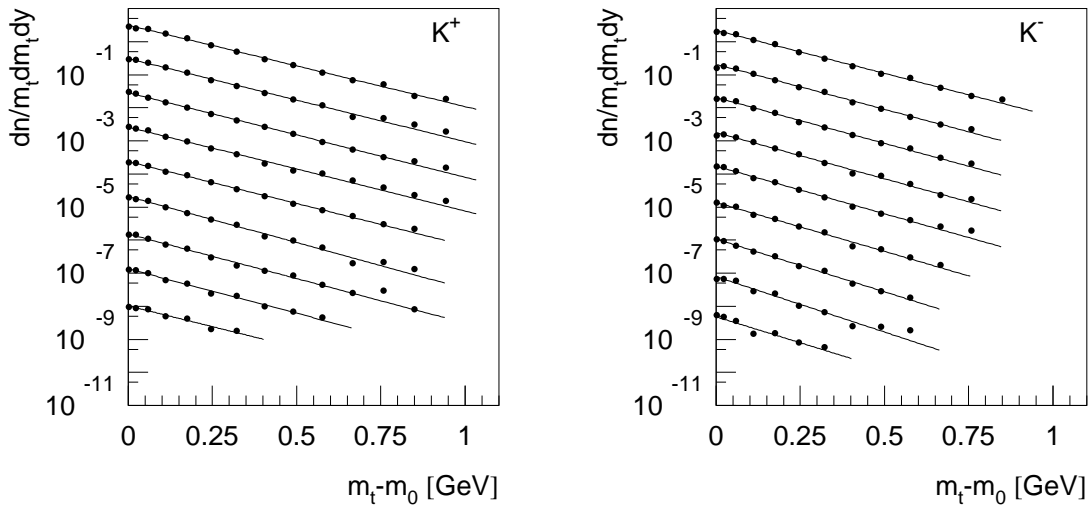


Figure 5.4: Transverse-mass distributions for kaons in minimum-bias p+p collisions in bins of rapidity. The upper curve is at midrapidity ($2.77 < y \leq 3$), the other spectra are successively scaled down by a factor of 10 for better visibility. The lowest spectrum corresponds to $4.62 < y \leq 4.85$. Lines show fits assuming a thermal m_t -distribution (formula 3.8).

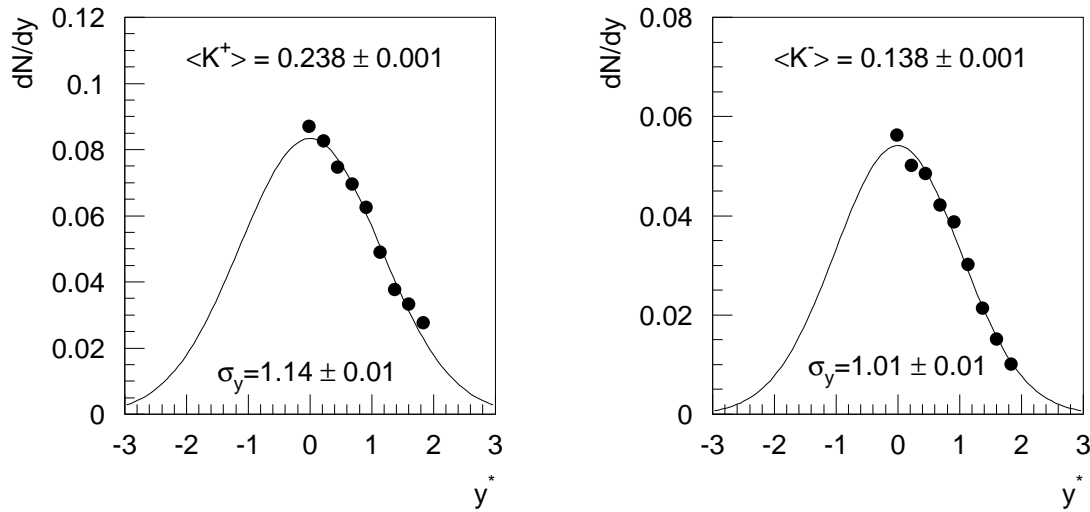


Figure 5.5: Rapidity distributions for kaons in minimum-bias p+p interactions. The distributions are fitted with a Gaussian, width and integrated yield are given in the figure. Errors are statistical only.

	K^+	K^-
$T _{y_{CMS}}$	$175 \pm 2 \pm 10$	$164 \pm 2 \pm 10$
σ_y	$1.14 \pm 0.01 \pm 0.06$	$1.01 \pm 0.01 \pm 0.05$
$dN/dy _{y_{CMS}}$	$0.085 \pm 0.001 \pm 0.009$	$0.0533 \pm 0.001 \pm 0.005$
$\langle K \rangle$	$0.238 \pm 0.001 \pm 0.024$	$0.138 \pm 0.001 \pm 0.014$

Table 5.2: Final results of kaons in minimum-bias p+p collisions at 158 GeV. The first error is statistical, the second systematic. For values at midrapidity the mean of the first two bins ($2.77 < y \leq 3.23$) is taken.

Rapidity distribution and integrated yield

p_t -integrated rapidity distributions are presented in fig. 5.5. As was already discussed, the large p_t coverage of yields requires only a small extrapolation ($\sim 5 - 10\%$). The main systematic uncertainties stem from the dE/dx fitting procedure. Results are summarized in table 5.2.

Systematic errors

Kaons are especially difficult to extract from dE/dx spectra because of their position between protons and pions. In case of K^- the situation is slightly better because of the small antiproton yield. The relative scaling position from the dE/dx calibration may not be completely correct. The effect of a possible mismatch is checked by fixing pion and proton position and varying the mean of kaons by $\pm 1\%$. Since the dE/dx resolution is about 4% this is a sizeable shift and visible in the spectra (see fig. in appendix C). The resulting error of the total yield is on the order of $\pm 8\%$ for K^+ and $\pm 6\%$ for K^- . An uncertainty increasing the kaon yields by

about the same amount stems from the correction for in-flight decay of kaons. As discussed in chapter 3.1.3 not all kaon tracks matched to the decay- μ were rejected. If this assumption was wrong and all these tracks are lost in the analysis, the kaon yields would be about 8 % and 6 % higher, respectively, mainly because the rapidity distribution would become wider.

Systematic changes of other parameters show much less effect on the kaon yield. The small effect of using asymmetric distributions for fitting the dE/dx spectra will be demonstrated for C+C and Si+Si. Changes for K^- are always slightly less than for K^+ , results of systematic variations of various parameters for K^+ are presented in fig. 5.6. A systematic error of 10 % on the kaon yield is reasonable.

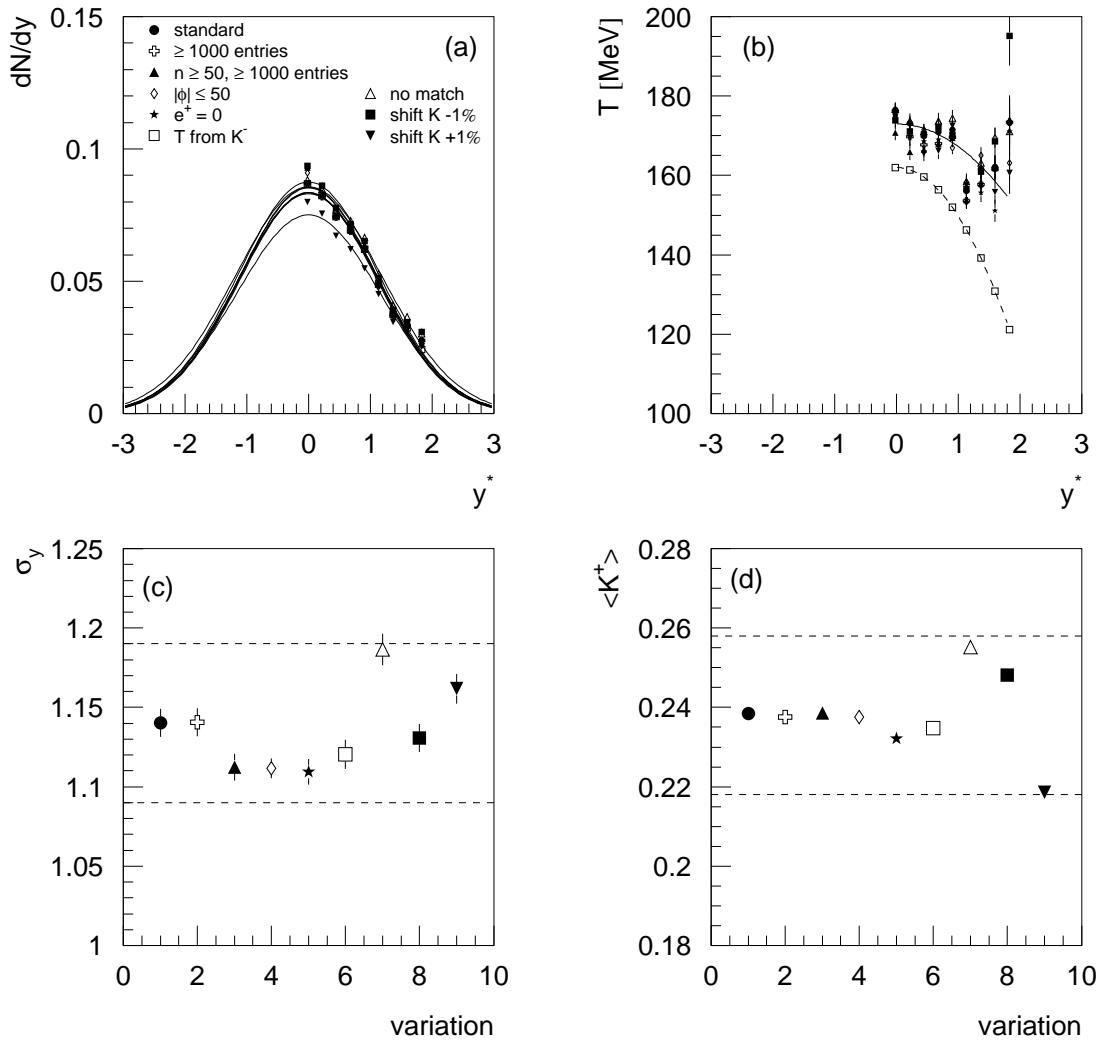


Figure 5.6: Systematic variation of parameters used in the K^+ analysis. The symbols as introduced in (a) are used for all figures. The solid line in (b) indicates a parabola fit to T from "standard", the dashed line the same for K^- showing the systematic difference in temperatures between the charged kaons. Dashed lines in (c) and (d) give a $\pm 4.4\%$ and $\pm 8.4\%$ band around the standard value, respectively, which is a lower estimation of the systematic error.

5.1.3 ϕ -meson

The ϕ -meson in minimum-bias p+p collisions was already analyzed in [100, 101], but the available statistics has increased by a factor of 5 since then. Thus it was reinvestigated, especially since enough statistics for the analysis in inelasticity bins of p+p interactions is now available.

For the extraction of the ϕ -meson in p+p collisions kaons with more than 30 points per track, momenta of $0.6 < \log_{10}(p) \leq 1.7$ and $0 \text{ GeV} < p_t \leq 1.5 \text{ GeV}$, and within a $\pm 1.5\sigma_{dE/dx}$ window around the mean dE/dx position as obtained from dE/dx fits were selected.

A typical background-subtracted signal with a simulation adjusted to it can be found in figure 5.7. The undershoot structure expected from the simulation is not observed in data (dashed line). Below the ϕ -signal a distortion remains which does not vanish even with very sharp selection criteria on the kaon identification, e. g. by the exclusion of either the proton or the pion contamination by choosing kaons only above and below the mean dE/dx value, respectively. In contrast to p+p collisions these clean-up procedures have a clear positive effect for C+C and Si+Si data (see next chapter). Probably, the observed structure in p+p is a remaining effect of kinematic correlations as discussed in section 3.2.2: Using only events with two kaons at minimum for the calculation of the event-mix background obviously does not account for the whole effect.

The distortion of the background below the ϕ -signal results in an uncertainty of the extracted yield. Averaging over the two most different cases gives a good estimation of yield and errors due to background treatment. In one case the distortion is ignored and the simulation including undershoots is fitted to the subtracted spectrum. In the other case, an additional straight line is adjusted to the subtracted

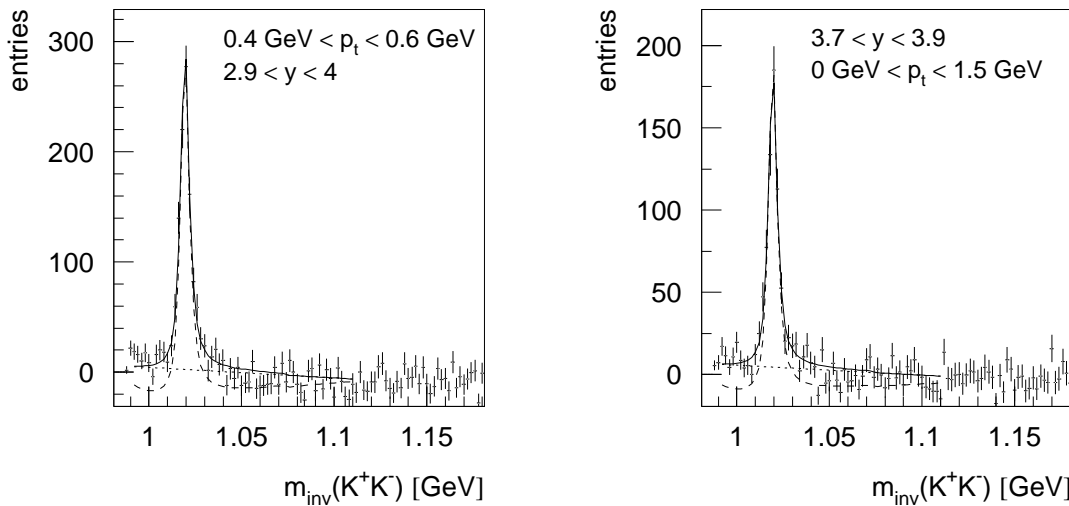


Figure 5.7: Invariant-mass spectra in kinematic bins as written in the figures. The remaining background below the ϕ -signal is clearly visible. As dashed line a fit ignoring the background is shown. The full line represents a Breit-Wigner function on top of the dotted straight line. Both fits differ by about 10-12 % in their yields, for final ϕ -yields the mean is used.

background and on top of this a pure Breit-Wigner function is fitted (figure 5.7). The first case probably overestimates the yield, the second might underestimate it. However, both yields differ by about 10-12 % only; for the final results the mean is chosen. Kinematic distributions for both cases are the same within errors, only for the transverse-momentum spectra a systematic difference in the inverse slope is observed; neglecting the distortion provides about 8 MeV larger temperatures. Systematic changes of the yields in dependence on selection criteria for the kaons were investigated for both cases. Since they are the same, they will be presented only for one study.

Bins for extracting the kinematic distributions of the ϕ were chosen such that they contain enough statistics and cover the available phase space (see acceptance in fig. 3.20). The transverse-momentum spectra were therefore extracted in a wider rapidity bin of [2.9,4]. For the p_t -integrated rapidity spectrum one aims at a large p_t -range to minimize the extrapolation to the full yield. The chosen range from 0 GeV to 1.5 GeV contains 98.6 % of all ϕ -mesons (for $T = 168$ MeV).

Mass and width of the ϕ -meson

Adjusting the simulated invariant-mass spectrum to real data is in principle a three-parameter problem: position, width and height of the signal are unknown. The height is connected to the yield of the ϕ -meson and varies depending on selection criteria for the current mass spectrum. Mass and width should be constant within the event sample but have to be determined once. Both parameters are basically known for the free particle [2], but depend also on experimental facts as, e.g., the momentum resolution of the spectrometer.

To account for the latter the width of the simulated signal is divided into two contributions: on the one hand the intrinsic width $\Gamma = 4.43$ MeV of the ϕ -meson, on the other hand a Gaussian broadening of the mass to account for the momentum resolution of the detector. From the simulation chain described in 3.2.5 it is known, that the kaons receive a momentum smearing of a few MeV. This

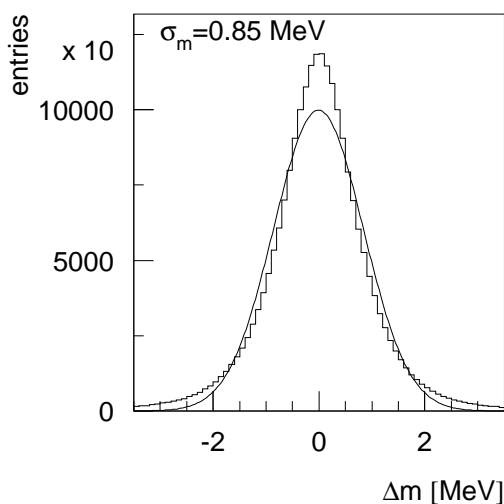


Figure 5.8: Distribution of the difference between generated and reconstructed ϕ -mass as described in 3.2 (histogram). This smearing of the ϕ -mass results from the momentum resolution of reconstructed kaons due to detector effects. It can be approximated by a Gaussian with a width $\sigma_m = 0.85$ MeV (line).

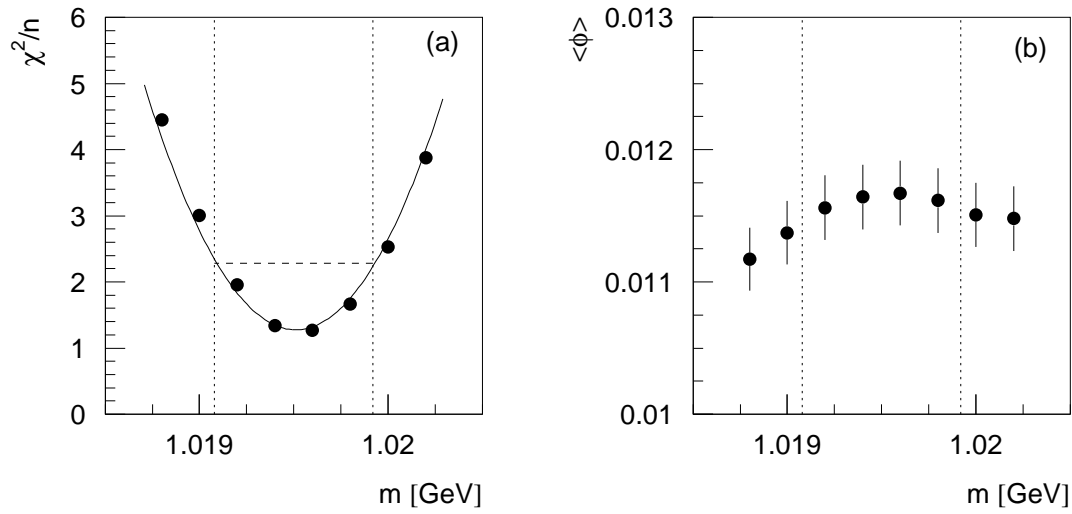


Figure 5.9: χ^2/n in dependence on the mass for a fixed width $\sigma_m = 0.85$ MeV (a). The line gives a parabola fitted to the data points from which mass and errors are extracted: $m_0 = (1019.5 \pm 0.4)$ MeV. (b) corresponding yield in dependence on the mass assumed for the fit. The dotted lines show the error margin from (a). As discussed in the text the yield is nearly independent of the mass; the variation is on the order of 2 % only.

results in a broadening of the reconstructed ϕ -mass (fig. 5.8). Approximation of the distribution by a Gaussian gives a width $\sigma_m = 0.85$ MeV. Since there is no reason to assume any change in the intrinsic ϕ -width in p+p collisions, Γ is fixed at 4.43 MeV and σ_m is taken as free parameter.

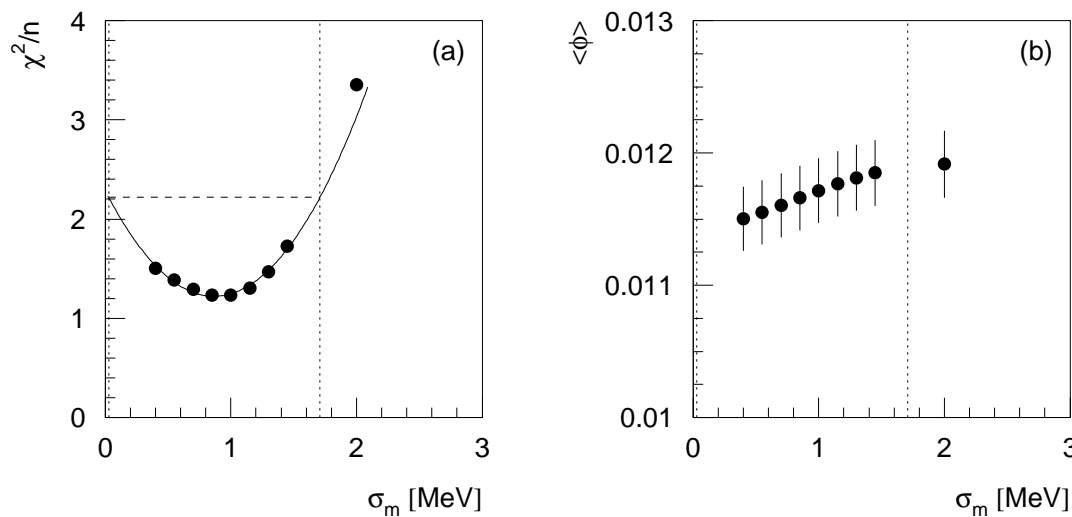


Figure 5.10: χ^2/n in dependence on the width σ_m of the Gaussian mass resolution of the ϕ -mass for a fixed mass $m = 1019.5$ MeV (a). The small curvature of the parabola results in a large error on the best fit for σ_m : $\sigma_m = (0.87 \pm 0.84)$ MeV. (b) corresponding yield in dependence on σ_m assumed for the fit. The dotted lines show the error margin from (a); the change in the yield is about 2 % only.

The fit of the simulation to data is optimized by minimization of the χ^2 . A Breit-Wigner function folded with a Gaussian is adjusted to the event-mix subtracted spectrum. The remaining distortions in the background are approximated by a straight line (see fig. 5.11). If the parameters to be determined are sufficiently independent of each other they can be fixed one by one. V. Friese discussed that position and width fulfill this criterium [64], for this work it was checked that also mass and amplitude, and mass and width are independent. χ^2/n distributions for deriving mass and width are shown in figures 5.9 and 5.10 (n is the number of degrees of freedom, i. e. the number of fitted channels minus three parameters).

If $\chi^2(a)$ varies like a parabola near a minimum a_0 , the error of a is given by the curvature in the region of the minimum [102]:

$$\sigma^2 = 2 \left(\frac{\partial^2 \chi^2}{\partial a^2} \right)^{-1} \quad (5.1)$$

An increase or decrease of the parameter a by one standard deviation σ increases χ^2 therefore by 1.

From figures 5.9 and 5.10 mass and mass-resolution of the ϕ -meson in p+p collisions are extracted:

$$m_0 = (1019.5 \pm 0.4) \text{ MeV} \text{ and } \sigma_m = (0.87 \pm 0.84) \text{ MeV}$$

An invariant-mass signal of the ϕ -meson with the best fit is presented in figure 5.11. The extracted mass is consistent with the value of $(1019.413 \pm 0.008) \text{ MeV}$ from the particle data group [2]. The value for the width agrees well with what is expected from the spectrometer resolution (fig. 5.8). The parameters given above are used in the following for all simulations of the ϕ -meson in p+p collisions.

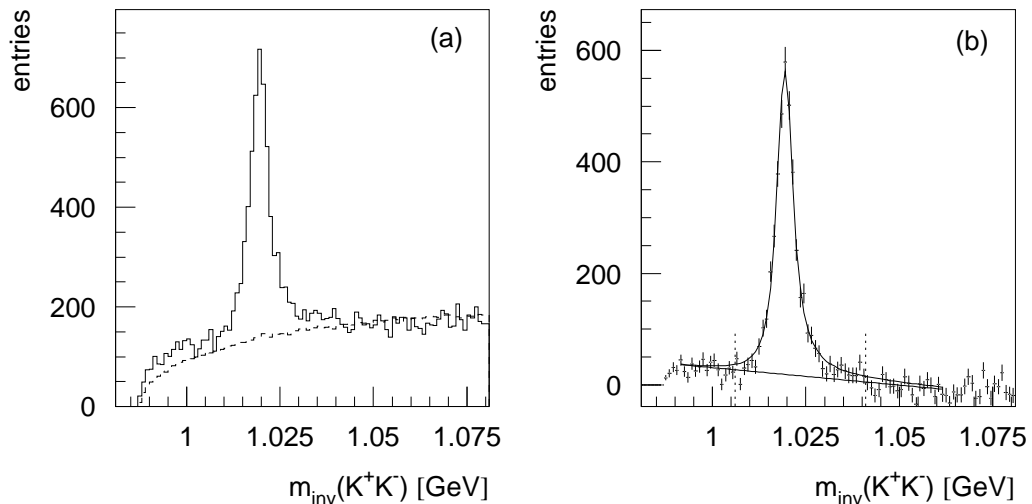


Figure 5.11: Invariant-mass distribution of the ϕ -meson in a rapidity range of 2.9 to 4 and a p_t -range of 0 GeV to 1.5 GeV (a); the dashed line is the calculated event-mix background. Event-mix-subtracted signal (b) with linear fit for the remaining distortion. The line represents a Breit-Wigner distribution folded with a Gaussian ($m = 1019.5 \text{ MeV}$, $\Gamma = 4.43 \text{ MeV}$ and $\sigma_m = 0.85 \text{ MeV}$) which is fitted to the data in the range indicated by the dashed lines.

Transverse-momentum distribution

Results for transverse-momentum distributions are presented in figure 5.12. The quoted error is statistical.

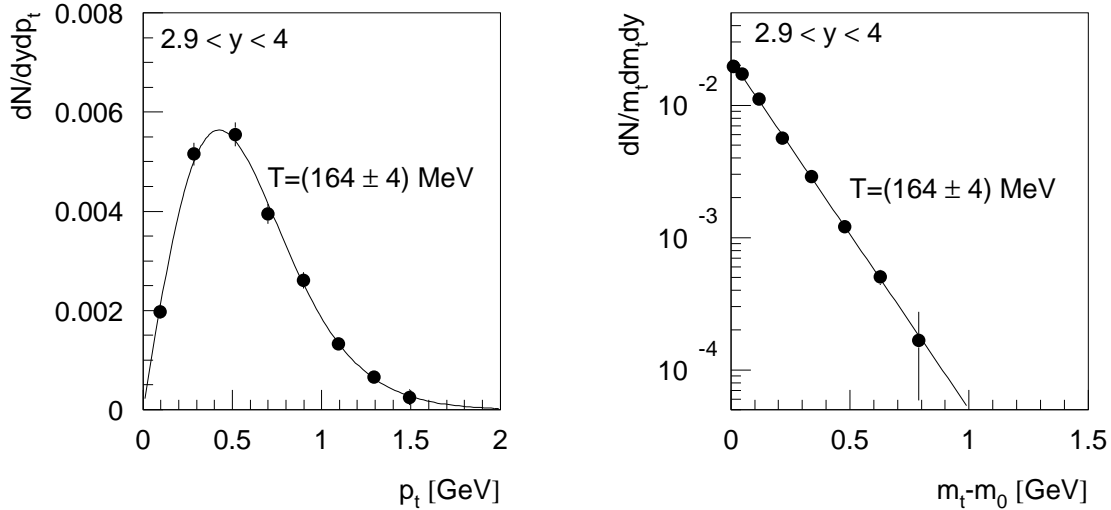


Figure 5.12: Transverse-momentum and transverse-mass spectrum of the ϕ -meson in minimum-bias p+p collisions. Lines correspond to fits assuming Boltzmann distributions (formula 3.7, 3.8).

Rapidity distribution and integrated yield

A p_t -integrated rapidity spectrum is presented in figure 5.13. Since the spectrum is obtained in a large p_t -range of [0.,1.5] GeV, the extrapolation using the p_t -distribution with mean temperatures as shown in fig. 5.12 is about 1-2 % only. The quoted error is statistical, the full yield is the integrated value of the Gaussian distribution fitted to the data.

Final results averaged over the two ways of background treatment are listed in table 5.3. The quoted systematic errors are estimated in the next paragraph.

m_0	(1019.5 ± 0.4) MeV
Γ_0	4.43 MeV (fixed)
σ_m	(0.87 ± 0.84) MeV
T	$(164 \pm 4 \pm 10)$ MeV
σ_y	$0.95 \pm 0.02 \pm 0.04$
$\langle \phi \rangle$	$0.0129 \pm 0.0002 \pm 0.0013$
$\frac{dN}{dy} \Big _{y_{CMS}}$	$0.00535 \pm 0.0003 \pm 0.00043$

Table 5.3: Summary of results for the ϕ -meson in minimum-bias p+p collisions. The first error quoted is statistical, the second systematic. For the midrapidity value the first bin ($2.9 < y \leq 3.1$) is used.

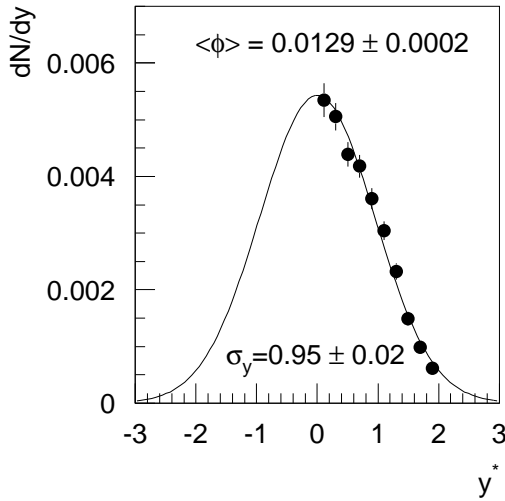


Figure 5.13: Rapidity distribution of the ϕ -meson in minimum-bias p+p collisions. The distribution is fitted by a Gaussian, the quoted error is statistical. The full yield is obtained by integrating the Gaussian.

Systematic errors

A first check for the consistency of the presented data is the comparison of yields extracted from integrating the p_t -distribution, the rapidity distribution, and from a fit to the invariant-mass signal in the full acceptance as performed for the determination of the ϕ -mass in the previous section. The consistency check presented here is for fitting a Breit-Wigner function on top of a straight line, it is the same for the other treatment of the background. Integration of the y -integrated p_t -distribution (fig. 5.12) yields

$$\int_0^\infty c \cdot p_t \exp\left(-\frac{m_t}{T}\right) dp_t = c \cdot T^2 \left(1 + \frac{m}{T}\right) \exp\left(-\frac{m}{T}\right) = 0.004532 \quad (5.2)$$

whereas the integration of the p_t -integrated rapidity distribution, the Gaussian in fig. 5.13, in the corresponding y -integral gives

$$\int_{2.9}^4 \frac{c}{\sigma_y \sqrt{2\pi}} \exp\left(-\frac{(y - 2.9)^2}{2\sigma^2}\right) dy = 0.004597. \quad (5.3)$$

The values agree within 3%. Figure 5.11 presents the invariant-mass of the ϕ -meson in a wide p_t and y -range, which covers nearly the full acceptance, $\langle\phi\rangle = 0.0122$. Integration of the rapidity spectrum yields 0.0121, which is only 1% below.

The rapidity spectrum is extracted for ϕ -mesons in a transverse-momentum bin of [0.,1.5] GeV assuming the same temperature for the full rapidity range. The p_t -interval contains 98.6% of all ϕ -mesons assuming a temperature of $T = 168$ MeV. The extrapolation is therefore small (factor of 1.014). Temperatures of 180 MeV or 140 MeV provide extrapolation factors of 1.02 and 1.005, respectively. The uncertainty in the temperature results in systematic errors on the ϕ -yield in bins of rapidity and for the full range of about ± 1 -2% only.

Several sources for systematic errors and their impact on the kinematic distributions and the total yield are investigated (fig. 5.14, 5.15). The study is presented

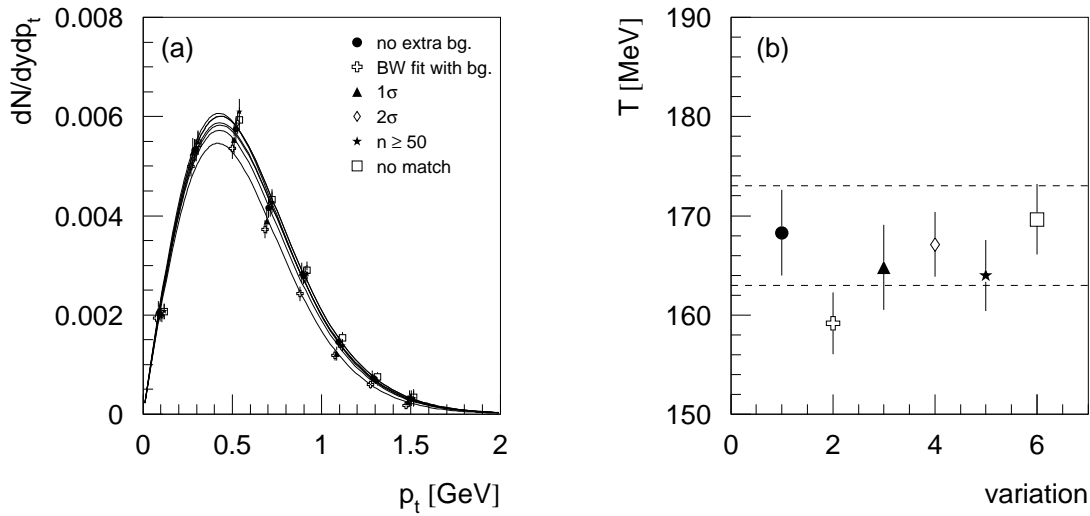


Figure 5.14: Transverse-momentum distributions for the various selection criteria as discussed in the text, in (a) and (b) the same symbols are used. For this figure, the ϕ -yield is extracted by fitting a simulation including the undershoot structure to the data. If a Breit-Wigner distribution on top of a straight line is used, the extracted temperature is 8 MeV lower, see open cross in (b). The scatter if varying other parameters is the same (not shown). The dashed lines indicate a range of (168 ± 5) MeV.

for invariant-mass fits neglecting the distortions in the background which means fitting a simulation including undershoots. The result for the other way of background treatment is also presented in the figures, systematic errors are the same there. Because final results are averaged over both methods, uncertainties due to background treatment reduce to about 6 %.

The uncertainty introduced by selecting kaons in a window in dE/dx is discussed in detail by V. Friese [64]. It can be minimized by choosing a symmetric window around the mean dE/dx position of kaons. To investigate the precision of the mean dE/dx and $\sigma_{dE/dx}$ values used for this analysis and to estimate systematic errors introduced by their uncertainty, ϕ -mesons are also extracted with a $1 \cdot \sigma_{dE/dx}$ and $2 \cdot \sigma_{dE/dx}$ window around the mean position.

The statistical error in the acceptance was calculated to 1-2 % on average (section 3.2). A systematic error can be investigated by choosing different selection criteria for kaons, e. g. requiring more than 50 number of points on the track. A remaining systematic uncertainty is the estimation of the identification capabilities of kaons which decayed in the TPCs. As discussed in section 3.2.5, not all kaon tracks, to which the track of the decay daughter was matched, were rejected for the calculation of the acceptance tables. If all these tracks were lost in the analysis, the ϕ -yield would rise by 5.5 %.

Figures 5.14 and 5.15 present kinematic distributions for the variation of extraction parameters of kaons. In general, a very good stability of yields in the various kinematic bins and of the integrated yield is found. From the scatter of T , σ_y and $\langle \phi \rangle$ a lower border of the systematic error is extracted and indicated in the plots. Since the various systematics can add in principle, the estimated total systematic error is larger, 10 % are reasonable for the total yield.

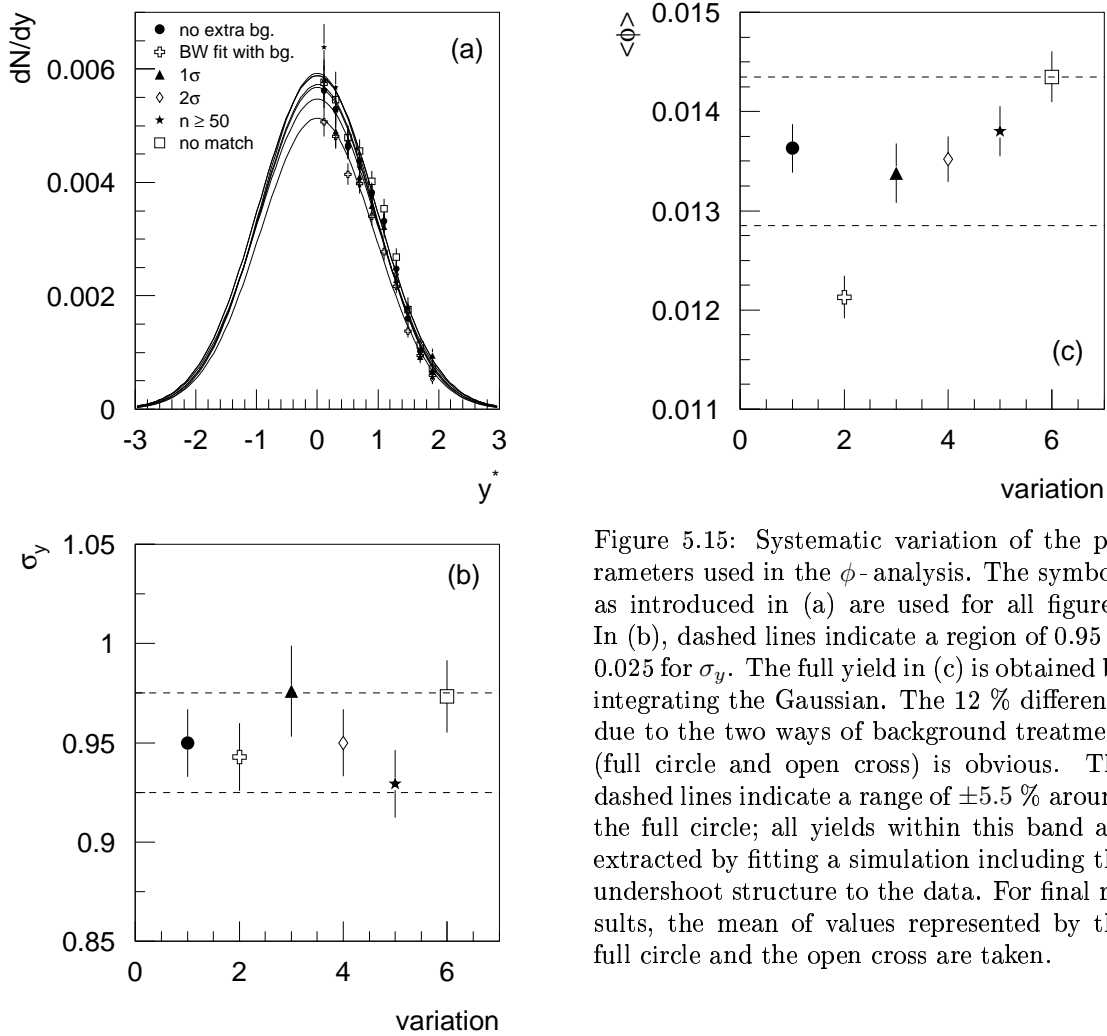


Figure 5.15: Systematic variation of the parameters used in the ϕ -analysis. The symbols as introduced in (a) are used for all figures. In (b), dashed lines indicate a region of 0.95 ± 0.025 for σ_y . The full yield in (c) is obtained by integrating the Gaussian. The 12 % difference due to the two ways of background treatment (full circle and open cross) is obvious. The dashed lines indicate a range of $\pm 5.5\%$ around the full circle; all yields within this band are extracted by fitting a simulation including the undershoot structure to the data. For final results, the mean of values represented by the full circle and the open cross are taken.

5.1.4 $K^*(892)^0$ and $\overline{K}^*(892)^0$

The analysis of the $K^*(892)^0$ and $\overline{K}^*(892)^0$ mesons is similar to the one for the ϕ -meson, only a higher resonance, the $K_2^*(1430)$, is included into the simulation of the resonance invariant-mass signal with a ratio of 3.7 : 1 for $K^*(892)^0$: $K_2^*(1430)$. The determination of this ratio will be described in the next paragraph.

Standard selection criteria for kaons and pions are as for the ϕ -meson: more than 30 points on the track, momentum cuts of $0.6 < \log_{10}(p) \leq 1.7$ and $0 \text{ GeV} < p_t \leq 1.5 \text{ GeV}$, and a $\pm 1.5\sigma_{dE/dx}$ window around the mean dE/dx position as obtained from dE/dx fits.

The invariant-mass spectrum of the $\overline{K}^*(892)^0$ is well described by the simulation, even the undershoot structure is reproduced (see fig. 5.16, 5.19). For the $K^*(892)^0$ the case is not as good, there seems to be a remaining structure in the background subtracted spectra. This tendency is strengthened in C+C and Si+Si interactions. A cleaner kaon identification, which excludes the protons by asymmetric windows in dE/dx , improves the remaining distortions in the background (see

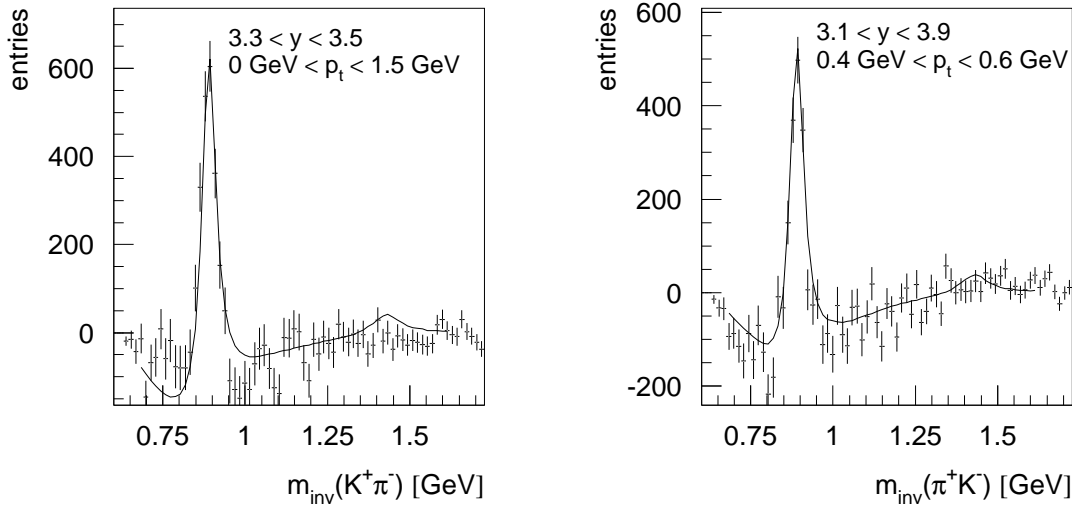


Figure 5.16: Examples of invariant-mass spectra of $K^*(892)^0$ (left) and $\bar{K}^*(892)^0$ (right) in kinematic bins as indicated in the figures.

discussion in section 3.2.2).

Transverse-momentum spectra were extracted in a rapidity range of [3.1,3.9]. The range was chosen slightly above midrapidity because at midrapidity the acceptance of $K^*(892)$ drops steeply, which is problematic because the yield becomes very sensitive to slight changes. The measured rapidity spectra indeed show that the midrapidity-yield is less stable against parameter variations. The range was chosen large enough that the statistics were satisfying for extraction of transverse-momentum spectra. The p_t -integrated rapidity spectrum was extracted in a p_t -range of [0.,1.5] GeV, only the last bin [4.7,4.9] had a reduced p_t -range of [0.,1.2] GeV because of the smaller acceptance. The large p_t -range contains 99.1 % of all $K^*(892)$ ($T = 160$ MeV).

Mass and width of $K^*(892)$ and contribution of $K_2^*(1430)$

In the context of the ϕ -meson it was already discussed that parameters for mass and width can be adjusted separately. The case is slightly different here, because the $K^*(892)$ has a much larger intrinsic width than the ϕ -meson, $\Gamma_0 = 50.5$ MeV. No effect is expected from an additional 1 MeV-broadening of the invariant-mass distribution due to detector resolution. Indeed, figure C.10 (appendix C) shows that a change in the width of the Gaussian broadening of the mass distribution neither influences the quality of the fit nor the yield of the $K^*(892)$. For consistency with the extraction of the ϕ -meson, a Gaussian broadening with $\sigma_m = 0.87$ MeV is used.

The mass is derived following the same strategy as for the ϕ -meson: the $K^*(892)$ is extracted in a region with good acceptance, and simulated invariant-mass distributions with different assumptions about the mass are fitted to the data. From curvature and minimum of the resulting χ^2/n distribution, the mass of the

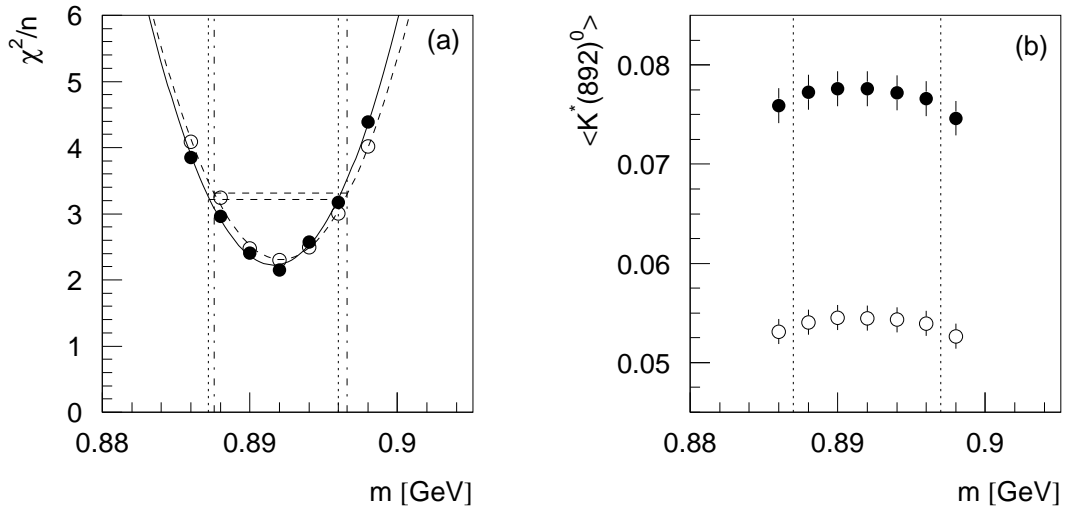


Figure 5.17: χ^2/n in dependence on the mass for $\sigma_m = 0.87$ MeV, chosen in consistency to the analysis of the ϕ -meson, and $\Gamma = 50.0$ MeV (a). In (b) the corresponding yield is shown which is rather independent on the mass. Within the vertical dotted error margins as obtained from (a) a variation of 2 % is observed. Full symbols present results for $K^*(892)^0$, open ones for $\bar{K}^*(892)^0$. A parabola fitted to (a) yields a mass of (891.6 ± 4.0) MeV for $K^*(892)^0$, and (892.1 ± 4.5) MeV for $\bar{K}^*(892)^0$. The horizontal dashed lines indicate $(\chi^2/n)_{min}+1$ from which the error margins are extracted and drawn as dotted and dashed-dotted lines.

$K^*(892)$ and its uncertainty can be determined (see fig. 5.17). The extracted mass of both, $K^*(892)^0$ and $\bar{K}^*(892)^0$, is basically the same and can be combined to

$$m_0 = (892 \pm 5) \text{ MeV}.$$

This mass is consistent with $m_0 = (896.1 \pm 0.28)$ MeV [2].

In chapter 3.2.2 the influence of higher K^* resonances on the $K^\pm\pi^\mp$ invariant-

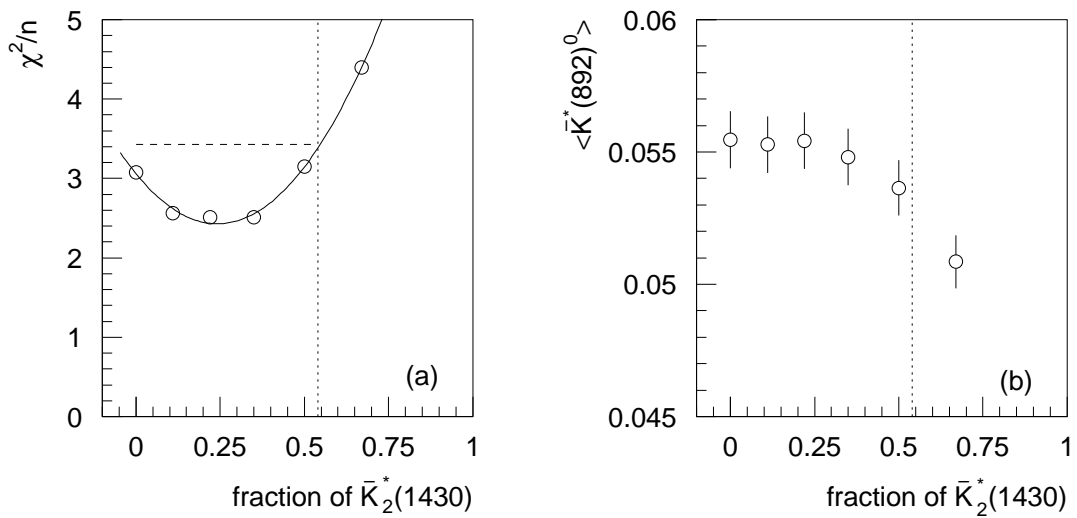


Figure 5.18: χ^2/n in dependence on the fraction of $\bar{K}_2^*(1430)$ compared to $\bar{K}^*(892)^0$. The minimum of the parabola gives a fraction of 1 : 0.24, or 4.2 : 1, for $\bar{K}^*(892)^0$: $\bar{K}_2^*(1430)$.

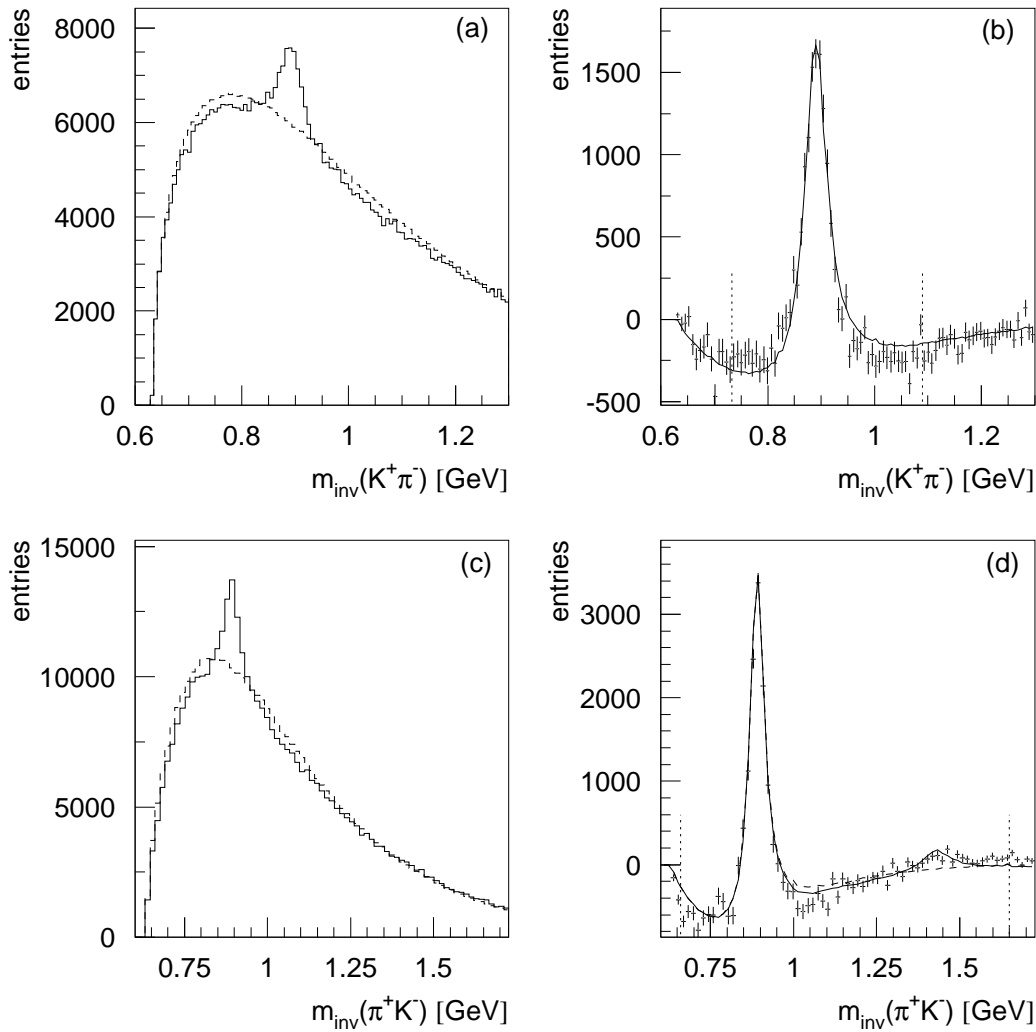


Figure 5.19: Invariant-mass distribution of the $K^*(892)^0$ in a rapidity range of $[3.5,5]$ and a p_t -range of $[0,1]$ GeV (a-b). The dashed line represents the event-mix background which is subtracted in (b). Here, the dotted lines give the fit-range for the simulated signal (full line). In (c) and (d) the same is presented for the $\overline{K}^*(892)^0$, but in a rapidity range of $[3.1,4.7]$, a p_t -range of $[0,1.5]$ GeV, and a larger range in mass such that the indication of the $K_2^*(1430)$ can also be seen. The dashed line in (d) shows a fit without inclusion of the $K_2^*(1430)$, the full line with.

mass spectrum was discussed. It was shown, that the $K_2^*(1430)$ is expected to appear as a broad peak in the spectrum. The yield of $K_2^*(1430)$ was estimated assuming an exponential decrease of the yield with the mass of the resonance; a ratio of 4 : 1 was obtained. In detail, this assumption can be checked in the same way as the mass was extracted (fig. 5.18). The result of 4.2 : 1 (or 3.7 : 1 depending on the presentation of the fraction) is close to what is expected from the exponential decrease of yields and agrees well with estimations from other experiments [80, 81, 103]. However, the uncertainty of this result is large, since the peak of the $K_2^*(1430)$ is not well developed in the experimental invariant-mass spectra (see fig. 5.16, and 5.19). The measured yield of $K^*(892)$ depends only weakly on assumptions about the $K_2^*(1430)$.

Even for a rather large ratio of 2 : 1, the extracted multiplicity of the $K^*(892)^0$ drops by about 3-4 % only. Invariant-mass spectra for $K^*(892)^0$ and $\bar{K}^*(892)^0$ with the best fit are presented in figure 5.19. The extracted parameters will be used in the following to measure the kinematic distributions of the $K^*(892)^0$.

Transverse-momentum distribution

Transverse-momentum and transverse-mass distributions for both, $K^*(892)^0$ and $\bar{K}^*(892)^0$ are presented in figure 5.20. The quoted errors are statistical.

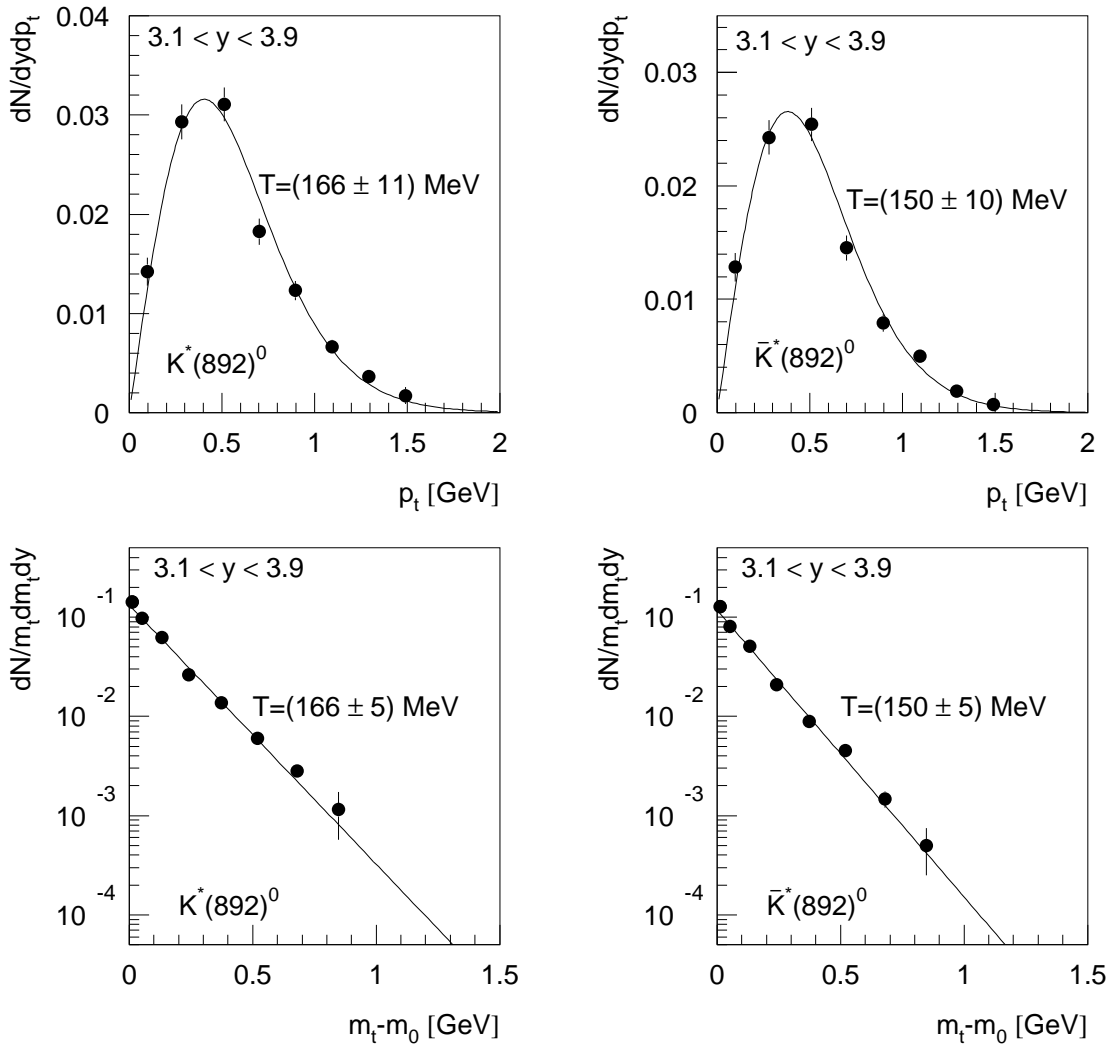


Figure 5.20: Transverse-momentum and transverse-mass spectrum of $K^*(892)^0$ (upper row) and $\bar{K}^*(892)^0$ (lower row) in minimum-bias p+p collisions. Lines correspond to thermal functions (equation 3.7, 3.8) with the indicated temperature.

Rapidity distribution and integrated yield

Rapidity distributions integrated over p_t are presented in figure 5.21. For integration a p_t -distribution with mean temperatures as shown in fig. 5.20 is used for the full y -range, but due to the large p_t -intervall chosen the extrapolation is small (1 %). From the error bars and scatter of yields one already gets an impression that the yield at midrapidity is more difficult to extract and has a larger systematic error than those at large rapidity. The total yield is extracted by fitting a Gaussian distribution, the quoted error is statistical.

Final results with systematic errors as determined in the next paragraph are summarized in table 5.4.

	$K^*(892)^0$	$\bar{K}^*(892)^0$
m_0	(892 ± 5) MeV	(892 ± 5) MeV
Γ_0	50.5 MeV (fixed)	50.5 MeV (fixed)
σ_m	0.87 MeV (fixed)	0.87 MeV (fixed)
T	$(166 \pm 11 \pm 10)$ MeV	$(150 \pm 10 \pm 10)$ MeV
σ_y	$1.17 \pm 0.03 \pm 0.07$	$1.01 \pm 0.02 \pm 0.06$
$\langle K^*(892) \rangle$	$0.0792 \pm 0.0016 \pm 0.0063$	$0.0559 \pm 0.0011 \pm 0.0045$
$\frac{dN}{dy} \Big _{y_{CMS}}$	$0.0275 \pm 0.0033 \pm 0.003$	$0.0196 \pm 0.0029 \pm 0.002$

Table 5.4: Summary of results for $K^*(892)^0$ and $\bar{K}^*(892)^0$ in minimum-bias p+p collisions. The first error quoted is statistical, the second systematic. For midrapidity values the mean of the first two bins is taken ($2.9 < y < 3.3$).

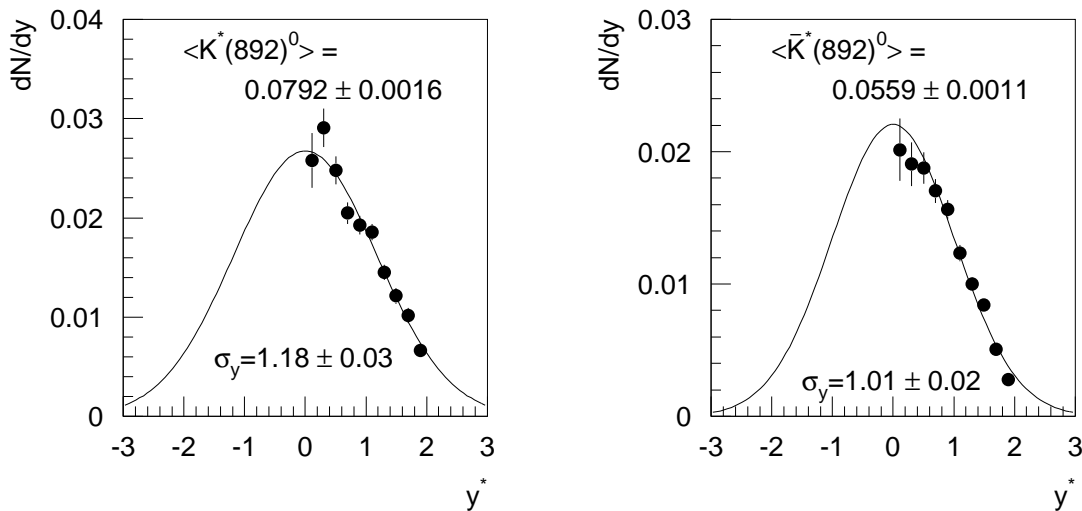


Figure 5.21: Rapidity distribution of $K^*(892)^0$ (a) and $\bar{K}^*(892)^0$ (b) in minimum-bias p+p collisions. The distribution is fitted by a Gaussian, the quoted error is statistical. The full yield is obtained by integrating the Gaussian.

Systematic errors

As for the ϕ -meson a first check of the extracted kinematic distributions and the full yield consists of the comparison of multiplicities obtained from the integration of p_t and y -distributions, and from a fit to the invariant-mass signal in the full acceptance. Within 5 % the results agree. The p_t -range used for the p_t -integrated rapidity spectrum is large, thus the error on the extrapolation factor has a negligible influence. As investigated above, the uncertainty in the mass of the $K^*(892)$ influences the yield by 2 % only.

More important for systematic errors is the influence of track cuts chosen for the extraction of the invariant-mass distributions (see the previous section with the ϕ -meson analysis for a more detailed discussion). They are systematically varied, results are shown in figures 5.22 and 5.23 for the $K^*(892)^0$ as example. The case is similar if not slightly better for the $\bar{K}^*(892)^0$. From the scatter of values for T , σ_y and $\langle K^*(892) \rangle$ a lower border of the systematic error is estimated. Since the various systematic errors can add in principle a larger error of 8 % is assigned to total yields.

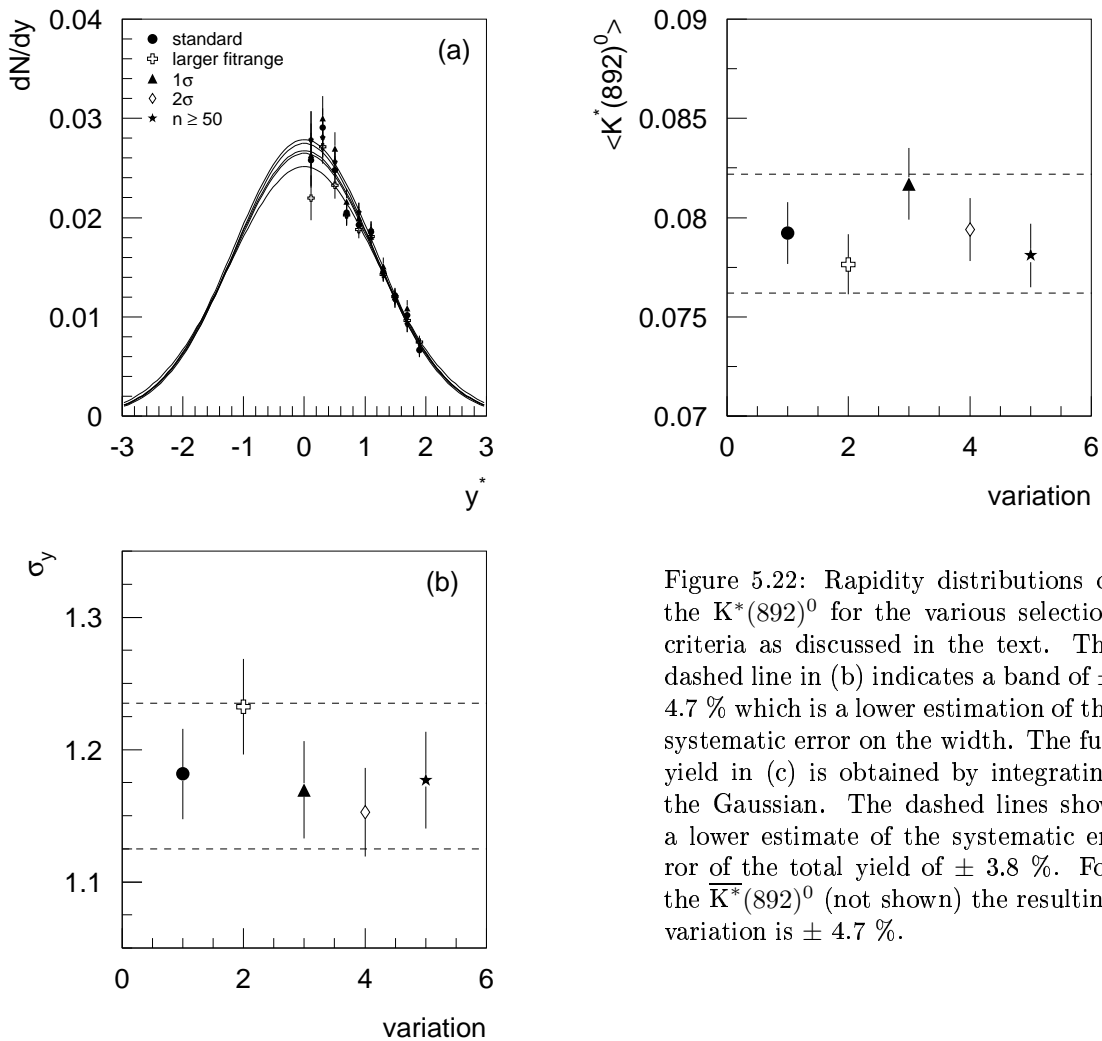


Figure 5.22: Rapidity distributions of the $K^*(892)^0$ for the various selection criteria as discussed in the text. The dashed line in (b) indicates a band of $\pm 4.7\%$ which is a lower estimation of the systematic error on the width. The full yield in (c) is obtained by integrating the Gaussian. The dashed lines show a lower estimate of the systematic error of the total yield of $\pm 3.8\%$. For the $\bar{K}^*(892)^0$ (not shown) the resulting variation is $\pm 4.7\%$.

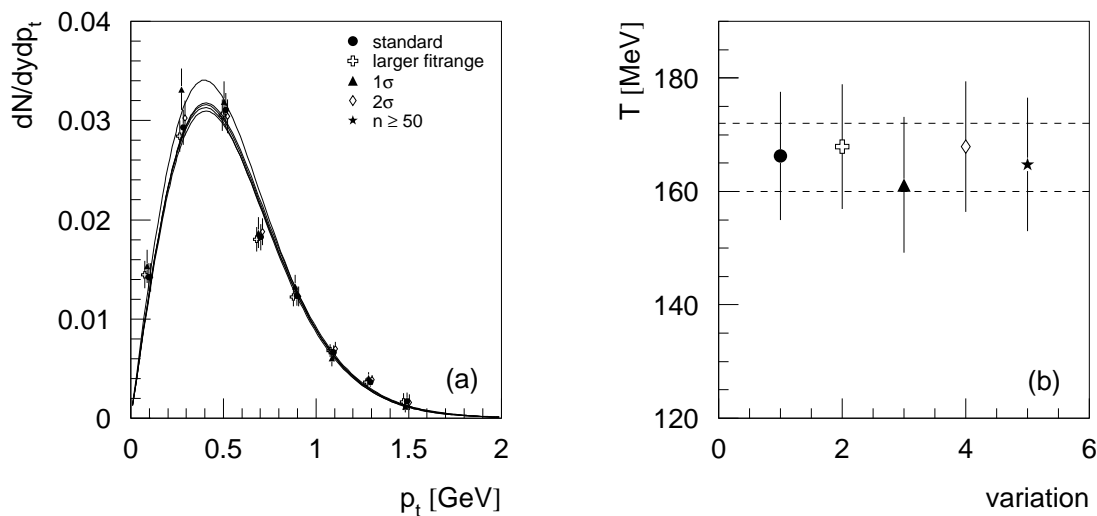


Figure 5.23: Transverse-momentum distributions for the various selection criteria as discussed in the text (a), here presented for $K^*(892)^0$. In (b) the same symbols are chosen to present the extracted temperatures. They all vary within the statistical error of the fit. A lower limit for a systematic uncertainty can be estimated, (166 ± 6) MeV are represented by the dashed line.

5.1.5 Summary of minimum-bias results and comparison to other experiments

Particle production in p+p collisions has been studied over a broad range of energies for several decades. Therefore many data exist to which the NA49 results can be compared. Since the focus of this work lies in the systematic investigation of strangeness production, minimum-bias p+p yields are mainly needed as reference data. Thus only a brief comparison of total yields with those from literature will be given, leaving aside most details of the kinematic distributions (see appendix C for a few comparisons of kinematic distributions with some from literature). However, the validity of the m_t -scaling in p+p collisions (see e.g. [3, 104]) should be mentioned: all transverse-momentum spectra can be described by a thermal function with a parameter T of about 160 MeV. Also, as expected, the width of the rapidity distribution of $K^*(892)^0$ and $\bar{K}^*(892)^0$ is similar to the one of K^+ and K^- , respectively. Both times, kaons show broader distributions than their antiparticles probably due to their associated production with Λ -baryons.

In figure 5.24 a comparison of NA49 minimum-bias yields to results from other experiments is presented. An overall good agreement is found.

For the comparison of pions to negatively charged hadrons in p+p and n+n interactions [106] the contribution of K^- and antiprotons ($\sim 5-6\%$) has to be taken into account (not included in pion yields from this work shown in fig. 5.24). The parametrization for pions from Rossi et al. [105] (line in figure) provides therefore slightly smaller values compared to the presented data points. By isospin invariance the π^- (h^-) multiplicity in n+n collisions should be the same as the π^+ (h^+) multiplicity in p+p [106]. Some direct measurements of pions [82, 107] are also included in

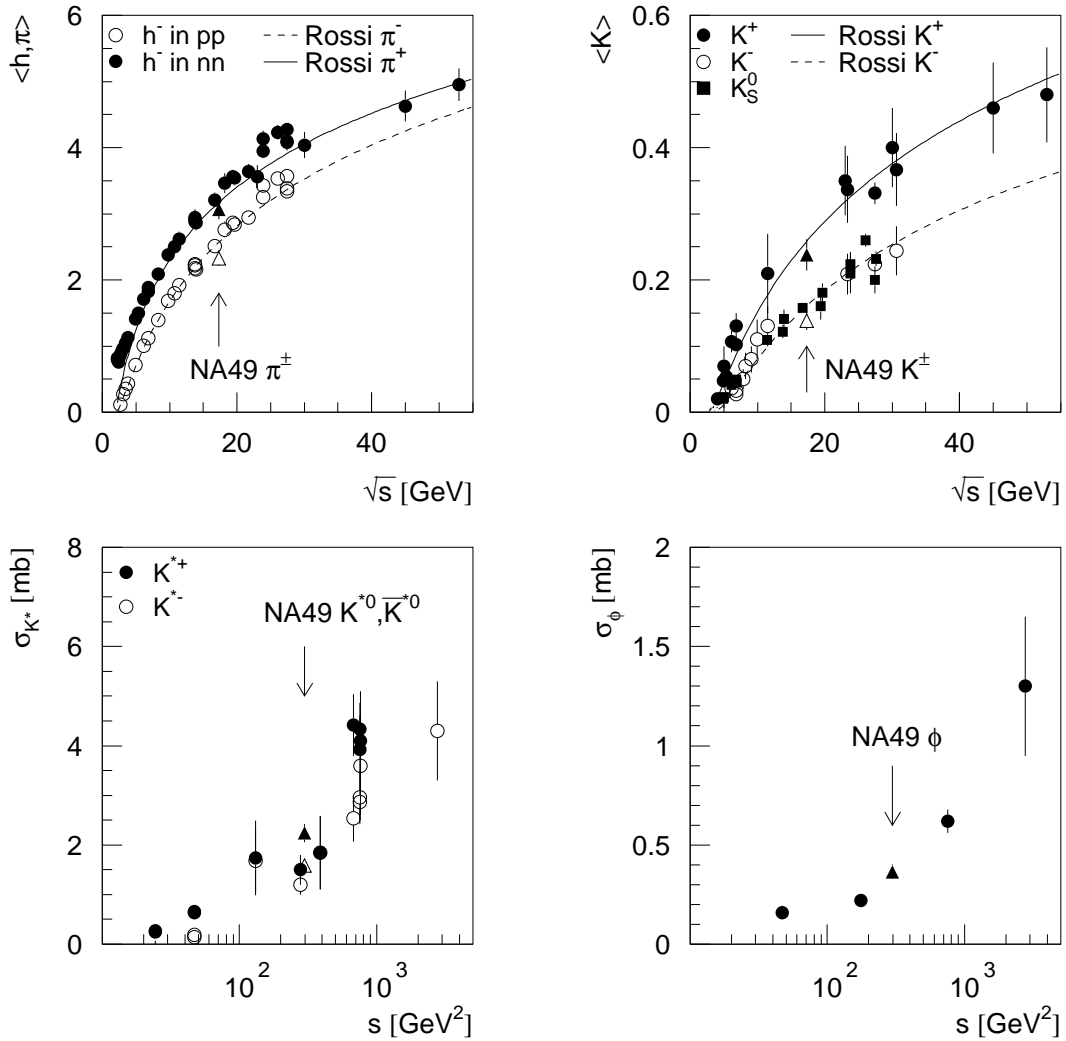


Figure 5.24: Yields or invariant cross sections of π , K , $K^*(892)$ and ϕ -mesons in minimum-bias p+p collisions in dependence on energy. π and K from NA49 (triangles) are presented within the minimum-bias trigger. Note, that π^- are compared with h^- in the figure, i.e. K^- and \bar{p} should be added (not done) which would increase the pion yields by about 5-7 %. Parametrizations from Rossi et al. [105] are included for comparison. Cross sections of $K^*(892)$ and the ϕ -meson are derived by multiplying the minimum-bias yield with the NA49 trigger cross section of 28.31 mb.

the figure (data points with error bars). Data for kaons are taken from [82, 107, 108]. For both, kaons and pions, a second analysis of the NA49 p+p data exists being consistent with the results of this work [12, 109]. A comparison of rapidity distributions can be found in appendix C. Also for $K^*(892)$ and the ϕ -meson other measurements are available in NA49 [101, 110, 111] to which the results of this work agree well¹.

Comparing total yields with literature shows a good agreement for $K^*(892)$ [80, 81, 82, 103, 112, 113, 114, 115, 116] and the ϕ -meson [80, 82, 117, 118]². The

¹In [111] yields for the $K^*(892)^0$ differ by a factor of two because erroneously a branching ratio of only $\frac{1}{3}$ was used there.

²The ϕ -meson was also measured in detail in pBe interactions [119, 120, 121]. Because of

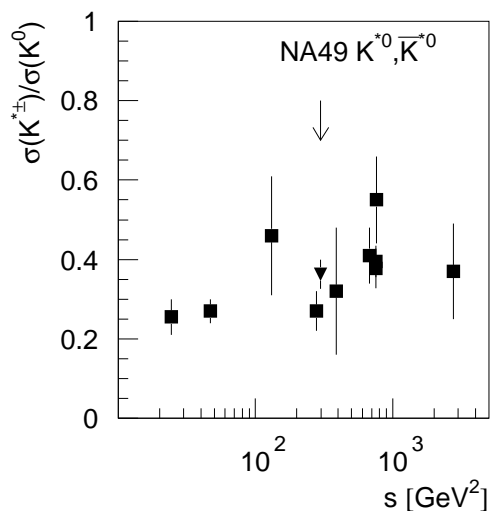


Figure 5.25: Ratio of $(K^*(892) + \bar{K}^*(892))$ to $(K+\bar{K})$ in dependence on energy; data are from [80, 81, 82, 103, 113, 114, 115, 116]. Mostly $K^{*\pm}$ and K_S^0 are available from experiments. NA49 and Drijard et al. [80] measure the $\bar{K}^*(892)^0$. The LEBC-EHS experiment [82] even all four types of $K^*(892)$ as well as charged kaons which can be used for normalization. For NA49, (K^++K^-) are taken for the denominator, in Drijard et al. [80] ($\sqrt{s}=52.5$ GeV) the $\bar{K}^*(892)^0$ is divided by K_S^0 .

presented cross-sections are derived by multiplying the minimum-bias multiplicities with the trigger cross-section, i. e. in this comparison it is assumed that no $K^*(892)$ and ϕ -mesons are produced in the missing 4.2 mb diffractive scattering events (see discussion below). However, the scatter of measurements is large, and especially for the ϕ -meson only a few results exist for comparison. A variation of 10 % would make no difference in the overall picture.

Most experiments measuring the $K^*(892)$ also studied K_S^0 , the fraction of both is rather constant in dependence on energy (fig. 5.25). Multiplying the presented ratio with the branching fraction of $K^{*\pm}$ to K^0 , or K^{*0} to K^\pm , which is $\frac{2}{3}$ for both cases, provides the fraction of K^0 , or K^\pm , stemming from the decay of their higher excited state, which gives about 25 % of all kaons. Performing the same exercise for the ϕ -meson, results in a fraction of 3 % of K^+ and 5 % of K^- stemming from a ϕ -decay at 17.3 GeV center-of-mass energy. New results at the threshold for ϕ production show that at very low energies ($^{58}\text{Ni}+^{58}\text{Ni}$ collisions at 1.93 AGeV) at least 20 % of all K^- mesons are a decay product of the ϕ -meson [123].

However, there are total scaling uncertainties of the NA49 minimum-bias yields. As discussed in section 4.1 the NA49 minimum-bias trigger covers only 27.4 mb of the nominally 31.6 mb inelastic cross section. 4.2 mb presumably mostly diffractive events are rejected by the trigger, whereas 1.1 mb elastic interactions are included. If none of the particles under study were produced in these 4.2 mb diffractive scattering events, all experimental multiplicities for particle production would have to be rescaled by $0.896 = \frac{28.31\text{mb}}{31.6\text{mb}}$. In particular for pions this assumption would not be true. The statistical error of this scaling factor is small ($< 1\%$), but at least 5 % total scaling uncertainty are realistic [124]. Because of these ambiguities only results for the minimum-bias trigger condition of NA49 are presented.

Another systematic uncertainty for total yields stems from the corrections ap-

scaling uncertainties to pp these measurements are not included in the comparison. Two further measurements of the ϕ meson in pp collisions are mentioned in [122], but were not published. However, they all would fit into the presented energy dependence.

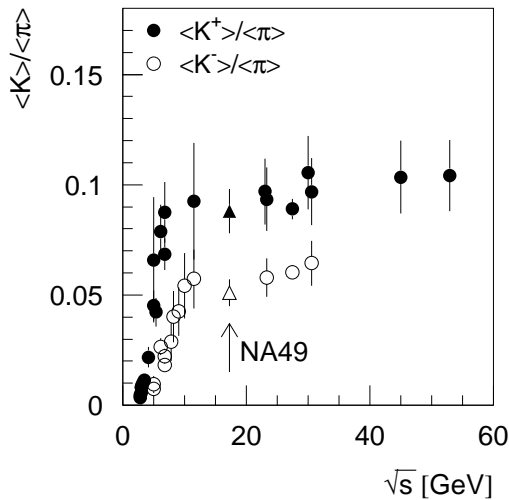


Figure 5.26: $\langle K \rangle / \langle \pi \rangle$ ratio in dependence on energy, data to which the measurement from this work is compared are from [82, 106, 107, 108]. $\langle \pi \rangle = \frac{1}{2} (\langle \pi^+ \rangle + \langle \pi^- \rangle)$.

plied for vertex reconstruction inefficiencies (see section 4.1.2). Recently, in the course of studies regarding a trigger-bias from the finite size of the S4 detector [89], it was found by eye-scans of single events that many of the interactions corrected for with the factor C0 and/or C2 look quite normal. Further studies are going on [89], but the discussion might show that total scaling uncertainties by at least 5 % are realistic for the presented minimum-bias yields. In addition, all analyzed data are taken with the STD+ configuration of the magnetic field in NA49. For central Pb+Pb events at 158 AGeV it was shown that results for STD+ and STD-configuration agree within 5 %.

The aim of this work is the study of strangeness production comparing p+p and A+A interactions, and also p+p reactions with different inelasticity selection. Therefore, ratios of strange particle yields to pions are of larger importance than total multiplicities. Fig. 5.26 shows that the $\langle K \rangle / \langle \pi \rangle$ ratio is found to agree well to what is known from other experiments.

5.2 Inelasticity-selected p+p events

In chapter 4.2 it was discussed in detail that classes of inelasticity can be defined for minimum-bias p+p collisions, because a certain range of energy is dissipated in the reaction depending on the energy which is lost by the incoming proton. Multiplicity or Feynman-x of the fastest proton in the event serve as variables to specify these classes in which yields of pions, kaons, the ϕ meson, $K^*(892)^0$ and $\bar{K}^*(892)^0$ are extracted in this section. Both, the observation of particle yields and the definition of inelasticity classes are based on measurements in the forward hemisphere of the collision. However, the results are representative for particle production in dependence on the available energy (see discussion in 4.2).

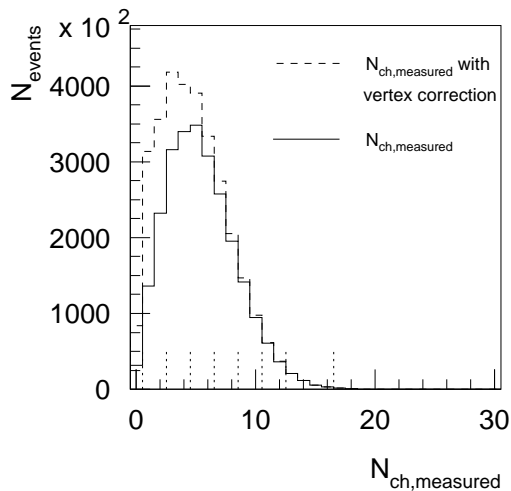


Figure 5.27: Multiplicity distribution within the NA49 spectrometer. Only tracks with more than 30 number of points are counted (line), therefore also entries at $N_{ch,measured} = 0$ are found. The same data are presented including corrections for vertex finding inefficiencies (dashed line). The mean number of charged tracks without accounting for the vertex losses is 5.43, with correction 4.54. The vertical dotted lines at the bottom indicate the multiplicity classes used for the analysis.

5.2.1 Multiplicity dependence

Multiplicity classes in minimum-bias p+p interactions are defined on the basis of the number of tracks measured per event (fig. 5.27). For protection against fake or split tracks a weak quality criterium is required, only tracks with more than 30 number of points are counted. As discussed in chapter 4.2, this number cannot be corrected for acceptance losses on an event-by-event basis; on average about 60 % of all charged particles are detected in the spectrometer (fig. 4.8).

Pions and kaons

Subdividing the minimum-bias p+p data into several event classes reduces statistics for each bin significantly, with more severe consequences for the kaon analysis. To partially overcome this problem a looser Φ cut of $|\Phi| \leq 50^\circ$ is applied and yields of kaons are extracted from dE/dx fits with larger bins in p_t ($\Delta p_t = 0.2$ GeV). In addition, the parameters used for the unfolding of the dE/dx distribution are fixed at the values obtained for minimum-bias data. Besides these changes yields are extracted as for minimum-bias data; systematic errors are of the same size.

Results for forward yields in dependence on the multiplicity as measured within the NA49 detector are presented in fig. 5.28. It is found that for pions σ_y decreases with increasing multiplicity from about 1.5 ± 0.02 (1.9 ± 0.03) for π^- (π^+) in the second bin ($3 \leq N_{ch,measured} \leq 4$) to 1 ± 0.02 in the highest bin ($13 \leq N_{ch,measured} \leq 16$). Also, the temperatures decrease with increasing multiplicity, i. e. mean transverse-momenta become smaller. These effects are intuitively clear considering diffractive production of pions and total energy conservation. Comparing results from various experiments, Golokhvastov [85] studied such characteristics of semi-inclusive p+p data at several energies; the results from NA49 are in good agreement. Both effects mentioned are much less pronounced for kaons.

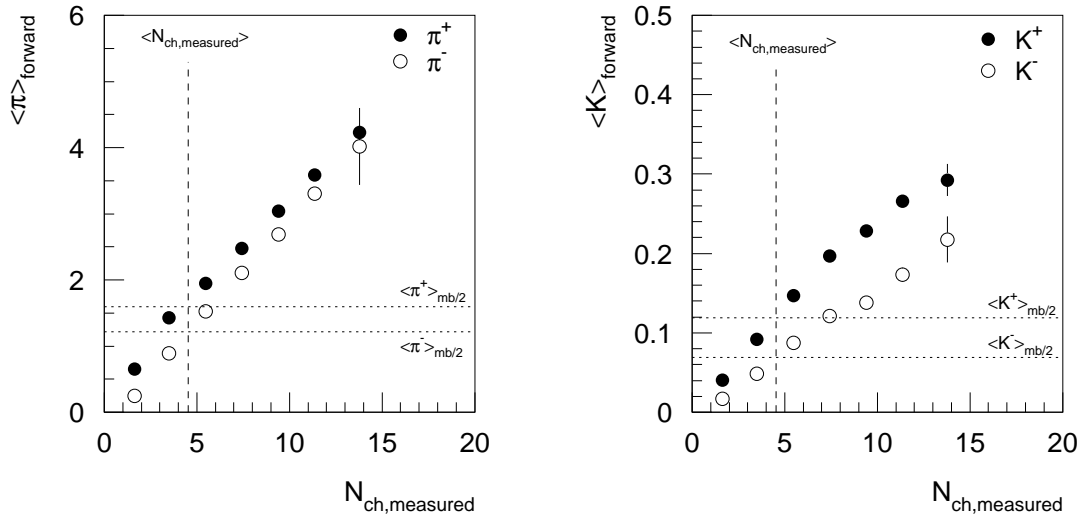


Figure 5.28: Forward yields of charged pions and kaons in dependence on multiplicity as measured in the NA49 detector. Only statistical errors are plotted. The horizontal dotted lines indicate half of the minimum-bias yield, "mb/2", (π not feed-down corrected). The mean value of $N_{\text{ch,measured}}$ in minimum-bias p+p collisions is indicated by the vertical dashed line.

$K^*(892)^0$, $\overline{K}^*(892)^0$ and the ϕ -meson

The analysis for $K^*(892)^0$, $\overline{K}^*(892)^0$ and the ϕ -meson is performed using invariant-mass distributions which are extracted in close to the full acceptance: a rapidity range of [2.9,4.7] for ϕ mesons and of [3.1,4.7] for $K^*(892)^0$ and $\overline{K}^*(892)^0$, and a p_t -range of [0.,1.5] GeV for all the three mesons is used. This procedure provides good signals in spite of the reduced statistics in the event classes. The K^* mesons

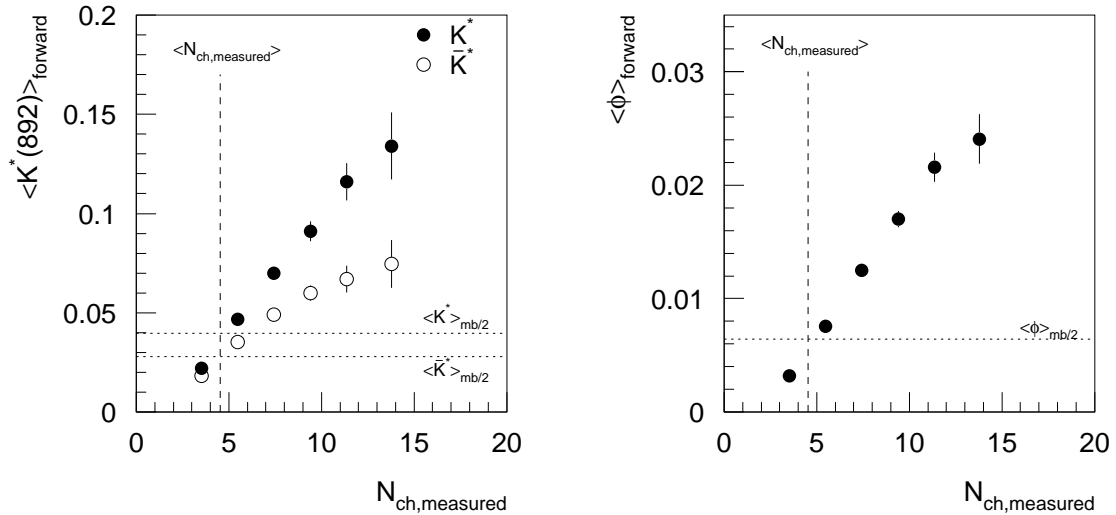


Figure 5.29: Forward yields of $K^*(892)^0$, $\overline{K}^*(892)^0$ and the ϕ -meson in dependence on multiplicity as measured in the NA49 detector. Only statistical errors are plotted. The horizontal dotted line indicates half of the minimum-bias yield, "mb/2". The mean value of $N_{\text{ch,measured}}$ in minimum-bias p+p collisions is indicated by the vertical dashed line.

ϕ			$K^*(892)$		
σ_y	T [MeV]	\overline{acc}	σ_y	T [MeV]	\overline{acc}
0.8	166	0.7409	0.8	166	0.4530
0.9	166	0.7320	0.9	166	0.4654
0.95	166	0.7253	1.0	166	0.4692
1.0	166	0.7172	1.1	166	0.4665
1.1	166	0.6981	1.2	166	0.4593
			1.3	166	0.4493
			1.4	166	0.4374
0.95	120	0.7379	1.2	120	0.4638
0.95	140	0.7341	1.2	140	0.4626
0.95	160	0.7253	1.2	160	0.4603
0.95	180	0.7180	1.2	180	0.4568
0.95	200	0.7074	1.2	200	0.4521

Table 5.5: Mean acceptance \overline{acc} of ϕ -mesons and $K^*(892)$ in the forward hemisphere in dependence on the kinematic distributions expressed by the parameters σ_y and T . The acceptance for ϕ -mesons is extracted in a rapidity range of [2.9,4.7] and a p_t -range of [0.,1.5] GeV. The acceptance for $K^*(892)$ is calculated for a rapidity range of [3.1,4.7] and a p_t -range of [0.,1.5] GeV. In both cases $n_{points} \geq 30$, a momentum range of $0.6 < \log_{10}(p) \leq 1.7$ and $0 \text{ GeV} < p_t \leq 1.5 \text{ GeV}$ is required for charged kaons and pions.

were extracted in a rapidity range starting slightly above midrapidity because of the steeply falling acceptance at midrapidity. This problem was already discussed for the extraction of minimum-bias yields. Further track quality cuts are used as for the p+p minimum-bias analysis.

It was shown in the previous section that yields calculated from the full signal are consistent with those determined in kinematic bins with integration afterwards. Systematic errors of the two methods are of the same order. As for the minimum-bias analysis, mean values from two methods of background subtraction are taken for the ϕ -meson. For K^* no additional treatment of the background is needed. The simulation for extracting yields was performed with parameters σ_y and T for the kinematic distributions as observed in minimum-bias p+p collisions.

A new source of uncertainty is introduced by the use of kinematic distributions from minimum-bias p+p in the simulation: As discussed in the previous subsection for pions, σ_y and T might vary with multiplicity also here. However, for kaons the variation is already much smaller than for pions and might even be less for $K^*(892)$ and ϕ . In order to study the influence of these uncertainties, the mean acceptance for $K^*(892)$ and ϕ -mesons in a certain (y, p_t) range in the forward hemisphere was calculated with different assumptions for σ_y and T (see table 5.5). For both, ϕ -mesons and the $K^*(892)^0$ (and thus also for the $\overline{K^*(892)^0}$), the variation is about 3-5 % only.

Figure 5.29 presents results of $K^*(892)^0$, $\overline{K^*(892)^0}$ and ϕ -mesons in dependence on multiplicity as measured in the NA49 detector. As for pions and kaons the minimum-bias yield at the measured mean charged-particle multiplicity fits well into the systematics.

5.2.2 Correlation between yields and Feynman-x of the leading proton

Leading protons are selected as introduced in chapter 4.2. Very unfortunate is the strong reduction of the number of events per inelasticity class due to the quality and selection criteria required. This significantly increases statistical and systematic errors. The effect of varying the selection criteria of the leading proton is studied for $\overline{K}^*(892)^0$ and the ϕ -meson for example, because the leading proton selection does not bias their extraction from the invariant-mass spectra.

Pions and kaons

Besides statistics another intrinsic problem arises for the extraction of K^+ : since the leading proton is selected by a window in dE/dx , resulting spectra in the corresponding momentum regions are strongly biased (two extreme examples can be found in fig. 5.30). Fitting the spectra only up to the mean position of protons, excluding bins where such a fit is not reasonable, or just skipping these bins (if it does not restrict the available phase space for K^+ extraction too much) allows to deal with this problem.

In fact, more problematic is the small number of events per inelasticity class. The phase space covered by reasonable dE/dx fits with the same procedure as for multiplicity classes (looser Φ -cut, fixing width and position in dE/dx at the minimum-bias values, $\Delta p_t = 0.2$ GeV) is too small for the usual procedure of measuring yields: the extraction of p_t -spectra in rapidity bins, thermal fits, an extrapolation to the full p_t -range and the derivation of rapidity spectra. Only, if allowing right-side and wrong-side tracks as well as all azimuthal angles Φ , this procedure is feasible. The observed inelasticity-dependence of mean transverse-momenta and of

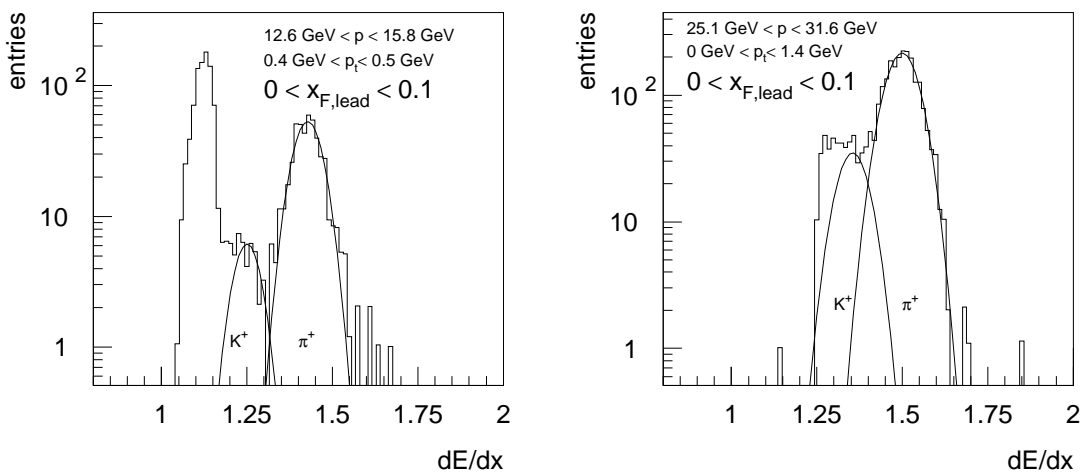


Figure 5.30: Examples for two extreme cases of biased dE/dx spectra due to the selection of leading protons are presented; either the fraction of protons below their mean dE/dx position is strongly enhanced (left) or none are left (right).

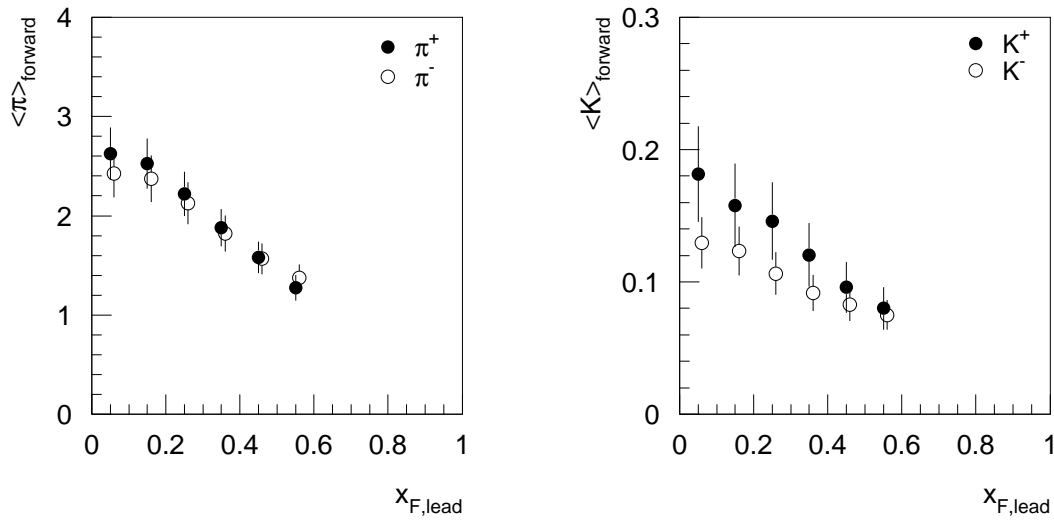


Figure 5.31: Forward yields of charged pions and kaons in dependence on Feynman- x of the leading proton. Since statistical errors are smaller than the symbol size due to their importance systematic errors are shown here. For better visibility negative particles are slightly shifted in x_F .

the width of the rapidity distribution is much weaker compared to their dependence on multiplicity bins. Apparently the multiplicity is the critical factor in this context.

On the other hand, p_t -integrated dE/dx spectra (0 GeV to 1.4 GeV) with stronger quality criteria ($n_{points} \geq 30$, $|\Phi| \leq 50^\circ$, right-side tracks) can be used to extract yields in bins of total momentum p . Width and position in dE/dx are

σ_y	T [MeV]	$\overline{acc} (\pi^+)$	$\overline{acc} (K^-)$
0.8	165		0.354
0.9	165		0.342
1.0	165	0.2242	0.329
1.1	165	0.2261	0.317
1.2	165	0.226	0.305
1.3	165	0.225	0.294
1.4	165	0.223	0.283
1.5	165	0.220	0.272
1.6	165	0.217	
2.0	165	0.199	
1.00	150		0.325
1.00	160		0.328
1.00	170		0.330
1.00	200		0.336
1.45	150	0.215	
1.45	160	0.219	
1.45	170	0.223	
1.45	180	0.227	
1.45	200	0.234	

Table 5.6: Mean acceptance of, e.g., π^+ and K^- in $0.6 \leq \log_{10}(p) < 1.7$ and $0 \text{ GeV} \leq p_t < 1.4 \text{ GeV}$ for an extrapolation to the forward hemisphere in dependence on kinematic distributions expressed by the parameters σ_y and T . Acceptances are calculated for $n_{points} \geq 30$, $|\Phi| \leq 50^\circ$ and right-side tracks only.

fixed at the minimum-bias values. These bins are summed in a p -range depending on available good quality fits, i.e. from $\log_{10}(p) = 0.6$ to 1.2, 1.5, or 1.7. This way, also a few pions and kaons from the backward hemisphere are included in the measurement (see, e.g. acceptance plots 3.6, 3.7). Yields are extrapolated to a full yield for the forward hemisphere assuming kinematic distributions as observed for minimum-bias p+p data (tab. 5.6). The uncertainty introduced by this assumption is again checked by varying σ_y and T . Taking into account, that the kinematic distributions change less than in multiplicity classes, uncertainties of 5-10 % are the result.

For results of pion and kaon yields in bins of Feynman- x of the leading proton as presented in fig. 5.31, the average of both extraction procedures is taken. Estimates of systematic errors for pions are 10 %, for K^- 15 % and for K^+ 20 %.

$K^*(892)^0$, $\bar{K}^*(892)^0$ and the ϕ -meson

Yields for $K^*(892)^0$, $\bar{K}^*(892)^0$ and the ϕ -meson were extracted as for the multiplicity classes. Results are presented in fig. 5.32, systematic uncertainties for extracting yields from spectra over the full acceptance were already discussed for the multiplicity bins and are the same here.

Since invariant-mass distributions are easier to handle also for small statistics and are free of bias problems as they appear for the dE/dx spectra, the influence of different selection criteria of leading protons on the yields of $\bar{K}^*(892)^0$ and ϕ -mesons is investigated (fig. 5.33). "Standard" corresponds to the method introduced in chapter 4.2.2. Not excluding neutrals with $x_F < 0.2$, which was introduced not to use K_L^0 as veto, does not change the yield (not shown). But loosening the high quality criteria by allowing also protons and neutrons identified by the VCHAM and RCAL setup as leading protons weakens the observed correlation ("p,n in V+R").

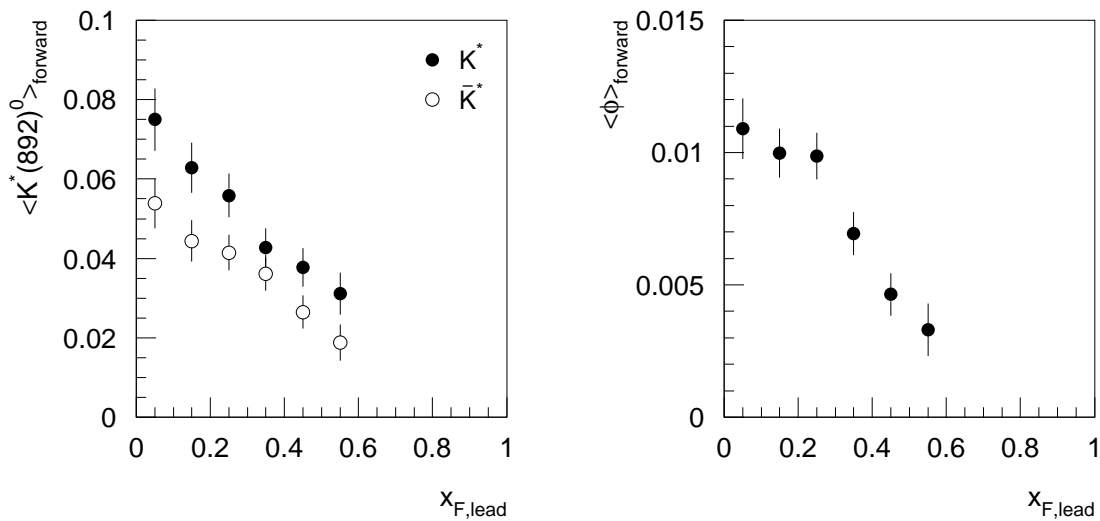


Figure 5.32: Forward yields of $K^*(892)^0$, $\bar{K}^*(892)^0$ and the ϕ meson in dependence on Feynman- x of the leading proton. Quoted errors are statistical only.

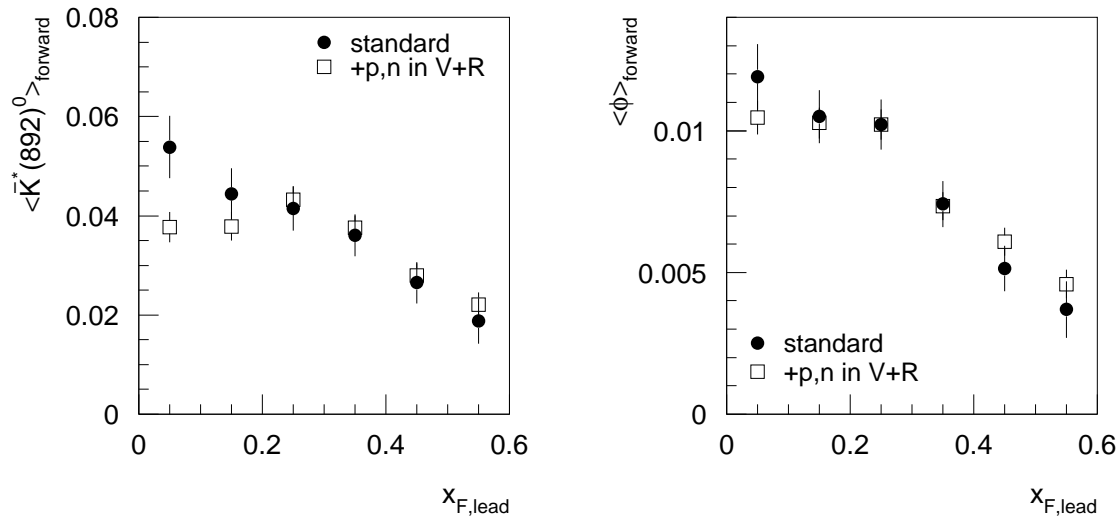


Figure 5.33: Forward yield of the $\bar{K}^*(892)^0$ and the ϕ -meson with two different selection methods of the leading baryon. Full circles correspond to the standard method, open boxes to loose selection criteria (see text). In "+p,n in V+R" especially the energy resolution of the chosen leading baryons is weaker compared to the standard method and, indeed, a flattening of the correlation is observed.

This effect can be understood as resulting from the bad energy resolution of the ring calorimeter which, to a certain extent, washes out the energy loss differences of the Feynman-x bins.

5.2.3 Discussion of results and comparison to FRITIOF simulations

Kaons are the most abundant strangeness-carrying mesons produced. Their behavior in relation to pions is therefore representative for the relative strangeness content in the final state of a collision. Fig. 5.34 and 5.35 summarize the experimental results obtained for p+p collisions at 158 GeV in dependence on the two inelasticity measures used: the charged-particle multiplicity and the Feynman-x of the leading proton. The experimentally accessible range for $x_F^{\text{leading proton}}$ is from 0 to 0.6 only, however, this is the range of interest for a comparison of ratios to A+A: In minimum-bias p+p the mean Feynman-x of protons is about 0.5, it is shifted to smaller values in A+A due to the increased stopping of nucleons. In the figures included are also the data for the strangeness-carrying resonances $K^*(892)$ and ϕ . Recall that all quantities refer to the forward hemisphere in the center of mass of the collision.

The general conclusion from both figures is, that there is little variation of the relative strangeness content in p+p interactions in dependence on the inelasticity of the collision. This statement is mainly based on the rather constant $\langle K \rangle / \langle \pi \rangle$ ratio. However, relative $K^*(892)$ and ϕ -production show an increase for higher inelasticity with a saturation at or close to the minimum-bias value; this will be explained as a threshold effect in the discussion below.

A good agreement of these results and previous investigations of particle production in dependence on multiplicity is found. In particular the $\langle K_S^0 \rangle / \langle \pi^0 \rangle$ ratio and Λ -production were studied before, an almost complete summary of experimental results in p+p collisions at various energies was performed by Whitmore [125] (see also references therein). For lower energies, a decrease of Λ -yield and $\langle K_S^0 \rangle / \langle \pi^0 \rangle$ ratio with multiplicity was observed, for higher energies similar to the one of NA49, Λ -yield and $\langle K_S^0 \rangle / \langle \pi^0 \rangle$ ratio were found to be rather constant over a wide range of multiplicity. As is understandable from energy conservation arguments, at very high multiplicities Λ -yield and ratio drop.

A constant Λ -yield in dependence on multiplicity implies a rather constant yield of K^+ stemming from associated ΛK^+ production. Since the K^+ yield rises with multiplicity, this production channel is in particular important for low multiplicities or very large x_F (> 0.6). The slight increase of the $\langle K^+ \rangle / \langle \pi \rangle$ ratio at low multiplicities might be due to this effect.

The inelasticity dependence observed for the ϕ -meson is in agreement to results from the HELIOS experiment in p+Be interactions at 450 GeV [126, 127]: They measured a linear increase of the $\phi / (\rho + \omega)$ ratio in dependence on the charged-particle multiplicity.

The increase of relative $K^*(892)$, ϕ -meson, and much less pronounced also of K^- production can be interpreted as threshold effect: On the one hand concerning the energy which is needed for the production of the particle under study. This energy can be larger than only the mass of the $K^*(892)$ or ϕ -meson for example, since due to strangeness-conservation further hadrons might be required. This also holds for the K^- . On the other hand there is an intrinsic correlation of the particle yield of interest and the measured charge-particle multiplicity: The observation of a $K^*(892)$ or ϕ -meson requires events with at least 2 charged particles observed in the detector.

Such a threshold effect has been observed in FRITIOF simulations for the same ratios in dependence on the string mass (section 4.2.4, fig. 4.11). In FRITIOF the string mass is the relevant parameter describing the energy available for particle production. It was shown that M_{string} is correlated to $x_F^{\text{leading proton}}$ and N_{ch} , therefore the threshold effect should reflect into the corresponding dependencies of multiplicity and Feynman-x.

In order to investigate if, indeed, the experimental results and the discussed assumptions concerning their interpretation are consistent with the commonly accepted hadronization picture, FRITIOF simulations are used to extract the same ratios also in dependence on $x_F^{\text{leading proton}}$ and N_{ch} (see chapter 4.2). Fig. 5.34 and 5.35 present the results in comparison to data, despite a difference in the total strangeness content qualitative trends agree well.

The overestimation of strange-particle yields is known from inelastic p+p interactions in comparison to minimum-bias p+p data (see table 5.7). This also causes ratios to saturate above the minimum-bias value which is in contrast to data. However, qualitative trends are of interest here, therefore a quantitative difference does not matter. Otherwise rapidity distributions (see appendix C) and p_t -distributions (not

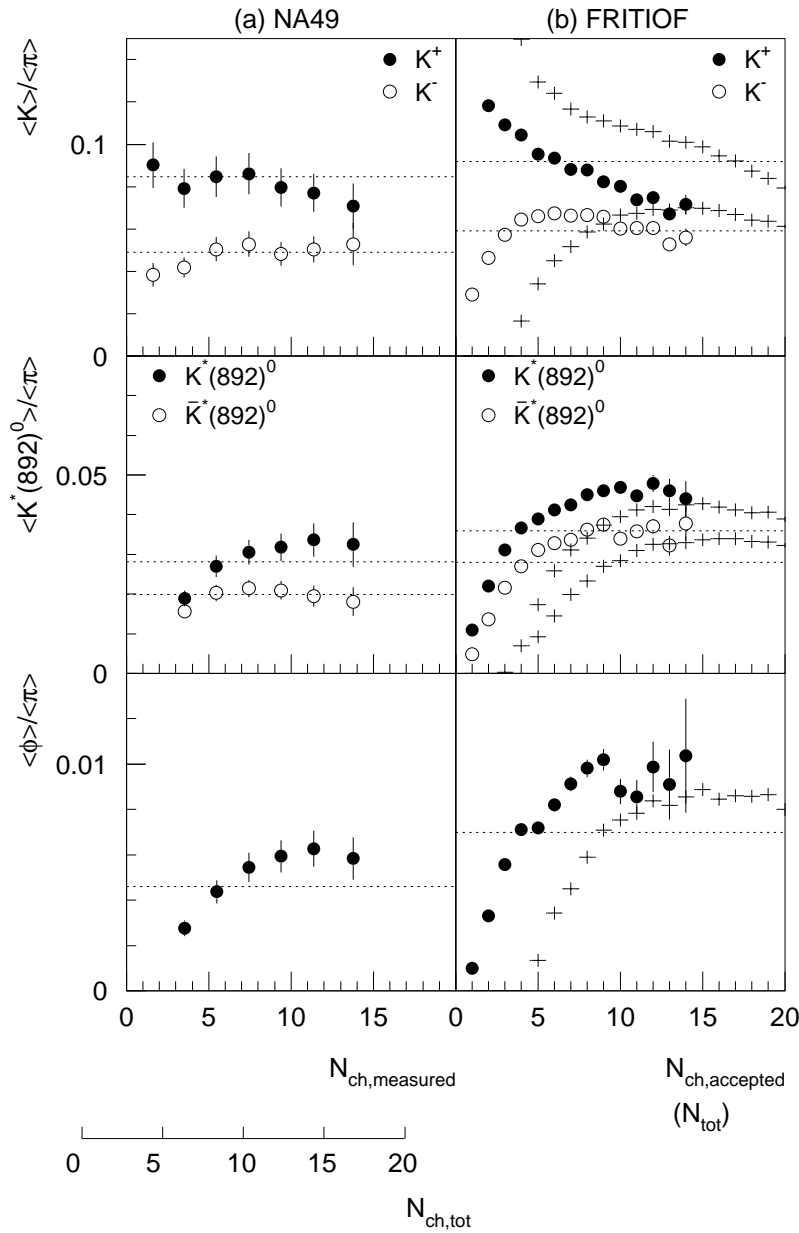


Figure 5.34: Particle ratios versus multiplicity in data (a) and from FRITIOF simulations (b). The second x-axis for data indicates the total charged multiplicity as obtained from FRITIOF simulations (see fig. 4.8). The most violent p+p events are found at large multiplicities. All quantities refer to the forward hemisphere, in the data statistical and systematic errors are added quadratically. For data no feed-down correction for pions is applied, correspondingly in FRITIOF Λ , Σ , their antiparticles and K_S^0 were allowed to decay; detector efficiencies are taken into account. Circles represent simulated data within the restrictions imposed by the NA49 detector setup. The crosses give the ratio of 4π yields in dependence on the total multiplicity. Dotted lines indicate the corresponding ratio in minimum-bias p+p collisions, for both, data and FRITIOF simulations. $\langle \pi \rangle = \frac{1}{2} (\langle \pi^- \rangle + \langle \pi^+ \rangle)$.

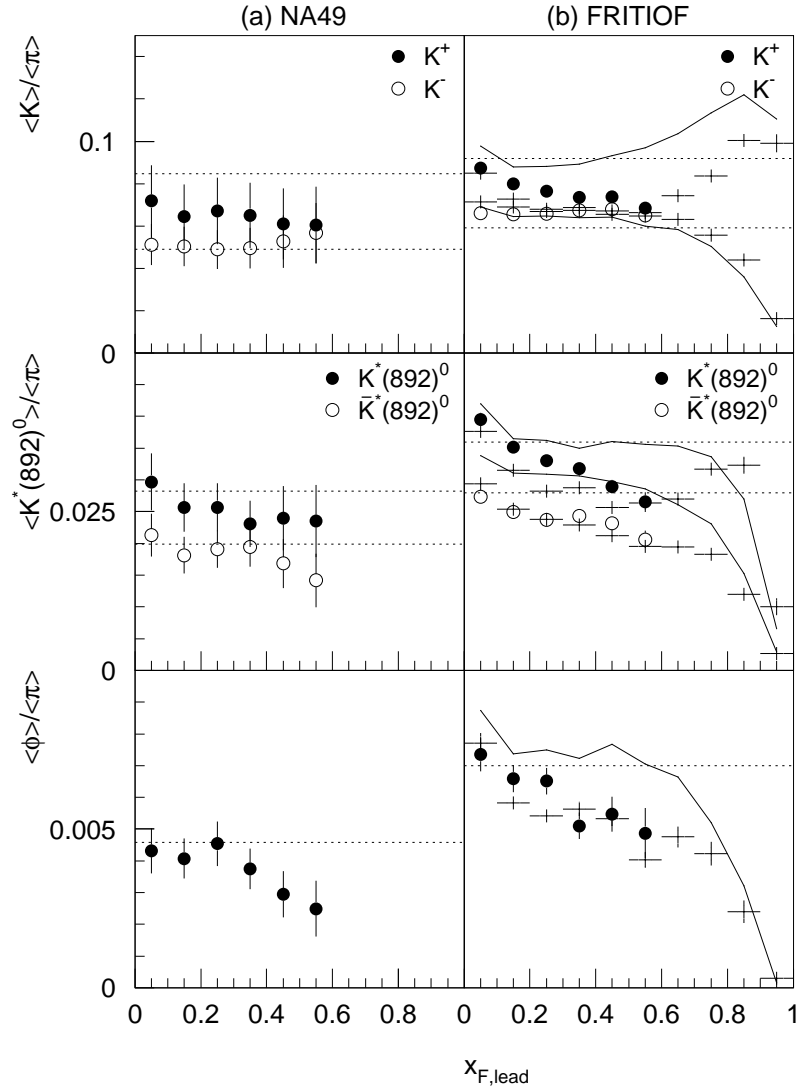


Figure 5.35: Particle ratios versus Feynman- x of the leading baryon in data (a) and from FRITIOF simulations (b). The most violent p+p events are found at small $x_F^{\text{leading proton}}$. All quantities refer to the forward hemisphere, in the data statistical and systematic errors are added quadratically. For data no feed-down correction for pions is applied, correspondingly in FRITIOF Λ, Σ , their antiparticles and K_S^0 were allowed to decay; detector efficiencies are taken into account. Circles represent simulated data within the restrictions imposed by the NA49 detector setup and particle identification capabilities. The crosses show the dependence of ratios in the forward hemisphere depending on the real leading proton, lines in dependence on the leading baryon (p,n, Λ). Dotted lines indicate the corresponding ratio in minimum-bias p+p collisions, for both, data and FRITIOF simulations. $\langle \pi \rangle = \frac{1}{2} (\langle \pi^- \rangle + \langle \pi^+ \rangle)$.

shown) have the same shape in the data and FRITIOF. The different x_F -distribution of protons (see appendix C) does not bias the comparison of inelasticity-dependent p+p interactions, because proton yields are not under study in this work, and for the investigation of particle yields in dependence on $x_F^{\text{leading proton}}$ separate bins are made in x_F and investigated independently.

Obviously, experimental restrictions do not impose a bias on the overall evolution. The threshold effect known from the dependence of particle ratios on M_{string} is also seen in N_{ch} and $x_F^{\text{leading proton}}$. Since the correlation in the experimentally accessible range of NA49 is stronger between M_{string} and N_{ch} , the effect is more pronounced in dependence on N_{ch} . Using the total multiplicity for subdividing p+p events and taking ratios of 4π yields without feed-down from Λ, Σ , their antiparticles, or K_S^0 to pions, the correlation between ratios and multiplicities is only shifted to higher N_{ch} . Also the bias introduced by using protons as leading baryons in the experimentally accessible range does not change the general trend. Only ratios in dependence on the ideal leading baryon are higher in general. The influence of leading Λ -baryons in particular on K^+ is clearly seen. The peak in the $\langle K^+ \rangle / \langle \pi \rangle$ ratio at large x_F , which corresponds also to low multiplicity, results from the discussed associated ΛK^+ pair production.

These results of the FRITIOF simulation support the conclusion from a discussion in section 4.2: Despite the experimental restrictions imposed by the NA49 detector both, Feynman-x of the leading proton and the charged-particle multiplicity serve well as parameters for the inelasticity. Measuring both, the inelasticity variable and the particle production in the same hemisphere of the collision system, i. e. forward in NA49, gives representative results for particle production in dependence on the available energy.

This conclusion is strongly supported by a measurement of Basile et al. [11]: Charged-particle multiplicity measured in p+p in dependence on an effective center-of-mass energy agrees well with results from e^+e^- annihilation into hadrons where

	FRITIOF	NA49 (min.bias)
π^+	3.03	$3.07 \pm 0.01 \pm 0.15$
π^-	2.34	$2.33 \pm 0.01 \pm 0.12$
K^+	0.267	$0.238 \pm 0.001 \pm 0.024$
K^-	0.172	$0.138 \pm 0.001 \pm 0.014$
$K^*(892)^0$	0.105	$0.0792 \pm 0.0016 \pm 0.0063$
$\bar{K}^*(892)^0$	0.081	$0.0559 \pm 0.0011 \pm 0.0045$
ϕ	0.021	$0.0129 \pm 0.0002 \pm 0.0013$
Λ	0.149	0.130 ± 0.012

Table 5.7: Comparison of particle yields in inelastic p+p collisions at $\sqrt{s} = 17.3$ GeV for FRITIOF simulations and minimum-bias data of NA49. Data for Λ -baryons are from T. Susa [136]. In the data pions are feed-down corrected (see chapter 5 for determination of yields), for FRITIOF no weak decays were allowed. Statistical errors on the yields in FRITIOF are below 1 %, for data the first error quoted is statistical, the second systematic.

all center-of-mass energy is used for hadron production. If, in this thesis, the selected leading proton indeed characterizes the inelasticity, the correlation found by Basile et al. should also hold.

Basile et al. assumed that, on average, particle production and energy loss of the leading proton are the same in both hemispheres. However, as was discussed in section 4.2, the NA22 collaboration [92] observed an energy dependent correlation strength between the two hemispheres; for center-of-mass energies of 17.3 GeV this correlation is rather weak. In the following the two extreme assumptions of either independence of forward and backward hemisphere, (a), or a symmetry on average, (b), are used for the calculation of effective center-of-mass energy $\sqrt{s_{\text{eff}}}$ and the correlated total charged-particle multiplicity N_{ch} . This gives an idea of the sensitivity of results on assumptions about the correlation of the hemispheres.

The energy available for particle production in the forward hemisphere can be approximated by $\frac{1}{2}\sqrt{s} \cdot (1 - x_F)$, with x_F being the remaining relative momentum of the leading proton. Using minimum-bias characteristics for the backward hemisphere in case of its independence, i. e. for case (a), and multiplying features of the forward hemisphere by 2 for case (b), the effective center-of-mass energy $\sqrt{s_{\text{eff}}}$ is calculated as:

$$\begin{aligned} (a) \quad \sqrt{s_{\text{eff}}} &= \frac{\sqrt{s}}{4} + \frac{1}{2}\sqrt{s} \cdot (1 - x_F) = \frac{\sqrt{s}}{2}(1.5 - x_F) \\ (b) \quad \sqrt{s_{\text{eff}}} &= 2 \cdot \frac{1}{2}\sqrt{s} \cdot (1 - x_F) = \sqrt{s}(1 - x_F) \end{aligned} \quad (5.4)$$

The charged-particle multiplicity in the forward hemisphere is defined as the sum of charged pions and kaons since they are the most abundant newly produced charged hadrons. For (a), half of the sum for minimum-bias p+p interactions is

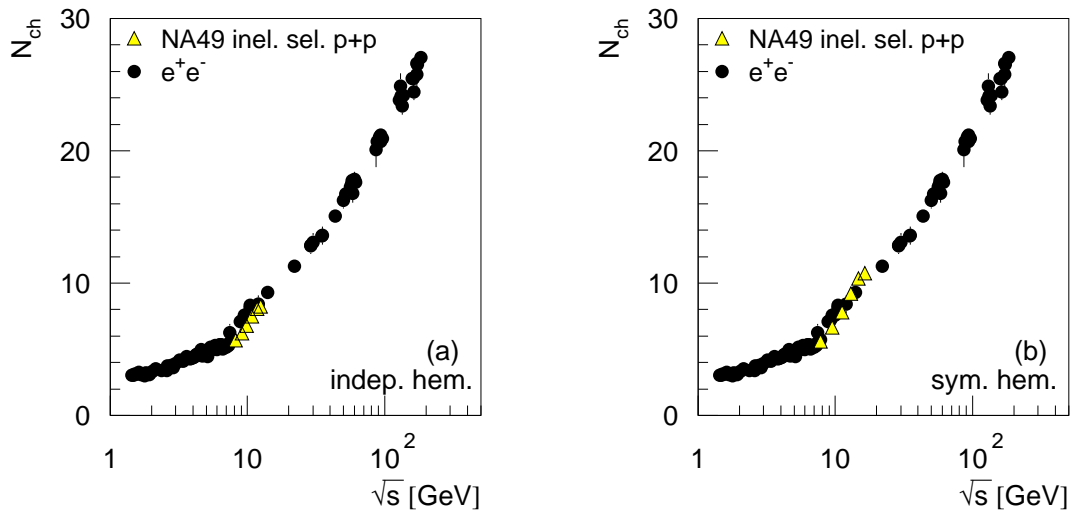


Figure 5.36: Charged multiplicity in e^+e^- collisions versus center-of-mass energy \sqrt{s} [2]. Included in the picture as light triangles are inelasticity selected p+p data, in (a) assuming both hemispheres of the collision to be independent, in (b) to be symmetric on average. For the definition of $\sqrt{s_{\text{eff}}}$ and the multiplicity see text.

added, for (b) the forward multiplicity is multiplied by 2. No extra term for baryons is needed since the probability for pair production of baryons is small. Baryon conservation is fulfilled by the leading protons, which are not regarded as being produced using energy from $\sqrt{s_{\text{eff}}}$.

The resulting correlation of charged-particle multiplicity and $\sqrt{s_{\text{eff}}}$ is compared to data from e^+e^- collisions (fig. 5.36). A good agreement is found for both cases. Obviously assumptions concerning the backward hemisphere are not crucial and the observation of the correlation of $x_F^{\text{leading proton}}$ and N_{ch} in one hemisphere only is representative for the whole p+p event.

The agreement of e^+e^- and inelasticity selected p+p data also proves that $x_F^{\text{leading proton}}$, as it is defined in NA49, is correlated to the effective center-of-mass energy and correctly serves for selecting the inelasticity of p+p interactions. The effective center-of-mass energy corresponding to this inelasticity selection covers a range of 8.2 GeV to 12.5 GeV (7.8 GeV to 16.4 GeV) assuming independence (symmetry on average) of the hemispheres. It was already argued in section 4.2.1 that qualitative features as, e. g., the relative strangeness production are not biased by the not measured backward hemisphere.

Chapter 6

C+C and Si+Si collisions

In this chapter particle yields and distributions in transverse momentum and rapidity are determined for the event samples with 15.3 % most central C+C and 12.2 % most central Si+Si collisions. Tables with numerical values of the results and additional figures can be found in appendix C. The summary and discussion of the results is postponed to the next chapter.

6.1 Pions

Pions were extracted as described in chapter 3.1, in principle using the same methods as already applied for p+p collisions. Since the event sample available for analysis is rather small, as standard parameter set for dE/dx spectra a Φ -wedge of $|\Phi| \leq 50^\circ$ is used, the other parameters remain the same: only right-side tracks with a minimum of 30 points per track were selected. For fitting dE/dx spectra a minimum of 500 entries is set; for π^- a momentum range of $0.6 < \log_{10}(p) \leq 1.7$ was used, for π^+ of $0.6 < \log_{10}(p) \leq 1.8(1.9)$ for C+C (Si+Si) collisions. Statistics was sufficient for the analysis of transverse-momenta up to 1.2 GeV at most.

Transverse-momentum distributions

Transverse-mass distributions with thermal fits in bins of rapidity are presented in fig. 6.1 (see appendix C for some p_t -spectra).

The p_t -range covered for midrapidity pion spectra is even more restricted than for p+p collisions, because in addition to the missing acceptance at low p_t the higher values are also lacking due to statistics problems. Temperatures from a free thermal fit are poorly defined, a constraint on its value from higher rapidity bins is used therefore (see fig. 6.4 (b)). In a thermalized hadron gas a functional dependence of $T \propto 1/\cosh(y)$ is expected. However, the observed dependence of T on rapidity is significantly broader (see also [70] and fig. 5.3 for pions in p+p). A similar trend is known from the rapidity distribution itself in comparison to the expectation from the thermalized hadron gas [41, 70]. The origin might be the elongation of particle production along the beam direction due to the high momenta of the incoming nuclei. The dependence of T on y is therefore approximated by a parabola; this

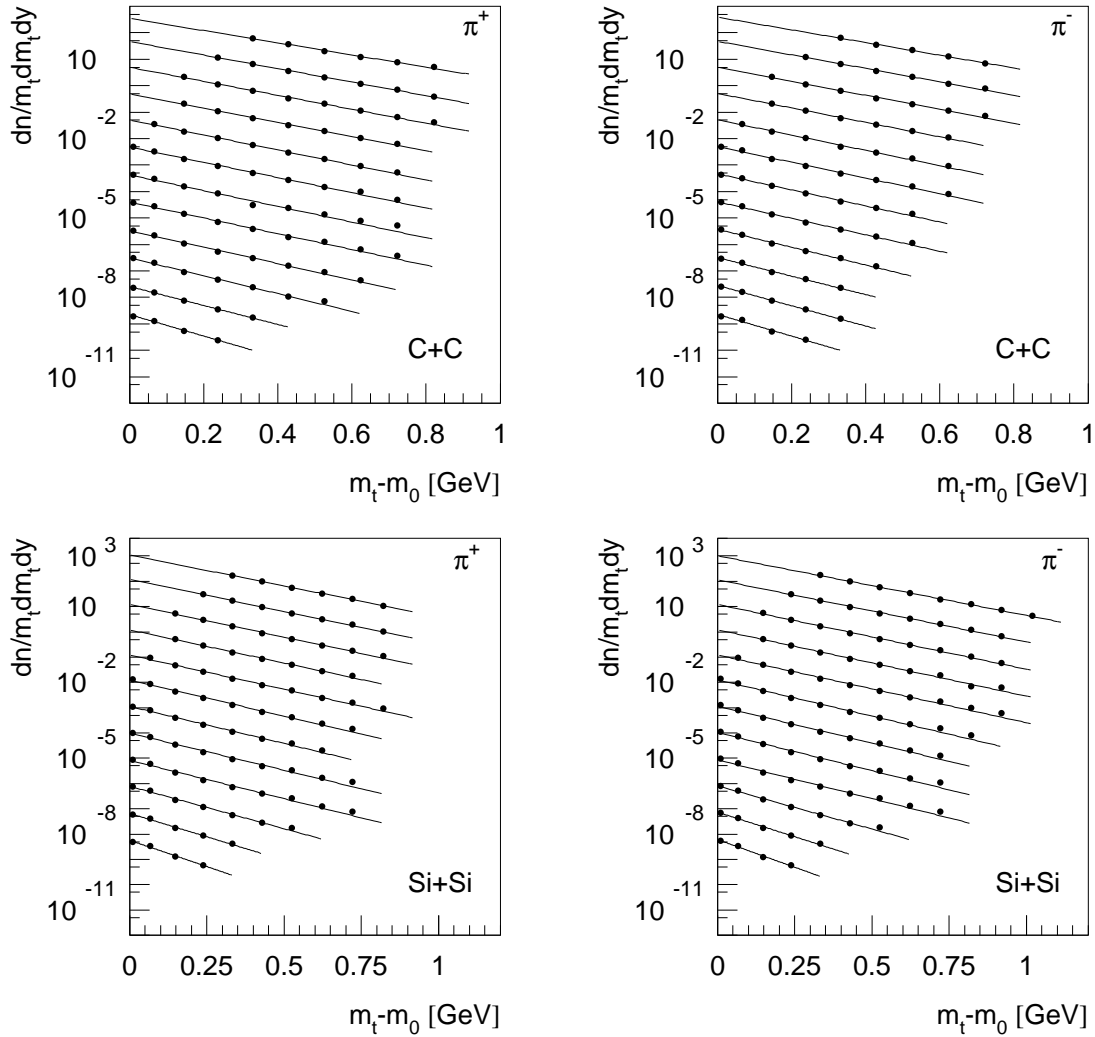


Figure 6.1: Transverse-mass distributions for pions in central C+C and Si+Si collisions in bins of rapidity. The upper curve is at midrapidity ($2.77 < y \leq 3$), the other spectra are successively scaled down by a factor of 10 for better visibility. The lowest spectrum corresponds to $5.31 < y \leq 5.54$. No feed-down correction for pions is applied yet. Lines correspond to fits assuming a thermal m_t -distribution (formula 3.8).

smoothed evolution can be used for the extraction of p_t -integrated yields, especially for higher rapidities (open circles in fig. 6.2).

However, for midrapidity the so-called low- p_t enhancement as, e.g. measured by the NA35 experiment [128, 129], is not considered in the above approximation: They extracted p_t -spectra of negatively charged hadrons in S+S collisions at 200 AGeV in various rapidity bins. Due to good statistics and a large coverage of phase space they observed that p_t -distributions of h^- cannot be fitted over the entire p_t -range with a single exponential in p_t or m_t . Transverse flow [130] and a large contribution of pions from strong decays of resonances [99] are discussed as origin.

A two-component thermal model fit of the form

$$\frac{dN}{dp_t} = c_1 \cdot p_t \exp\left(-\frac{m_t}{T_1}\right) + c_2 \cdot p_t \exp\left(-\frac{m_t}{T_2}\right) \quad (6.1)$$

fits well to their data over the full measured range. In particular at low p_t ($p_t \lesssim 0.3$ GeV) and high p_t ($p_t \gtrsim 1$ GeV) the two-component model gives a better description of the data, while the single exponential underestimates the yield. Typical temperature parameters are 84 MeV and 190 MeV in [129], for spectra presented in [128] 110 MeV and 235 MeV can be extracted.

Pion yields at midrapidity for C+C and Si+Si are derived using the NA35 data at midrapidity for extrapolation. Since energy and system size are similar this should also hold for the functional form of the spectra, see appendix C for figures. Available p_t -values from data are summed. The missing fraction is calculable with the introduced two-component fit of the NA35 data (see full circles at midrapidity in fig. 6.2). As expected, these p_t -integrated values are slightly higher than those from a single exponential fit. They are supported by a preliminary analysis of negatively charged hadrons (see next paragraph and figures in appendix C).

Rapidity distribution and integrated yields

Feed-down corrected, p_t -integrated rapidity spectra are presented in fig. 6.2. Double Gaussians provide a better description of the functional form of the spectra, for comparison single Gaussians are also printed. Integrating the latter gives about 3-6 % higher yields. The full width at half maximum (FWHM) for the double Gaussian

C+C	π^+	π^-
$T _{y_{CM}}$	$165 \pm 4 \pm 10$	$163 \pm 4 \pm 10$
σ_y	1.14 ± 0.06	1.12 ± 0.06
y_Δ	0.85 ± 0.04	0.84 ± 0.05
$dN/dy _{y_{CM}}$	$5.71 \pm 0.23 \pm 0.6$	$5.83 \pm 0.25 \pm 0.6$
$\langle\pi\rangle$	$22.5 \pm 0.3 \pm 1.6$	$22.2 \pm 0.3 \pm 1.6$
Si+Si	π^+	π^-
$T _{y_{CM}}$	$170 \pm 3 \pm 10$	$172 \pm 3 \pm 10$
σ_y	1.06 ± 0.04	1.06 ± 0.03
y_Δ	0.89 ± 0.02	0.89 ± 0.02
$dN/dy _{y_{CM}}$	$14.98 \pm 0.54 \pm 1.5$	$15.47 \pm 0.53 \pm 1.5$
$\langle\pi\rangle$	$57.0 \pm 0.7 \pm 4$	$57.8 \pm 0.7 \pm 4$

Table 6.1: Final results of pions in 15 % most central C+C and 12 % most central Si+Si collisions at 158 AGeV. Parameters for a double Gaussian fit as introduced in formula 3.9 are presented. If two errors are given, the first is statistical, the second systematic. Temperatures are taken from the constrained fit, the given value is averaged over the first two rapidity bins ($2.77 < y \leq 3.23$) as is also $dN/dy|_{y_{CM}}$.

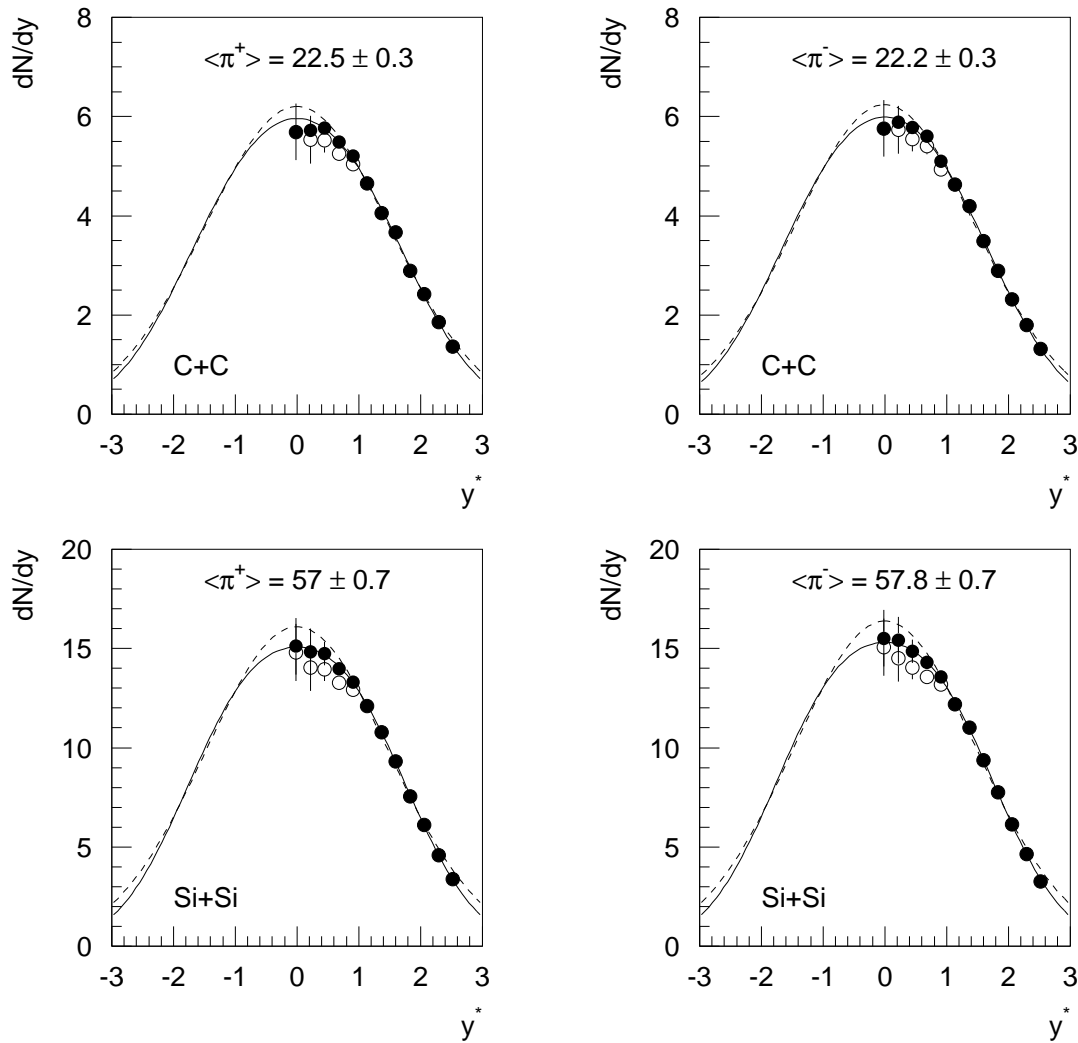


Figure 6.2: Feed-down corrected rapidity distributions for pions in central C+C and Si+Si interactions. The distributions are fitted with both, a double Gaussian (solid line) and a single Gaussian (dashed line). The integrated value of the double Gaussian fit is printed in the figures; the single Gaussian provides yields of 23.3 ± 0.2 (60.1 ± 0.4) for π^+ and 22.9 ± 0.2 (61.0 ± 0.3) for π^- in C+C (Si+Si) collisions with a σ_y of 1.47 to 1.50. Besides additional systematic errors for midrapidity values (see text) only statistical errors are included in the figure. For the difference between open and close symbols see text. For the open circles the extrapolation in p_t is calculated assuming a ± 10 MeV error on the temperature.

is 3.65 (3.69) for π^+ , and 3.6 (3.69) for π^- in C+C (Si+Si) collisions. Final results are summarized in table 6.1.

As was discussed in the previous paragraph the extrapolation of the measured p_t -spectra to the full range is especially difficult for midrapidity.

An independent check of, in particular π^- , would be the measurement of negatively charged hadrons. The contribution of the comparatively rare K^- and \bar{p} can be determined with the help of simulations. Here, a preliminary analysis of h^- was performed aiming at a crosscheck of the rapidity distribution, in particular

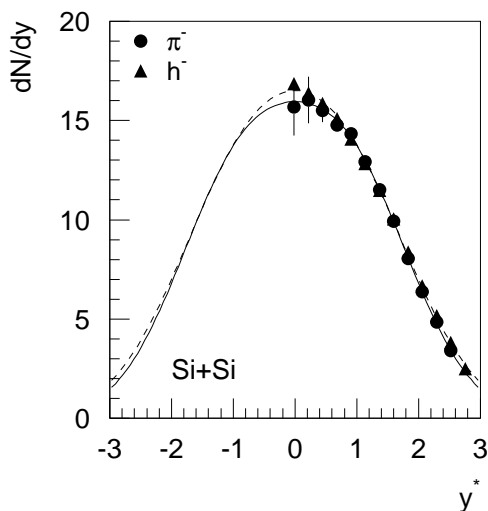


Figure 6.3: Rapidity distribution of π^- in Si+Si in comparison to the preliminary h^- analysis. After subtraction of the K^- and \bar{p} contribution the h^- distribution is scaled to the one of π^- in the rapidity range $3.91 < y \leq 4.62$ to account for remaining background in the h^- . Both distributions are not feed-down corrected, however, the correction would be the same. The solid line represents a double-Gaussian fit to π^- , the dashed line to h^- . Integrated yields are 60.2 and 62.2, respectively.

the midrapidity yields. Negatively charged hadrons with track cuts as used for the pion analysis were extracted in bins of rapidity; a correction for the acceptance was applied. K^- and \bar{p} are subtracted using VENUS simulations. The remaining background is, at least to first order, assumed to be equally distributed in rapidity. This is supported by the analysis of h^- in central Pb+Pb collisions [71]. This assumption allows to scale the h^- rapidity distributions to the one extracted for π^- (and π^+) using the energy-loss measurements. The adjustment was done in the rapidity range $3.92 < y \leq 4.62$ where a full coverage in p_t is available for pions; typical scaling factors are about 0.93. This additional scaling factor is in agreement with the analysis for h^- in central Pb+Pb [71].

A comparison of h^- and π^- distribution for Si+Si collisions is presented in fig. 6.3 (for figures for C+C and p+p see appendix C). Midrapidity yields from the preliminary h^- analysis are about 8 % and 2 % higher for the first two bins, total yields differ by 3 % only. This confirms the results obtained before and presented in fig. 6.2.

Systematic errors

Although the event sample is rather small, statistical errors for single (y, p_t) -bins are minor in the accepted $y-p_t$ range. However, statistics significantly limit the available phase space which introduces systematic errors, especially for midrapidity pions as was discussed above. Fig. 6.4 shows, e. g., for π^- in C+C collisions the temperature parameters from the free fit as well as smoothed values. The temperature parameter is not well defined if low and high p_t are missing, which results also in larger errors of the extrapolation (see appendix C for some p_t -spectra). A variation by about ± 10 MeV changes the yields by ± 8 %, ± 5 %, and ± 3 % in the first three rapidity bins. This also changes total yields of pions by ± 3 -4 %. Requiring more than 50 points on each track reduces the statistics further, in particular yields at midrapidity are even less certain then. Assuming asymmetric Gaussian shapes for fitting the dE/dx spectra has a small influence. Here $\delta = 0.07$ was used as typical

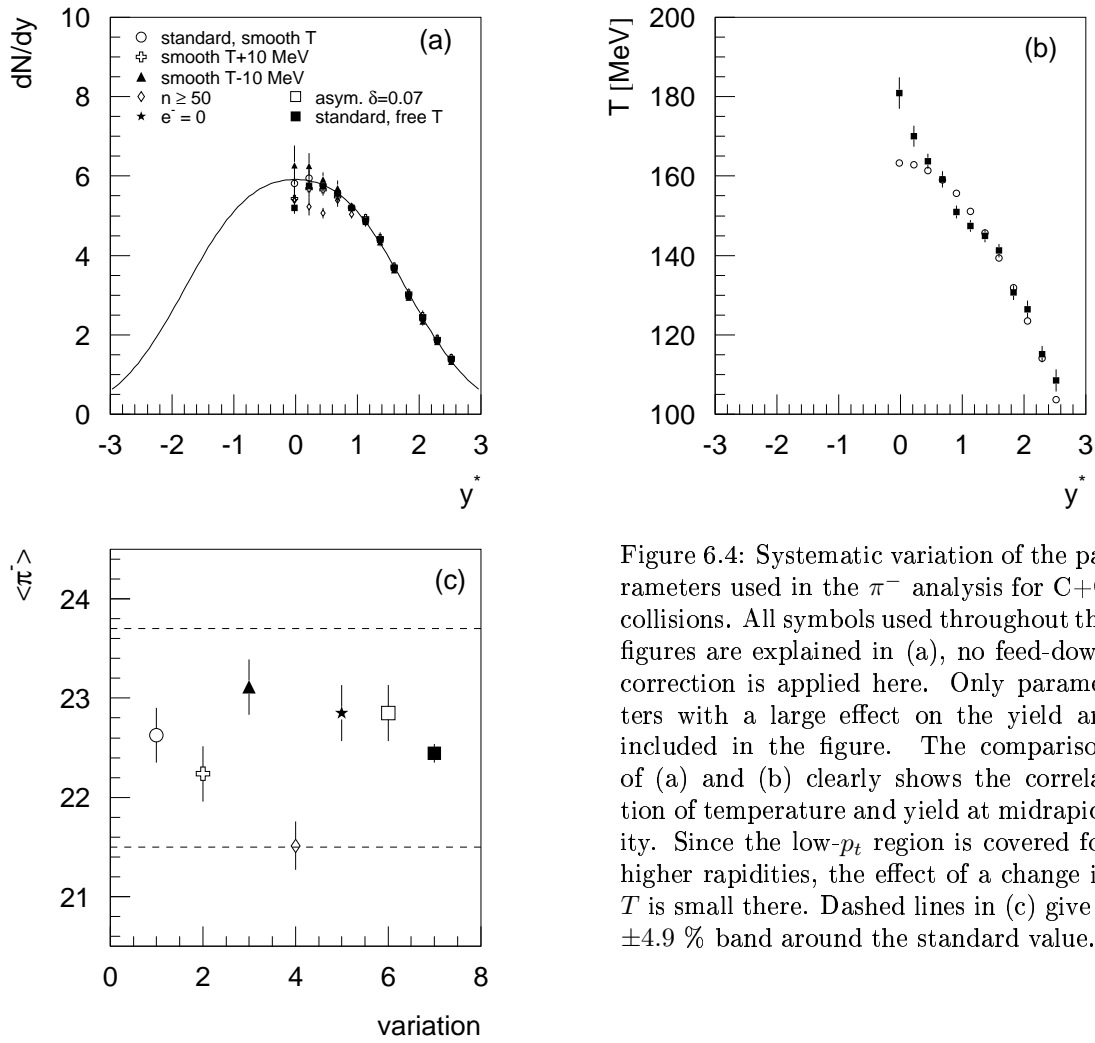


Figure 6.4: Systematic variation of the parameters used in the π^- analysis for C+C collisions. All symbols used throughout the figures are explained in (a), no feed-down correction is applied here. Only parameters with a large effect on the yield are included in the figure. The comparison of (a) and (b) clearly shows the correlation of temperature and yield at midrapidity. Since the low- p_t region is covered for higher rapidities, the effect of a change in T is small there. Dashed lines in (c) give a $\pm 4.9\%$ band around the standard value.

value extracted for central Pb+Pb at 158 AGeV [70] (see definitions in section 3.1.2).

Considering also the preliminary analysis of h^- mesons introduced above, systematic errors of 10 % on the midrapidity yields and 7 % on total yields are reasonable.

6.2 Kaons

Kaons were extracted in the same way as pions. Standard parameters for the fits were reported above, only the momentum range is $0.6 < \log_{10}(p) \leq 1.7$ for both, K^+ and K^- . Spectra are better defined here because of the more convenient acceptance.

Transverse-momentum distributions

Transverse-mass spectra in bins of rapidity are presented in fig. 6.5. Because of the good acceptance for midrapidity kaons also at small transverse-momenta yields are more stable in this region.

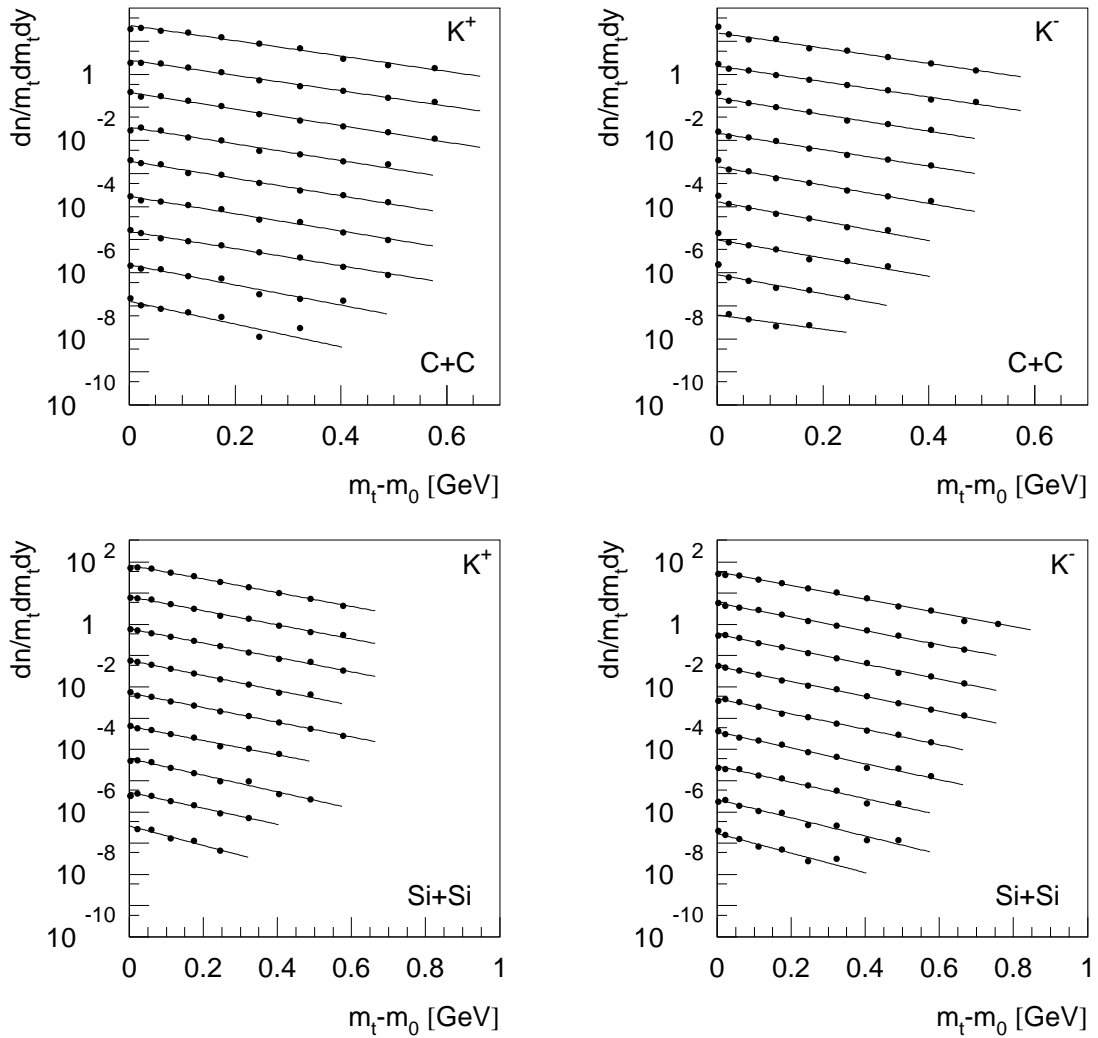


Figure 6.5: Transverse-mass distributions for kaons in C+C and Si+Si collisions in bins of rapidity. The upper curve is at midrapidity ($2.77 < y \leq 3$), the other spectra are successively scaled down by a factor of 10 for better visibility. The lowest spectrum corresponds to $4.62 < y \leq 4.85$. Lines correspond to fits assuming a thermal m_t -distribution (formula 3.8).

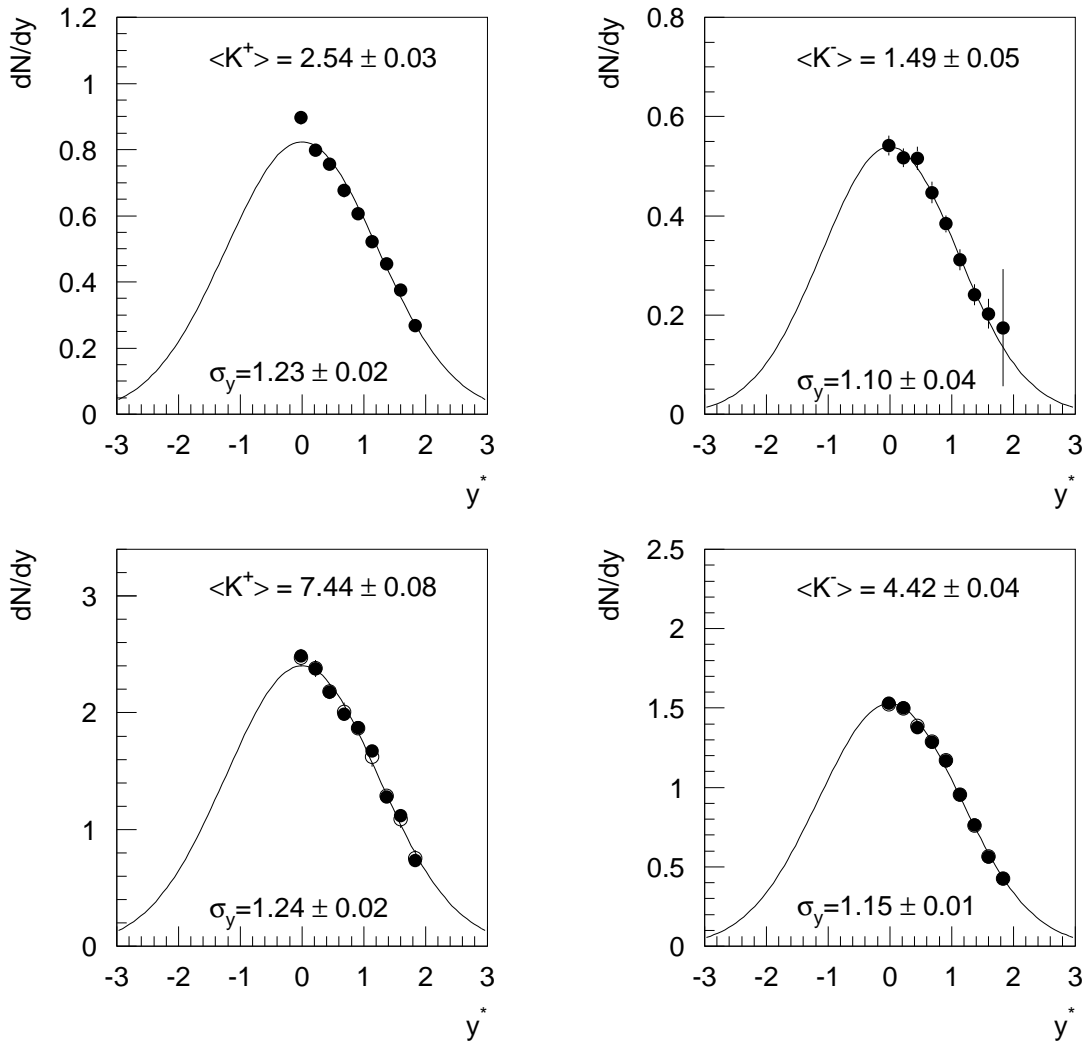


Figure 6.6: Rapidity distributions for kaons in C+C and Si+Si interactions. The distributions are fitted with a Gaussian, width and integrated yield are included in the figure. Errors are statistical only. Open symbols (hardly visible) present yields obtained by choosing T according to the line in fig. 6.7 (b).

Rapidity distribution and integrated yields

p_t -integrated rapidity distributions are presented in fig. 6.6. A Gaussian gives a good description of the distribution. Using smoothed temperatures as for pions or the ones directly from the fit does not change the yields significantly, also summing bins or integrating the function does not make a difference. Systematic errors are investigated below, final results can be found in table 6.2.

Systematic errors

As for p+p collisions the main systematic uncertainties for kaons stem from the dE/dx fit and the remaining uncertainty in the decay correction. The effect of their variation and of the change of other variables is investigated. Fitting asymmetric

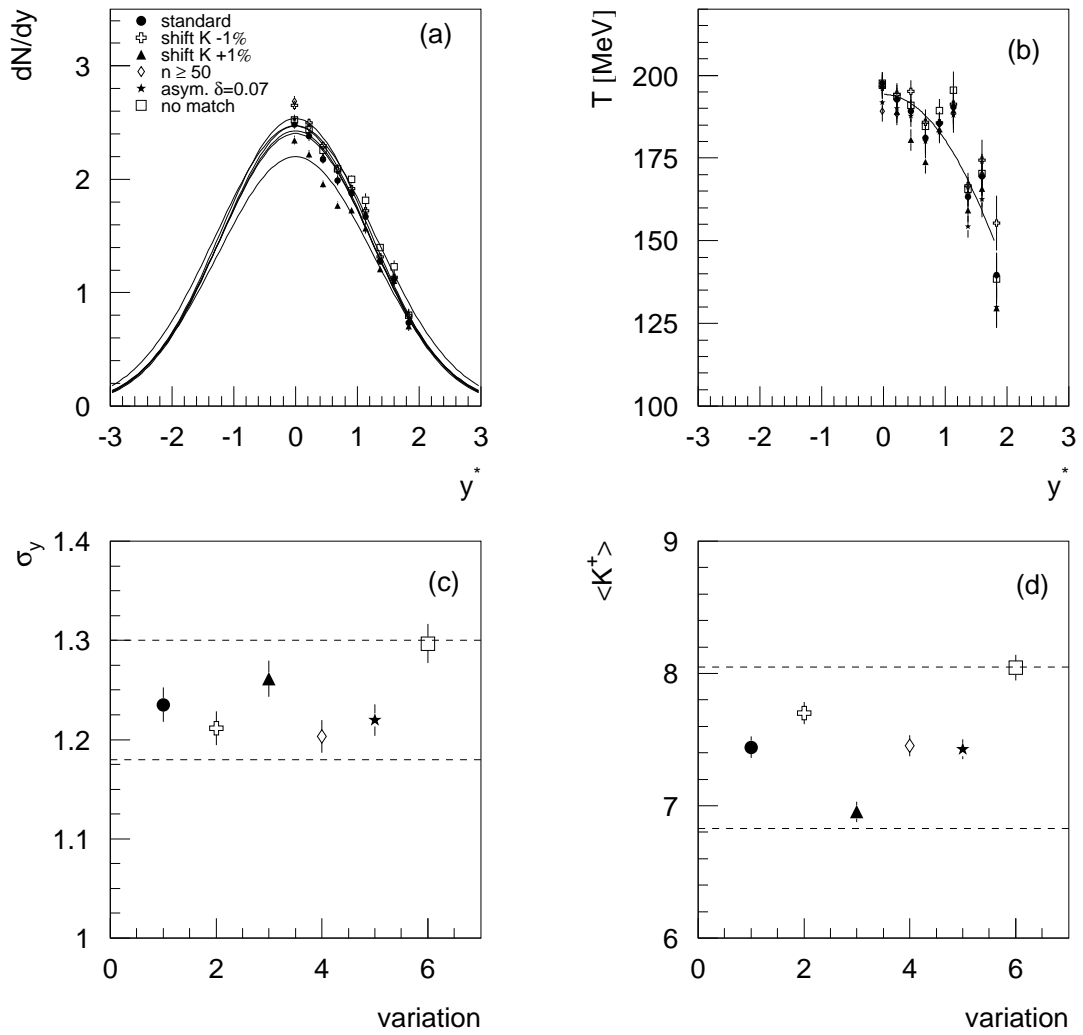


Figure 6.7: Systematic variation of parameters used for the K^+ extraction in Si+Si collisions. The line in (b) indicates a parabola fit to the temperature values from "standard". Dashed lines in (c) and (d) give a $\pm 4.8\%$ and $\pm 8.2\%$ band around the standard value, respectively.

C+C	K^+	K^-
$T _{y_{CM}}$	$188 \pm 4 \pm 10$	$187 \pm 5 \pm 10$
σ_y	$1.23 \pm 0.02 \pm 0.08$	$1.1 \pm 0.04 \pm 0.09$
$dN/dy _{y_{CM}}$	$0.848 \pm 0.015 \pm 0.085$	$0.529 \pm 0.014 \pm 0.05$
$\langle K \rangle$	$2.54 \pm 0.03 \pm 0.25$	$1.49 \pm 0.05 \pm 0.15$
Si+Si	K^+	K^-
$T _{y_{CM}}$	$195 \pm 3 \pm 10$	$198 \pm 3 \pm 10$
σ_y	$1.24 \pm 0.02 \pm 0.08$	$1.15 \pm 0.01 \pm 0.07$
$dN/dy _{y_{CM}}$	$2.43 \pm 0.03 \pm 0.24$	$1.52 \pm 0.02 \pm 0.15$
$\langle K \rangle$	$7.44 \pm 0.08 \pm 0.74$	$4.42 \pm 0.04 \pm 0.44$

Table 6.2: Final results for kaons in C+C and Si+Si collisions at 158 AGeV. Midrapidity values for T and dN/dy are averaged over the first two bins, i.e. $2.77 < y \leq 3.23$. The first error is statistical, the second systematic.

Gaussians ($\delta = 0.07$) to the dE/dx spectra has a small influence on the yield only. As example, results for K^+ in Si+Si interactions are shown in fig. 6.7. The variations are slightly less for K^- , the situation in C+C is similar to Si+Si.

6.3 ϕ -meson

The ϕ -meson in C+C and Si+Si collisions is extracted as already described for p+p interactions. The event-mix gives a slightly better description of the background compared to p+p: The peak at threshold just below the ϕ -signal has basically disappeared (fig. 6.8). Instead, distortions show up behind the ϕ -signal, especially for Si+Si collisions. As discussed in chapter 3.2.2 these distortions can be attributed to reflections of the $N^*(1440)$ or Δ resonances. Indeed, the distortions vanish (not shown), if protons and π^- are suppressed by selecting only K^+ above and K^- below the mean dE/dx -value. Unfortunately statistics become meager at the same time and an asymmetric window in dE/dx is rather sensitive to the correct determination of the mean dE/dx position. Since the dE/dx resolution increases for longer tracks which also reduces the overlap of the distributions, a minimum of 50 points per track is required for the ϕ -signal in Si+Si collisions. The remaining effect of the distortions on the yield is estimated as for p+p: On the one hand, a pure Breit-Wigner distribution with Gaussian broadening for the detector resolution is fitted to the signal on top of a straight line, which is adjusted to the background around the ϕ -meson. On the other hand, a simulation including undershoots is fitted to the data. The mean of both yields is taken for the final values.

Kaons are selected according to the following criteria: more than 30 (C+C) or

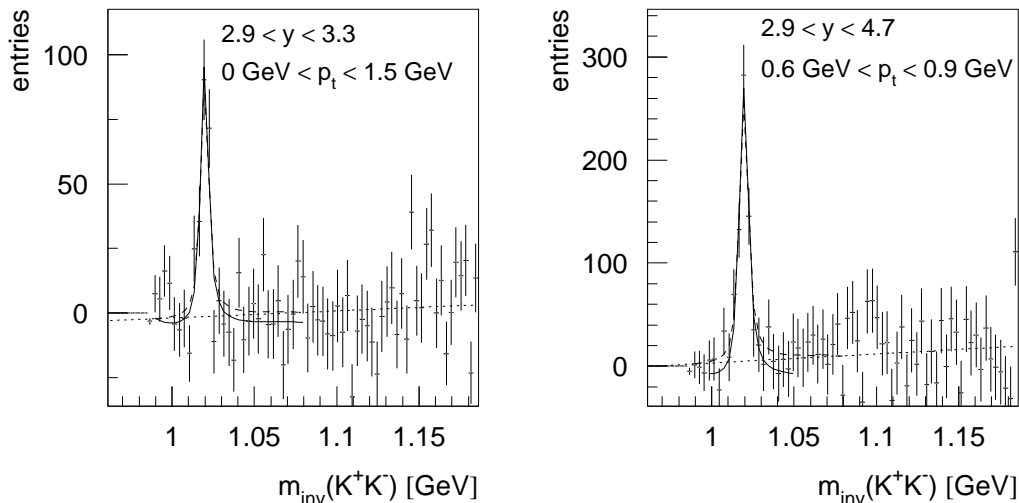


Figure 6.8: Invariant-mass spectra in kinematic bins as indicated in the figures, left for C+C ($n_{points} \geq 30$) and right for Si+Si ($n_{points} \geq 50$). Some background remains behind the ϕ -meson after subtraction of the event-mix spectrum. Solid lines show a fit of the simulation including undershoots. The dashed line represents a Breit-Wigner function adjusted to the data on top of the dotted straight line. For final results the mean of both fits is taken.

50 (Si+Si) points per track, a momentum range of $0.6 < \log(p) \leq 1.7$ and a reduced range in p_t compared to p+p reactions of $0 \text{ GeV} < p_t \leq 1 \text{ GeV}$. This reduction was necessary, because dE/dx -fits giving reliable parameters for mean position and width could only be performed up to 1 GeV in p_t due to the limited number of events. This cut restricts the ϕ -acceptance to $p_t < 1.6 \text{ GeV}$. Kaons are selected in a $\pm 1.5\sigma_{dE/dx}$ window around the mean dE/dx position.

Transverse-momentum distributions are extracted in a rapidity interval of $[2.9, 4.7]$, for the p_t -integrated rapidity spectra a p_t -range of $[0, 1.5] \text{ GeV}$ is chosen. Since the extracted temperature is larger than in p+p collisions this p_t -range covers only 94 % of all ϕ -mesons.

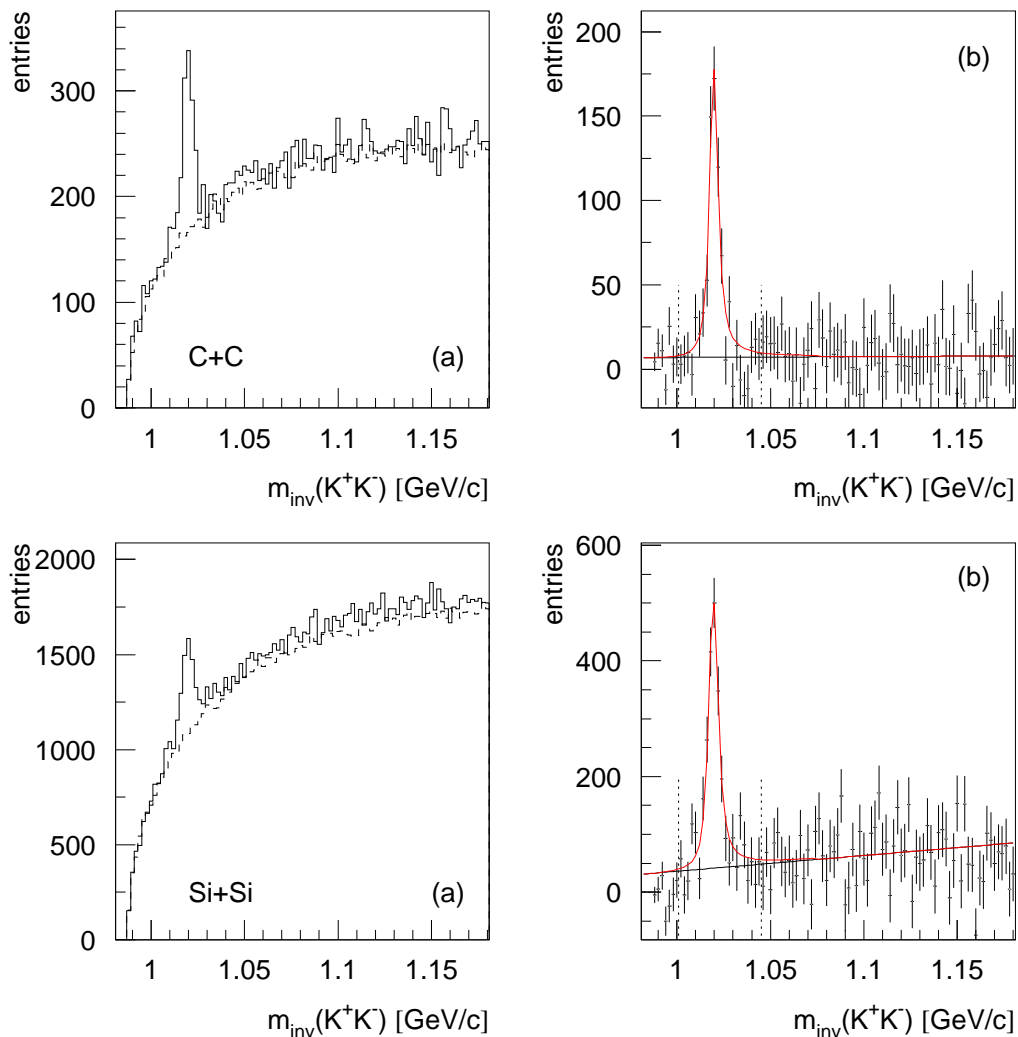


Figure 6.9: Invariant-mass distributions of the ϕ -meson in C+C and Si+Si collisions in a rapidity range of 2.9 to 4 and a p_t -range of 0 GeV to 1.5 GeV (a); the dashed line represents the calculated event-mix background. Event-mix-subtracted signals (b) with linear fit for the remaining distortion and a Breit-Wigner fit to the signal: $m = 1019.8 \text{ MeV}$ (C+C), $m = 1019.6 \text{ MeV}$ (S+Si), and $\Gamma = 4.43 \text{ MeV}$. The signal is broadened with a Gaussian with $\sigma_m = 0.85 \text{ MeV}$ (C+C) and $\sigma_m = 1.3 \text{ MeV}$ (Si+Si). The vertical dashed lines indicate the fit range.

Mass and width of the resonance

Before extracting the ϕ -meson from the data, mass and width of the signal in the invariant-mass spectrum are reinvestigated. As for p+p the intrinsic width of the ϕ -meson, $\Gamma = 4.43$ MeV, is fixed, only the broadening of the mass due to detector resolution is varied. In central Pb+Pb collisions a slightly larger width ($\sigma_m = 1.6$ MeV) compared to p+p was observed [64]; probably a consequence of the higher track density and the use of a different reconstruction chain for the data processing.

Parameters are extracted with the same method as described in detail in chapter 5.1.3; invariant-mass distributions from which mass and width are extracted can be found in fig. 6.9. In C+C collisions mass and width of the ϕ -meson are determined to (see fig. 6.10 and 6.11)

$$m_0 = (1019.8 \pm 1.2) \text{ MeV and } \sigma_m = (0.71 \pm 2.12) \text{ MeV,}$$

and in Si+Si interactions to

$$m_0 = (1019.6 \pm 1.1) \text{ MeV and } \sigma_m = (1.41 \pm 1.79) \text{ MeV.}$$

A more precise determination of these parameters is impossible because of the limited statistics; especially the accuracy of the extracted width is unsatisfactory. For the further extraction of the ϕ -yield in C+C the same width as in p+p collisions is assumed, for Si+Si interactions the increased width of 1.4 MeV is taken. A change in σ_m from 1 MeV to 2 MeV results in 5-8 % difference in the extracted yields. The ϕ -mass for both collision systems is consistent with the mass reported in [2], $m_0 = (1019.413 \pm 0.008)$ MeV.

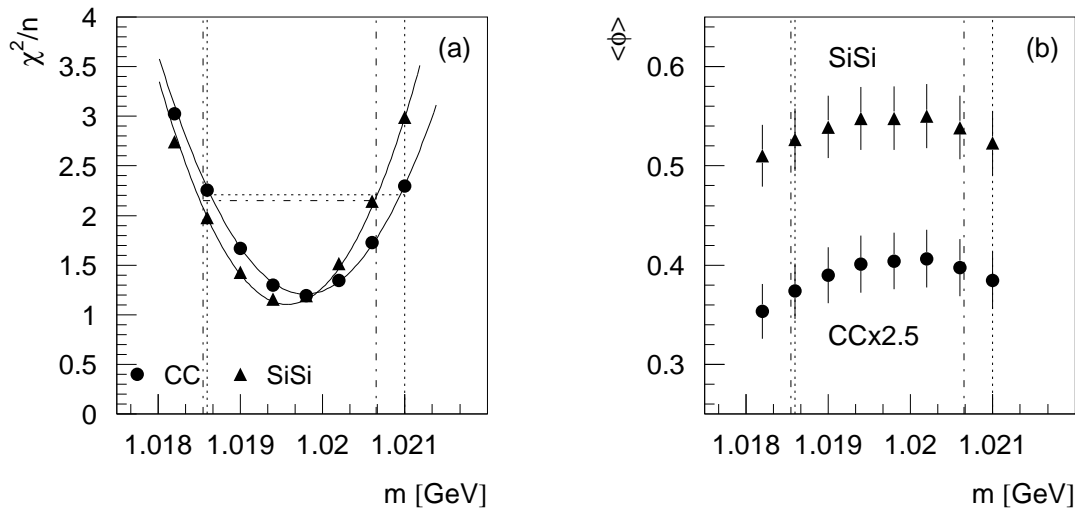


Figure 6.10: χ^2/n in dependence on mass for a fixed width $\sigma_m = 0.85$ MeV/c (a). The line gives a parabola fitted to the data points from which mass and errors are extracted. The dotted lines belong to data on C+C collisions, the dashed-dotted lines to Si+Si. (b) corresponding yield in dependence on the mass assumed for the fit. The vertical lines show the error margin from (a).

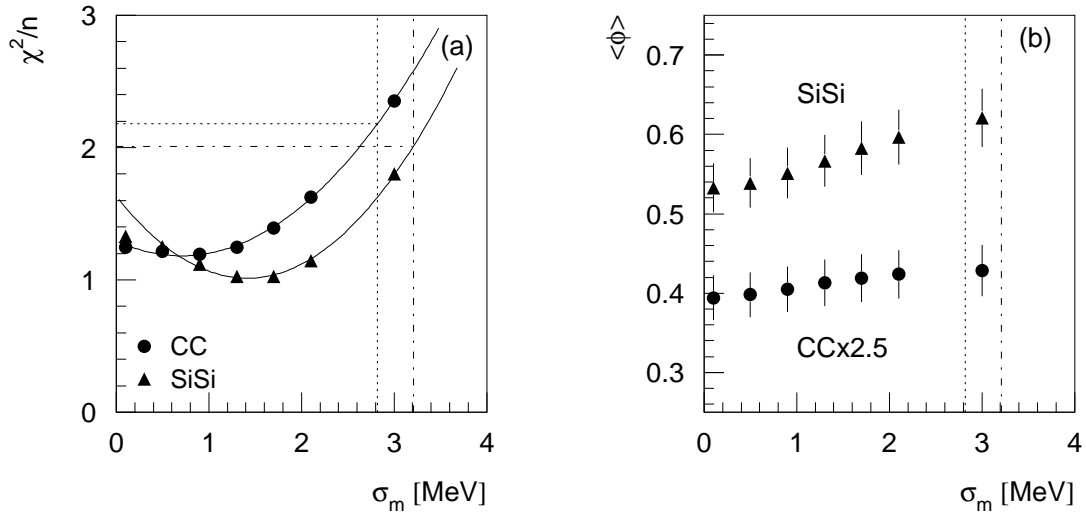


Figure 6.11: χ^2/n in dependence on the sigma for the Gaussian smearing of the ϕ -mass for a fixed mass $m = 1019.8$ MeV for C+C, and $m = 1019.6$ MeV for Si+Si collisions (a). The small curvature of the parabola results in a large error on the best fit for σ_m . (b) corresponding yield in dependence on σ_m assumed for the fit. The vertical dotted lines show the upper error margin from (a).

Rapidity distribution and integrated yields

The rapidity spectra presented in fig. 6.12 are extracted for a large p_t -range which contains 94 % of all ϕ -mesons (for $T = 220$ MeV). A summary of results for the ϕ -meson including systematic errors as they are investigated below can be found in table 6.3.

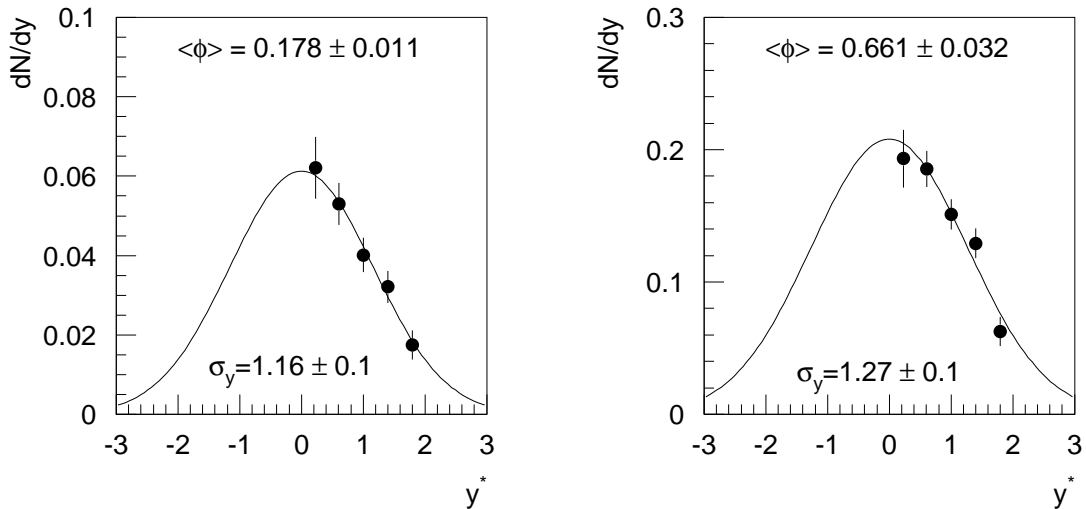


Figure 6.12: Rapidity distribution of the ϕ -meson in C+C (left) and Si+Si (right) collisions. The distribution is fitted with a Gaussian, the quoted error is statistical. The full yield is from integration.

	C+C	Si+Si
m_0	(1019.8 ± 1.2) MeV	(1019.6 ± 1.1) MeV
Γ_0	4.43 MeV (fixed)	4.43 MeV (fixed)
σ_m	(0.71 ± 2.12) MeV	(1.41 ± 1.79) MeV
T	$(189 \pm 28 \pm 10)$ MeV	$(220 \pm 28 \pm 10)$ MeV
σ_y	$1.16 \pm 0.1 \pm 0.05$	$1.27 \pm 0.1 \pm 0.05$
$\langle \phi \rangle$	$0.178 \pm 0.011 \pm 0.021$	$0.661 \pm 0.032 \pm 0.079$
$\frac{dN}{dy} \Big _{y_{CM}}$	$0.0622 \pm 0.0078 \pm 0.008$	$0.193 \pm 0.022 \pm 0.02$

Table 6.3: Summary of results for the ϕ -meson in 15 % central C+C and 12 % central Si+Si collisions at 158 AGeV. The first error quoted is statistical, the second systematic.

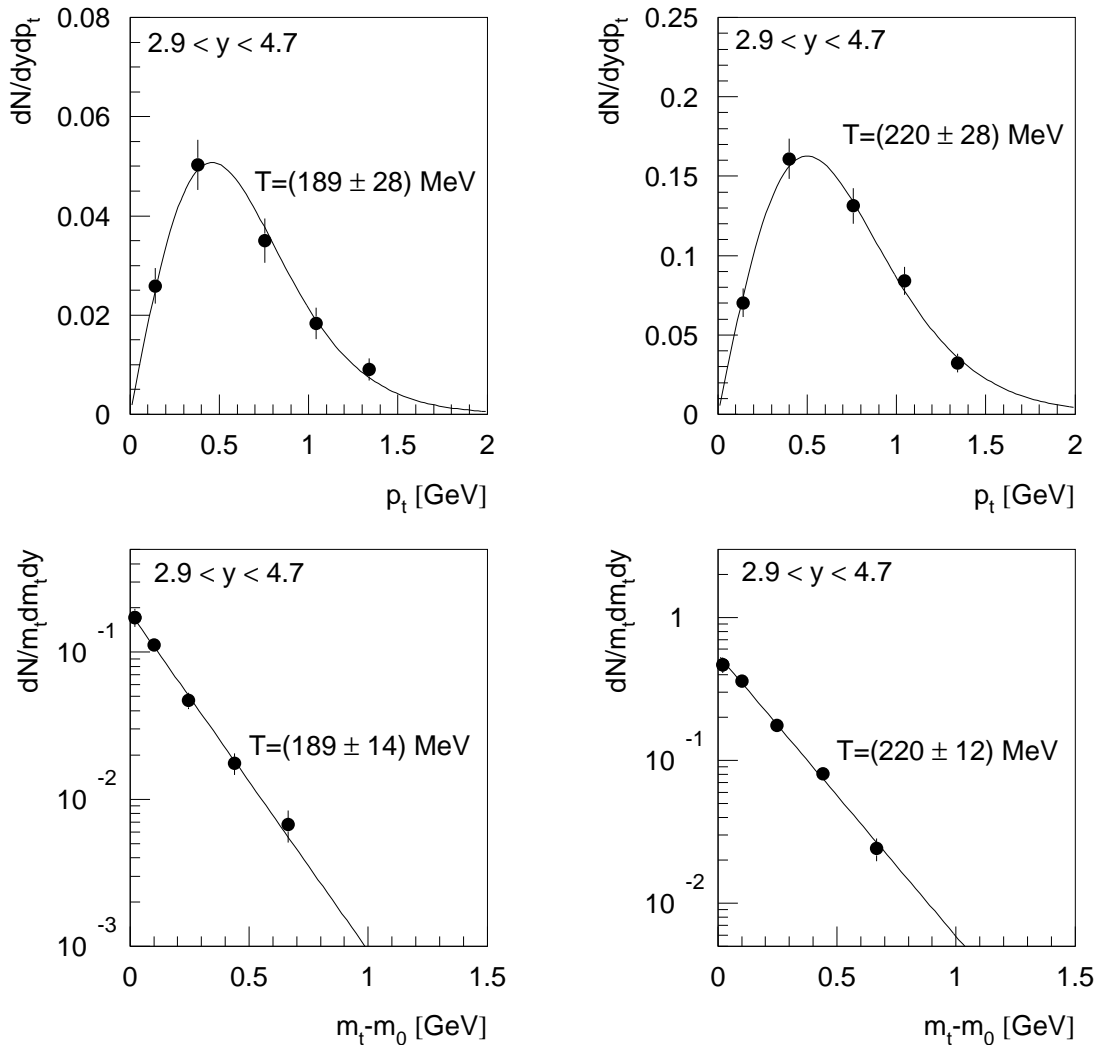


Figure 6.13: Transverse-momentum and transverse-mass spectrum of the ϕ -meson in C+C (upper row) and Si+Si (lower row). A thermal function is fitted to the data, the result is indicated by the line and the inverse slope with the statistical error of the fit is given.

Transverse-momentum distribution

Transverse-momentum distributions extracted for C+C and Si+Si collisions are presented in figure 6.13 together with thermal fits. Errors differ depending on which presentation the adjustment is done; the fit to the m_t -distribution has the tendency to underestimate the real errors.

Systematic errors

As for p+p collisions the first check of the data consists in a comparison between the yields obtained from integrating the transverse-momentum spectra with those from rapidity distributions and from the extraction of the invariant-mass signal in close to the full acceptance of the ϕ -meson. Yields are found to agree within 3 %.

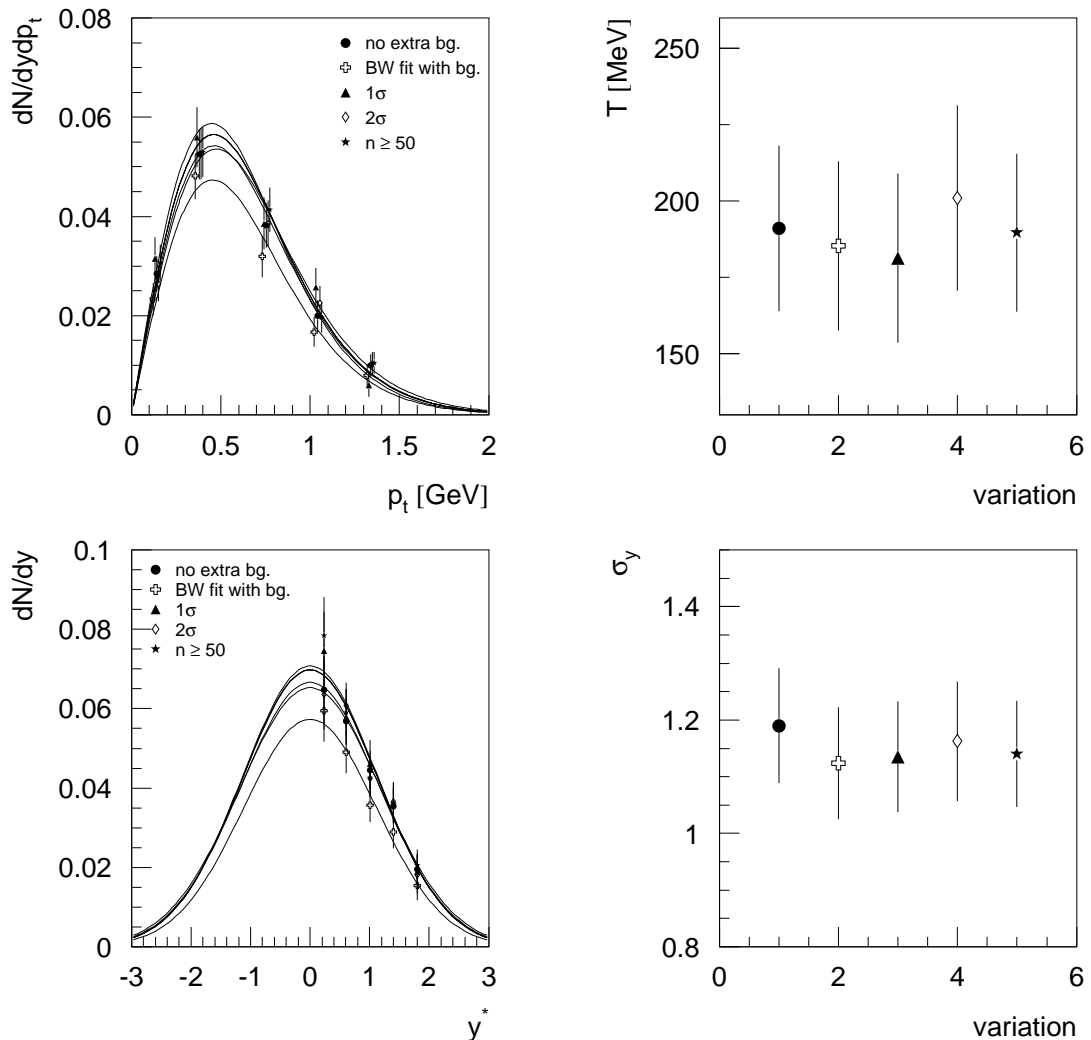


Figure 6.14: Transverse-momentum and rapidity distributions of the ϕ -meson in C+C collisions for various selection criteria. Symbols introduced in the upper row are also used below. The change of the extracted parameters is found to be well within the statistical error (lower row).

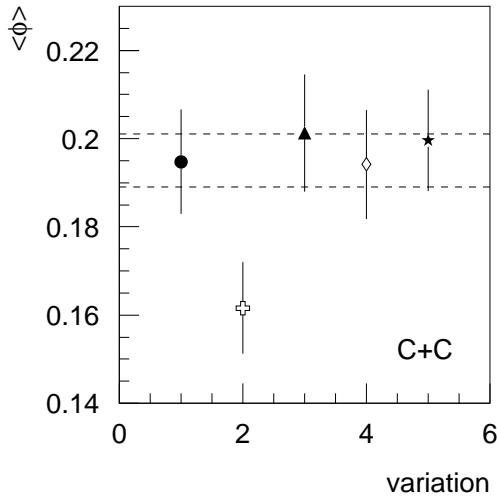


Figure 6.15: Variation of the total ϕ -yield from different kaon selection criteria and background treatment, symbols are defined in fig. 6.14. The latter causes the largest uncertainties (15-20 %), other variations change the yield by 3 % (C+C) and 4.3 % (Si+Si) only (dashed lines). For final results the mean of the two ways of background treatment is taken (full circle and open cross).

The stability of the results against variation of selection parameters for kaons is tested for both methods of background treatment and is found to be the same. Results for the ϕ -meson in C+C collisions for adjusting a simulation with undershoot are presented in figure 6.14. Mainly due to the reduced statistics the stability is not as good as for p+p collisions but still satisfactory. Temperatures and σ_y change within the statistical error. The largest uncertainty stems from background subtraction, total yields for C+C differ by 20 %, for Si+Si by 13 %. A total systematic error on the mean value of 12 % is therefore assumed.

6.4 $K^*(892)^0$ and $\overline{K}^*(892)^0$

For $K^*(892)^0$ and $\overline{K}^*(892)^0$ the presently available number of events was not sufficient to extract rapidity and transverse-mass distributions because of the reduced statistical significance of the signal. Therefore only total yields could be estimated from the $K^*(892)^0$ and $\overline{K}^*(892)^0$ signals in close to the full acceptance: invariant-mass distributions in a rapidity range of [3.1,4.7] and p_t -range of [0.,1.5] GeV were extracted (fig. 6.16 and 6.17). For both, kaons and pions, a momentum range of $0.6 < \log_{10}(p) \leq 1.7$ and $0 \text{ GeV} < p_t \leq 1 \text{ GeV}$ is used. The required minimum number of points per track and the window for kaon and pion selection in dE/dx is chosen as indicated in the figure captions.

$K^*(892)^0$ and $\overline{K}^*(892)^0$ are hardly visible in the original invariant-mass spectra. In the event-mix subtracted distributions a clear signal at the right mass is found, however, with moderate statistical significance. Applying selection criteria for kaons and pions as used for p+p, a background remains below the signal which reminds of distortions from reflections of $N^*(1440)$ and Δ resonances (see chapter 3.2.2): The $K^*(892)$ is decaying into $K^+\pi^-$, protons from the rather frequent $N^*(1440)$ or Δ resonances misidentified as K^+ enter the invariant-mass spectrum. Since $\overline{N}^*(1440)$ and $\overline{\Delta}$ are more rare and the fraction of \overline{p} misidentified as K^- is also smaller, the distortion due to reflections from baryonic-resonances is expected to be smaller for

σ_y	T [MeV]	\overline{acc}
1.1	220	0.138
1.2	220	0.138
1.3	220	0.136
1.4	220	0.133
1.2	160	0.146
1.2	180	0.143
1.2	200	0.141
1.2	220	0.138
1.2	240	0.135
1.2	260	0.131

Table 6.4: Mean acceptance \overline{acc} of $K^*(892)$ in a rapidity range of [3.1,4.7] and a p_t -range of [0.,1.5] GeV depending on assumptions about the kinematic distributions expressed by the parameters σ_y and T . The acceptance is calculated for $n_{points} \geq 100$ and a momentum range of $0.6 < \log_{10}(p) \leq 1.7$ and $0 \text{ GeV} < p_t \leq 1 \text{ GeV}$ for K^+ and π^- .

the $\overline{K}^*(892)^0$. Indeed, in the event-mix subtracted spectra for $\overline{K}^*(892)^0$ slightly less background seems to remain, however, due to the large statistical fluctuations this is difficult to judge.

The quality of the signal can be improved significantly by reducing the contribution of (anti-)protons to the kaon sample, unfortunately at the cost of the statistics in the peak. Besides selecting kaons in asymmetric windows in dE/dx , also requiring more points per track improves the signal, since for longer tracks the overlap of the dE/dx distributions is smaller due to a smaller $\sigma_{dE/dx}$. Choosing appropriate criteria, rather distortion-free spectra can be achieved (see fig. 6.16 (c) and 6.17 (c), cuts are described in the caption, see also fig. 3.16).

The total yield of $K^*(892)^0$ and $\overline{K}^*(892)^0$ is estimated by extracting the invariant-mass spectrum for different selection criteria for kaons and pions in a large rapidity and p_t -range. On the one hand sharp criteria for a clean spectrum, on the other hand standard cuts are used. In the latter case a linear and a polynomial background is fitted to the remaining distortion and the simulated signal is adjusted on top of it. In all cases both, a pure Breit-Wigner distribution and a full simulation including the undershoot structure are fitted to the data. The simulation is performed assuming a rapidity distribution as extracted for kaons, i. e. a Gaussian with a width of $\sigma_y = 1.2$. For the inverse slope of the transverse-momentum distribution, values similar to those of the ϕ -meson are taken in accordance with the transverse-flow systematics, i. e. $T = 190 \text{ MeV}$ and 220 MeV (see section 7.1). Statistical errors of the extracted yields are 15-20 %.

The influence of assumptions about the kinematic distributions on the total yield is investigated, the mean acceptance of $K^*(892)^0$ in the chosen y and p_t -range

	C+C	Si+Si
$\langle K^*(892)^0 \rangle$	0.8 ± 0.24	2.2 ± 0.66
$\langle \overline{K}^*(892)^0 \rangle$	0.43 ± 0.14	1.3 ± 0.4

Table 6.5: Estimation of $K^*(892)$ -yield in C+C and Si+Si collisions at 158 AGeV.

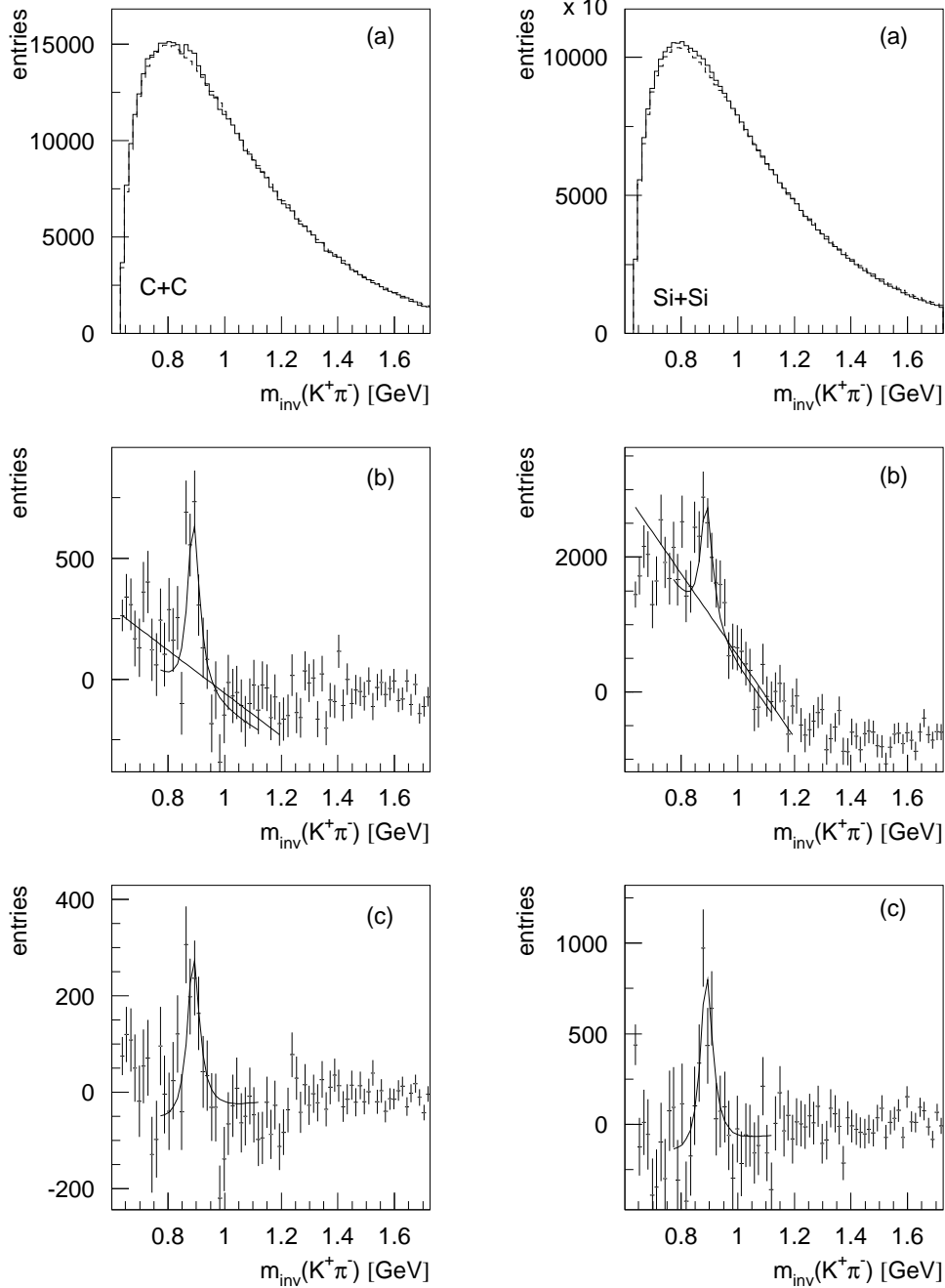


Figure 6.16: Invariant-mass distribution for $K^*(892)^0$ in C+C (left) and Si+Si (right). In (a) the original spectrum for track cuts of $n_{points} \geq 50$ and $\pm 1.5 \sigma_{dE/dx}$ is shown; the dashed line corresponds to the event-mix spectrum. In (b) the background-subtracted signal is shown with a Breit-Wigner distribution adjusted on top of a straight line, which approximates the remaining distortion. In (c) the cleanest background-subtracted signal is presented, track selection criteria are $n_{points} \geq 100$, $\pm 1.5 \sigma_{dE/dx}$ for π^- and $[-0.5, 1.5] \sigma_{dE/dx}$ for K^+ . The line corresponds to a simulation.

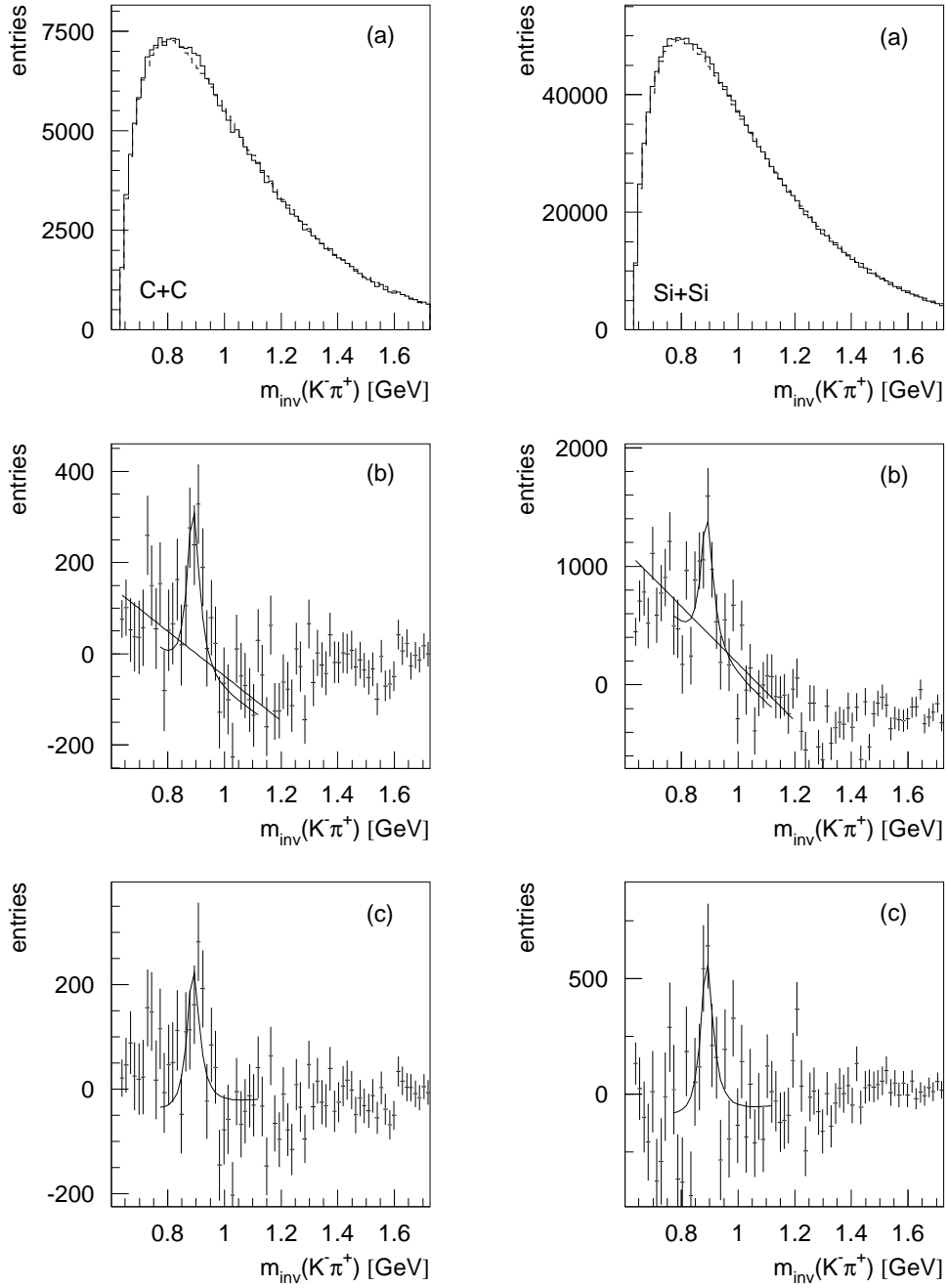


Figure 6.17: Invariant-mass distribution for $\overline{K}^*(892)^0$ in C+C (left) and Si+Si (right). In (a) the original spectrum for track cuts of $n_{points} \geq 50$ and $\pm 1.5 \sigma_{dE/dx}$ is shown; the dashed line corresponds to the event-mix spectrum. In (b) the background-subtracted signal is presented with a Breit-Wigner distribution adjusted on top of a straight line approximating the remaining distortion. In (c) the best background-subtracted signal is presented, track selection criteria are $n_{points} \geq 50$, $\pm 1.5 \sigma_{dE/dx}$ for π^+ and $[-0.5, 1.5] \sigma_{dE/dx}$ for K^- for C+C. In case of Si+Si, $n_{points} \geq 100$ and $\pm 1.5 \sigma_{dE/dx}$ is required for both, π^+ and K^- . The line corresponds to a simulation.

can be found in table 6.4 for one type of selection criteria. The extrapolation factor, i. e. the inverse of $\overline{ac\bar{c}}$, varies by 11 % between $T = 160$ MeV and 260 MeV. For temperatures of the $K^*(892)^0$ probably lying somewhere in between, about 6 % systematic uncertainties for the extrapolation are the result.

For the final estimate of the total yields of $K^*(892)^0$ and $\bar{K}^*(892)^0$ (table 6.5), results from the variation of selection criteria and additional assumptions concerning the remaining background are averaged. The scatter of the results is an indication of the systematic error stemming from problems describing the background. Results differ by ± 15 % for $\bar{K}^*(892)^0$ in Si+Si at the most. A reasonable combined statistical and systematic accuracy for the estimate of total yields is ± 30 %.

Once the expected factors 5 and 3.5 in the number of events will be available for C+C and Si+Si collisions (see table 4.5), the signals will improve significantly and an analysis of $K^*(892)^0$ and $\bar{K}^*(892)^0$ possibly with extraction of their kinematic distributions should be achievable.

Chapter 7

Discussion

In this work, the system-size dependence of strangeness production in A+A collisions is investigated experimentally by studying the yields of charged kaons, $K^*(892)^0$, the ϕ -meson, and pions from p+p, central C+C and Si+Si interactions. Together with other published results these data open the possibility to study the influence of a systematic variation of entrance channel parameters. Aim of these studies is the understanding of one of the central questions in heavy-ion physics, the origin of strangeness enhancement in A+A relative to p+p. Recently, NA49 measured the energy dependence of strangeness production in central Pb+Pb collisions between 20 AGeV and 158 AGeV beam energy [71, 131]. The alternative chosen in this work is a variation of the mass of the colliding nuclei in order to study the onset of the strangeness enhancement in comparison to p+p in dependence on the system size.

In this chapter, the experimental results obtained in this work will be discussed. First, the data are summarized and compared to measurements by NA49 and other experiments which are relevant in this context (section 7.1). Then, possible sources of the increased ratio of strange to non-strange particles will be investigated before summarizing the arguments and proposing a conclusion (section 7.6):

- Rescattering, i. e. interactions in the final hadronic phase of the collision could influence the observed yields of strange and non-strange hadrons (section 7.2).
- The consequence of sequential N+N interactions occurring in A+A collisions and continuously exciting the nucleons will be tested under the assumption that each excited nucleon or string collects the energy in its successive interactions and decays or hadronizes independently in the end (section 7.3).
- Empirical scaling variables taking into account the different geometry of all collision systems compared, central interactions of light nuclei and centrality-selected Pb+Pb, might point at physical parameters being important or crucial for the onset of strangeness enhancement (section 7.4).
- Statistical models for particle yields imply a volume dependence of strangeness production. It will be studied whether this provides an explanation of the observed system-size effect in the data (section 7.5).

7.1 Experimental results

The analysis of the data obtained in this work for minimum-bias and inelasticity selected p+p as well as for central C+C and Si+Si collisions is described in chapters 5 and 6. The results for particle yields are summarized in tables 7.1 and 7.2. A list of inelasticity-dependent yields in p+p can be found in appendix C. In section 5.1.5 minimum-bias yields measured in p+p were compared to results from literature. For C+C and Si+Si collisions no direct comparison is available, the most similar reaction system is central S+S at 200 AGeV beam energy measured by the NA35 experiment [128, 132, 133]. A comparison of transverse momentum and rapidity distributions can be found in appendix C, as well as a comparison of pions and kaons from this work with a preliminary analysis of the NA49 data from F. Sikler [12]. Overall, a good agreement is found, for more details see appendix C.

In the following discussion other data providing additional information on the system-size dependence of strangeness production are included (see also table 7.1):

- NA35 measured charged pions, charged kaons, the K_S^0 , Λ and $\bar{\Lambda}$ -baryons in central S+S collisions at 200 AGeV beam energy ($\sqrt{s} = 19.4$ GeV) [132, 133, 137]. Results for Λ and $\bar{\Lambda}$ -baryons differ systematically by 15 % and 47 %, respectively, between [137] and [133]. However, they agree within their large errors. For the comparison in this work the higher yields of [133] are used since these values stem from the final analysis of NA35. The center-of-mass energy for NA35 is slightly higher than for the collisions investigated in this work, but from the observed energy dependence of relative strangeness production one expects only a weak change, if any at all, in the ratios under investigation from 158 AGeV to 200 AGeV beam energy [71, 138]. However, if considering particle yields, about 6-12 % higher values are expected for 200 AGeV due to the energy dependence of multiplicities (see fig. 5.24 for p+p).
- NA49 took data of central Pb+Pb collisions at 158 AGeV. This is the heaviest system which can be investigated and, as it turns out, represents the asymptotic situation concerning strangeness enhancement at this energy. For the comparison in this work only data of pion, charged kaon, ϕ , Λ and $\bar{\Lambda}$ production, as well as preliminary results on $K^*(892)^0$ and $\bar{K}^*(892)^0$ yields are used [71, 101, 111, 138].
- NA49 also investigated minimum-bias Pb+Pb interactions at 158 AGeV; preliminary results are available for charged pions and kaons, the ϕ -meson and $\bar{K}^*(892)^0$ [109, 111, 135]. The events can be divided into intervals of centrality or impact parameter range [74]. At first, it seems that this should be an equivalent tool to vary the number of participants and to study the system-size dependence of particle production. However, at the same number of participants the geometry of the interaction differs strongly between peripheral Pb+Pb and central C+C or Si+Si collisions. As will become clear later, besides the number of participants also other conditions change which are important for the ratios of strange to non-strange particles (see section 7.4). It should be emphasized that

fraction of cross section	C+C		Si+Si		S+S		Pb+Pb				
	15.3 %	12.2 %	2 %	5 %	7.5 %	11 %	10 %	10 %	10 %	17 %	57 %
$\langle\pi^+\rangle$	22.5 ± 0.3	57.0 ± 0.7	91±3	619 ± 17	519 ± 1.5	394 ± 1	290 ± 1	191 ± 1	105 ± 1		
$\langle\pi^-\rangle$	22.2 ± 0.3	57.8 ± 0.7	12.5 ± 0.4	639 ± 17	480 ± 1.5	360 ± 1	267 ± 1	174 ± 1	98 ± 1		
$\langle K^+\rangle$	2.54 ± 0.03	7.44 ± 0.08	6.9 ± 0.4	103 ± 5	80±1	54±1	35.5 ± 1	20.5 ± 1	10.3 ± 1		
$\langle K^-\rangle$	1.49 ± 0.05	4.42 ± 0.04		51.9 ± 1.9	45.1 ± 0.5	29.7 ± 0.5	20.2 ± 0.5	11.8 ± 0.5	5.5 ± 0.5		
$\langle K^*(892)^0\rangle$	0.8 ± 0.24	2.2 ± 0.66		12.9 ± 1.4							
$\langle K^*(892)^0\rangle$	0.43 ± 0.14	1.3 ± 0.4		8.21 ± 0.75	6.48 ± 0.55	4.24 ± 1.46	3.59 ± 1.04	3.05 ± 0.59	1.37 ± 0.43		
$\langle\phi\rangle$	0.178 ± 0.011	0.661 ± 0.032		7.6 ± 1.1	5.6 ± 0.43	3.63 ± 0.36	2.51 ± 0.19	1.46 ± 0.1	0.65 ± 0.08		
$\langle\Lambda\rangle$	1.43 ± 0.05	4.50 ± 0.16	9.4 ± 1.0	49 ± 5							
$\langle\bar{\Lambda}\rangle$	0.27 ± 0.06	0.66 ± 0.20	2.2 ± 0.4	4.3 ± 0.3							
$\langle N_{part}\rangle$	16.3 ± 1	41.4 ± 2	54	366 ± 8	309 ± 10	242 ± 10	178 ± 10	132 ± 10	85 ± 6		
$\langle N_{wound}\rangle$	14 ± 2	37 ± 3	(~51)	352	281	204	134	88	42		
$\langle\nu_{wound}\rangle$	1.9	2.5	2.7	4.6	4.3	3.9	3.4	2.9	2.2		
f	0.536	0.70	0.751	0.90	0.85	0.80	0.742	0.680	0.546		
$\langle\rho_{wound}\rangle$	0.96	1.49	1.66	2.95	2.78	2.52	2.14	1.78	1.10		
$\langle\rho_{inel coll}\rangle$	3.31	4.58	5.04	7.27	6.27	5.37	4.40	3.43	1.96		

Table 7.1: Particle yields for central C+C and Si+Si from this work and [134], and for centrality-selected Pb+Pb collisions from NA49 for $E_{lab} = 158$ AGeV [71, 78, 101, 109, 111, 135], as well as for central S+S interactions at 200 AGeV from NA35 [132, 133]. Only statistical errors are quoted, systematic errors are typically 5-7 % for pions, 10 % for kaons and the ϕ -meson and 10-30 % for the $K^*(892)$. Λ and $\bar{\Lambda}$ have 20 % and 40-50 % systematic errors in C+C and Si+Si, but less in Pb+Pb. The centrality given in the 2nd row is specified by the fraction of the cross section selected in the reaction. For C+C, Si+Si, S+S, and for the first Pb+Pb column it holds for the most central collisions. For the other Pb+Pb data the fractions belong to consecutive centrality intervals with increasing impact parameter [74]. N_{part} and N_{wound} were determined in chapter 4.3 (C+C, Si+Si) and by G. Cooper [74] (Pb+Pb). The calculation of the other centrality parameters in the lower 4 rows of the table is explained in appendix D. Typical errors of these values are on the order of 5-10 %.

	p+p (NA49 min. bias)
$\langle\pi^+\rangle$	$3.07\pm 0.01 \pm 0.15$
$\langle\pi^-\rangle$	$2.33\pm 0.01 \pm 0.12$
$\langle K^+\rangle$	$0.238\pm 0.001 \pm 0.024$
$\langle K^-\rangle$	$0.138\pm 0.001 \pm 0.014$
$\langle K^*(892)^0\rangle$	$0.0792\pm 0.0016 \pm 0.0063$
$\langle \bar{K}^*(892)^0\rangle$	$0.0559\pm 0.0011 \pm 0.0045$
$\langle\phi\rangle$	$0.0129\pm 0.0002 \pm 0.0013$
$\langle\Lambda\rangle$	0.130 ± 0.012
$\langle\bar{\Lambda}\rangle$	0.015 ± 0.001

Table 7.2: Particle yields in minimum-bias p+p collisions from NA49 data for $E_{lab} = 158$ GeV, i. e. $\sqrt{s} = 17.3$ GeV, from this work. The first error is statistical, the second systematic. Yields for Λ and $\bar{\Lambda}$ baryons are from T. Susa [136].

these minimum-bias Pb+Pb data are preliminary. Two analyses with differing results exist for kaons and pions [12, 109] and also for the ϕ -meson [110, 135]. For the comparison in this work ref. [109, 135] are used. The results on kaons are supported by a recent analysis of kaon yields at midrapidity using the time-of-flight identification procedure [139]. For the ϕ -meson the most recent analysis presented also at conferences was chosen.

- For C+C and Si+Si collisions a measurement of Λ and $\bar{\Lambda}$ baryons is also available [134]. The yields will be included in the discussion only in section 7.5, since no inelasticity-dependent data in p+p interactions and no centrality-dependent yields in Pb+Pb exist. In addition, the Λ as a baryon shows a stronger sensitivity to the baryochemical potential as, e. g., the K^+ . As a leading baryon it also experiences a larger stopping in A+A collisions compared to p+p.

Due to strangeness conservation yields of kaons and Λ -baryons should approximately fulfill the following relation: $1.6(\Lambda - \bar{\Lambda}) = 2(K^+ - K^-)$. In this equation Ξ and Ω are disregarded which is excusable because of their small yields; the factor 1.6 takes Σ -baryons into account. Kaons from this work and Λ from [134] are consistent according to this equation.

Centrality-dependent strangeness production in Pb+Pb collisions at 158 AGeV was also measured by the experiments NA52 [140, 141], and WA97 and its successor NA57 (see [25] for a recent summary of results, see also fig. 1.13). WA97 and NA57 are designed to observe strange baryons at midrapidity, NA52 measured charged kaons in the rapidity range $3.1 < y < 4.4$. Both experiments present their yields normalized to the number of wounded nucleons (WA97, NA57) or participants (NA52)¹. The observed ratios increase slightly with centrality, at least concerning single strange hadrons. NA52 observes a threshold behavior for very small N_{part} . Both measurements are consistent with the data from NA49 which are shown in fig. 7.9 in the corresponding presentation.

¹The N_{part} values of NA52 are close to the values for N_{wound} of NA49, which suggests different definitions.

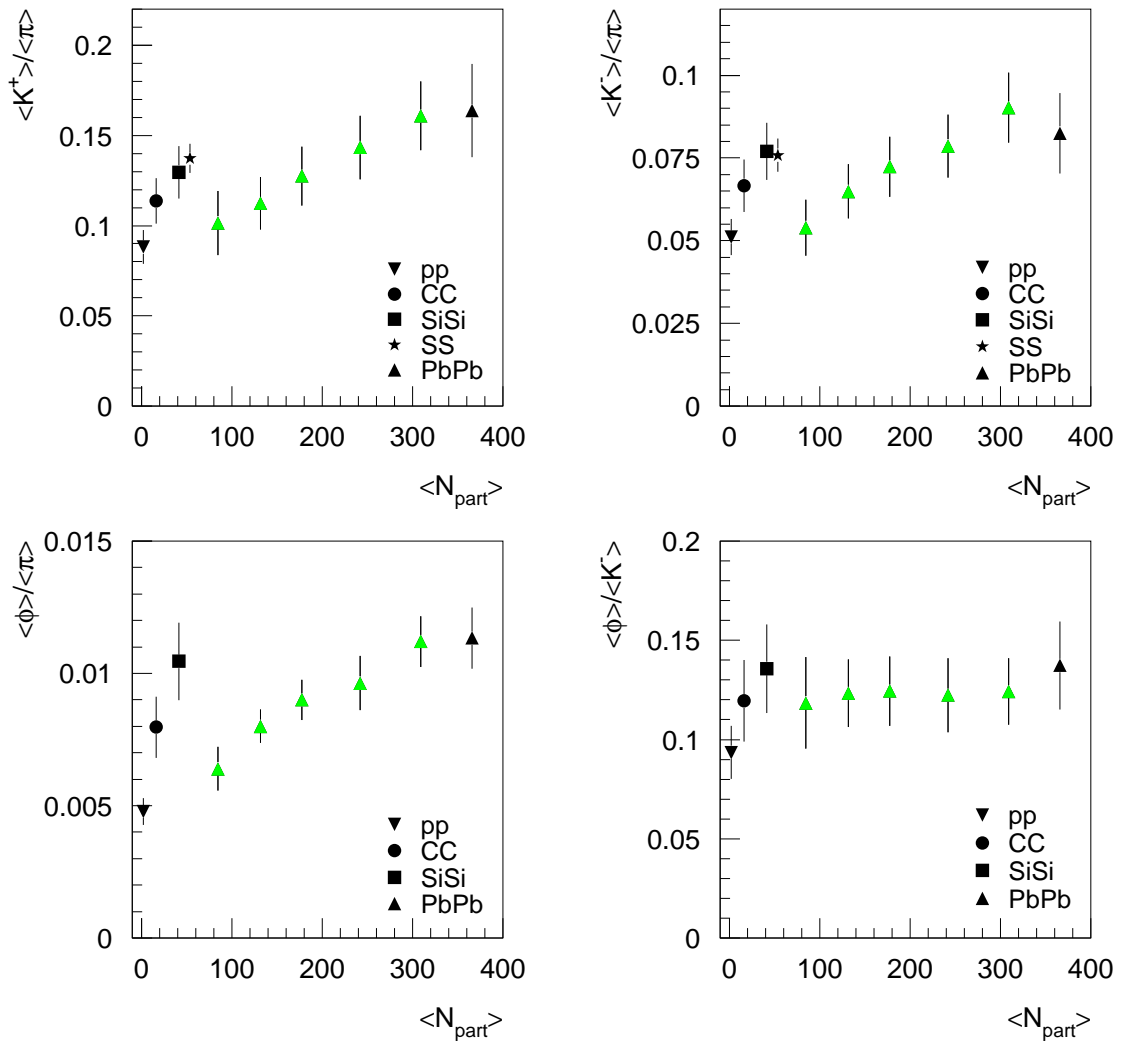


Figure 7.1: Particle ratios in dependence on the number of participants, see text for discussion. $\langle \pi \rangle = \frac{1}{2} (\langle \pi^- \rangle + \langle \pi^+ \rangle)$.

Relative strangeness production would be best measured by the Wroblewski factor $\lambda_s = \frac{2\langle s\bar{s} \rangle}{\langle u\bar{u} + d\bar{d} \rangle}$. Since kaons are the most abundant strangeness-carrying mesons and pions the most abundant mesons carrying up and down quarks, their ratio behaves like λ_s and represents the relative strangeness content in the final state of a collision.

Figure 7.1 presents the most important ratios of particle yields for the discussion of strangeness production in dependence on the size of the collision system. Two main observations based on the $\langle K \rangle / \langle \pi \rangle$ and $\langle \phi \rangle / \langle \pi \rangle$ ratios shall be emphasized:

- A significant increase of relative strangeness production compared to p+p is found already in the light collision systems C+C and Si+Si with only 16 and 41 participating nucleons. The level reached in Si+Si interactions is close to the one known from central S+S reactions at 200 AGeV and central Pb+Pb at 158 AGeV: Relative strangeness production rises fast in dependence on N_{part} and,

given the available data, seems to saturate above ~ 60 participants if comparing central A+A interactions only (see also fig. 7.17).

- $\langle K \rangle / \langle \pi \rangle$ and $\langle \phi \rangle / \langle \pi \rangle$ ratios show a discontinuity in dependence on N_{part} comparing central collisions of light systems and peripheral Pb+Pb. This *geometry dependence* is caused by the different spatial arrangement of the nucleons in these two types of collision systems.

ϕ -meson and $K^*(892)$ show further interesting features:

The ϕ -meson carries two strange quarks which could result in the ϕ -enhancement behaving as the square of the kaon enhancement. As the $\langle K \rangle / \langle \pi \rangle$ ratio is observed to increase rather proportionally with N_{part} in either the light central collisions or the peripheral Pb+Pb, a linear increase of the $\langle \phi \rangle / \langle K^- \rangle$ ratio would be expected for this case. Fig. 7.1 (lower right) demonstrates, that this is indeed observed comparing p+p, C+C, and Si+Si collisions. However, for centrality-selected Pb+Pb the rise is very weak. An indication of the geometry effect is found also here. In fig. 7.1 negatively charged kaons were chosen for normalization since they represent the abundance of newly created strange quarks without the influence of associated $K\Lambda$ production. Normalizing the various ratios to their value in p+p, the $\langle \phi \rangle / \langle \pi \rangle$ ratio indeed increases to a very good approximation as the square of the $\langle K^- \rangle / \langle \pi \rangle$ or $\langle K^+ \rangle / \langle \pi \rangle$ ratio (fig. 7.2).

At first, kaons and the $K^*(892)$ as their excited states are expected to experience the same evolution with the size of the collision system. However, obviously the $K^*(892)$ is not enhanced in A+A collisions compared to pions, but is even significantly suppressed compared to kaons (fig. 7.3). This special role of $K^*(892)$ can be understood as a consequence of their short lifetime ($\tau = 3.9$ fm/c) and will be discussed in chapter 7.2.

Before discussing in detail the observed strangeness enhancement and its possible origin, the development of pion production with system size and systematic trends in kinematic distributions of the measured hadrons shall be investigated:

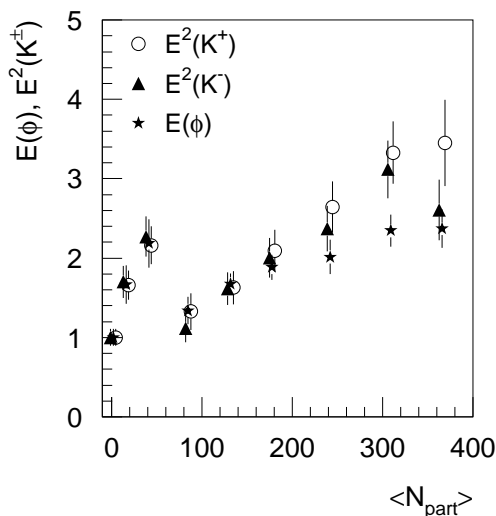


Figure 7.2: Comparison of the relative ϕ -enhancement normalized to p+p with the square of the respective kaon enhancement. For better visibility the single measurements are slightly displaced in N_{part} .

$$E(K^\pm) = \frac{(\langle K^\pm \rangle / \langle \pi \rangle)_{AA}}{(\langle K^\pm \rangle / \langle \pi \rangle)_{pp}}, \quad E(\phi) = \frac{(\langle \phi \rangle / \langle \pi \rangle)_{AA}}{(\langle \phi \rangle / \langle \pi \rangle)_{pp}}.$$

$$\langle \pi \rangle = \frac{1}{2} (\langle \pi^- \rangle + \langle \pi^+ \rangle).$$

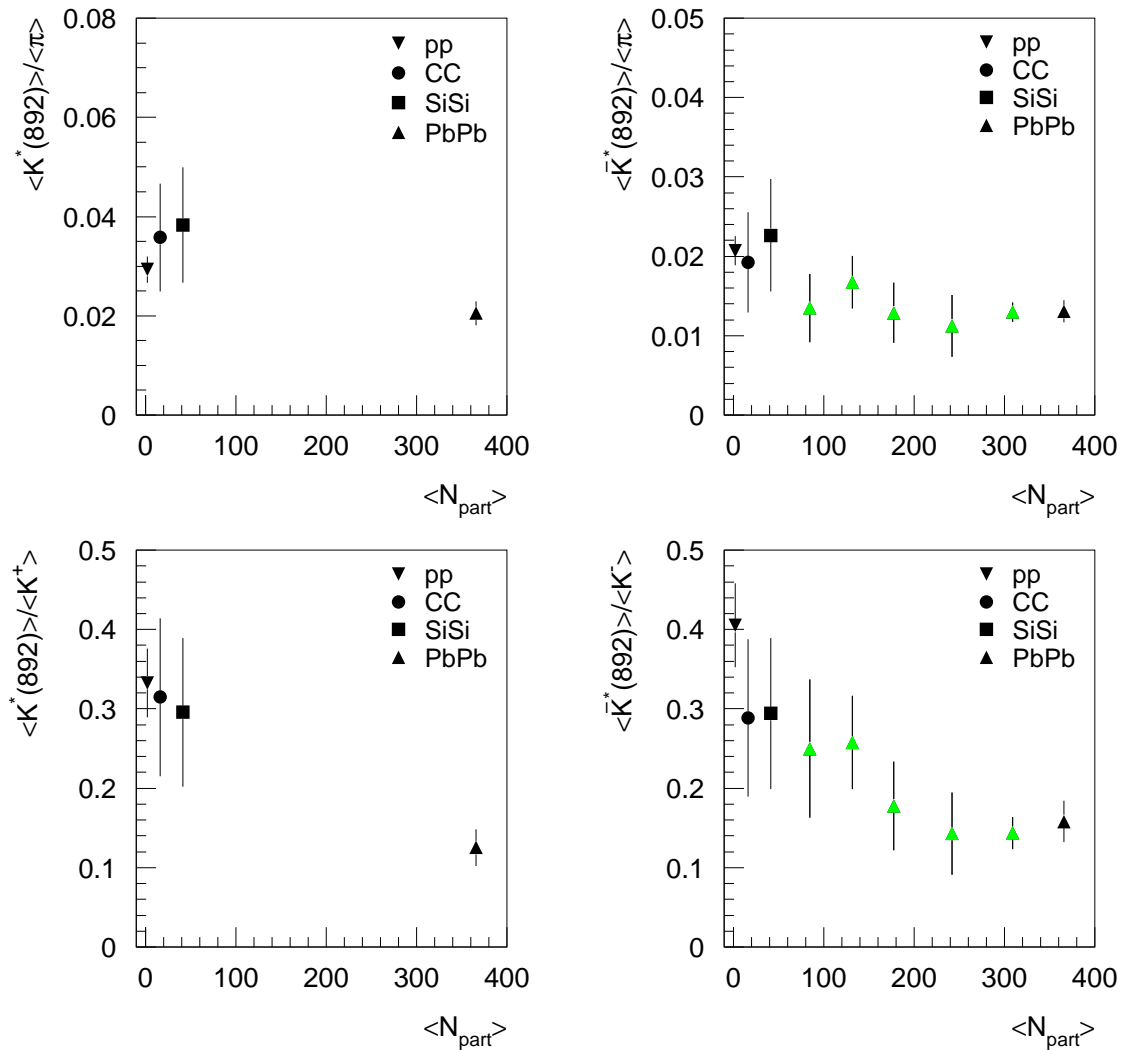


Figure 7.3: Particle ratios in dependence on the number of participants, see text for discussion. $\langle \pi \rangle = \frac{1}{2} (\langle \pi^- \rangle + \langle \pi^+ \rangle)$.

Characterizing the system size by the number of wounded nucleons N_{wound} or participating nucleons N_{part} (see section 4.3 and 7.4 for a definition of both quantities), the evolution of pion production may be investigated relative to them (fig. 7.4). Overall, relative pion yields rise by about 30 % from p+p to central Pb+Pb. Relative to N_{wound} a significant increase is found already in C+C and Si+Si collisions. While the number of participants is approximately proportional to the pion production, a large excess of pions relative to N_{wound} in peripheral Pb+Pb compared to all central A+A collisions is observed: N_{wound} and N_{part} differ by a factor of two in peripheral Pb+Pb but only by 4 % in central Pb+Pb collisions (see table 7.1). Obviously many nucleons re-scatter in the large amount of spectator matter present in peripheral collisions. The discontinuity can be understood considering that nucleons participating in the reaction only via secondary collisions might not experience energy losses as large as the primary colliding nucleons. They would in particular produce light pions.

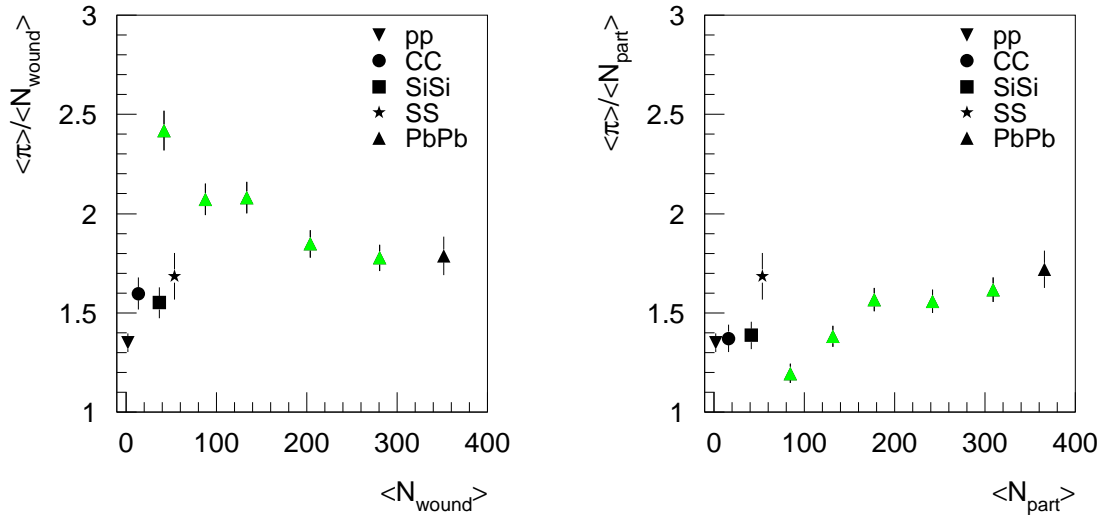


Figure 7.4: Ratio of total pion yield to the number of wounded (left) and participating nucleons (right) in dependence on the number of wounded nucleons or participants. S+S data are from [132], data on Pb+Pb collisions from [71, 109], $\langle \pi \rangle = 0.5 \cdot (\langle \pi^+ \rangle + \langle \pi^- \rangle)$. Pion yields from S+S are not corrected for the higher energy, a reduction by $\sim 7\%$ would be expected using the parametrization of Rossi et al. [105].

Transverse-momentum distributions of all mesons investigated in this work show a continuous change when increasing the size of the collision system. The effect is illustrated in fig. 7.5. Effective temperatures from the thermal fits increase with the mass of the emitted particles and with system size. The increase with particle mass is commonly interpreted as a sign for transverse flow taking place in the created fireball [40, 41] (see also chapter 1.4.5). The flow velocity is added to the thermal transverse-momentum distribution. This results in effective temperature parameters that are larger than in p+p collisions and increase with mass. In addition the flow increases with system size.

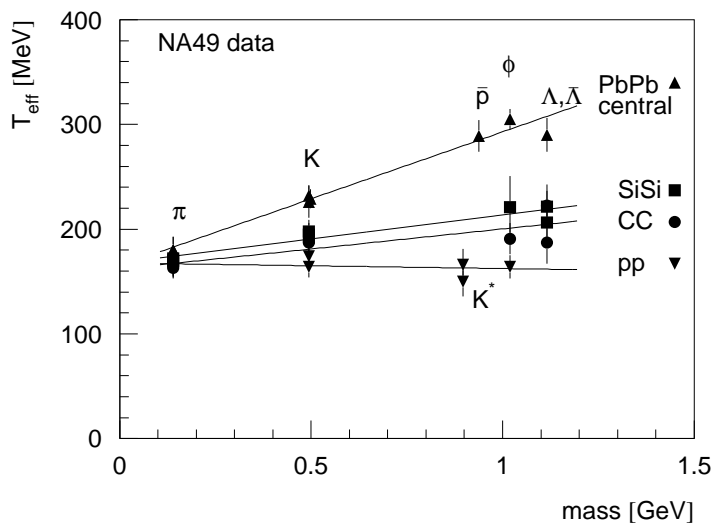


Figure 7.5: Effective temperatures versus the mass of the emitted particles for different collision systems. Data included in the picture are from [134] ($\Lambda, \bar{\Lambda}$ in C+C and Si+Si), [71, 78, 101] (central Pb+Pb collisions), and this work.

For the longitudinal distribution the same effect should hold, but already in p+p collisions rapidity distributions are wider than expected from a purely thermal source [41]. Obviously, a longitudinal expansion originating from the incoming projectiles is dominating. An additional longitudinal flow in A+A collisions should appear only as a small effect in the width of the spectra. Indeed, rapidity distributions indicate only a slight broadening by about 10 % between p+p and C+C and Si+Si collisions, which might be caused by the discussed flow effect. The strongest change is observed for the ϕ -meson. Here, σ_y is significantly larger in C+C and Si+Si collisions compared to p+p ($\sigma_y^{pp} = 0.95 \pm 0.045$, $\sigma_y^{CC} = 1.16 \pm 0.11$, $\sigma_y^{SiSi} = 1.27 \pm 0.11$), whereas the width in Pb+Pb ($\sigma_y^{PbPb} = 1.22 \pm 0.16$ [64, 101]) is similar to the intermediate systems. Apparently, the broadening sets in very fast with increasing system size.

7.2 Rescattering

Secondary interactions between the produced particles in the expanding hadron gas are called *rescattering*. They may still change kinematic properties and hadron abundances of the system: Elastic interactions increase the mean transverse momenta and are therefore at least partially responsible for the development of transverse flow. This effect can be reproduced in models, see e. g. [33, 142]. Inelastic interactions on the other hand influence particle abundances by reactions like $\pi + \pi \rightarrow K + \bar{K}$, $\pi + N \rightarrow \Lambda + K$, $N + N \rightarrow \Lambda + K + N$, or $\bar{K} + N \rightarrow \Lambda + \pi$, to mention a few of them affecting strange particles. However, relative yields are only changed by these processes, if the hadron gas is not in chemical equilibrium; otherwise reverse reactions would take place with the same frequency. According to statistical model calculations, a higher strange particle content is expected in an equilibrated hadron gas compared to the observed final state of p+p interactions (see section 1.3.4). The amount of the enhancement depends on temperature and baryochemical potential.

The frequency of these secondary interactions and their influence are difficult to estimate because of the lack of a direct measurement. Basically, there are two ways to obtain information. On the one hand experimental evidence can be collected supporting or questioning the influence of rescattering processes. Some data, together with theoretical information, also provide quantitative arguments. The second approach is based on microscopic simulations of A+A collisions.

The increase of mean transverse momenta compared to p+p interactions, i. e. the observation of higher effective temperatures in the p_t -spectra, can be taken as experimental evidence for the presence of elastic scattering processes. A clear indication for this so-called transverse flow was found in C+C and Si+Si collisions (fig. 7.5), but the effect is still much weaker than in central Pb+Pb. However, it is not mandatory to explain the flow pattern by elastic interactions. It can also be argued that it is built up mainly in an early (partonic) phase [58, 142].

The assumption that rescattering is the origin of the observed strangeness enhancement would imply that already in the rescattering phase of Si+Si interactions

the hadron gas reaches chemical equilibrium, because the $\langle K \rangle / \langle \pi \rangle$ ratio in Si+Si collisions is close to the one in central Pb+Pb. However, this is inconsistent compared to results from peripheral Pb+Pb interactions. Here, multiplicities are much larger (see e.g. pion yields in table 7.1) than in Si+Si reactions and this leads to a higher frequency of rescattering processes (see discussion below in context with the UrQMD simulations). Consequently, if in Si+Si interactions the hadron gas reaches chemical equilibrium it should also do so in peripheral Pb+Pb and result in the same $\langle K \rangle / \langle \pi \rangle$ ratio. However, this is in contradiction to the data.

In addition, from other measurements it can be argued that the time for a rescattering phase is too short for thermal and chemical equilibration. Experimental evidence for the short lifetime of the fireball comes from Bose-Einstein correlations of pions in the final state. They carry information about source size and time span of their final kinetic decoupling from the fireball. Experimental measurements indicate that in central Pb+Pb collisions pions are emitted within a very short time span ($\Delta\tau \approx 3-4$ fm/c) around a mean expansion time of about 8 fm/c [143]. In S+S collisions at 200 AGeV an even shorter duration of pion emission is measured ($\Delta\tau < 2$ fm/c) with a mean emission time of 4 fm/c [144]. On the other hand, hadronic equilibration times at SPS energies are calculated to be much longer, depending on the model from 10 fm/c to more than 40 fm/c concerning, for example, kaons [24, 56].

The investigation of very short-lived resonances with a mean lifetime comparable to that of the fireball offers a more quantitative approach (see e.g. [145, 146]). Possible candidates are the $K^*(892)$ with a mean lifetime of 3.91 fm/c, but also the $\Lambda(1520)$ with $\tau = 12.7$ fm/c. A sizeable fraction of these resonances decays in the dense hadron gas and their decay products experience at least part of the rescattering phase. If one of the decay products is destroyed in an inelastic collision, the resonance cannot be reconstructed anymore and is lost for analysis. The result would be a suppression of the specific resonance in comparison to its abundance in p+p collisions, the more, the more frequent rescattering processes take place. However, the resonances can also be regenerated by coalescence of, e.g., kaons and pions in case of the $K^*(892)$.

Indeed, an indication of $K^*(892)$ suppression is found in C+C and Si+Si interactions; it becomes more obvious in central Pb+Pb collisions (fig. 7.3): Contrary to kaons the $\langle K^*(892) \rangle / \langle \pi \rangle$ ratio stays rather constant or even decreases in A+A collisions compared to p+p. Since to first order the relative production rate of kaons and $K^*(892)$ should not change from p+p to A+A interactions, their different evolution is even better seen in the $\langle K^*(892) \rangle / \langle K \rangle$ ratio. Unfortunately the errors are large; the trend of gradual suppression, however, is clearly visible.

Drawing conclusions about the effect of rescattering processes on the total strangeness yield via the $K^*(892)$ suppression needs a translation of this observation into a general influence or abundance of rescattering processes. This can only be done by employing model calculations. Independently of the $K^*(892)$, microscopic models are of interest because they allow to study the influence of rescattering processes on particle abundances.

	p+p	C+C $b < 2$ fm	Si+Si $b < 2.5$ fm	Pb+Pb $b < 3.5$ fm
$\langle N_{part} \rangle$	2	20	48.6	394.3
$\langle \pi^+ \rangle$	2.49	29.2	78.	764.
$\langle \pi^- \rangle$	1.99	29.1	77.5	795.
$\langle K^+ \rangle$	0.208	2.88	7.88	91.9
$\langle K^- \rangle$	0.136	1.89	5	53.5
$\langle K^*(892)^0 \rangle$	0.0783	1.104	3.28	
$\langle \bar{K}^*(892)^0 \rangle$	0.0442	0.602	1.77	
$\langle \phi \rangle$	0.00489	0.0738	0.235	
$\langle K^+ \rangle / \langle \pi \rangle$	0.093	0.099	0.101	0.118
$\langle K^- \rangle / \langle \pi \rangle$	0.061	0.065	0.064	0.069
$\langle K^*(892)^0 \rangle / \langle \pi \rangle$	0.035	0.038	0.0422	
$\langle \bar{K}^*(892)^0 \rangle / \langle \pi \rangle$	0.020	0.021	0.023	
$\langle K^*(892)^0 \rangle / \langle K^+ \rangle$	0.376	0.383	0.416	
$\langle \bar{K}^*(892)^0 \rangle / \langle K^- \rangle$	0.325	0.319	0.354	
$\langle \phi \rangle / \langle \pi \rangle$	0.0022	0.0025	0.0030	
$\langle \phi \rangle / \langle K^- \rangle$	0.036	0.039	0.047	

Table 7.3: Particle yields and ratios in inelastic p+p, central C+C, Si+Si and Pb+Pb collisions from UrQMD simulations for $E_{lab} = 158A$ GeV; $\langle \pi \rangle = \frac{1}{2}(\langle \pi^+ \rangle + \langle \pi^- \rangle)$. Losses of decay products of $K^*(892)$ and ϕ due to inelastic scattering are not taken into account here. Statistical errors for the particles yields are $< 1 - 2$ %.

In this work the UrQMD model was used for this purpose because it includes rescattering and the space-time evolution of all particles involved in a high energy nucleus-nucleus collision within a pure hadronic scenario. Several thousand events of inelastic p+p, central C+C ($b < 2$ fm), Si+Si ($b < 2.5$ fm), and Pb+Pb ($b < 3.5$ fm, but only 100 events for comparison) were generated with the UrQMD model (version 1.2)². All parameters were left in standard settings, only a geometrically weighted impact parameter distribution was chosen (CTOption(5)=1), the calculation time span was 50 fm/c. Production and secondary interactions of pions, kaons, $K^*(892)$ and the ϕ -meson were studied.

Mean multiplicities of the particles under study from these UrQMD simulations are summarized in table 7.3. Besides the ϕ -meson, yields approximately match the data for p+p interactions (tab. 7.2). For the simulated A+A collisions the mean number of participants indicates that the centrality is slightly larger than in the data, although a proper range of impact parameters is chosen. Most probably, this is a result of the simplified initialization of the nuclei in version 1.2 of UrQMD, but

²For these simulations (spherical) nuclear density distributions with a sharp surface were assumed. A more realistic initialization as described in chapter 1.4.4 was only implemented from version 1.3 on which was not available at the time these simulations have been carried out. For central collisions the density distribution is not too far from reality, at least for the larger nuclei, but peripheral collisions and thus also minimum-bias interactions are not reproduced well. Particle yields are overestimated because too many participants are involved. Nevertheless, the importance of rescattering effects can be studied.

it does not harm the study of rescattering effects. Therefore, in particular in the lighter systems particle yields might be slightly higher than observed in the data. This holds for charged kaons; pions, however, are largely overestimated which is a general trend known for UrQMD [147]. Therefore only a very weak strangeness enhancement emerges from the UrQMD model, by far below that of the data. Only the ϕ -meson experiences a strong increase in its abundance, because with higher multiplicities K^+K^- coalescence becomes an increasingly important production channel in UrQMD (see also [148]). However, from p+p collisions it is seen that the other production channel via string excitation and decay in inelastic N+N collisions is largely underestimated.

In general, in UrQMD creation of new particles takes place via string excitation and decay (inelastic collisions), feed-down from resonances and coalescence. On the other hand particles get lost by the same processes: inelastic collisions, decay and coalescence. UrQMD allows to follow the sequence in time of all processes taking place. For each process all particles involved are listed. Time is always measured in the center-of-mass system. In fig. 7.6, e. g., the evolution in time of K^+ production divided into a few production mechanisms is presented. For all collision systems the spike from the inelastic N+N interactions right at the beginning is clearly visible, afterwards the rescattering phase and feed-down of short lived resonances becomes important. In p+p collisions only production via string excitation and decay as well as feed-down plays a role. But already in C+C interactions rescattering processes are more frequent and particles are produced or destroyed in further inelastic reactions. The influence of rescattering is strongest in central Pb+Pb. In table 7.4 relative production rates from the different processes are summarized.

Rescattering processes are more frequent and more important for particle production the larger the system is, i. e. the more particles are available for reactions. A kind of measure for the frequency of rescattering processes are, e. g., losses due to secondary interactions. In C+C interactions about 8-15 % of all produced particles – the fraction depends slightly on the particle species – get lost in inelastic interactions or via coalescence. This fraction increases to 15-25 % in Si+Si and to 46-60 % in Pb+Pb interactions while being on a 1-2 % level in p+p reactions. On the other hand particles are produced in secondary collisions without projectiles involved, their fraction can also be taken as measure for rescattering. Production rates for particles via rescattering are below one percent in p+p interactions, about 10-13 % in C+C, 15-21 % in Si+Si and 26-38 % in Pb+Pb collisions. In case of resonances as the $K^*(892)$ (ϕ) an increasing fraction is produced additionally by coalescence, i. e. about 1 % (5 %) in p+p, 8-10 % (15 %) in C+C, and 16-17 % (27 %) in Si+Si interactions. For central Pb+Pb collisions a fraction of 58 % of all ϕ -mesons stemming from coalescence was reported in [148].

The rescattering rates listed above suggest a minor influence on the strange-particle abundance in C+C and Si+Si interactions, because even with the very unlikely assumption that twice as many kaons as pions are produced in each inelastic rescattering process, this would increase the $\langle K \rangle / \langle \pi \rangle$ ratio by about 12 % (20 %) in C+C (Si+Si) collisions over that in p+p reactions. The experimentally observed enhancement is 30 % (48 %).

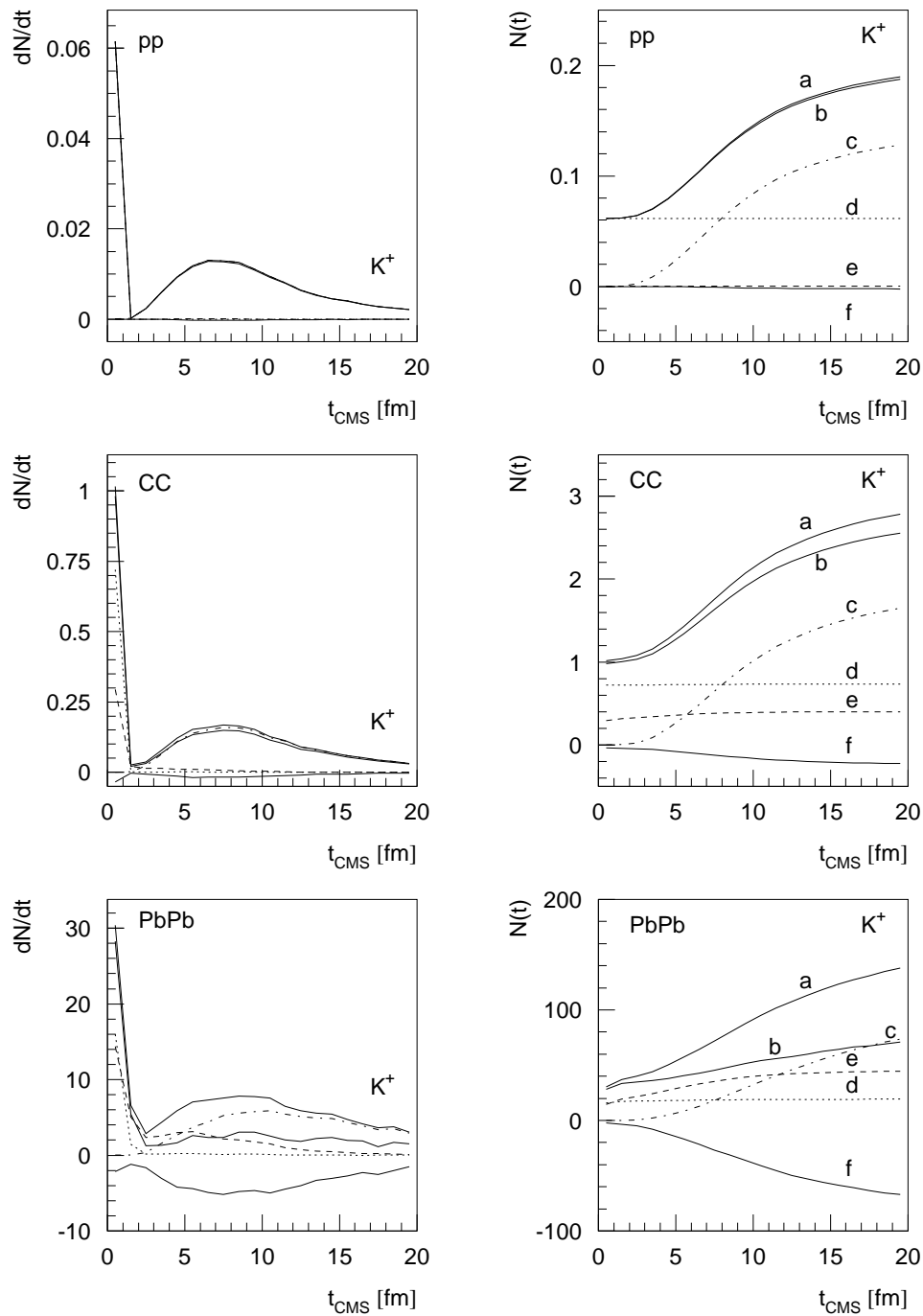


Figure 7.6: K^+ production in UrQMD. The top row shows production rates of K^+ in the first 20 fm/c in p+p, the middle row for central C+C and the lower row for central Pb+Pb collisions. Right, integrated yields are shown as they are evolving in time: (a) all generated K^+ ; (b)=(a)-(f) net generation of kaons; (c) kaons from feed-down; (d) kaons from inelastic baryon-baryon collisions which are mainly the N+N interactions in the very beginning when the nuclei pass through each other; (e) kaons from all other inelastic collisions which are mostly meson-baryon or meson-meson reactions in the course of the rescattering phase; (f) losses of K^+ due to inelastic collisions or coalescence with, e. g., pions to form a K^* .

		p+p	C+C $b < 2$ fm	Si+Si $b < 2.5$ fm	Pb+Pb $b < 3.5$ fm
inel. BB coll. and feed-down	c+d	100 %	87.5 %	82.8 %	73 %
rescattering	e		12.5 %	17.2 %	27 %
feed-down	c	71 %	64 %	62 %	62 %
all inel. coll.	d+e	29 %	36 %	38 %	38 %
inel. coll. with proj.		29 %	34 %	34.6 %	28 %
... BB	d	29 %	23.5 %	20.8 %	11 %
... MB	e		10.5 %	13.8 %	17 %
inel. coll. with no proj.			2 %	3.4 %	10 %
... MM	e		2 %	3 %	8 %
... MB	e			0.4 %	2 %
losses	f	1 %	8 %	15 %	46 %
... inel. coll.			1.6 %	3 %	6 %
... coalescence		1 %	6.4 %	12 %	40 %

Table 7.4: Relative production rates from the different processes in UrQMD for K^+ . BB stands for baryon-baryon collisions, MB for meson-baryon, and MM for meson-meson interactions. The quoted letters refer to fig. 7.6. In the first row, K^+ production is differentiated into the sum of inelastic BB collisions and feed-down, and into rescattering. In p+p, inelastic BB collisions and feed-down are the only source of particles. The term "rescattering" includes all inelastic collisions which are *not* BB interactions with at least one baryon being a projectile. In the second row, K^+ production is split into feed-down and inelastic collisions; in the block below the inelastic collisions are further divided into those, where an original projectile is participating, or those where not. For these two cases the contributions of BB, MB, or MM collisions are specified. The last block contains information on losses. Rates from production processes below one percent are neglected in the table.

The $K^*(892)$ meson takes part with similar rates in all the rescattering processes as described for kaons. But in addition, part of its decay products are destroyed in inelastic collisions, which leaves for Si+Si interactions only ~ 80 % of the $K^*(892)$ to be reconstructed via the invariant mass method (fig. 7.7). The losses quoted in tab. 7.5 are the net-losses taking into account a regeneration of $K^*(892)$ mesons by coalescence of kaons and pions, rates for the latter processes were reported in the last paragraph. As seen in fig. 7.7 a small fraction of $\bar{K}^*(892)$ (~ 6.3 %) takes part in elastic interactions. Elastic collisions of decay products strongly broaden the $\bar{K}^*(892)$ mass. But due to their small fraction (~ 7.2 % of all $\bar{K}^*(892)$) the overall mass shift and broadening is below the sensitivity of NA49. Rapidity distributions are not affected by these rescattering processes but the transverse momenta show an increase of the effective temperature by about 20 MeV (fig. 7.7). Once kinematic distributions are available from NA49 this effect might be accessible by measurements. However, a significant suppression of $K^*(892)$ mesons in A+A collisions due to rescattering of decay products is expected (see table 7.5). Since the mean lifetime of the ϕ -meson is 10 times longer than the one of the $K^*(892)$ all effects are developed more weakly here, see tab. 7.5 for the reduction of rates.

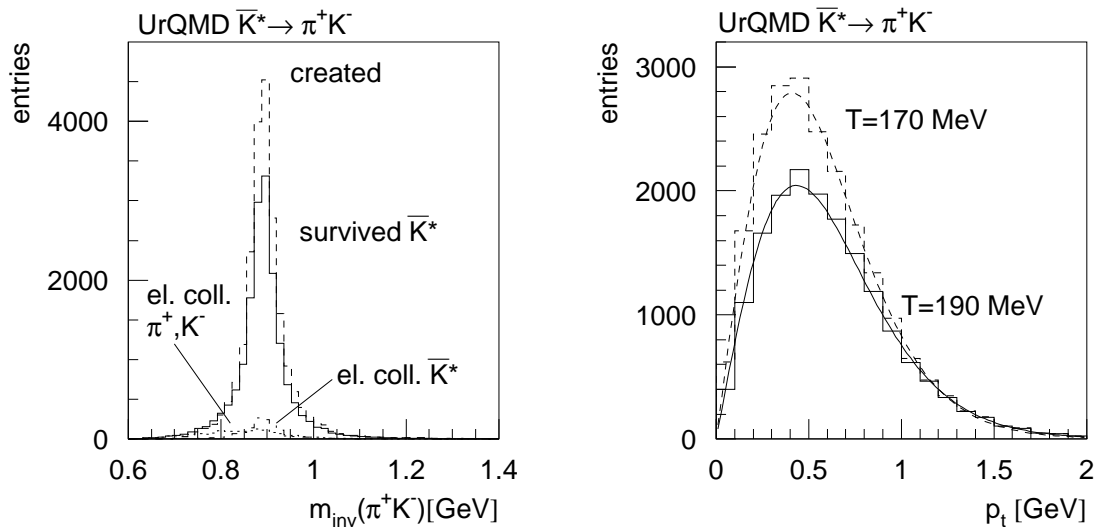


Figure 7.7: $\bar{K}^*(892)^0$ in central ($b < 2.5$ fm) Si+Si collisions from UrQMD simulations. Left, the invariant-mass distribution of $\bar{K}^*(892)^0$ decaying into π^+K^- and surviving is shown (surviving in the sense that the decay products were not destroyed). The distribution after elastic collisions of the $\bar{K}^*(892)$ or its decay products is also shown, but their fraction is too small to cause a significant and measurable mass shift or mass broadening of the $\bar{K}^*(892)^0$ -mass. Right, p_t -distributions of decaying (dashed) and surviving (solid) $\bar{K}^*(892)^0$ are shown; the quoted temperatures are from a thermal fit.

Unfortunately the large errors on the $K^*(892)$ yield in data make a quantitative comparison rather unsafe. The currently available data show that the $\bar{K}^*(892)$ is significantly stronger affected than the $K^*(892)$. Taking the mean of both, the $\langle K^*(892) \rangle / \langle K \rangle$ ratio is by 15 % (18 %) lower in C+C (Si+Si) interactions compared to p+p. This is at least of the same order as calculated in UrQMD. This supports that also for other results concerning rescattering processes discussed in this section the UrQMD model provides a satisfying description. Once full statistics are available for C+C and Si+Si data, a more precise statement should be feasible.

To summarize this section, the presented arguments lead to the conclusion that in C+C and Si+Si collisions rescattering processes play only a minor role and are not responsible for the (major part) of the strangeness enhancement observed in the data.

	C+C	Si+Si
	$b < 2$ fm	$b < 2.5$ fm
$\langle K^*(892)^0 \rangle$	10.5 %	19.4 %
$\langle \bar{K}^*(892)^0 \rangle$	11.4 %	21.7 %
$\langle \phi \rangle$	1.3 %	2.8 %

Table 7.5: Losses of $K^*(892)$ and ϕ mesons in UrQMD due to inelastic collisions of their decay products. These losses increase for the the $K^*(892)$ in central Pb+Pb interactions to 66 % [149]; for the ϕ to 11.6-25 % [148, 149, 150].

7.3 Independent superposition of N+N interactions

In A+A collisions each participating nucleon undergoes several interactions, e. g. 1.9 in central C+C and 4.6 in central Pb+Pb on average. In the center-of-mass system of the collision the two nuclei penetrate each other in 1-2 fm/c. This time can even be less in the center-of-mass systems of the individual nucleons. It is commonly believed that these times are much too short to allow for successive string excitation, decay, new excitation and so on. Due to the multiple interactions, each incoming nucleon loses more energy than in p+p which shows up as the so-called stopping in the rapidity distribution of protons (see fig. 1.9). In this section the question is addressed, whether the resulting increased excitation of nucleons in A+A compared to average single collisions in p+p could cause the observed strangeness enhancement. Assuming, that each excited nucleon or string collects the energy of its successive interactions and decays or hadronizes independently in the end, this scenario can be tested already in p+p collisions by studying interactions with more or less excitation of the proton.

It was discussed in section 4.2 and investigated with help of FRITIOF simulations that multiplicity as well as Feynman-x of the leading proton are correlated to the excitation of the string which is originating from the interacting nucleon. Particle production in p+p reactions was studied in dependence on both variables, due to the limited acceptance of the TPCs leading protons could only be selected in the Feynman-x range from 0 to 0.6. However, this is the excitation range of interest for this investigation since protons lose on average about half their energy in minimum-bias p+p, which means $x_F \simeq 0.5$ on average. In A+A collisions their energy loss is larger, shifting the mean Feynman-x to smaller values. It was observed that the $\langle K \rangle / \langle \pi \rangle$ ratio is nearly independent of multiplicity and Feynman-x of the leading proton (see fig. 5.34, 5.35 and discussion in section 5.2.3). Since kaons are the most abundant strangeness carrying mesons, this observation lead to the conclusion that there is no significant strangeness enhancement for p+p interactions in which the proton was higher excited than on average.

However, the other strange mesons under study show a slight increase relative to pions in dependence on Feynman-x and more pronounced in bins of multiplicity. They saturate at the minimum-bias value of p+p. This behavior was interpreted as a threshold effect. Since their contribution to the total produced strangeness is minor, this does not weaken the above statement.

These experimental results are consistent with the commonly accepted hadronization picture as it is, e. g., implemented in FRITIOF. The data and results from FRITIOF simulations were shown to agree well concerning the qualitative development. A detailed discussion can be found in section 5.2.3.

In principle, particle production in dependence on string energy can be directly studied in the hadronic channel of e^+e^- collisions, since there the whole center-of-mass energy is available for the creation of new hadrons. Fig. 7.8 (left) shows that the $\langle K \rangle / \langle \pi \rangle$ ratio is rather independent on energy over a very broad range, for K_S^0 even a decrease for higher energies is observed. However, measurements below

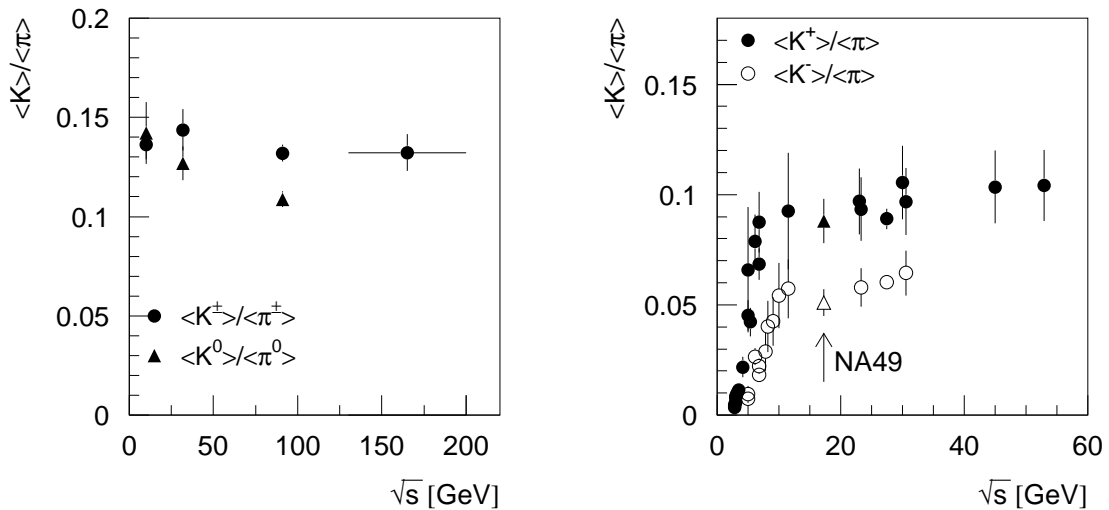


Figure 7.8: Energy dependence of $\langle K \rangle / \langle \pi \rangle$ ratio in e^+e^- and p+p collisions. Data on e^+e^- interactions are from [2], the energy dependence in p+p was already shown in fig. 5.26.

$\sqrt{s} = 10$ GeV are missing, this means that the threshold region, where the $\langle K \rangle / \langle \pi \rangle$ ratio has to increase, is not known.

In minimum-bias p+p interactions on average about $\frac{1}{2}$ of the center-of-mass energy is used for particle production, i. e. for the excitation of projectile and target string. In p+p reactions at $\sqrt{s} = 17.3$ GeV the mean excitation energy of each string is therefore about 4.3 GeV. This is well below 10 GeV and might be in the threshold region. However, in this case the $\langle K \rangle / \langle \pi \rangle$ ratio should change if varying the inelasticity of the p+p interactions, which is not observed in the data.

The energy dependence of the $\langle K \rangle / \langle \pi \rangle$ ratio in p+p reactions also supports that collisions at $\sqrt{s} = 17.3$ GeV lie above threshold (fig. 7.8, right): For center-of-mass energies higher than ~ 10 GeV the $\langle K \rangle / \langle \pi \rangle$ ratio increases very weakly.

Summarizing this discussion, no clear strangeness enhancement in sub-samples of p+p collisions is observed. Results from e^+e^- annihilation into hadrons indicate that above threshold the $\langle K \rangle / \langle \pi \rangle$ ratio is rather independent of the excitation energy of the string. It was argued that minimum-bias collisions at $\sqrt{s} = 17.3$ GeV lie already in the saturation region concerning the $\langle K \rangle / \langle \pi \rangle$ ratio.

Excited nucleons or strings collecting energy in the successive interactions of A+A collisions and decaying or hadronizing independently in the end can be compared to a string which has been highly excited in a violent p+p interaction, more than in an average single N+N collision. The conclusion of this section is, that no strangeness enhancement is expected in the final hadronic state from this decay.

7.4 Empirical scaling parameters

The strangeness enhancement as observed in the $\langle K \rangle / \langle \pi \rangle$ and also in the $\langle \phi \rangle / \langle \pi \rangle$ ratios shows a discontinuity in dependence on the number of participants, if one compares central collisions of light systems with peripheral Pb+Pb (fig. 7.1). This was introduced as geometry dependence of strangeness production in section 7.1. It is caused by the different spatial arrangement of the nucleons in these two types of systems. Obviously, N_{part} is not a parameter determining the relative strangeness production commonly for all systems.

Recently, several attempts were made to describe, e. g., the $\langle K \rangle / \langle \pi \rangle$ ratio for different collision systems or energies with one scaling parameter. F. Sikler observed that by using the macroscopic parameter $(R - b/2)$ a smooth evolution of the system-size dependence can be obtained [151] (R nuclear radius, b impact parameter). Adopting Bjorken's formula to peripheral A+A collisions, F. Wang has shown that the $\langle K \rangle / \langle \pi \rangle$ ratio in dependence on the energy density ϵ lies to a good approximation on a common curve for data from several energies and collision systems [152]. A similar ansatz was used by S. Kabana before, however, she extrapolated all experimental results at finite μ_B to zero baryochemical potential and then compared to an initial energy density [153, 154]. Both, F. Wang and S. Kabana observed a threshold behavior for a certain energy density.

Here, a microscopic approach is pursued. The strategy is to search for a common scaling parameter that eliminates the geometry effect in the system-size dependence of the $\langle K \rangle / \langle \pi \rangle$ and $\langle \phi \rangle / \langle \pi \rangle$ ratio. The hope is to localize the origin of strangeness enhancement in terms of microscopic parameters.

In A+A collisions one distinguishes between the number of wounded nucleons N_{wound} and participating nucleons N_{part} (see section 4.3): Nucleons colliding during the penetration phase of the two nuclei are called *wounded nucleons*. In the term *participating nucleons* also those involved in secondary interactions with nucleons or produced particles are included. It was discussed in section 7.1 that, in particular in peripheral A+A collisions, the difference between both numbers is large, probably caused by the large amount of spectator matter in these interactions. It was shown in fig. 7.4 that the pion yields scale better with N_{part} . On the other hand, as demonstrated in fig. 7.9, the strange-meson yields are better correlated with N_{wound} . The different behavior of kaons and pions is probably caused by the fact that in rescattering processes of wounded nucleons in the surrounding spectator matter at low center-of-mass energies pions are produced but essentially no strange hadrons. These pions dilute the hadron gas and account for the low $\langle K \rangle / \langle \pi \rangle$ and $\langle \phi \rangle / \langle \pi \rangle$ ratios in peripheral Pb+Pb.

These observations give an explanation for the geometry effect; they do not explain the strangeness enhancement itself. However, they point to an origin in the first phases of the collision, which are characterized by excitation of the nucleons and their decay.

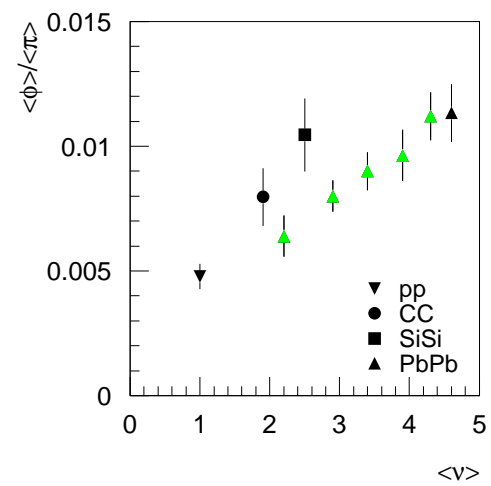
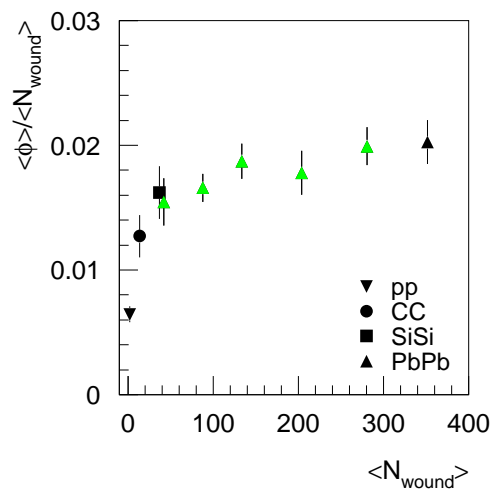
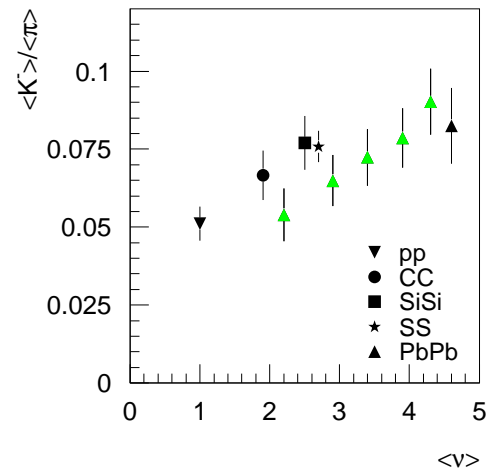
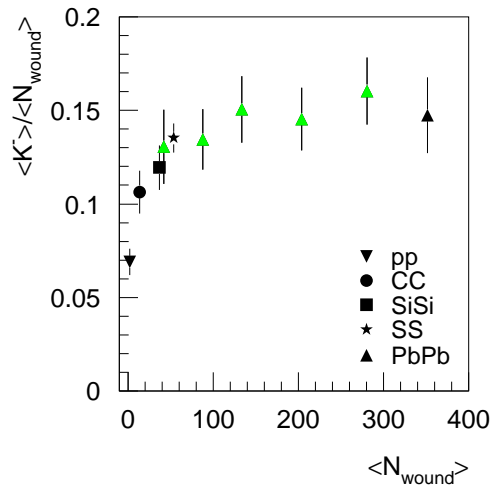
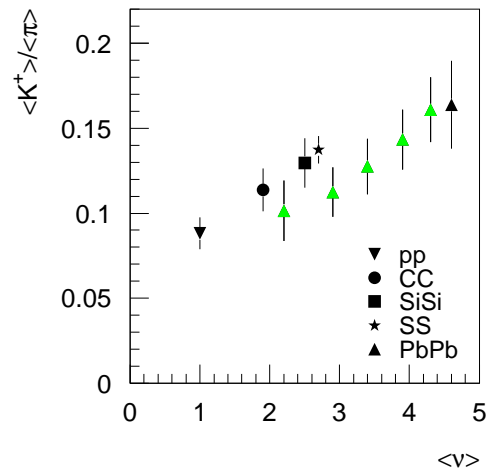
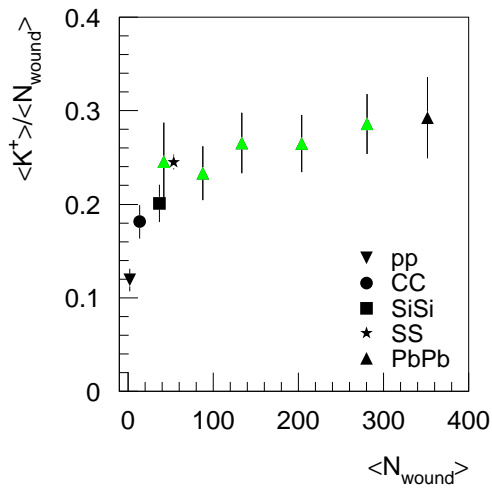


Figure 7.9: Yields of charged kaons and the ϕ -meson relative to the number of wounded nucleons in dependence on N_{wound} .

Figure 7.10: Strange-meson yields relative to pions in dependence on the mean number of collisions per wounded nucleon $\langle \nu \rangle$. $\langle \pi \rangle = \frac{1}{2} (\langle \pi^- \rangle + \langle \pi^+ \rangle)$.

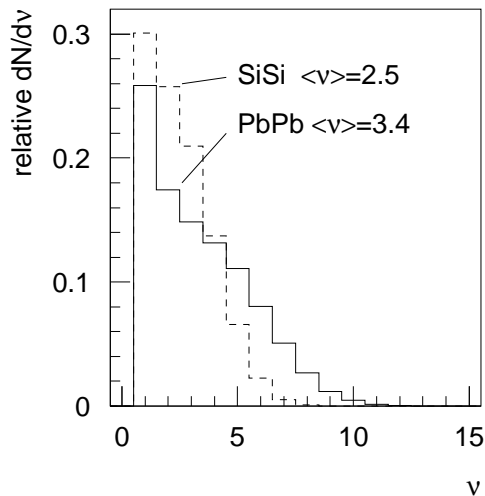


Figure 7.11: Distribution of ν in central Si+Si ($b = 2$ fm) and peripheral Pb+Pb ($b = 8.3$ fm) collisions. The data show a similar $\langle K \rangle / \langle \pi \rangle$ ratio in these two systems.

The simplest parameter characterizing this phase is the mean number $\langle \nu \rangle$ of collisions each wounded nucleon undergoes while passing the other nucleus³. Indeed, fig. 7.10 shows that a somewhat better scaling is observed using $\langle \nu \rangle$ on the horizontal axis instead of N_{part} . A view on not only the mean value of ν but also on its distributions helps to understand the reason for the remaining discrepancy. In fig. 7.11 the distribution of ν is presented from Wounded Nucleon Model (WNM)⁴ simulations for central Si+Si and peripheral Pb+Pb collisions, for which a similar $\langle K \rangle / \langle \pi \rangle$ and $\langle \phi \rangle / \langle \pi \rangle$ ratio is observed. Obviously, the long tail to 10 collisions and more increases the average for peripheral Pb+Pb while the fraction of nucleons that collide only once ($\nu = 1$) is rather similar to central Si+Si. This large spread of ν is even more pronounced in the most peripheral bin of Pb+Pb: about 46 % of the wounded nucleons collide only once but the long tail shifts the mean value to 2.6. Therefore, one may try the fraction of nucleons colliding more than once, i. e. $f = 1 - \frac{N_{\nu=1}}{\sum_{i=1}^{\infty} N_{\nu=i}}$ as scaling parameter – and interestingly, it works rather well (fig. 7.12). This scaling is consistent with the conclusion stated in section 7.3 that in the A+A collisions under study N+N interactions do not superimpose independently.

For a long time, energy density and string fusion have been discussed as critical parameters for an increased production of strangeness or even the creation of a quark-gluon plasma (see e. g. [19, 155] and references therein). In microscopic string models assumptions about the influence of an increased string density are often used to reach a strangeness enhancement as observed in data: For example, in the VENUS model double strings are implemented [33], in RQMD string fusion (color rope formation) is included [156, 157], or in UrQMD string density effects are phenomenologically taken into account either by increasing the string tension κ or decreasing the mass of the strange quark, i. e. the difference ($m_s^2 - m_{u/d}^2$) in the Schwinger formula 1.5 [158].

³For a detailed description of simulations yielding $\langle \nu \rangle$ and the other parameters discussed in the following see appendix D.

⁴Wounded Nucleon Model (WNM), simple numerical implementation of the Glauber model, see appendix D.

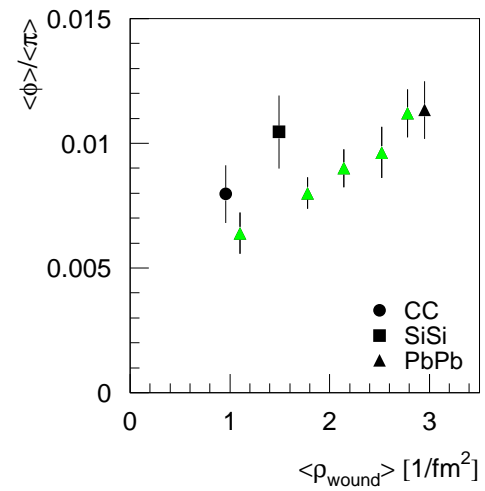
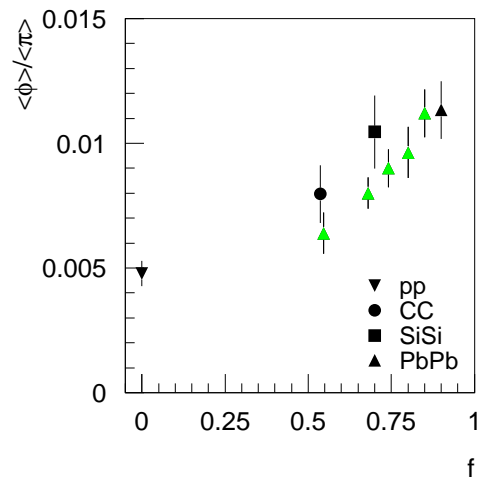
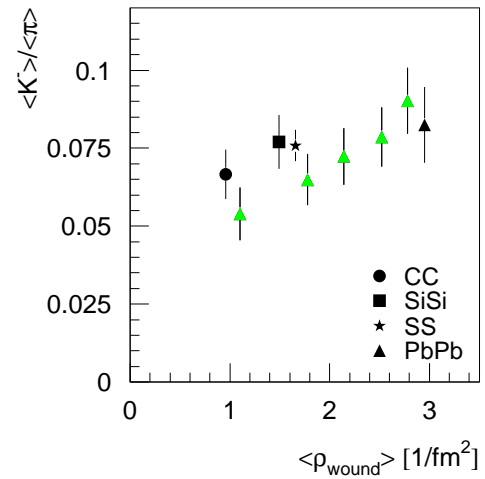
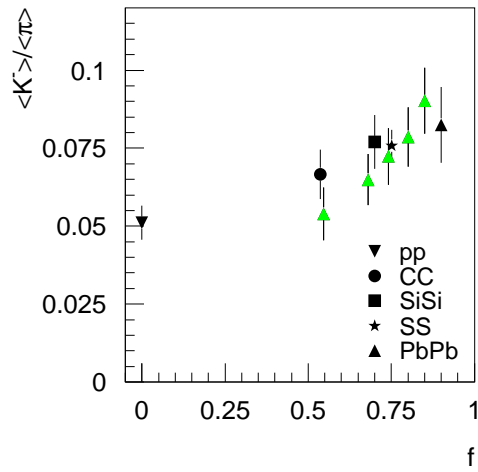
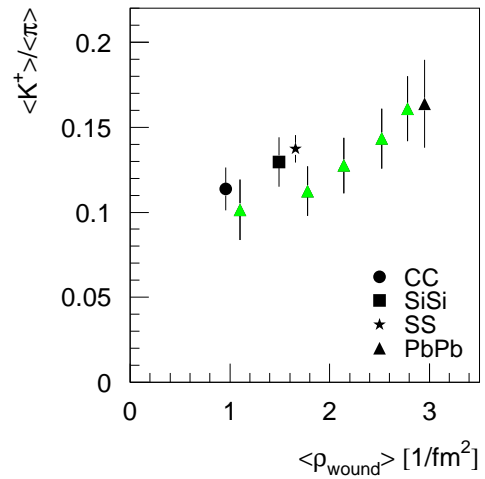
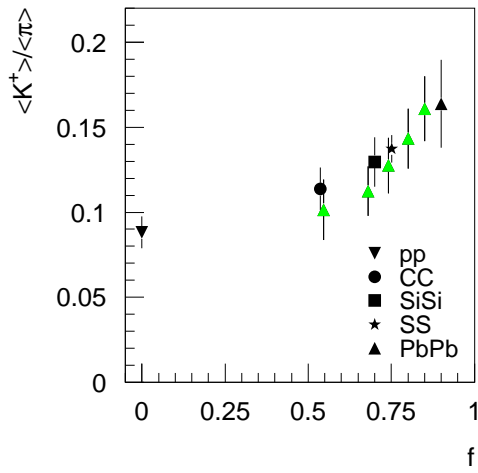


Figure 7.12: Strange-meson yields relative to pions in dependence on the fraction f of wounded nucleons being struck more than once. $\langle \pi \rangle = \frac{1}{2} (\langle \pi^- \rangle + \langle \pi^+ \rangle)$.

Figure 7.13: Yields of strange mesons relative to pions in dependence on the 2-dimensional wounded-nucleon density. $\langle \pi \rangle = \frac{1}{2} (\langle \pi^- \rangle + \langle \pi^+ \rangle)$.

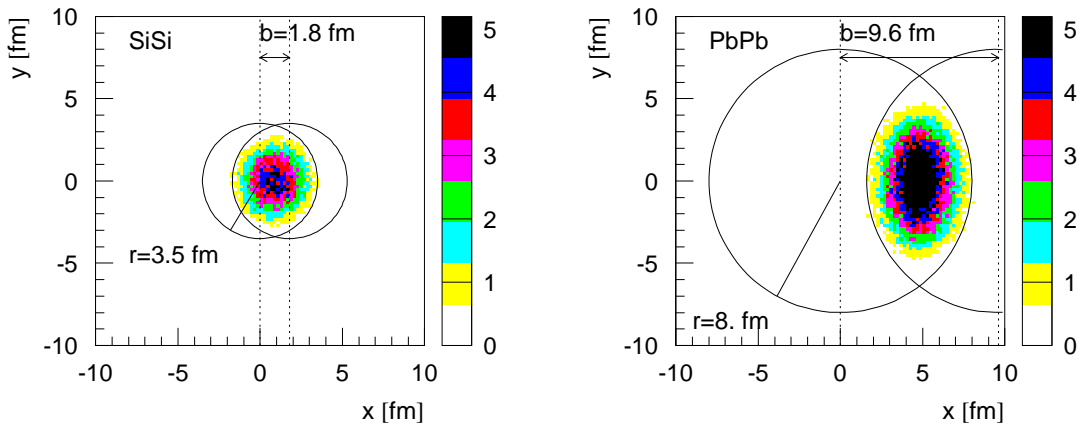


Figure 7.14: Distribution of wounded nucleons projected onto the plane transverse to the beam (x - y plane) for Si+Si and Pb+Pb collisions with a similar $\langle K \rangle / \langle \pi \rangle$ ratio in the data. The impact parameter was chosen as indicated in the plots, the circles roughly illustrate the colliding nuclei.

A high energy or string density in the system must be correlated to a high density of collisions or wounded nucleons. In A+A not only several successive interactions take place per nucleon as discussed above, there are also several collision chains close by in space.

In fig. 7.14 the 2-dimensional projection of the wounded nucleons into the x - y plane is shown as obtained from simulations of central Si+Si and peripheral Pb+Pb interactions. Both systems are chosen to have a similar $\langle K \rangle / \langle \pi \rangle$ ratio in the data and, indeed, the 2-dimensional participant densities turn out to be similar. Fig. 7.13 presents the attempt to use this mean wounded-nucleon density $\langle \rho_{wound} \rangle$ as scaling parameter⁵. The results show that this approach is insufficient, presumably because of the neglect of the 3rd and 4th dimension: Since Pb-nuclei are larger and contain more nucleons, a two-dimensional projection of wounded nucleons leads necessarily to higher densities in Pb+Pb. However, even if in the center-of-mass system each Pb-nucleus is contracted by $\gamma = 9.2$ to a thin disk of about 1.5 fm thickness $\left(= \frac{2r}{\gamma} \approx \frac{2 \cdot 1.16 A^{\frac{1}{3}}}{9.2} \right)$, this length is not negligible and might result in a separation of strings in the longitudinal direction. Also the penetration of the nuclei takes more time in Pb+Pb interactions (about 1.8 fm/c) than in Si+Si (about 1.2 fm/c in the center-of-mass system of the collision).

UrQMD simulations provide information about each collision in space and time. They are an appropriate tool to calculate a mean collision density of inelastic interactions in the 4-dimensional space $\langle \rho_{inel\ coll} \rangle$, the average being taken over the time span in which the nuclei penetrate each other. Indeed, as shown in fig. 7.15 this mean collision density acts as a common scaling parameter for all systems under investigation.

⁵A similar approach can be found in [159], however, kaon yields presented there differ from those used in this thesis.

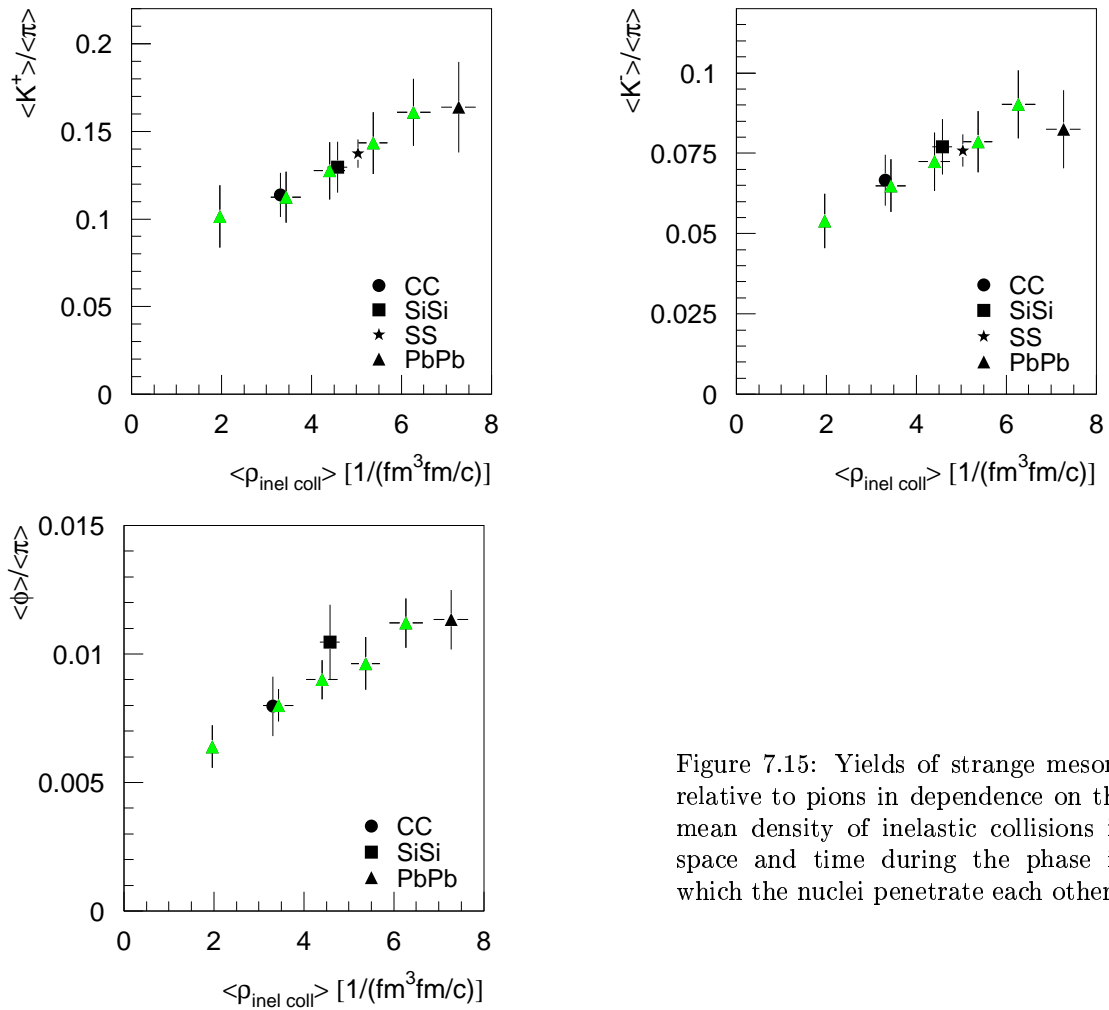


Figure 7.15: Yields of strange mesons relative to pions in dependence on the mean density of inelastic collisions in space and time during the phase in which the nuclei penetrate each other.

Obviously the density of N+N collisions in space and time is a variable that controls relative strangeness production. A possible interpretation is that with increasing collision density the excited nucleons or strings, and/or their de-excitation or hadronization may be no longer independent. Subsystems comprising several strings or, in the limit, a single system may be formed which hadronize coherently as quantum-mechanical entity. The suggestion is that this may change the $\langle K \rangle / \langle \pi \rangle$ and $\langle \phi \rangle / \langle \pi \rangle$ ratios.

A plausible argument for the formation of fused systems is given by the fact that already in ground state nuclear matter nucleons are densely packed inside the nucleus. Mean excitation energies of about 4 GeV or more ($> \frac{\sqrt{s}}{4}$) may easily create spatially overlapping resonances, and, excitations by about four times the nucleon rest mass imply that partonic degrees of freedom become relevant. The idea of a coherent system is also consistent with the consideration that several interactions in less than 1 fm/c in time and 1 fm in longitudinal direction with excitation energies of the order of GeV might also be no longer resolvable from the point of quantum mechanics and the uncertainty principle ($\hbar c = 0.197$ GeV·fm).

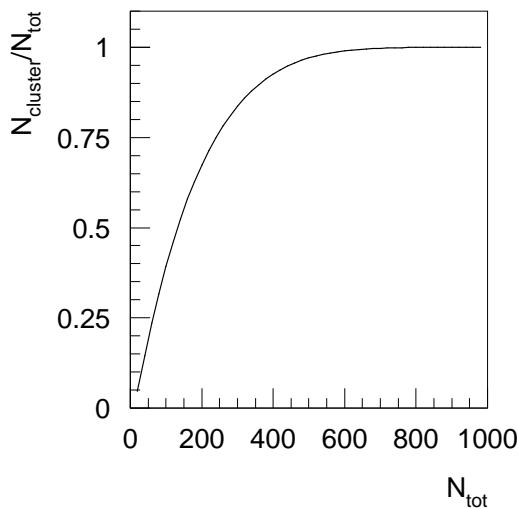


Figure 7.16: Result of a simple percolation model suggested in [161]: A large cube (representing the collision volume) is divided into 1000 small cubes of equal size. They are populated randomly (\rightarrow strings, resonances); their total number is called N_{tot} . If two of them touch side by side they are assumed to form a cluster. $N_{cluster}$ is the number of occupied cubes participating at least in one cluster (\rightarrow fused/coalesced strings). $N_{cluster}/N_{tot}$ rises fast with N_{tot} and saturates once all cubes take part in clusters. Not only the number of cubes participating in clusters, but also the cluster size increases with the density.

Quantitative percolation calculations are an appropriate tool to study whether such a fusion mechanism seizes all colliding nucleons or only fractions and what the critical parameters are. Fig. 7.16 shows the result of a percolation calculation to illustrate its applicability: Rather fast with increasing density all elements contribute to clusters. Satz started a more detailed investigation of percolation theory in 2 dimensions [160]. However, the different scaling behavior in data with the 2-dimensional $\langle \rho_{wound} \rangle$ and the 4-dimensional $\langle \rho_{inel\ coll} \rangle$ densities indicates that considering only 2 dimensions might be an oversimplified picture. The different geometry of peripheral Pb+Pb and central collisions of light systems is not accounted for completely in the model of Satz: In central A+A collisions at $\sqrt{s} = 20$ GeV percolation sets in from $A \gtrsim 60$ on, whereas for centrality-dependent Pb+Pb interactions the percolation point is $N_{part} \simeq 150$ ($b \simeq 6$ fm). Data presented in this thesis suggest smaller A and larger N_{part} .

The question remains why such *coherent (sub)systems* yield more strangeness compared to a single N+N collision. Two explanations have been discussed before: First, the identification of the coherent subsystems with small regions of quark matter. Second, the assumption of fused strings with increased string tension. A third suggestion will be discussed in the next section.

7.5 System-size dependence in the statistical model

Relative strangeness production depends on the size of the collision system, fig. 7.17 shows the relevant experimental results. Because of the geometry dependence discussed in section 7.4 the data on peripheral Pb+Pb collisions are disregarded for the moment and only central symmetric A+A collisions are considered. NA49 and NA35 data on Λ and $\bar{\Lambda}$ production are included in fig. 7.17 [78, 133, 134, 136]. The strangeness enhancement, also for Λ -baryons, shows a steep rise as a function of the number of nucleons participating in a collision. It seems to reach a saturation level

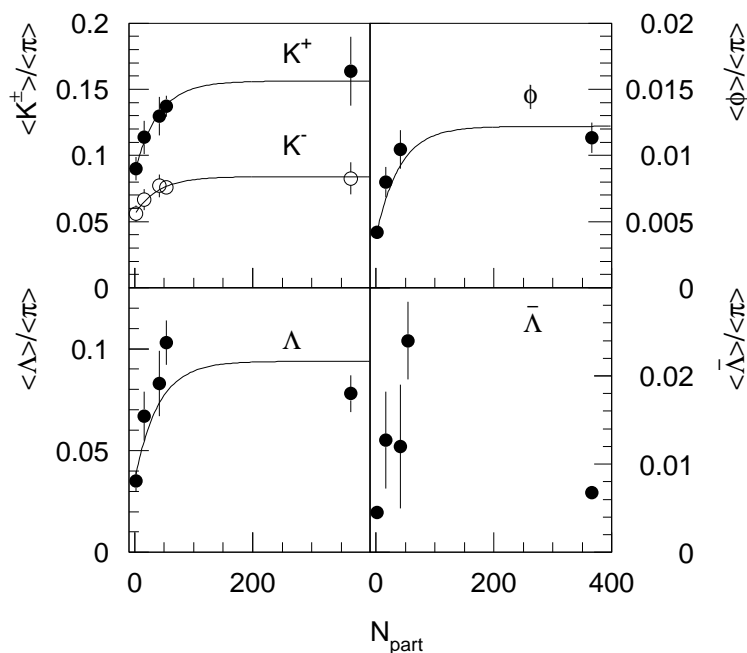


Figure 7.17: Yields of strange hadrons relative to pions in symmetric central A+A collisions. References for the data are listed in table 7.1 and 7.2. Curves represent a functional form $a - b \cdot \exp(-N_{part}/40)$; they are only to guide the eye.

already at N_{part} around 60. Unfortunately, data are lacking in the intermediate mass range, but at the moment no physical effects are conceivable that could modulate this behavior. The situation is not so clear for the $\bar{\Lambda}$. The data points have large error bars, on the other hand an increase of the baryochemical potential with system size might lead to a smaller yield for central Pb+Pb [134].

In the last section it was shown that the density of inelastic collisions in the penetration phase of the nuclei plays a decisive role in determining the strangeness production. It was argued that a high collision density leads to excited systems comprising several strings or resonances. It is natural to assume and supported by microscopic simulations that this effect becomes more important with increasing number of participants. However, it remained an open question *why* strangeness production is enhanced in these fused systems.

Mean excitation energies of the nucleons or resulting strings of roughly 4 GeV are reached in N+N interactions at $\sqrt{s} = 17.3$ GeV. Due to multiple collisions and an increased stopping of the nucleons even larger values are expected in A+A. The proposed fused systems, to be interpreted as coherent systems in a quantum-mechanically sense, will therefore have many excited internal degrees of freedom and many open decay channels. Their hadronization must be amenable to a statistical description. This assumption offers a bridge from the microscopic view of a collision to a thermodynamical description of the system. In the latter, a size, i. e. a volume dependence, and with that also the enhancement itself can easily be understood.

It is a well known phenomenon in thermodynamics that for a conserved quantum number (such as strangeness) a canonical description has to be used if the number of carriers is small, whereas a grand-canonical formulation can be applied

if the number is large. As the number of strange quark pairs increases with system size this translates into a volume dependence. Due to restrictions imposed by strangeness conservation the resulting yield is larger in the grand-canonical case and thus for large volumes. This effect was called "canonical strangeness suppression" and has been discussed for years as a possible explanation for strangeness enhancement (see the short introduction in chapter 1.4.5).

Quantitative calculations of the volume dependence of strangeness enhancement on the basis of a hadron gas in thermal equilibrium were performed by Rafelski and Danos [42], Hagedorn and Redlich [43], Cleymans et al. [45], and more recently by Hamieh et al. [44] (see also fig. 1.24) or Rafelski and Letessier [46]. Qualitatively their curves show the same behavior as observed in the data: Strangeness enhancement rises fast and saturates at volumes of about $(30 \pm 10) \text{ fm}^3$ for single strange particles at top SPS energies. The saturation volume V^* depends on T , μ_B and the strangeness content of the particles – the more strangeness a particle carries, the larger V^* is, in addition the total enhancement increases with strangeness content. Total strangeness enhancement and V^* also depend on the volume V_h assumed for a p+p collision ($V_h \approx 7.4 \text{ fm}^3$ in [44] and $V_h \approx 4.2 \text{ fm}^3$ in [42, 46]). Altogether, the models show about a factor 2 enhancement from small to large systems for particles carrying one strange quark. This is consistent with the enhancement observed for kaons and Λ -baryons (~ 1.8 and ~ 1.6 for K^+ and K^- , respectively, and ~ 1.6 for Λ comparing central Pb+Pb and minimum bias p+p).

The question shall be briefly addressed whether a hadron gas is the adequate model here. In the last section it was already mentioned that mean excitation energies per nucleon of 4 GeV or more imply that partonic degrees of freedom become relevant. Also the behavior of the ϕ -meson is difficult to understand in a hadron gas model, but it would, at least qualitatively, be explainable assuming a partonic phase: As a carrier of hidden strangeness it is of internal $s\bar{s}$ structure, but as a hadron it is color-neutral. In a hadron gas in full thermal equilibrium it should therefore not be sensitive to canonical strangeness suppression, whereas the data show an even stronger decrease to small systems compared to kaons (fig. 7.1 and 7.2). If the strangeness is determined in a partonic phase, the ϕ -meson would be sensitive to the strange quark abundance and should respond more strongly to it than single strange hadrons.

A further argument supporting a partonic phase is based on the observed size of the strangeness enhancement. In most hadronic models describing total yields a strangeness undersaturation factor γ_s is introduced in order to reach a satisfactory agreement with the data (see e. g. [50, 162] for a parametrization of the system-size dependence). This factor can be explained under the assumption that strangeness is in thermal equilibrium in a partonic phase and its relative abundance survives in the final state. Then, hadron yields after hadronization show a strangeness undersaturation compared to an equilibrated hadron gas (e. g. [163]). γ_s thus carries information on the preceding phase in this interpretation. Calculations pointing out that the equilibrium strangeness per entropy is lower in a QGP than in a hadron

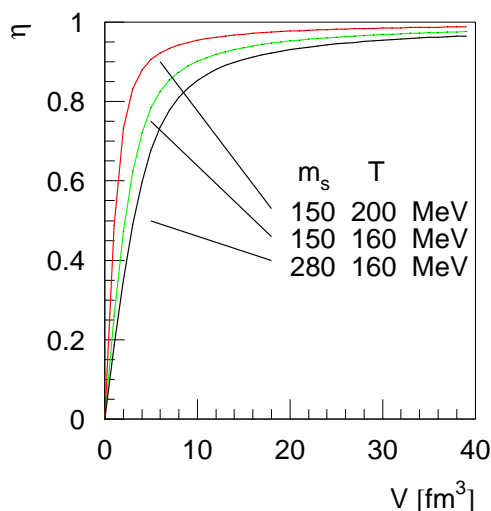


Figure 7.18: Canonical strangeness suppression factor η for $s\bar{s}$ pairs for different values of T and m_s . η is calculated according to Rafelski and Danos [42]: $\eta = \frac{I_1(x)}{I_0(x)}$, $x = \sqrt{4 \cdot 36y}$, 36 is the statistical factor for strange quarks in quark matter, $y = \left(\frac{VT^3}{2\pi^2(\hbar c)^3}\right)^2 \left(\frac{m_s}{T}\right)^4 K_2\left(\frac{m_s}{T}\right)^2$. They used the parameter combination $T = 150$ MeV and $m_s = 280$ MeV, the volume for an elementary interaction was assumed to be $V_h = \frac{4}{3}\pi(1\text{fm})^3$.

gas at the same temperature were already discussed in section 1.3.4.

Concerning the qualitative trends a partonic system shows the same behavior of canonical strangeness suppression as the hadron gas models [42]. Also the saturation volume is of comparable size, however it depends on T and m_s (fig. 7.18). The size of the strangeness enhancement varies strongly with different assumptions about T , m_s , and in particular about the volume V_h assumed for a p+p collision. Obviously also quark matter droplets formed within the high collision density regions as suggested at the end of the last section would experience a size dependence.

However, experimentally observable quantities are *hadrons* in the final state, i. e. the hadronized system only. In the last paragraph it was argued that the proposed coherent systems are most probably of partonic nature. The hadronization volume should therefore be the relevant volume determining the relative strangeness content. On the current experimental basis the two following hadronization scenarios are indistinguishable and probably even interwoven: First one might think of a thermalized partonic phase which is described by statistical models. Hadrons are mainly formed by coalescence during hadronization. Second, it might be the decay itself, i. e. the hadronization process which is amenable to a statistical description. The decay of the coherent system fills phase space as a whole appearing as a hadron gas in equilibrium, if necessary with strangeness undersaturation. Apparently, thermal models on the basis of an equilibrated hadron gas capture the average phase space dependence of the population resulting from this decay [57].

What remains to be done is a quantitative comparison of coherence volumes as calculated from thermal models and as estimated from data (table 7.6). The estimate of the latter is based on UrQMD simulations (see appendix D for details of the calculation). The volume in which the primary collisions take place, $V_{\text{collision}}$, is derived from an enclosure of the simulated collision points. It is approximately the same as the volume of the nucleus itself, Lorentz-contracted by a γ of 9.2. The hadronization volumes are expected to be larger because of longitudinal expansion of the strings/coherent subsystems. Assuming a mean expansion of 1 fm in both

system	UrQMD		thermal models	
	$V_{collision}$	$V_{hadronization}$	(1)	(2)
C+C	6-12 fm ³	28-55 fm ³	10-11 fm ³	6-7 fm ³
Si+Si	10-20 fm ³	47-90 fm ³	14-17.5 fm ³	8.5-11 fm ³
S+S	14-30 fm ³	50-100 fm ³	14-17.5 fm ³	8.5-11 fm ³

Table 7.6: Comparison of collision volumes from UrQMD simulations and from the thermal model. $V_{collision}$ is derived from an enclosure of the simulated collision points (see appendix D). For $V_{hadronization}$ an additional longitudinal expansion by 1 fm in both directions is assumed. Volumes from two different thermal models are used for comparison: (1) Tounsi and Redlich [47], see fig. 1.24, $V = 3.5N_{part}$; (2) Rafelski and Danos [42], see fig. 7.18 ($T = 150$ MeV and $m_s = 280$ MeV). Volumes are extracted from the quoted figures assuming $\eta \approx 0.5$ for p+p: On the one hand volumes are read off for the experimentally observed enhancement of the $\langle K^+ \rangle / \langle \pi \rangle$ ratio, in this case for central Pb+Pb the saturation value $\eta = 1$ is not reached. On the other hand it is assumed, that indeed the saturation level is reached for central Pb+Pb, therefore the factor 2 enhancement from $\eta = 0.5$ to $\eta = 1$ is re-scaled to 1.82, which is the $\langle K^+ \rangle / \langle \pi \rangle$ enhancement in central Pb+Pb compared to p+p. The variation in the volumes for each model stems from these two procedures, the difference within the models may be taken as indication of the theoretical uncertainty in general.

directions leads to the quoted $V_{hadronization}$. The last two columns contain values from two different calculations, Tounsi and Redlich [47] and Rafelski and Danos [42]. Fig. 1.24 and 7.18 were used to read off the volumes corresponding to the strangeness enhancement measured in the data.

Despite the uncertainties in determining the volumes, the estimated hadronization volumes $V_{hadronization}$ are larger than those expected from thermal models, whereas the volume of the primary collision zone $V_{collision}$ is similar. Using additional experimental information, the difference might qualitatively be understandable: Net-proton distributions from central Pb+Pb collisions at 158 AGeV show a forward – backward separation of 2.5 units in rapidity in the final state [164]. The large span of longitudinal momenta suggests that only part of the strings/excited resonances created in central A+A collisions may form coherent volumes in the primary collision zone which then separate during the expansion of the system.

The preliminary data on peripheral Pb+Pb collisions can be included into the overall picture by assuming that the coherence volume in peripheral Pb+Pb is smaller than in central collisions of light nuclei at the same number of participants. This is plausible, because more or less diffuse edges of the nuclei collide which gives less opportunity for formation of coherent subsystems. The calculated collision density is an appropriate scale proportional to size and/or number of these subsystems.

7.6 Conclusion

As a function of system size the experimental data for central A+A collisions show a steep rise of relative strangeness production saturating above roughly 60 participating nucleons (fig. 7.17). The different enhancement behavior of preliminary results from peripheral Pb+Pb interactions in dependence on the number of participants could be ascribed to the very different geometry of the colliding nuclear matter (section 7.4). Summarizing the arguments of the preceding sections, an explanation of the strangeness enhancement is proposed in this conclusion.

Schematically a collision between two nuclei may be subdivided into three phases (similar to fig. 1.11):

Excitation – During the interpenetration of the nuclei the participating nucleons are excited by sequential interactions into baryonic resonances or strings.

Decay/hadronization – The excited objects decay or hadronize either independently of each other or after formation of a partially or completely coherent state.

Rescattering – The final expanding hadronic state.

From experimental evidence as well as from microscopic simulations of the reaction as discussed in section 7.2 it appears unlikely, in particular for C+C and Si+Si, that hadron-hadron interactions in the third phase are the source for the increased strangeness production in A+A compared to p+p.

Assuming that the influence of rescattering processes on the hadron abundances is minor, the final hadrons result therefore from the decay or hadronization of the excited states in the second phase. The mere excitation is located in the first phase. Characteristic for A+A collisions is the multiple excitation of the nucleons by successive interactions. In section 7.3 the question was addressed, whether the higher excitation obtained in A+A could be the origin of the strangeness enhancement. Under the assumption that these higher excited resonances or strings are still independent and decay or hadronize also independently, they can be compared to highly excited strings in violent p+p interactions. The experimental investigation of inelasticity-dependent p+p reactions gave no indication for a significant strangeness excess in subclasses with excitation energies higher than the single-collision average.

The conclusion is inevitable that some kind of collective phenomenon causing the strangeness enhancement develops in the second phase of the reaction. In section 7.4 the geometry dependence of the $\langle K \rangle / \langle \pi \rangle$ and $\langle \phi \rangle / \langle \pi \rangle$ ratios was utilized to obtain hints on microscopic parameters being relevant for an increased strangeness production and on the nature of the processes enhancing strangeness. It was found that the density of inelastic collisions in space and time during the interpenetration of the nuclei plays an important role. This suggests immediately the formation of coherent excited states comprised of several strings and their decay as a quantum-mechanical entity.

This point was further pursued in section 7.5, in particular the question why these coherent states exhibit a strangeness enhancement and/or their decay leads to

a higher strangeness content in the final hadronic state. Connected to this topic is the search for an explanation of the observed system-size dependence of the strangeness enhancement. It was argued that the introduced coherent excited states must have many excited internal degrees of freedom and many open decay channels. These states themselves and their hadronization are therefore amenable to a statistical description and the phenomenon of canonical strangeness suppression, or grand-canonical strangeness enhancement, must apply. This would explain the trend seen in the data and the enhancement itself in a natural way.

By this interpretation the gap between a microscopic picture of the reaction and the description of the final hadronic state by statistical models is bridged. To improve the understanding of the interplay between collision density and formation of coherent states percolation calculations are a promising field. However, the nature of the excited coherent systems is not easily accessible. Considering the excitation energies involved, the stronger canonical suppression for ϕ -mesons compared to kaons, and the observed strangeness undersaturation in the final hadronic state compared to an equilibrated hadron gas, a partonic nature of this state is suggested.

The interpretation given in this section is consistent with a conclusion that can be drawn from the energy dependence of strangeness production, namely that above 30-40 GeV beam energy a partonic system is formed in central Pb+Pb collisions [71, 131].

The explanation of strangeness enhancement and its system-size dependence proposed in this thesis is independent of energy, once excitation energies are high enough for the formation of coherent systems. If rescattering effects can be neglected, a similar shape of the system-size dependence as measured for central A+A interactions at 158 AGeV should also be observable for other collision energies.

Appendix A

Kinematic variables, cross sections and variable transformation

In high-energy collisions a large variety of particles is produced. A full observation of the final state requires an *exclusive* measurement including all particles produced per event, which is difficult experimentally. Therefore *inclusive* measurements are preferred where a single particle c is investigated independent on whatever else is produced along with it (X). If a and b are projectile and target, an inclusive reaction as considered in this work can be written as:

$$a + b \longrightarrow c + X \quad (\text{A.1})$$

In so-called *semi-inclusive* processes additional constraints on the type of collision are imposed, e. g. a specific centrality. In this terminology only the minimum bias p+p interactions studied in this work are (close to) inclusive measurements. They still have a small bias because of the exclusion of part of the elastic and diffractive cross section in the trigger selection. The semi-inclusive event samples studied for p+p, C+C and Si+Si interactions are selected according to their collision centrality as described in chapter 4.

The invariant cross section for a (semi-)inclusive measurement of particle c , $E \frac{d^3\sigma_c}{d\vec{p}^3}$, is related to the invariant yield $E \frac{d^3N_c}{d\vec{p}^3}$ by the total cross section σ_{a+b} for the specific trigger selection:

$$E \frac{d^3\sigma_c}{d\vec{p}^3} = E \frac{d^3N_c}{d\vec{p}^3} \cdot \sigma_{a+b} \quad (\text{A.2})$$

dN_c is the number of particles c in the momentum bin $d\vec{p}^3$, E the energy of particle c measured in the same momentum frame as \vec{p} . For the total inclusive cross section this equation reduces to

$$\sigma_c = \langle n_c \rangle \cdot \sigma_{tot}^{inel} \quad (\text{A.3})$$

where $\langle n_c \rangle$ is the mean multiplicity and σ_{tot}^{inel} the total inelastic cross section of the reaction $a + b$.

In NA49 the coordinate system is defined such that the positive z -axis goes along the beam direction. The plane transverse to the beam direction is spanned

by the horizontal x -axis and the vertical y -axis. The bending plane of the magnets corresponds to the $x - z$ plane.

The *right hemisphere* in NA49 is the half which is on the righthand side of the beam axis if looking downstream, i. e. in positive z -direction. The *left hemisphere* is defined accordingly.

Because of symmetries imposed by the collision cylindrical coordinates are more appropriate than cartesian ones. For kinematic variables for the transverse plane relative to the beam the transverse momentum p_t

$$p_t = \sqrt{p_x^2 + p_y^2} \quad (\text{A.4})$$

and azimuth ϕ

$$\phi = \arctan\left(\frac{p_y}{p_x}\right) \quad (\text{A.5})$$

are used in this work. For a particle of mass m the transverse mass m_t is defined as

$$m_t = \sqrt{p_t^2 + m^2}. \quad (\text{A.6})$$

For the longitudinal direction either Feynman- x x_F or rapidity y can be taken depending on the subject of interest.

$$x_F = \frac{p_{z,CM}}{p_{max}} \approx \frac{2p_{z,CM}}{\sqrt{s}} \quad (\text{A.7})$$

Here, $p_{z,CM}$ is the longitudinal momentum in the center-of-mass frame of the collision and $p_{max} = \sqrt{\left(\frac{\sqrt{s}}{2}\right)^2 - m_p^2}$ the maximum momentum for produced particles in case of a proton as projectile with mass m_p . The Lorentz transformation from labsystem to center-of-mass system reads

$$p_{z,CM} = \gamma(p_z - \beta E) \quad (\text{A.8})$$

with $\beta = \frac{p_{1,lab}}{E_{1,lab} + m_2}$ and $\gamma = \frac{1}{\sqrt{1 - \beta^2}}$. $p_{1,lab}$ and $E_{1,lab}$ are momentum and energy of the projectile, m_2 is the target mass.

Feynman- x is very useful as longitudinal variable if projectile or target fragmentation regions are under study. Since rapidity is a logarithmic variable the center-of-mass region is stretched and the fragmentation regions are squeezed. This variable is used for the study of produced particles.

$$y = \frac{1}{2} \ln\left(\frac{E + p_z}{E - p_z}\right) = \ln\left(\frac{E + p_z}{m_t}\right) \quad (\text{A.9})$$

It has the additional advantage that it is additive under a Lorentz boost by velocity β which also leaves the functional form invariant:

$$y \rightarrow y + \frac{1}{2} \left(\frac{1 + \beta}{1 - \beta} \right) \quad (\text{A.10})$$

The invariant cross section $E \frac{d^3\sigma}{d\vec{p}^3}$ can be expressed in these different kinematic variables:

$$\begin{aligned}
 E \frac{d^3\sigma}{d\vec{p}^3} &= \frac{E p_t}{p_t p} \frac{d^3\sigma}{d\phi dp dp_t} \\
 &= \frac{1}{p_t} \frac{d^3\sigma}{d\phi dy dp_t} \\
 &= \frac{1}{m_t} \frac{d^3\sigma}{d\phi dy dm_t} \\
 &= \frac{E_0}{p_t p_0} \frac{d^3\sigma}{d\phi dx_F dp_t}
 \end{aligned}
 \tag{A.11}$$

When considering just multiplicities, i. e. invariant yields, $d^3\sigma$ is replaced by d^3N . As introduced in chapter 3 particle yields N_i are measured in a (p, p_t, ϕ) -bin. The extracted $\frac{N_i}{\Delta\phi\Delta p\Delta p_t}$ corresponds to $\frac{d^3N}{d\phi dp dp_t}$ in the formula. The equations above give rules for the transformation of the multiplicities in dependence on different kinematic variables. The transformation coefficients are calculated at the geometrical center of each bin.

In addition it has to be taken into account that the shape of the bins change (fig. A.1). Since the bins are small here this effect is neglected and the multiplicity is straight forward transformed from the (p, p_t) -bin to a rectangular bin in (y, p_t) .

The binsize in y is chosen such that a one to one mapping from $\log p$ to y is achieved which is approximately fulfilled by $dy \approx \ln 10 \cdot d(\log p)$ (see equations below); thus $dy = 6/26 \approx 0.23$ is a good choice for $d(\log p) = 0.1$. In fact this mapping works for the whole acceptance region in (y, p_t) of NA49.

$$\frac{dN}{d(\log p)} = \frac{dN}{dy} \frac{dy}{d(\log p)}
 \tag{A.12}$$

$$\frac{dy}{d(\log p)} = p \cdot \ln 10 \cdot \frac{dy}{dp} \approx \ln 10
 \tag{A.13}$$

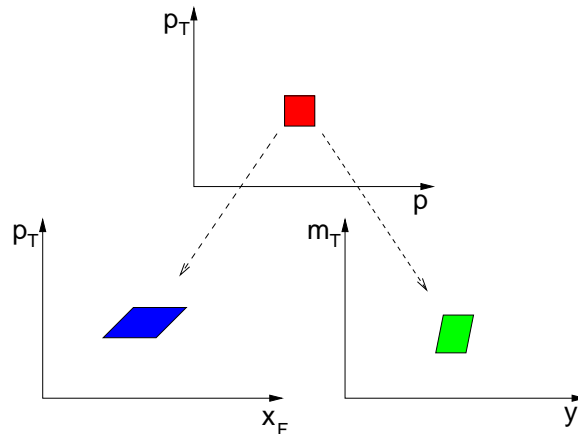


Figure A.1: Change of binshape going along with the transformation of the kinematic variables. (From [65].)

$$\begin{aligned}
\frac{dy}{dp} &= \frac{1}{p} \frac{1}{E + p_z} \left(\frac{p^2}{E} + \frac{p^2}{p_z} \right) \\
&= \frac{1}{p} \frac{1}{E + p_z} \left(E - \frac{m^2}{E} + p_z + \frac{p_t^2}{p_z} \right) \\
&= \frac{1}{p} \left(1 + \frac{1}{E + p_z} \left(\frac{p_t^2}{p_z} - \frac{m^2}{E} \right) \right) \\
&\approx \frac{1}{p} (1 + \dots)
\end{aligned} \tag{A.14}$$

As it is common practice $c = \hbar = 1$ is used, i. e. the unit of masses and momenta is "GeV". For clearness "fm/c" is still used for times. Typical numbers for kinematic quantities in NA49 can be found in table A.1.

\sqrt{s}	17.27 GeV
γ_{CM}	9.2
β_{CM}	0.994
y_{CM}	2.9 in labsystem
$p_{z,max}$	8.58 GeV
pions at y_{CM} and small p_t	$p \approx 1-3$ GeV
kaons at y_{CM} and small p_t	$p \approx 4-6$ GeV
protons at y_{CM} and small p_t	$p \approx 8-10$ GeV

Table A.1: Typical numbers for kinematic quantities in NA49 as a fixed-target experiment with a beam energy of 158 AGeV.

Appendix B

Clebsch-Gordan coefficients

$K^*(892)$ is an isospin 1/2 state which is decaying into K (isospin 1/2) and π (isospin 1) via the strong interaction which conserves the isospin (see table B.1).

The relative weights of the final $K\pi$ states are given by the Clebsch-Gordan coefficients which can be found in [2]. In case of, e. g., the $K^*(892)^+$ and $\overline{K}^*(892)^0$ decay the corresponding wave function reads [1]

$$|\xi(\frac{1}{2}, \frac{1}{2})\rangle = \sqrt{\frac{2}{3}}|\phi_1(\frac{1}{2}, -\frac{1}{2})\rangle|\phi_2(1, 1)\rangle - \sqrt{\frac{1}{3}}|\phi_1(\frac{1}{2}, \frac{1}{2})\rangle|\phi_2(1, 0)\rangle. \quad (\text{B.1})$$

Resulting branching ratios for the various $K\pi$ channels are summarized in table B.2.

$K^*(892)^+$	$\longrightarrow K^0\pi^+$	$K^*(892)^-$	$\longrightarrow \overline{K}^0\pi^-$
1/2	-1/2 1	-1/2	1/2 -1
	$\longrightarrow K^+\pi^0$		$\longrightarrow K^-\pi^0$
1/2	1/2 0	-1/2	-1/2 0
$\overline{K}^*(892)^0$	$\longrightarrow K^-\pi^+$	$K^*(892)^0$	$\longrightarrow K^+\pi^-$
1/2	-1/2 1	-1/2	1/2 -1
	$\longrightarrow \overline{K}^0\pi^0$		$\longrightarrow K^0\pi^0$
1/2	1/2 0	-1/2	-1/2 0

Table B.1: Decay channels with isospin-3 components of $K^*(892)$.

$K^*(892)^\pm$	$\longrightarrow K^0\pi^\pm$	$\longrightarrow K^\pm\pi^0$
	2/3	1/3
$K^*(892)^0$	$\longrightarrow K^\pm\pi^\mp$	$\longrightarrow K^0\pi^0$
	2/3	1/3

Table B.2: Branching ratios for $K^*(892)$.

Appendix C

Particle distributions: tables and figures

Only tracks stemming from the main vertex and having a reasonable momentum fit are accepted in the analyzed track sample [66]. In the NA49 DST structures this requires for the track vertex: $\text{vertex.id_vtx} = 0$, $\text{vertex.pchi2} > 0$ (C+C, Si+Si) or $\text{vertex.pchi2} \geq 0$ (p+p), and $\text{vertex.iflag} = 1$ (C+C, Si+Si) or $\text{vertex.iflag} = 1$ or $\text{vertex.iflag} = 4$ (p+p), respectively. The track itself has to fulfill $\text{track.iflag} = 0$ and has to have a reasonable momentum, i. e. $\frac{\text{charge}}{\sqrt{p_x^2 + p_z^2}} \geq 0.00001 \text{ GeV}^{-1}$, $p_t \leq 9.9 \text{ GeV}$ and $0.01 \text{ GeV} \leq p \leq 999 \text{ GeV}$. These quality cuts are applied for the whole analysis in this thesis.

Yields are extracted in bins of y and p_t for $K^*(892)$ and the ϕ -meson, and in bins of p and p_t with transformation to y and p_t afterwards for pions and kaons. Mean values of the kinematic bins are usually calculated at the geometrical center of the bin. However, for large bins and strongly changing distributions the mean should be calculated differently taking into account these facts [165]. For the ϕ -meson and the $K^*(892)$ means were calculated according to Lafferty and Wyatt [165]. The difference is negligible here (see tables).

In the following tables only statistical errors are given, see chapters 5 and 6 for a discussion of systematic uncertainties.

A few kinematic distributions are compared to results from literature, other measurements in NA49 and simulations. In particular a comparison to midrapidity p_t -spectra and/or the midrapidity region of y -distributions of pions is of interest because of the large extrapolation which is necessary for the NA49 data.

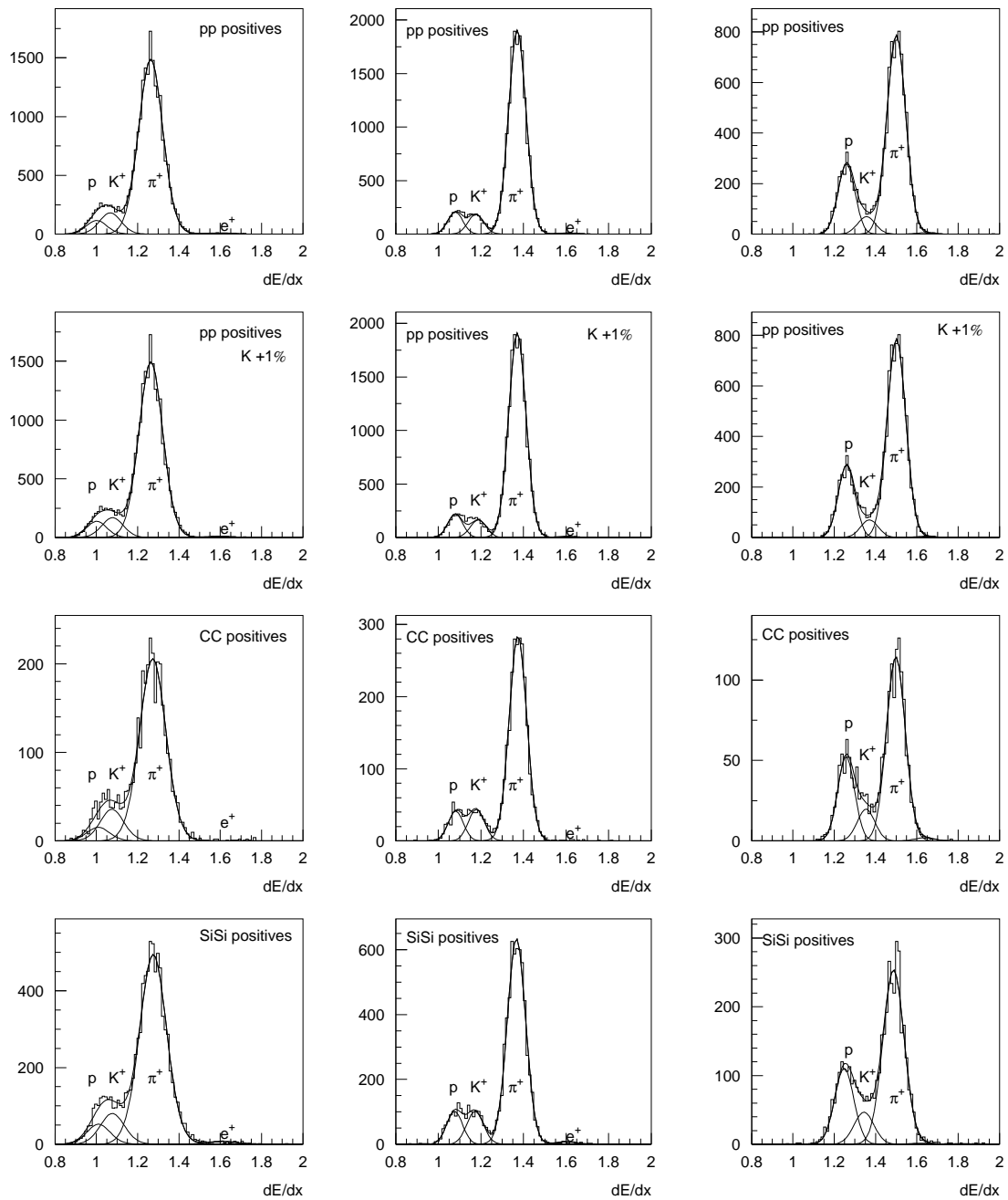


Figure C.1: Energy loss distribution in a small (p, p_t) bin for positive particles from p+p, C+C and Si+Si interactions; for p+p also fits with a +1 % shift of the mean position of K^+ is shown. The p_t -range is $0.3 < p_t \leq 0.4$ GeV for all spectra, the p -range is chosen as follows: $4 < p < 5$ GeV (left), $7.9 < p < 10$ GeV (middle), and $25.1 < p < 31.6$ GeV (right). For all tracks in p+p $N_{points} \geq 30$, $|\phi| \leq 30^\circ$ and right-side type is required. For C+C and Si+Si the Φ -range is slightly enlarged, $|\phi| \leq 50^\circ$.

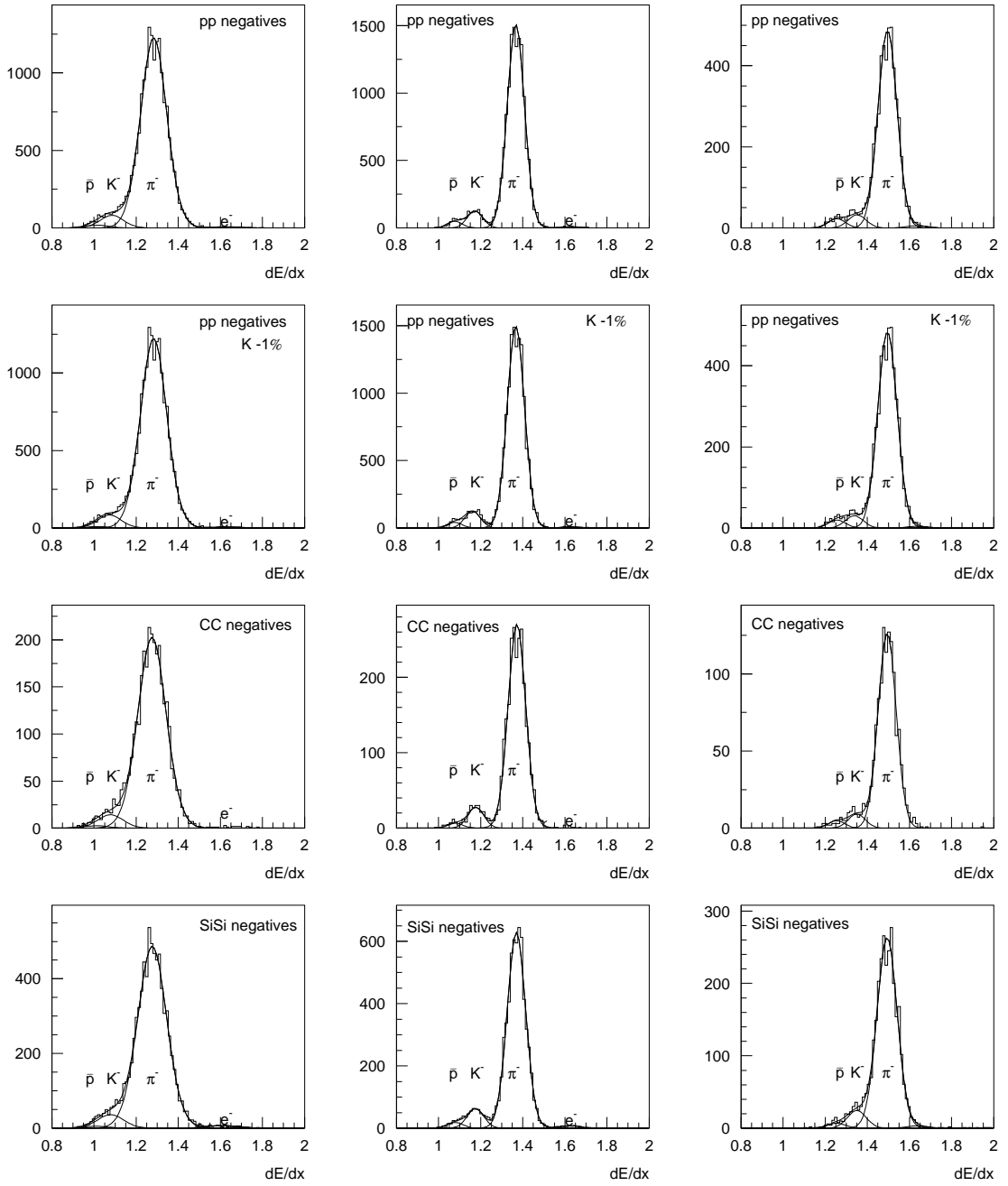


Figure C.2: Energy loss distribution in a small (p, p_t) bin for negative particles from p+p, C+C and Si+Si interactions; for p+p also fits with a -1 % shift of the mean position of K^- is shown. The p_t -range is $0.3 < p_t \leq 0.4$ GeV for all spectra, the p -range is chosen as follows: $4 < p < 5$ GeV (left), $7.9 < p < 10$ GeV (middle), and $25.1 < p < 31.6$ GeV (right). For all tracks in p+p $N_{points} \geq 30$, $|\phi| \leq 30^\circ$ and right-side type is required. For C+C and Si+Si the Φ -range is slightly enlarged, $|\phi| \leq 50^\circ$.

C.1 p+p collisions

y -range	\bar{y}	π^+		π^-	
		$\frac{\Delta N}{\Delta y}$	T [MeV]	$\frac{\Delta N}{\Delta y}$	T [MeV]
2.77 - 3.00	2.88	0.775 ± 0.048	167.5	0.681 ± 0.043	166.1
3.00 - 3.23	3.12	0.767 ± 0.031	167.3	0.681 ± 0.028	165.8
3.23 - 3.46	3.35	0.770 ± 0.016	166.7	0.659 ± 0.014	164.7
3.46 - 3.69	3.58	0.737 ± 0.015	165.8	0.615 ± 0.014	162.8
3.69 - 3.92	3.81	0.711 ± 0.007	164.4	0.563 ± 0.006	160.1
3.92 - 4.15	4.04	0.663 ± 0.006	162.6	0.504 ± 0.005	156.7
4.15 - 4.38	4.27	0.596 ± 0.005	160.4	0.450 ± 0.005	152.5
4.38 - 4.62	4.50	0.511 ± 0.005	157.8	0.372 ± 0.004	147.5
4.62 - 4.85	4.73	0.420 ± 0.006	154.8	0.285 ± 0.004	141.7
4.85 - 5.08	4.96	0.342 ± 0.009	151.5	0.215 ± 0.005	135.2
5.08 - 5.31	5.19	0.261 ± 0.015	147.7	0.152 ± 0.008	127.9
5.31 - 5.54	5.42	0.197 ± 0.016	143.5	0.101 ± 0.008	119.8

Table C.1: Feed-down corrected and p_t -integrated y -distribution of pions in minimum bias p+p collisions; center-of-mass rapidity is 2.9. Only statistical errors are quoted. The smoothed temperature is given, for an explanation of their calculation see section 6.1.

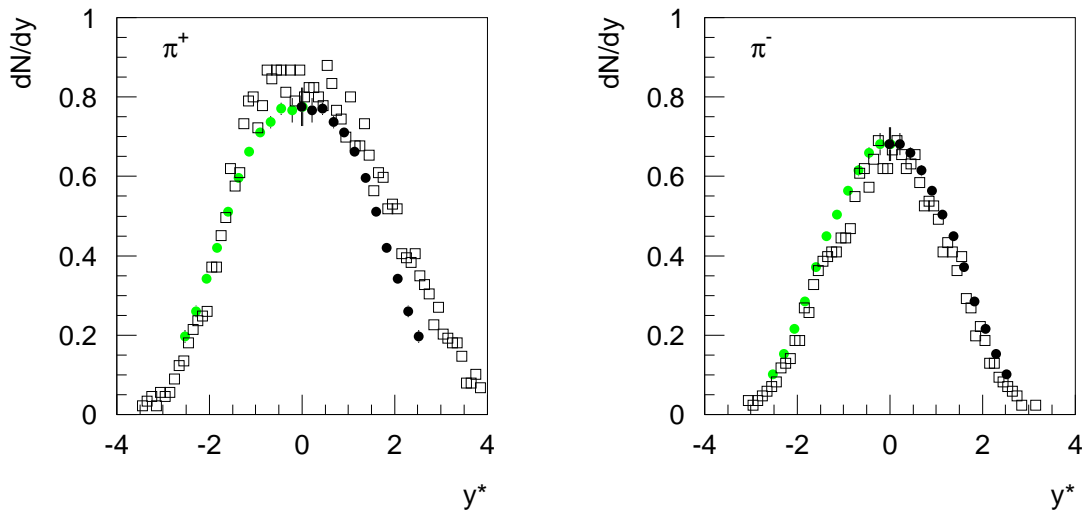


Figure C.3: Comparison of p_t -integrated y -distributions from this work (circles) with data from Morse et al. [166] (open squares), grey circles are yields from this thesis but reflected at midrapidity. Morse et al. analyzed p+p data at 100 GeV. For this figure their yields were scaled according to the energy dependence derived by Rossi et al. [105], i.e. π^- are multiplied by 1.17 and π^+ by 1.128.

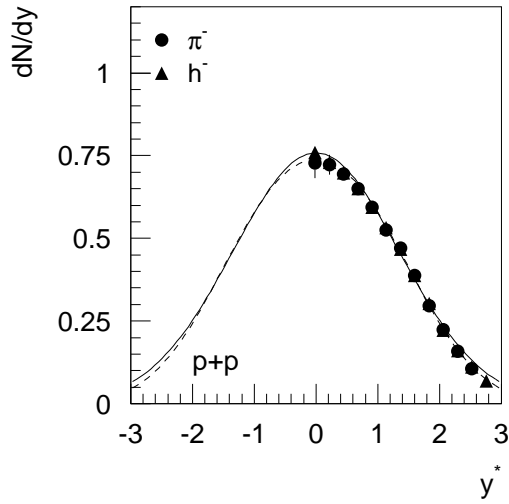


Figure C.4: Rapidity distribution of π^- in p+p in comparison to the preliminary h^- analysis (see section 6.1). After subtraction of the K^- and \bar{p} contribution the h^- distribution is scaled to the one of π^- in the rapidity range $3.91 < y \leq 4.62$ to account for remaining background in the h^- . Both distributions are not feed-down corrected, however, the correction would be the same. The solid line represents a double-Gaussian fit to π^- , the dashed line to h^- .

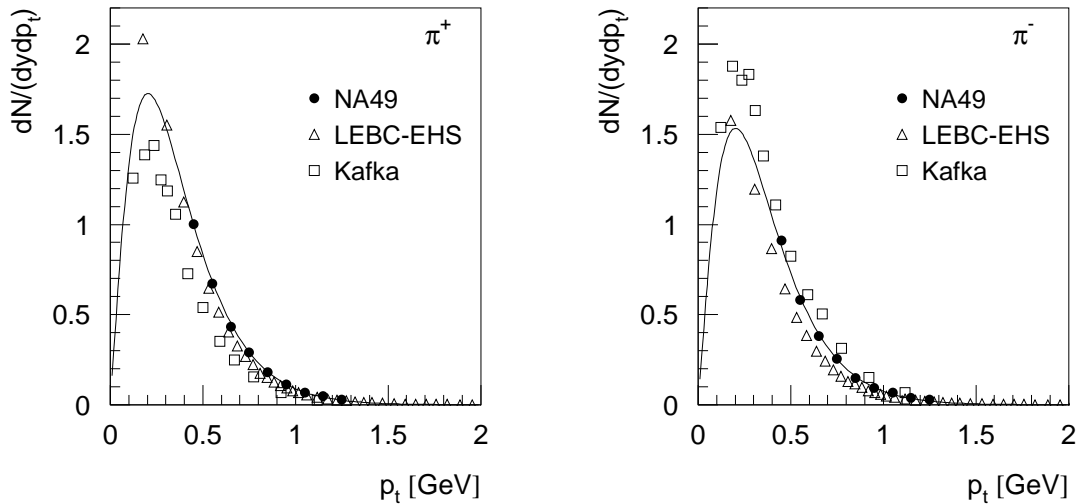


Figure C.5: Comparison of midrapidity p_t -distributions of this work ($2.77 < y < 3$) with results for p+p interactions at 205 GeV from Kafka et al. [167] and at 400 GeV from the LEBC-EHS experiment [82]. Yields of both experiments are scaled according to the energy dependence derived by Rossi et al. [105]; a total inelastic trigger cross section of 33 mb is used to extract multiplicities [2]. The line corresponds to a thermal fit to the data of this thesis assuming a temperature as given in table C.1. This distribution was used to extract the p_t -integrated pion yield at midrapidity.

y -range	\bar{y}	feed-down correction [%]	
		π^+	π^-
2.77 - 3.00	2.88	5.86 ± 0.28	6.44 ± 0.31
3.00 - 3.23	3.12	5.82 ± 0.29	5.83 ± 0.30
3.23 - 3.46	3.35	5.18 ± 0.29	5.10 ± 0.31
3.46 - 3.69	3.58	5.00 ± 0.31	5.57 ± 0.36
3.69 - 3.92	3.81	4.43 ± 0.32	5.01 ± 0.38
3.92 - 4.15	4.04	3.78 ± 0.33	4.14 ± 0.39
4.15 - 4.38	4.27	3.38 ± 0.34	4.43 ± 0.43
4.38 - 4.62	4.50	2.71 ± 0.33	4.18 ± 0.47
4.62 - 4.85	4.73	2.73 ± 0.37	3.67 ± 0.50
4.85 - 5.08	4.96	1.88 ± 0.35	3.67 ± 0.56
5.08 - 5.31	5.19	1.97 ± 0.40	3.49 ± 0.63
5.31 - 5.54	5.42	1.77 ± 0.47	3.84 ± 0.76

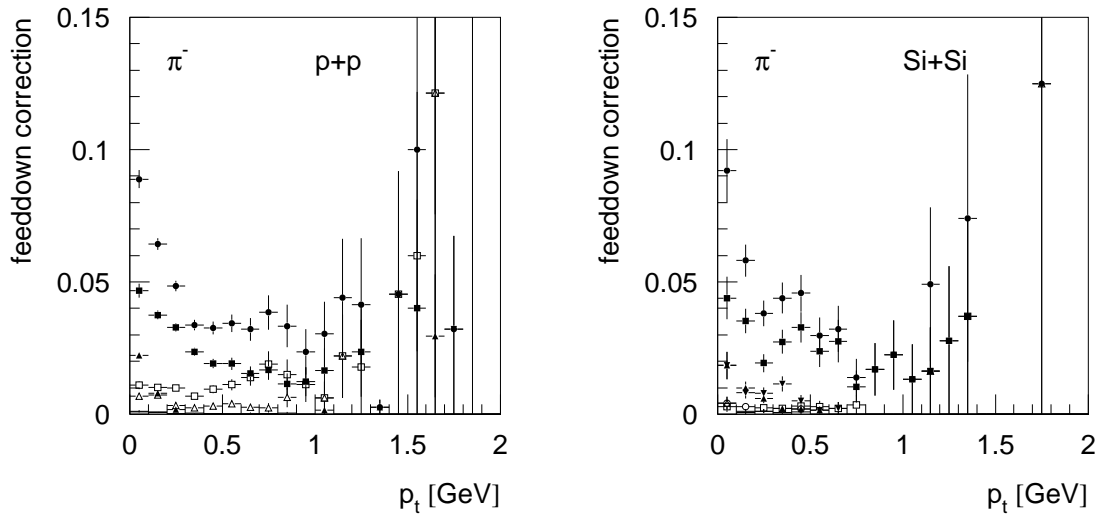
Table C.2: Feed-down correction in dependence on y for pions in minimum-bias p+p.

Figure C.6: Relative feed-down correction for π^- in p+p and Si+Si in dependence on p_t for $y > 0$. \bullet is the total feed-down correction. Contributions from the different sources are indicated as follows: \blacksquare π from K_S^0 , \blacktriangle π from Λ , \circ π from Ξ , \blacktriangledown π from Σ , \square π from secondary interactions (in particular important for p+p due to the extended proton target), and \triangle π from split tracks and similar sources.

y -range	\bar{y}	K^+		K^-	
		$\frac{\Delta N}{\Delta y}$	T [MeV]	$\frac{\Delta N}{\Delta y}$	T [MeV]
2.77 - 3.00	2.88	0.0870 ± 0.0010	177 ± 2	0.0563 ± 0.0008	168 ± 2
3.00 - 3.23	3.12	0.0827 ± 0.0010	173 ± 2	0.0502 ± 0.0007	160 ± 2
3.23 - 3.46	3.35	0.0747 ± 0.0009	170 ± 2	0.0485 ± 0.0007	157 ± 2
3.46 - 3.69	3.58	0.0696 ± 0.0009	171 ± 2	0.0421 ± 0.0007	155 ± 2
3.69 - 3.92	3.81	0.0625 ± 0.0008	171 ± 2	0.0388 ± 0.0006	151 ± 2
3.92 - 4.15	4.04	0.0491 ± 0.0007	156 ± 2	0.0302 ± 0.0005	147 ± 3
4.15 - 4.38	4.27	0.0377 ± 0.0006	162 ± 3	0.0214 ± 0.0004	136 ± 3
4.38 - 4.62	4.50	0.0333 ± 0.0006	162 ± 3	0.0151 ± 0.0004	130 ± 3
4.62 - 4.85	4.73	0.0277 ± 0.0012	173 ± 6	0.0101 ± 0.0005	139 ± 7

Table C.3: p_t -integrated y -distribution of kaons in minimum bias p+p collisions; center-of-mass rapidity is 2.9. Only statistical errors are quoted. The quoted temperature stems from a thermal fit to the p_t -spectra.

Comparing results from this work with an analysis of the same p+p data from F. Sikler [12] gives an overall good agreement. For pions the main discrepancy lies in the midrapidity values which were shown to have a systematic uncertainty if extracted from dE/dx fits. K^+ are systematically different, the rapidity distributions of F. Sikler are always broader and lower at midrapidity due to a different treatment of the separation of kaons from protons. For C+C and Si+Si collisions (see below) the agreement is slightly better. However, the same systematic differences persist.

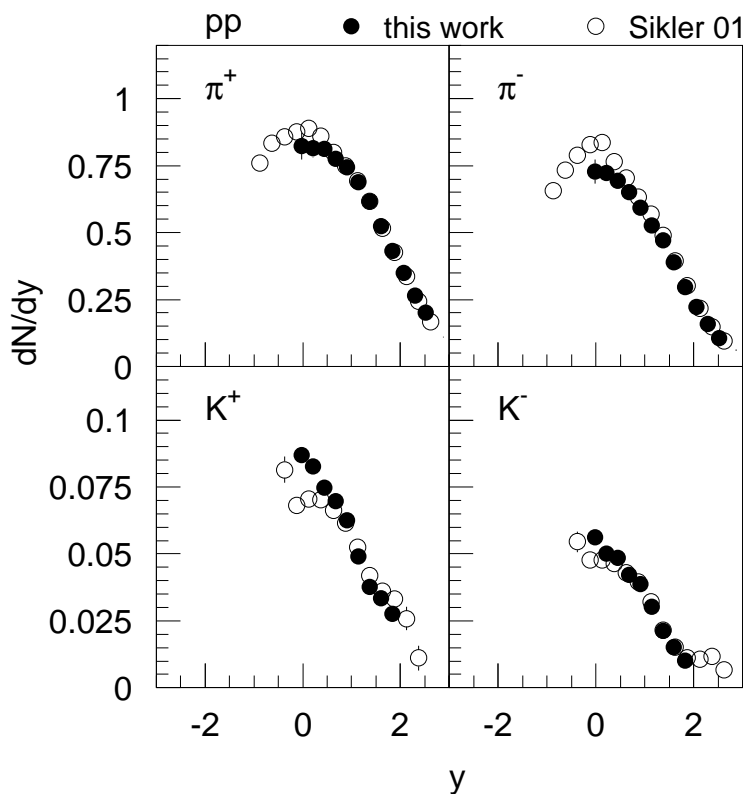


Figure C.7: Comparison of rapidity distributions for charged pions (not feed-down corrected) and kaons in minimum-bias p+p collisions at 158 GeV from this work with results from F. Sikler [12]. Total yields are consistent within the systematic errors: they differ by 7 % for π^- , for the other mesons the difference is less (1-4 %).

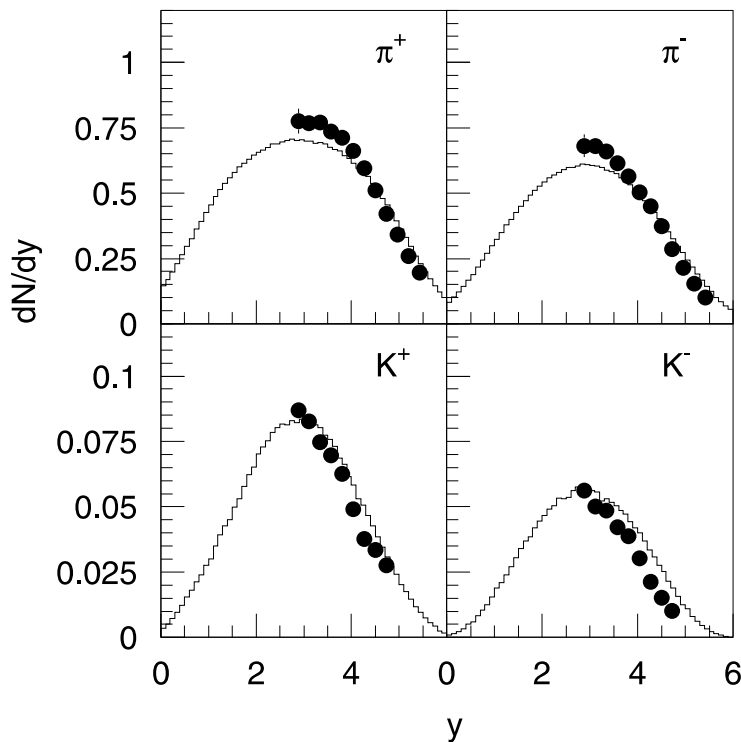
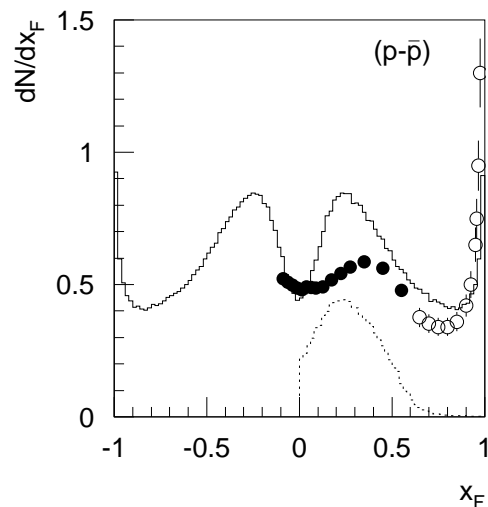


Figure C.8: Comparison of y -distributions of pions and kaons from FRITIOF (histogram) with data (circles) for inelastic p+p collisions at $\sqrt{s} = 17.3$ GeV. Data are feed-down corrected, in FRITIOF decays of weak resonances were not allowed.

FRITIOF simulations were studied in context of the investigation of inelasticity-dependent p+p interactions (see chapters 4.2, 5.2.3). For the discussion a comparison of minimum-bias distributions and yields is also of interest. Fig. C.8 shows that rapidity distributions of pions and kaons agree rather well to the data. The same holds for p_t -spectra (not shown). However, the x_F -distribution of protons is significantly different compared to data.

Figure C.9: Comparison of x_F -distribution of net-protons ($p-\bar{p}$) from FRITIOF (histogram) with data (circles) for inelastic p+p collisions at $\sqrt{s} = 17.3$ GeV. The same p+p data as in figure 1.9 are used, filled circles correspond to feed-down-corrected p+p data from NA49 [12], the open symbols are a compilation of data from other experiments [13]. In FRITIOF, decay of weak resonances was not allowed. The dotted line presents the x_F distribution of leading protons in FRITIOF under experimental restrictions as described in chapter 4.2.



p_t -range [GeV]	\overline{p}_t [GeV]	$\frac{\Delta N}{\Delta p_t \Delta y}$	$\overline{m}_t - m_0$ [GeV]	$\frac{\Delta N}{m_t \Delta m_t \Delta y}$
0.0 - 0.2	0.10	0.00198 ± 0.00015	0.010	0.01976 ± 0.00148
0.2 - 0.4	0.29	0.00516 ± 0.00023	0.047	0.01720 ± 0.00077
0.4 - 0.6	0.52	0.00555 ± 0.00024	0.118	0.01112 ± 0.00047
0.6 - 0.8	0.70	0.00395 ± 0.00020	0.217	0.00565 ± 0.00029
0.8 - 1.0	0.90	0.00261 ± 0.00016	0.339	0.00291 ± 0.00018
1.0 - 1.2	1.10	0.00132 ± 0.00012	0.477	0.00121 ± 0.00011
1.2 - 1.4	1.29	0.00065 ± 0.00008	0.628	0.00050 ± 0.00007
1.4 - 1.6	1.49	0.00025 ± 0.00016	0.789	0.00017 ± 0.00011

Table C.4: p_t and m_t - distribution of the ϕ -meson in minimum bias p+p collisions in the rapidity range [2.9,4]. Here, mean values are calculated according to [165]. Obviously the difference to the geometrical center of the bin is small.

y -range	\overline{y}	$\frac{\Delta N}{\Delta y}$
2.9 - 3.1	3.015	0.005348 ± 0.000296
3.1 - 3.3	3.205	0.005054 ± 0.000244
3.3 - 3.5	3.402	0.004391 ± 0.000214
3.5 - 3.7	3.601	0.004180 ± 0.000199
3.7 - 3.9	3.800	0.003609 ± 0.000182
3.9 - 4.1	4.000	0.003045 ± 0.000168
4.1 - 4.3	4.199	0.002325 ± 0.000147
4.3 - 4.5	4.398	0.001492 ± 0.000121
4.5 - 4.7	4.598	0.000985 ± 0.000102
4.7 - 4.9	4.797	0.000621 ± 0.000096

Table C.5: p_t -integrated y -distribution of the ϕ -meson in minimum bias p+p collisions; center-of-mass rapidity is 2.9. Mean values are calculated according to [165]; the difference is small to the geometrical center of the bin.

y -range	\overline{y}	$K^*(892)$	$\overline{K}^*(892)$
		$\frac{\Delta N}{\Delta y}$	$\frac{\Delta N}{\Delta y}$
2.9 - 3.1	3.02	0.0258 ± 0.0027	0.0201 ± 0.0024
3.1 - 3.3	3.21	0.0291 ± 0.0019	0.0191 ± 0.0017
3.3 - 3.5	3.40	0.0248 ± 0.0014	0.0188 ± 0.0012
3.5 - 3.7	3.60	0.0205 ± 0.0011	0.0170 ± 0.0009
3.7 - 3.9	3.80	0.0193 ± 0.0009	0.0156 ± 0.0007
3.9 - 4.1	4.00	0.0186 ± 0.0008	0.0123 ± 0.0006
4.1 - 4.3	4.20	0.0145 ± 0.0008	0.0100 ± 0.0005
4.3 - 4.5	4.40	0.0121 ± 0.0008	0.0084 ± 0.0005
4.5 - 4.7	4.60	0.0102 ± 0.0008	0.0051 ± 0.0004
4.7 - 4.9	4.80	0.0066 ± 0.0007	0.0028 ± 0.0004

Table C.6: p_t -integrated y -distribution of $K^*(892)^0$ and $\overline{K}^*(892)^0$ in minimum bias p+p collisions; center-of-mass rapidity is 2.9.

p_t -range [GeV]	\overline{p}_t [GeV]	$K^*(892)^0$	$\overline{K}^*(892)^0$
		$\frac{\Delta N}{\Delta p_t \Delta y}$	$\frac{\Delta N}{\Delta p_t \Delta y}$
0.0 - 0.2	0.10	0.0142 ± 0.0014	0.0128 ± 0.0013
0.2 - 0.4	0.28	0.0293 ± 0.0018	0.0243 ± 0.0015
0.4 - 0.6	0.51	0.0311 ± 0.0017	0.0254 ± 0.0015
0.6 - 0.8	0.70	0.0183 ± 0.0013	0.0145 ± 0.0011
0.8 - 1.0	0.90	0.0123 ± 0.0010	0.00793 ± 0.00078
1.0 - 1.2	1.10	0.0066 ± 0.0007	0.00498 ± 0.00054
1.2 - 1.4	1.29	0.0036 ± 0.0005	0.00192 ± 0.00036
1.4 - 1.6	1.49	0.0017 ± 0.0009	0.00075 ± 0.00037
$\overline{m}_t - m_0$ [GeV]		$\frac{\Delta N}{m_t \Delta m_t \Delta y}$	$\frac{\Delta N}{m_t \Delta m_t \Delta y}$
0.011		0.1424 ± 0.0141	0.1284 ± 0.0127
0.053		0.0978 ± 0.0058	0.0810 ± 0.0051
0.132		0.0623 ± 0.0034	0.0510 ± 0.0029
0.241		0.0262 ± 0.0019	0.0208 ± 0.0016
0.373		0.0137 ± 0.0011	0.0088 ± 0.0009
0.520		0.0060 ± 0.0006	0.0045 ± 0.0005
0.680		0.0028 ± 0.0004	0.00148 ± 0.00028
0.847		0.0011 ± 0.0006	0.00050 ± 0.00025

Table C.7: p_t and m_t -distribution of $K^*(892)^0$ and $\overline{K}^*(892)^0$ in minimum bias p+p collisions in the rapidity range [3.1,3.9]. Mean values are calculated according to [165].

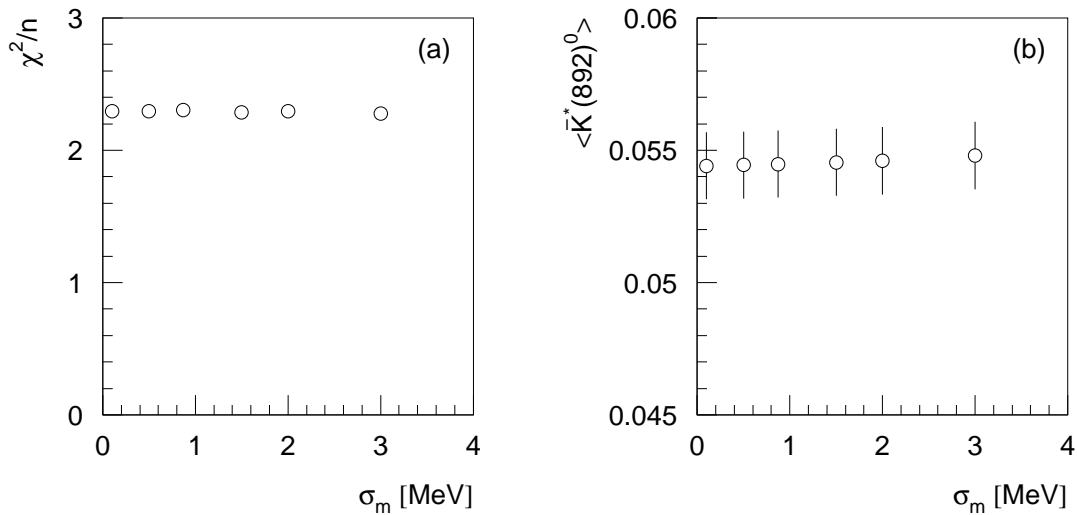


Figure C.10: Additional figure to chapter 5.1.4: χ^2/n in dependence on the width σ_m of the Gaussian broadening of the $\overline{K}^*(892)^0$ -mass for a fixed mass $m = 892$ MeV (a). Since the intrinsic width of the $K^*(892)$ is much larger, the additional Gaussian shows no effect, neither on χ^2/n (a) nor on the yield (b).

$n_{ch,measured}$	range	$\overline{n_{ch,measured}}$	$\langle\pi^+\rangle$	$\langle\pi^-\rangle$	$\langle K^+\rangle$	$\langle K^-\rangle$
1 - 2		1.6	0.652 ± 0.007	0.250 ± 0.005	0.0407 ± 0.0014	0.0173 ± 0.0016
3 - 4		3.5	1.430 ± 0.036	0.892 ± 0.007	0.0919 ± 0.0019	0.0485 ± 0.0011
5 - 6		5.5	1.949 ± 0.016	1.522 ± 0.012	0.1471 ± 0.0027	0.0874 ± 0.0016
7 - 8		7.4	2.474 ± 0.018	2.104 ± 0.016	0.1972 ± 0.0032	0.1208 ± 0.0023
9 - 10		9.4	3.041 ± 0.026	2.686 ± 0.025	0.2281 ± 0.0046	0.1380 ± 0.0031
11 - 12		11.4	3.590 ± 0.044	3.306 ± 0.046	0.2658 ± 0.0082	0.1734 ± 0.0087
13 - 16		13.8	4.233 ± 0.087	4.017 ± 0.582	0.2925 ± 0.0202	0.2177 ± 0.0293

$n_{ch,measured}$	range	$\overline{n_{ch,measured}}$	$\langle K^*(892)\rangle$	$\langle K^*(892)\rangle$	$\langle\phi\rangle$
1-2			0.0220 ± 0.0009	0.0181 ± 0.0007	0.0032 ± 0.0002
3-4	3.5		0.0468 ± 0.0016	0.0352 ± 0.0013	0.0076 ± 0.0003
5-6	5.5		0.0700 ± 0.0028	0.0490 ± 0.0021	0.0125 ± 0.0004
7-8	7.4		0.0911 ± 0.0050	0.0599 ± 0.0037	0.0170 ± 0.0007
9-10	9.4		0.1160 ± 0.0094	0.0669 ± 0.0068	0.0216 ± 0.0013
11-12	11.4		0.1340 ± 0.0169	0.0747 ± 0.0121	0.0241 ± 0.0022
13-16	13.8				

Table C.8: Yields in the forward hemisphere in dependence on the measured number of charged particles for p+p collisions at $\sqrt{s} = 17.3$ GeV.

$x_{F,lead}$ range	$\overline{x_{F,lead}}$	$\langle \pi^+ \rangle$	$\langle \pi^- \rangle$	$\langle K^+ \rangle$	$\langle K^- \rangle$ multicolumn
0.0 - 0.1	0.05	2.63 ± 0.28	2.43 ± 0.26	0.182 ± 0.0406	0.130 ± 0.023
0.1 - 0.2	0.15	2.53 ± 0.26	2.37 ± 0.25	0.158 ± 0.035	0.123 ± 0.021
0.2 - 0.3	0.25	2.22 ± 0.23	2.13 ± 0.22	0.146 ± 0.032	0.106 ± 0.018
0.3 - 0.4	0.35	1.88 ± 0.20	1.82 ± 0.19	0.120 ± 0.027	0.092 ± 0.016
0.4 - 0.5	0.45	1.58 ± 0.33	1.57 ± 0.32	0.096 ± 0.022	0.083 ± 0.015
0.5 - 0.6	0.55	1.27 ± 0.27	1.37 ± 0.29	0.080 ± 0.021	0.075 ± 0.015

$x_{F,lead}$ range	$\overline{x_{F,lead}}$	$\langle K^*(892) \rangle$	$\langle K^*(892) \rangle$	$\langle \phi \rangle$
0.0-0.1	0.05	0.0750 ± 0.0078	0.0538 ± 0.0063	0.0109 ± 0.0011
0.1-0.2	0.15	0.0628 ± 0.0063	0.0444 ± 0.0052	0.0100 ± 0.0009
0.2-0.3	0.25	0.0559 ± 0.0055	0.0415 ± 0.0045	0.0099 ± 0.0009
0.3-0.4	0.35	0.0427 ± 0.0049	0.0360 ± 0.0042	0.0069 ± 0.0008
0.4-0.5	0.45	0.0377 ± 0.0048	0.0265 ± 0.0042	0.0046 ± 0.0008
0.5-0.6	0.55	0.0312 ± 0.0053	0.0188 ± 0.0046	0.0033 ± 0.0010

Table C.9: Yields in the forward hemisphere in dependence on the Feynman-x of the leading proton for p+p collisions at $\sqrt{s} = 17.3$ GeV. Leading protons are selected according to the standard method described in chapter 4.2.

C.2 C+C collisions

y -range	\bar{y}	$\frac{\Delta N}{\Delta y}$ π^+	T [MeV]	$\frac{\Delta N}{\Delta y}$ π^-	T [MeV]
2.77 - 3.00	2.88	5.69 ± 0.57	165.5	5.76 ± 0.57	163.3
3.00 - 3.23	3.12	5.73 ± 0.48	165.1	5.89 ± 0.48	162.9
3.23 - 3.46	3.35	5.77 ± 0.24	163.9	5.78 ± 0.24	161.5
3.46 - 3.69	3.58	5.49 ± 0.14	161.8	5.60 ± 0.17	159.0
3.69 - 3.92	3.81	5.20 ± 0.09	158.8	5.10 ± 0.11	155.6
3.92 - 4.15	4.04	4.65 ± 0.08	155.0	4.63 ± 0.10	151.2
4.15 - 4.38	4.27	4.06 ± 0.06	150.3	4.20 ± 0.11	145.7
4.38 - 4.62	4.50	3.67 ± 0.06	144.8	3.49 ± 0.09	139.3
4.62 - 4.85	4.73	2.89 ± 0.06	138.3	2.89 ± 0.10	131.9
4.85 - 5.08	4.96	2.42 ± 0.06	131.0	2.32 ± 0.12	123.5
5.08 - 5.31	5.19	1.86 ± 0.09	122.9	1.80 ± 0.09	114.1
5.31 - 5.54	5.42	1.37 ± 0.10	113.9	1.31 ± 0.09	103.7

Table C.10: Feed-down corrected and p_t -integrated y -distribution of pions in 15 % most central C+C collisions; center-of-mass rapidity is 2.9. For the first three midrapidity bins a systematic error of 10 %, 8 % and 4 % is given due to uncertainties in the p_t -extrapolation. Otherwise only statistical errors are quoted. The smoothed temperature is also included in the table, for an explanation of their calculation see section 6.1.

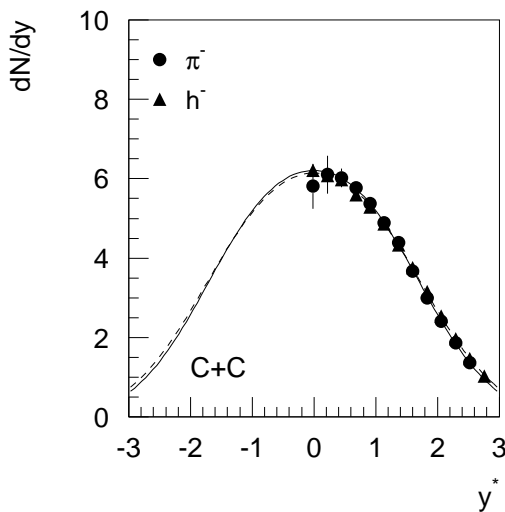


Figure C.11: Rapidity distribution of π^- in C+C in comparison to the preliminary h^- analysis. After subtraction of the K^- and \bar{p} contribution the h^- distribution is scaled to the one of π^- in the rapidity range $3.91 < y \leq 4.62$ to account for remaining background in the h^- . Both distributions are not feed-down corrected, however, the correction would be the same. The solid line represents a double-Gaussian fit to π^- , the dashed line to h^- .

y -range	\bar{y}	feed-down correction [%]	
		π^+	π^-
2.77 - 3.00	2.88	1.19 ± 0.85	0.88 ± 0.89
3.00 - 3.23	3.12	4.23 ± 1.05	3.49 ± 1.12
3.23 - 3.46	3.35	3.69 ± 0.71	3.93 ± 0.82
3.46 - 3.69	3.58	4.53 ± 0.68	3.01 ± 0.57
3.69 - 3.92	3.81	3.92 ± 0.58	5.12 ± 0.71
3.92 - 4.15	4.04	4.76 ± 0.64	5.48 ± 0.71
4.15 - 4.38	4.27	3.58 ± 0.59	4.31 ± 0.64
4.38 - 4.62	4.50	4.13 ± 0.69	5.16 ± 0.78
4.62 - 4.85	4.73	3.31 ± 0.66	3.42 ± 0.68
4.85 - 5.08	4.96	3.12 ± 0.73	3.60 ± 0.77
5.08 - 5.31	5.19	1.73 ± 0.62	3.68 ± 0.94
5.31 - 5.54	5.42	2.71 ± 0.92	3.83 ± 0.08

Table C.11: Feed-down correction in dependence on y for pions in C+C, statistical errors are rather large due to the small number of VENUS events available for this correction. .

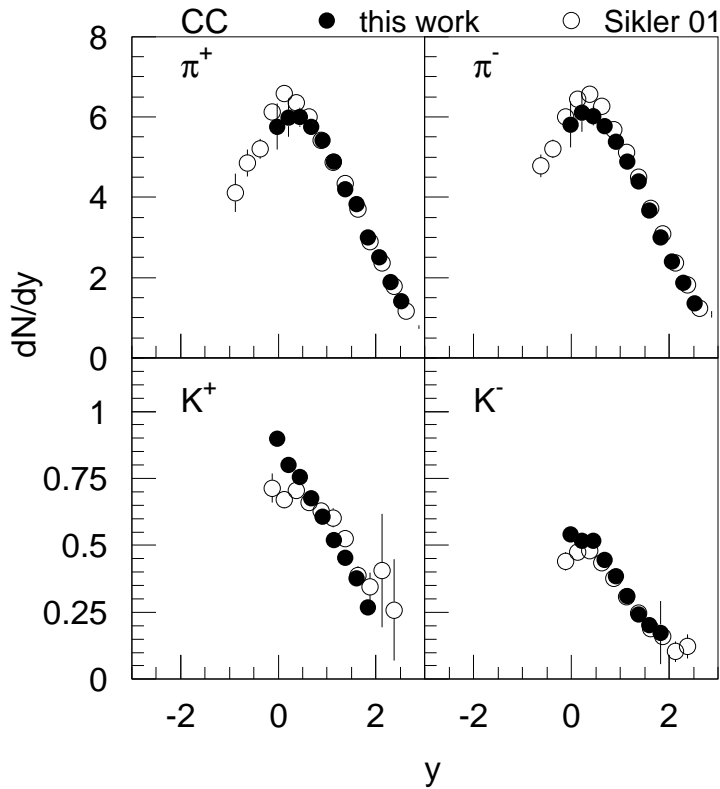


Figure C.12: Comparison of rapidity distributions for charged pions (not feed-down corrected) and kaons in the 15 % most central C+K collisions at 158 AGeV from this work with results from F. Sikler [12].

y -range	\bar{y}	K^+		K^-	
		$\frac{\Delta N}{\Delta y}$	T [MeV]	$\frac{\Delta N}{\Delta y}$	T [MeV]
2.77 - 3.00	2.88	0.897 ± 0.021	187 ± 5	0.541 ± 0.020	188 ± 7
3.00 - 3.23	3.12	0.799 ± 0.020	188 ± 5	0.517 ± 0.019	185 ± 7
3.23 - 3.46	3.35	0.756 ± 0.019	174 ± 5	0.516 ± 0.023	173 ± 8
3.46 - 3.69	3.58	0.677 ± 0.020	172 ± 6	0.447 ± 0.022	174 ± 8
3.69 - 3.92	3.81	0.606 ± 0.018	165 ± 6	0.384 ± 0.017	157 ± 8
3.92 - 4.15	4.04	0.521 ± 0.016	167 ± 6	0.311 ± 0.021	148 ± 10
4.15 - 4.38	4.27	0.454 ± 0.015	168 ± 6	0.241 ± 0.021	158 ± 13
4.38 - 4.62	4.50	0.376 ± 0.014	143 ± 6	0.202 ± 0.030	150 ± 16
4.62 - 4.85	4.73	0.267 ± 0.014	126 ± 7	0.174 ± 0.118	204 ± 62

Table C.12: p_t -integrated y -distribution of kaons in 15 % most central C+C collisions; center-of-mass rapidity is 2.9. The quoted temperature stems from a thermal fit to the p_t -spectra.

p_t -range [GeV]	\bar{p}_t [GeV]	$\frac{\Delta N}{\Delta p_t \Delta y}$	$\overline{m_t - m_0}$ [GeV]	$\frac{\Delta N}{\overline{m_t} \Delta m_t \Delta y}$
0.0 - 0.3	0.14	0.0284 ± 0.0036	0.0213	0.1896 ± 0.0240
0.3 - 0.6	0.38	0.0525 ± 0.0050	0.1008	0.1170 ± 0.0112
0.6 - 0.9	0.75	0.0382 ± 0.0045	0.2465	0.0511 ± 0.0060
0.9 - 1.2	1.04	0.0200 ± 0.0031	0.4394	0.0191 ± 0.0030
1.2 - 1.5	1.34	0.0100 ± 0.0022	0.6639	0.0075 ± 0.0017

Table C.13: p_t and m_t -distribution of the ϕ -meson in 15 % most central C+C collisions in the rapidity range [2.9,4.7].

y -range	\bar{y}	$\frac{\Delta N}{\Delta y}$
2.9 - 3.3	3.13	0.0648 ± 0.0085
3.3 - 3.7	3.51	0.0569 ± 0.0058
3.7 - 4.1	3.90	0.0446 ± 0.0048
4.1 - 4.5	4.30	0.0353 ± 0.0044
4.5 - 4.9	4.70	0.0195 ± 0.0041

Table C.14: p_t -integrated y -distribution of the ϕ -meson in 15 % most central C+C collisions; center-of-mass rapidity is 2.9.

C.3 Si+Si collisions

y -range	\bar{y}	π^+		π^-	
		$\frac{\Delta N}{\Delta y}$	T [MeV]	$\frac{\Delta N}{\Delta y}$	T [MeV]
2.77 - 3.00	2.88	15.12 ± 1.43	169.9	15.52 ± 1.43	172.0
3.00 - 3.23	3.12	14.83 ± 1.17	169.5	15.42 ± 1.17	171.5
3.23 - 3.46	3.35	14.74 ± 0.59	168.1	14.85 ± 0.59	169.9
3.46 - 3.69	3.58	13.97 ± 0.34	165.7	14.29 ± 0.30	167.2
3.69 - 3.92	3.81	13.32 ± 0.178	162.4	13.57 ± 0.17	163.3
3.92 - 4.15	4.04	12.11 ± 0.19	158.1	12.18 ± 0.16	158.3
4.15 - 4.38	4.27	10.79 ± 0.21	152.8	11.00 ± 0.16	152.2
4.38 - 4.62	4.50	9.32 ± 0.14	146.6	9.38 ± 0.14	145.0
4.62 - 4.85	4.73	7.56 ± 0.11	139.4	7.75 ± 0.11	136.6
4.85 - 5.08	4.96	6.11 ± 0.14	131.2	6.14 ± 0.14	127.2
5.08 - 5.31	5.19	4.57 ± 0.23	122.0	4.65 ± 0.22	116.6
5.31 - 5.54	5.42	3.37 ± 0.25	111.9	3.27 ± 0.24	104.9

Table C.15: Feed-down corrected and p_t -integrated y -distribution of pions in 12 % most central Si+Si collisions; center-of-mass rapidity is 2.9. For the first three midrapidity bins a systematic error of 9 %, 7.5 % and 4 % is given due to uncertainties in the p_t -extrapolation. Otherwise only statistical errors are quoted. The smoothed temperature is also included, for an explanation of their calculation see section 6.1.

y -range	\bar{y}	feed-down correction [%]	
		π^+	π^-
2.77 - 3.00	2.88	1.32 ± 0.94	0.98 ± 0.99
3.00 - 3.23	3.12	4.51 ± 1.12	3.82 ± 1.23
3.23 - 3.46	3.35	3.98 ± 0.77	4.23 ± 0.88
3.46 - 3.69	3.58	4.86 ± 0.73	3.24 ± 0.61
3.69 - 3.92	3.81	4.22 ± 0.63	5.44 ± 0.75
3.92 - 4.15	4.04	5.12 ± 0.68	5.82 ± 0.75
4.15 - 4.38	4.27	3.85 ± 0.63	4.55 ± 0.68
4.38 - 4.62	4.50	4.41 ± 0.73	5.48 ± 0.83
4.62 - 4.85	4.73	3.59 ± 0.72	3.61 ± 0.72
4.85 - 5.08	4.96	3.33 ± 0.78	3.80 ± 0.81
5.08 - 5.31	5.19	1.84 ± 0.66	3.86 ± 0.98
5.31 - 5.54	5.42	2.83 ± 0.96	4.10 ± 1.16

Table C.16: Feed-down correction in dependence on y for pions in Si+Si. See fig. C.6 for correction factors in dependence on p_t .

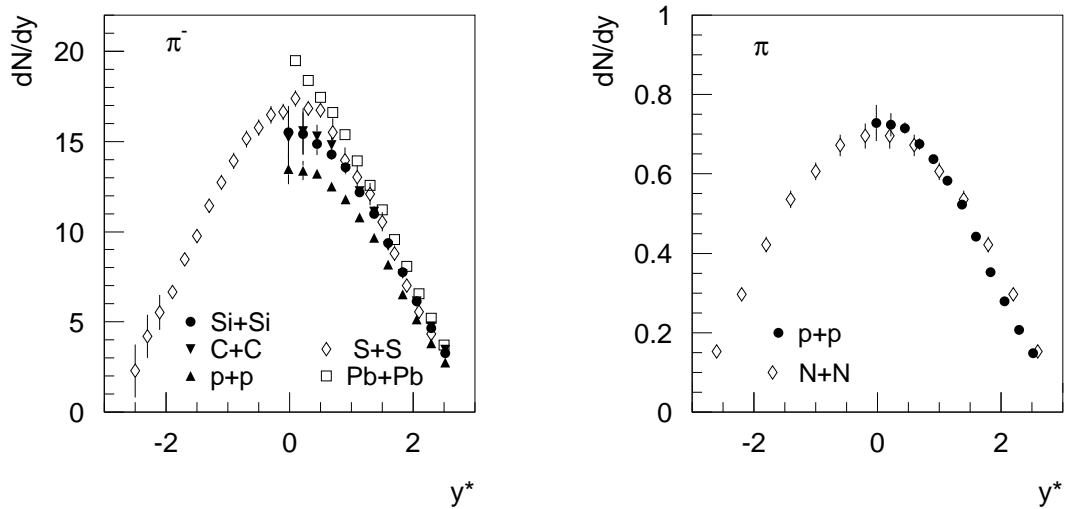


Figure C.13: Left: Comparison of y -distributions of π^- from this work for Si+Si collisions with those from minimum-bias p+p and central C+C, with results from NA49 in central Pb+Pb collisions at 158 AGeV [71], and with results from the NA35 experiment for central S+S collisions at 200 AGeV [128]. For this presentation yields of the other collision systems were scaled with the number of wounded nucleons (see table 7.1). In addition, negatively charged hadrons from NA35 were scaled by factors 0.92 and 0.93 to approximately take into account the contribution of K^- and \bar{p} [128] and the energy dependence of pions [105], respectively.

Right: Comparison of pions ($\frac{1}{2}(\langle\pi^+\rangle + \langle\pi^-\rangle)$) from this work with h^- in N+N as they are used by NA35 for comparison or their yields [128]. Yields from NA35 were multiplied by 0.92 and 0.93 for reasons as described above.

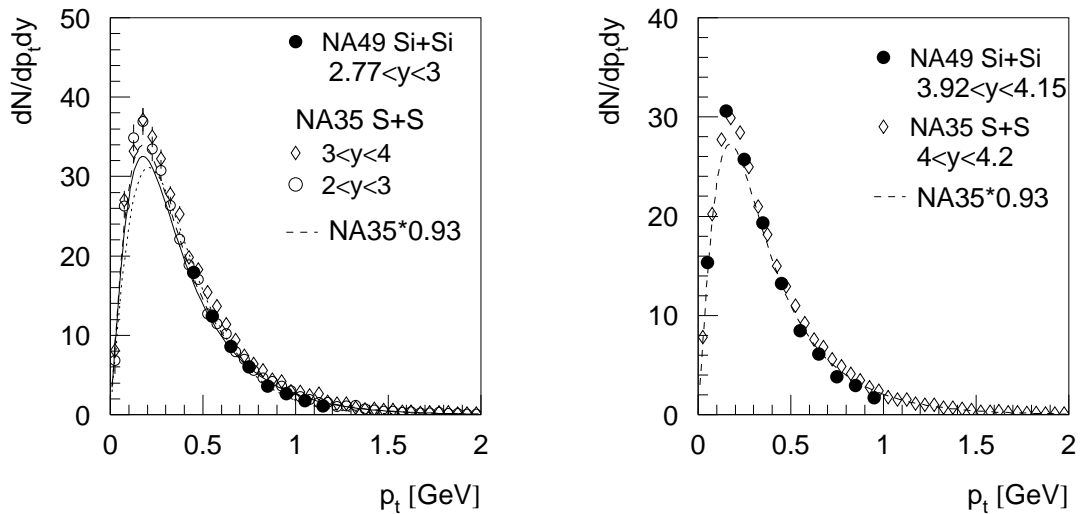


Figure C.14: Comparison of p_t -distribution of π^- from this work with an analysis of h^- from NA35 [128], left for midrapidity ($y_{CM} = 3$ for S+S at 200 AGeV), right for a bin more forward in rapidity. Presented data from NA35 were scaled by 0.92 to account for the contribution of K^- and \bar{p} [128]. A two-component thermal fit to the NA35 data (formula 6.1) scaled by 0.93 for the energy dependence [105] is presented by the dashed line in both figures. The solid line in the left figure indicates the extrapolation used for midrapidity yields in this work (functional form from NA35 but scaled by the pion yield in Si+Si in the measurable p_t -range, see description in chapter 6.1). The dotted line presents a simple thermal fit (formula 3.7) to π^- in Si+Si with a fixed temperature of $T=172$ MeV (see table C.15).

y -range	\bar{y}	K^+		K^-	
		$\frac{\Delta N}{\Delta y}$	T [MeV]	$\frac{\Delta N}{\Delta y}$	T [MeV]
2.77 - 3.00	2.88	2.484 ± 0.039	198 ± 3	1.530 ± 0.026	199 ± 3
3.00 - 3.23	3.12	2.378 ± 0.038	193 ± 3	1.503 ± 0.027	196 ± 4
3.23 - 3.46	3.35	2.176 ± 0.036	189 ± 3	1.379 ± 0.025	182 ± 4
3.46 - 3.69	3.58	1.988 ± 0.039	181 ± 4	1.286 ± 0.024	182 ± 4
3.69 - 3.92	3.81	1.874 ± 0.032	185 ± 3	1.169 ± 0.024	176 ± 4
3.92 - 4.15	4.04	1.671 ± 0.051	190 ± 5	0.955 ± 0.021	171 ± 4
4.15 - 4.38	4.27	1.280 ± 0.026	163 ± 4	0.764 ± 0.020	166 ± 5
4.38 - 4.62	4.50	1.119 ± 0.048	169 ± 6	0.563 ± 0.016	149 ± 5
4.62 - 4.85	4.73	0.734 ± 0.048	140 ± 7	0.427 ± 0.023	139 ± 8

Table C.17: p_t -integrated y -distribution of kaons in 12 % most central Si+Si collisions; center-of-mass rapidity is 2.9. The quoted temperature stems from a thermal fit to the p_t -spectra.

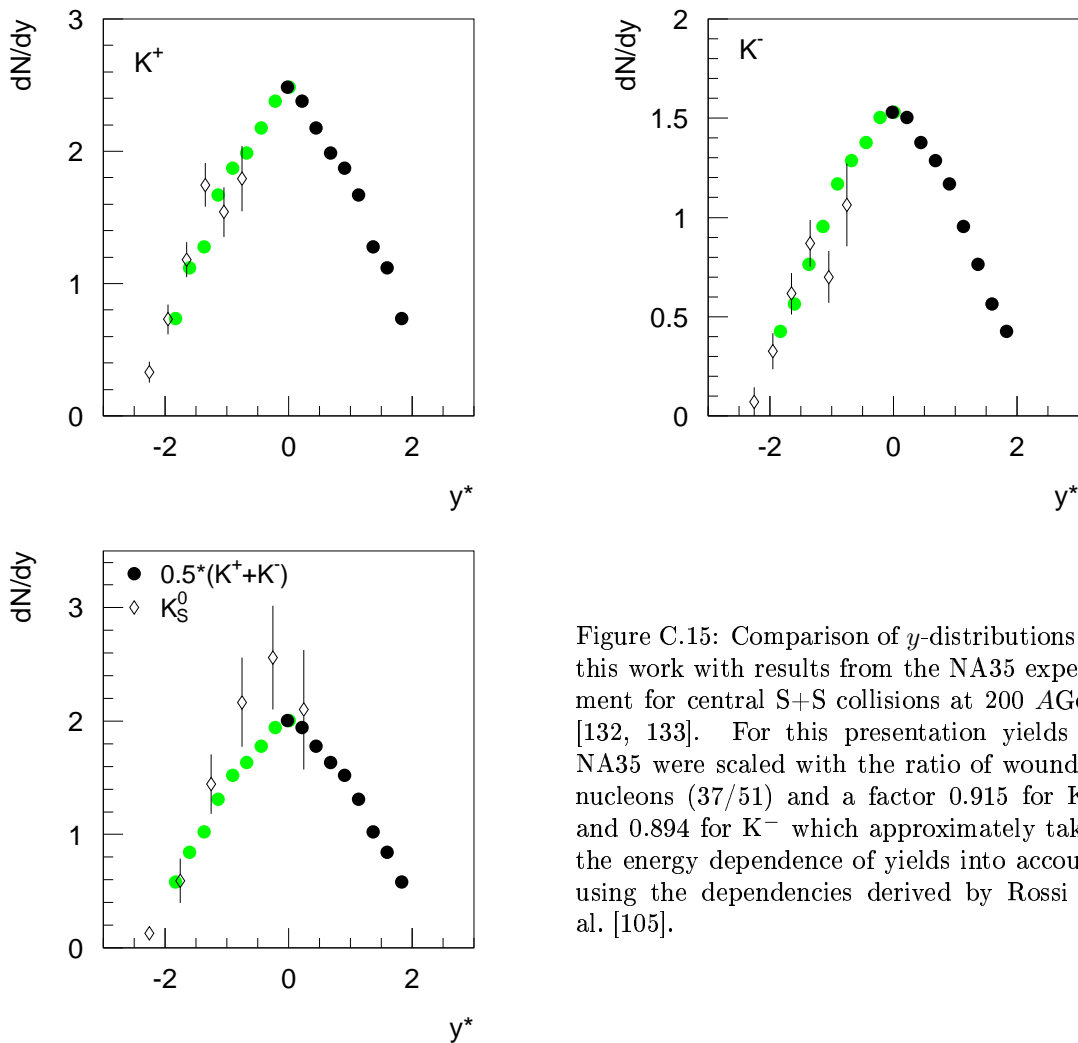


Figure C.15: Comparison of y -distributions of this work with results from the NA35 experiment for central S+S collisions at 200 AGeV [132, 133]. For this presentation yields of NA35 were scaled with the ratio of wounded nucleons (37/51) and a factor 0.915 for K^+ and 0.894 for K^- which approximately takes the energy dependence of yields into account using the dependencies derived by Rossi et al. [105].

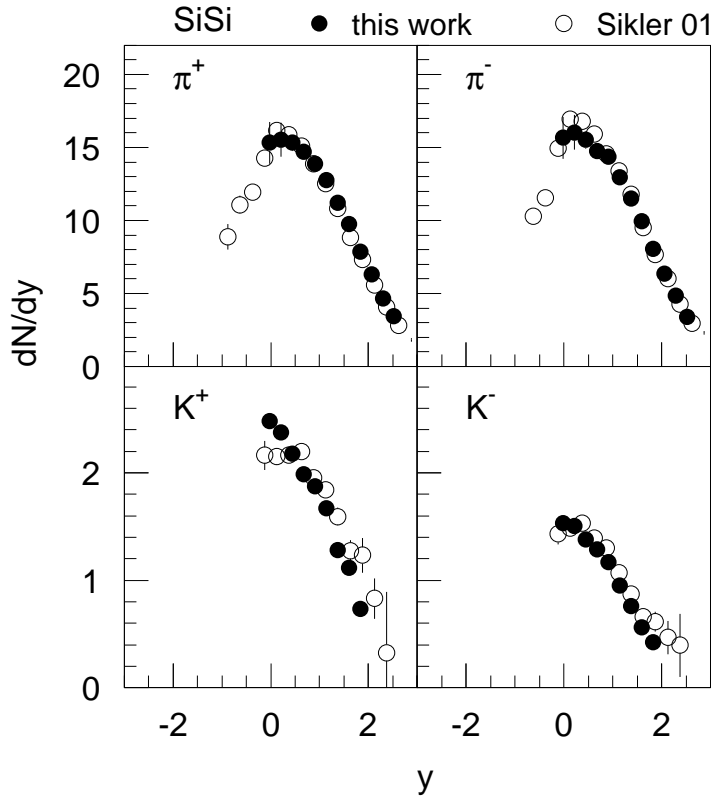


Figure C.16: Comparison of rapidity distributions for charged pions (not feed-down corrected) and kaons in the 12 % most central Si+Si collisions at 158 AGeV from this work with results from F. Sikler [12].

p_t -range [GeV]	\overline{p}_t [GeV]	$\frac{\Delta N}{\Delta p_t \Delta y}$	$\overline{m}_t - m_0$ [GeV]	$\frac{\Delta N}{m_t \Delta m_t \Delta y}$
0.0 - 0.3	0.14	0.0758 ± 0.0090	0.0214	0.5052 ± 0.0602
0.3 - 0.6	0.40	0.1692 ± 0.0127	0.1013	0.3768 ± 0.0284
0.6 - 0.9	0.76	0.1392 ± 0.0113	0.2474	0.1862 ± 0.0152
0.9 - 1.2	1.05	0.0913 ± 0.0087	0.4407	0.0874 ± 0.0084
1.2 - 1.5	1.34	0.0340 ± 0.0059	0.6656	0.0254 ± 0.0044

Table C.18: p_t and m_t -distribution of the ϕ -meson in 12 % central Si+Si collisions in the rapidity range [2.9,4.7].

y -range	\overline{y}	$\frac{\Delta N}{\Delta y}$
2.9 - 3.3	3.13	0.205 ± 0.024
3.3 - 3.7	3.51	0.197 ± 0.015
3.7 - 4.1	3.90	0.161 ± 0.013
4.1 - 4.5	4.30	0.139 ± 0.012
4.5 - 4.9	4.70	0.066 ± 0.012

Table C.19: p_t -integrated y -distribution of the ϕ -meson in 12 % central Si+Si collisions; center-of-mass rapidity is 2.9.

Appendix D

System-size parameters

Parameters for the system-size dependence based basically on the geometry of the colliding nuclei can be extracted with satisfying precision from Glauber model type simulations such as VENUS or FRITIOF. Here, a simple numerical realization of the Glauber model is used, the Wounded Nucleon Model (WNM) [168]: Nuclei are initialized with a Woods-Saxon density profile for the distribution of nucleons and propagated through each other. Cross sections are interpreted as geometrical areas and two nucleons collide if their areas overlap. This calculation provides the mean number of wounded nucleons $\langle N_{wound} \rangle$, the mean number of collisions per wounded nucleon $\langle \nu \rangle$ and the distribution of ν as well as 2-dimensional wounded nucleon or collision densities. The numbers agree with those from analytic calculations [159].

As input into the model the impact parameter is given to control the centrality, either a fixed value or a certain range. Both are known from the centrality determination in chapter 4.3 for C+C and Si+Si collisions, and from G. Cooper [74] for the centrality-dependent Pb+Pb interactions. As control for the agreement of centrality in data and this simulation the number of wounded nucleons is chosen, a better agreement was found using fixed values for b . The deviation of numbers calculated in this model from those by G. Cooper and from chapter 4.3 is on the order of 3-5 % for all bins except the most peripheral bin in Pb+Pb (8 %). Varying slightly the impact parameter to better adjust the number of wounded nucleons changes the calculated centrality parameters by about 3-5 % or 8 %. This can be taken as estimate for the errors on the various parameters.

The number of wounded nucleons and the number of collisions per wounded nucleon are counted straightforward. The fraction of multiple collisions, $f = 1 - \frac{N_{\nu=1}}{\sum_{i=1}^{\infty} N_{\nu=i}}$ with $N_{\nu=i}$ being the number of nucleons taking part in i collisions, is extracted from the distribution of ν , see fig. 7.11 for illustration. The 2-dimensional mean density of wounded nucleons is calculated as weighted mean of the density (see also [159]):

$$\langle \rho_{wound} \rangle = \frac{\int dx dy (\rho_{wound}(x, y))^2}{\int dx dy \rho_{wound}(x, y)} \quad (\text{D.1})$$

For practical reasons the sum in a x-y plane with small bins is used instead of the integral (see e. g. fig. 7.14).

	b [fm]	$\langle N_{wound} \rangle$	$\langle \nu_{wound} \rangle$	$\langle f \rangle$	$\langle \rho_{wound} \rangle$
C+C	1.9	13.5	1.9	0.536	0.96
Si+Si	2.0	39	2.5	0.70	1.49
S+S	1.5	51	2.7	0.751	1.66
Pb+Pb	2.4	363	4.6	0.90	2.95
	4.6	287.5	4.3	0.85	2.78
	6.5	210	3.9	0.80	2.52
	8.3	137.5	3.4	0.742	2.14
	9.6	91	2.9	0.68	1.78
	11.5	38.6	2.2	0.546	1.10

Table D.1: Centrality parameters as calculated in the WNM, for definitions see text.

The mean density of inelastic collisions in space and time is calculated with UrQMD simulations (version 1.2/1.3)¹, which provide place and time for every single interaction in the course of an A+A reaction, see fig. D.1 for an illustration. Here, only the first phase of inelastic collisions while the nuclei penetrate each other is of interest, i. e. the time span from zero to 1-2 fm/c. For each type of A+A collision and centrality, between 176 (most central Pb+Pb) and 7000 (C+C, Si+Si, most peripheral Pb+Pb) UrQMD events were generated, the number was chosen such that collision statistics is sufficient. Calculation times of the evolution of the A+A interaction were 6 fm/c and 50 fm/c, respectively, all options were left in standard settings, b was fixed at the values given in table D.2.

For calculating $\langle \rho_{\text{inel coll}} \rangle$, space is divided into 3-dimensional boxes and the density of inelastic collisions in these boxes, $\frac{N_{\text{coll}}(x,y,z,t)}{\Delta t V} = \rho(x, y, z, t)/\Delta t$ is calculated in time steps Δt . For each time step the density is averaged over all boxes providing a time dependent mean collision density $\langle \rho(t) \rangle$, respectively $\langle \rho(t) \rangle/\Delta t$ (fig. D.2 (b)). The averaging is done analogous to formula D.1:

$$\langle \rho(t) \rangle = \frac{\sum_{x,y,z} (\rho(x, y, z, t))^2}{\sum_{x,y,z} \rho(x, y, z, t)} \quad (\text{D.2})$$

Averaging also over time yields the mean density $\langle \rho_{\text{inel coll}} \rangle$ quoted in table D.2 (solid line in fig. D.2 (c)). The time maximum t_{max} until which the averaging is performed is chosen at the end of the primary collision peak as indicated in figure D.2.

$$\langle \rho_{\text{inel coll}} \rangle = \frac{\sum_{t=0}^{t_{\text{max}}} \sum_{x,y,z} (\rho(x, y, z, t)/\Delta t)^2}{\sum_{t=0}^{t_{\text{max}}} \sum_{x,y,z} \rho(x, y, z, t)/\Delta t} = \frac{1}{\Delta t} \frac{\sum_{t=0}^{t_{\text{max}}} \sum_{x,y,z} (\rho(x, y, z, t))^2}{\sum_{t=0}^{t_{\text{max}}} \sum_{x,y,z} \rho(x, y, z, t)} \quad (\text{D.3})$$

¹In UrQMD version 1.2 no Woods-Saxon density distribution for the nucleons inside the nuclei is implemented but they are distributed according to a hard sphere. However, for the calculation of centrality parameters a correct implementation is essential. The author thanks the UrQMD collaboration for making the preliminary version 1.3 available where this problem is cured. For the calculations in this work only the initialization routine for nuclei from version 1.3 was used (cascinit.f), the other routines were still taken from version 1.2.

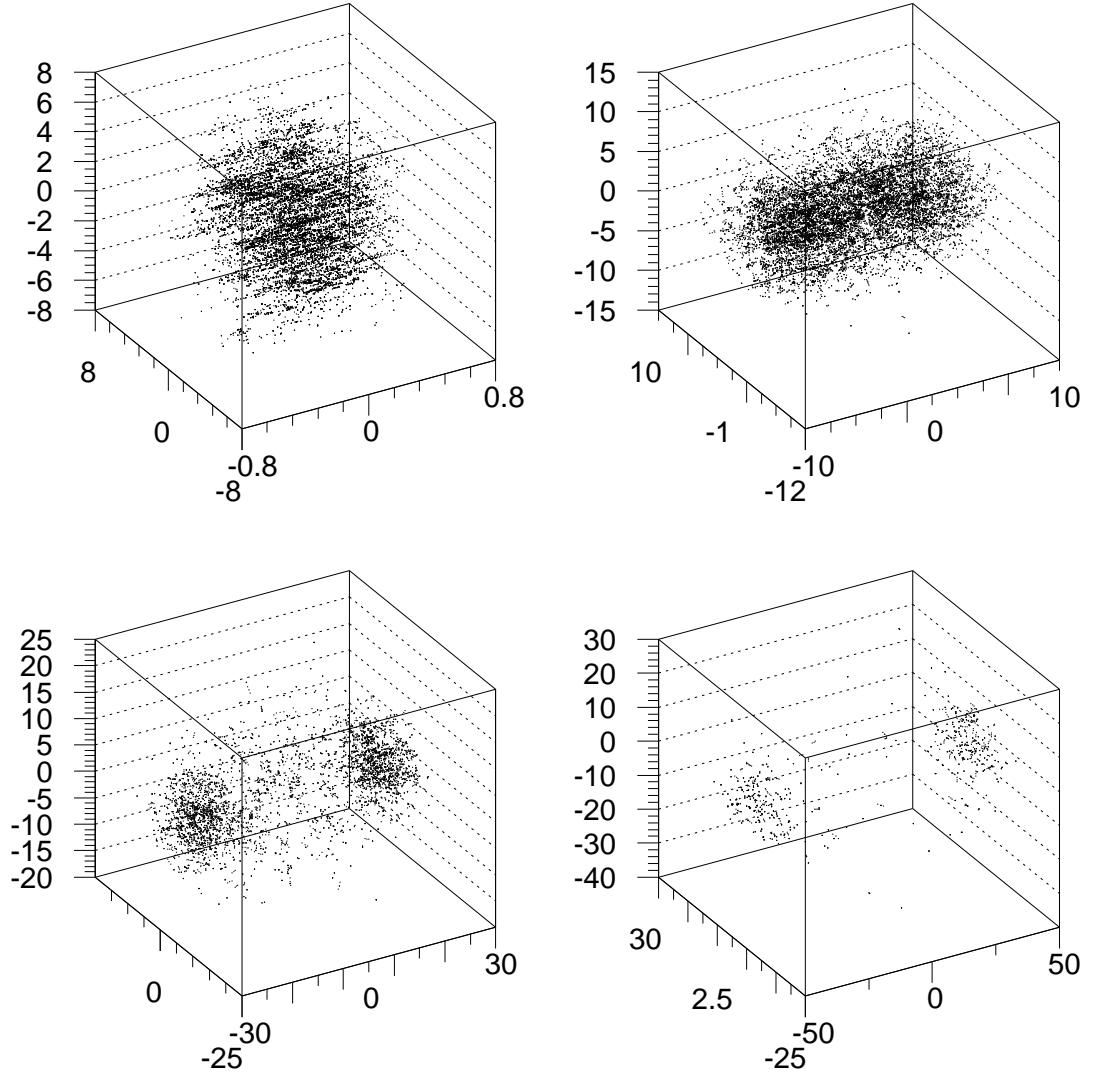


Figure D.1: Central Pb+Pb collision in UrQMD, $b = 2.2$ fm. For a few events each single collision at time t is presented by a dot for, from left to right, $t < 1$ fm/c, $5 < t < 10$ fm/c, $20 < t < 30$ fm/c, and $40 < t < 50$ fm/c. Note the changing scales.

Another possibility for averaging is to take the mean of the already averaged density per time bin $\langle \rho(t) \rangle / \Delta t$ (dashed line in fig. D.2 (c)).

$$\langle \rho_{\text{inel coll}} \rangle = \frac{\sum_{t=0}^{t_{\text{max}}} (\langle \rho(t) \rangle / \Delta t)^2}{\sum_{t=0}^{t_{\text{max}}} \langle \rho(t) \rangle / \Delta t} = \frac{1}{\Delta t} \frac{\sum_{t=0}^{t_{\text{max}}} \langle \rho(t) \rangle^2}{\sum_{t=0}^{t_{\text{max}}} \langle \rho(t) \rangle} \quad (\text{D.4})$$

The difference of these two methods is largest for central Pb+Pb collisions ($\sim 6\%$); see fig. D.2 (right) for the same plots in central C+C interactions.

As for the WNM calculations the agreement of centrality between simulations and data is best checked by comparing the number of wounded nucleons or participants. For UrQMD the number of participants is better defined, but as seen from

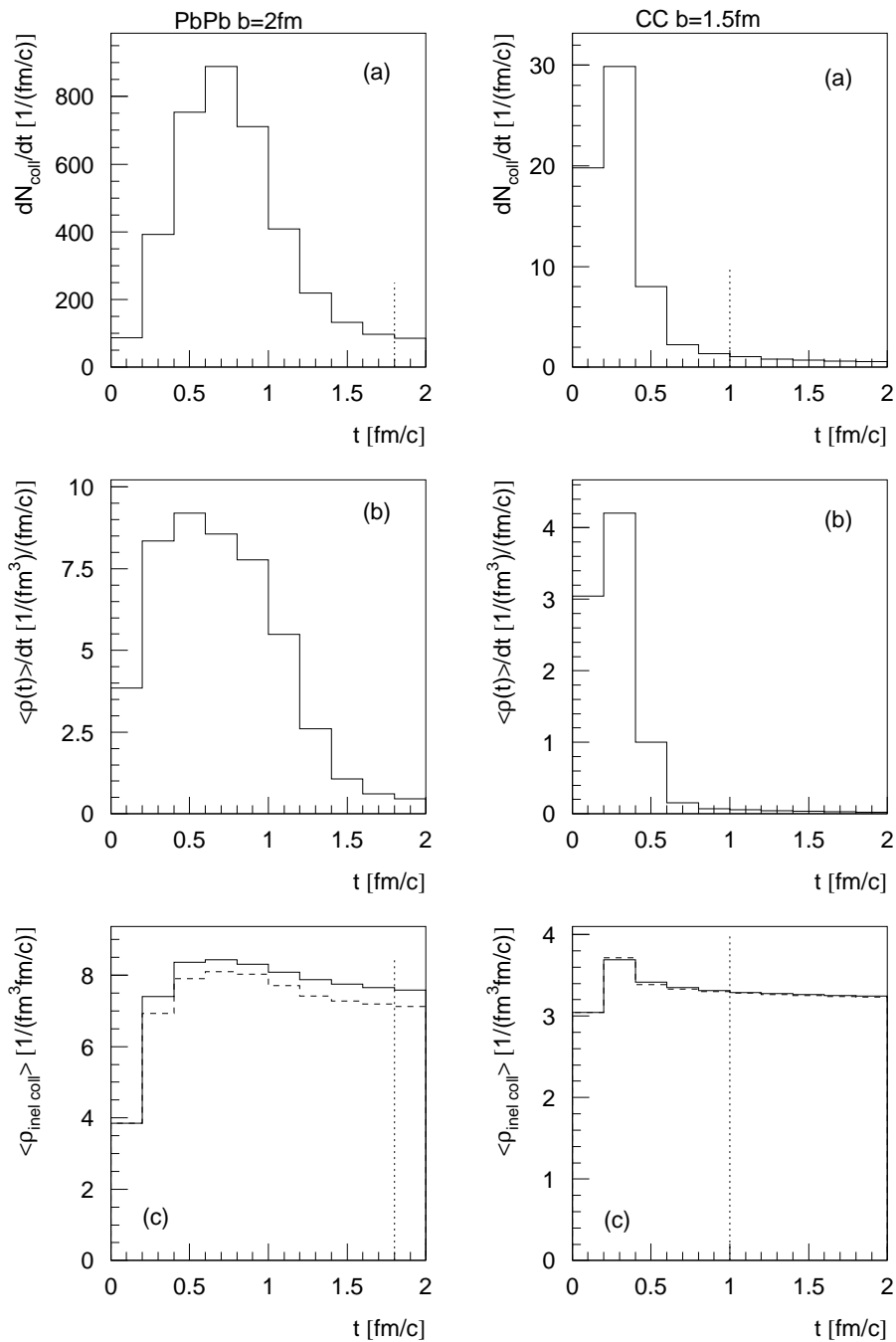


Figure D.2: Calculation of collision density in central Pb+Pb interactions ($b = 2.2$ fm) (left), and central C+C ($b = 1.5$ fm) (right): (a) number of collisions per time step, (b) mean collision density per time step, (c) averaged mean collision density until time t . t_{max} as used for the final calculations is indicated by the vertical dotted line. For the difference between solid and dashed line see text.

table D.2 and fig. D.3 the values are up to 23 % higher compared to data. Interpolating between N_{part} from UrQMD allows to extract a rescaled $\rho_{in\,el\,coll}$, see fig. D.3 and table D.3. The mean of calculated and rescaled value is used for chapter 7, the

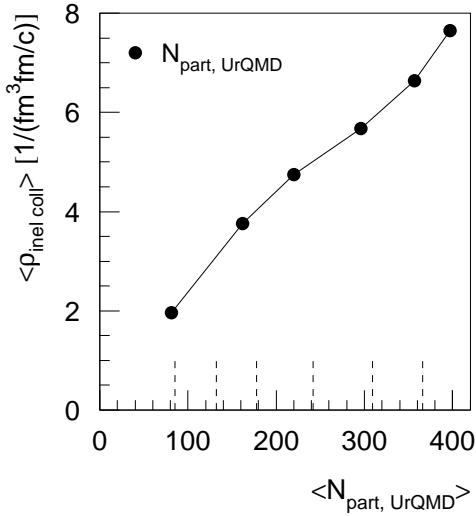


Figure D.3: Collision density in dependence on N_{part} for Pb+Pb interactions in UrQMD, see table D.2 for impact parameters defining the various centralities. As vertical dashed lines on the bottom values for N_{part} from the data [74] are indicated. The corresponding $\rho_{\text{inel coll}}$ can be read off from interpolations between the values from UrQMD.

difference is taken as estimate of the uncertainty in this parameter which amounts to 5-10 %.

The number of participants in C+C and S+S collisions from UrQMD agrees well with those determined from data. Only the centrality for Si+Si collisions is overestimated by about the same percentage compared to central Pb+Pb interactions. For table D.3, $\rho_{\text{inel coll}}$ for Si+Si reactions is thus scaled by the same factor as central Pb+Pb.

The UrQMD calculations also allow to estimate the volume of the primary reaction zone, i. e. the volume of collisions taking place for $t < 1-2$ fm/c. Depending on the definition of the envelope of the collision points the volume varies by a factor 2: Projecting all collision points onto the x -, y - and z -direction allows to extract a kind of radius r_x, r_y, r_z . Possible definitions are $r_x = 2.5 \cdot \sigma_x$ from fitting a Gaussian to the distributions, or via $N_{\text{coll}}(r_x) = \frac{1}{10} \cdot N_{\text{coll}}(0)$. The volume can then be either calculated as ellipse with $V = \frac{4}{3}\pi r_x r_y r_z$ or as cylinder with length $2r_z$,

	b [fm]	t_{max} [fm/c]	$\langle N_{\text{wound}} \rangle^*$	$\langle N_{\text{part}} \rangle$	$\langle \rho_{\text{inel coll}} \rangle$	$V_{\text{collision}}$ [fm ³]
C+C	1.5	1	14.9	16.2	3.31	6-12
Si+Si	1.8	1.2	41.2	44.9	4.8	10-20
S+S	1.5	1.4	50.2	54.3	5.04	14-30
Pb+Pb	2.2	1.8	379	397	7.65	70-140
	4.6	1.8	309	357	6.64	55-120
	6.5	1.8	232	296	5.68	45-90
	8.3	1.8	157	220	4.75	32-70
	9.6	1.8	105	162	3.76	26-55
	11.5	1.8	46	81	1.96	17-40

Table D.2: Centrality parameters as calculated with UrQMD. $\langle N_{\text{wound}} \rangle^*$ are all participants within the first 6 fm/c of the collision, $\langle N_{\text{part}} \rangle$ those after 50 fm/c. Since the penetration of the nuclei takes about 1-2 fm/c $\langle N_{\text{wound}} \rangle^*$ is expected to be slightly higher compared to a Glauber model. For definition of the other parameters see text.

	N_{part}	$\rho_{inel\ coll}^{scale}$	$\overline{\rho_{inel\ coll}}$
C+C	16.2	3.31	3.31
Si+Si	41.4	4.36	4.58 ± 0.22
S+S	54.3	5.04	5.04
Pb+Pb	366	6.89	7.27 ± 0.38
	309	5.90	6.27 ± 0.37
	242	5.05	5.37 ± 0.32
	278	4.05	4.40 ± 0.35
	132	3.10	3.43 ± 0.33
	81	1.96	1.96

Table D.3: Centrality parameters readjusted to N_{part} as measured in the experiment: $\rho_{inel\ coll}^{scale}$ is extracted from fig. D.3 for the N_{part} values given in the table. The last column contains the mean of $\rho_{inel\ coll}^{scale}$ and $\langle \rho_{inel\ coll} \rangle$ from table D.2, the given error is half of their difference. The value $\overline{\rho_{inel\ coll}}$ is used for fig. 7.15.

$V = \pi r_x r_y \cdot 2r_z$. The range of resulting values is given in table D.2. The calculated volume is approximately the same as the volume of the nucleus itself, Lorentz-contracted by a γ of 9.2. Within the large errors stemming from the method, it is proportional to the number of participants.

Bibliography

- [1] D. Perkins. *Introduction to high energy physics* (Addison-Wesley Publishing Company, Inc., 1987).
- [2] K. Hagiwara et al. *Review of Particle Physics*. Phys. Rev. D, **66**, 010001 (2002).
- [3] C. Wong. *Introduction to High-Energy Heavy-Ion Collisions* (World Scientific, 1994).
- [4] K. Rajopal. *Mapping the QCD Phase Diagram*. Nucl. Phys., **A661**, 150c (1999).
- [5] Y. Iwasaki, K. Kanaya, S. Kaya, S. Sakai, and T. Yoshié. *Finite temperature transitions in lattice QCD with Wilson quarks: Chiral transitions and the influence of the strange quark*. Phys. Rev., **D54**, 7010 (1996).
- [6] K. Kanaya. *Recent lattice results relevant for heavy ion collisions*. Nucl. Phys., **A715**, 233c (2003).
- [7] F. Brown et al. *On the Existence of a Phase Transition for QCD with Three Light Quarks*. Phys. Rev. Lett., **65**, 2491 (1990).
- [8] Z. Fodor and S. Katz. *Lattice determination of the critical point of QCD at finite T and μ* . JHEP, **03**, 014 (2002).
- [9] C. R. Allton et al. *The QCD thermal phase transition in the presence of a small chemical potential*. hep-lat/0204010 (2002).
- [10] H. Satz. *Limits of Confinement: The first 15 years of ultra-relativistic heavy ion studies*. Nucl. Phys., **A715**, 3c (2003).
- [11] M. Basile et al. *Charged-Particle Multiplicities in pp Interactions and Comparison with e^+e^- Data*. Il Nuovo Cimento, **65 A**, 400 (1981).
- [12] F. Sikler. Hadron production in nuclear collisions, Spectra of identified particles from CERN-NA49 using dE/dx , January 2001, private communication.
- [13] H. G. Fischer (NA49). Private communication.

- [14] T. Alber et al. *Transverse Energy Production in $^{208}\text{Pb}+\text{Pb}$ Collisions at 158 GeV per Nucleon*. Phys. Rev. Lett., **75**, 3814 (1995).
- [15] P. Steinberg. *Global observables at RHIC*. Nucl. Phys., **A698**, 314c (2002).
- [16] T. Ullrich. *Experimental summary on global observables, hadron spectra and ratios*. Nucl. Phys., **A715**, 399c (2003).
- [17] J. Bjorken. *Highly relativistic nucleus-nucleus collisions: The central rapidity region*. Phys. Rev., **D27**, 140 (1983).
- [18] P. Sonderegger. *Ultrarelativistic heavy ion physics*. CERN/PPE, **94-21** (1994).
- [19] H. Schmidt and J. Schukraft. *The physics of ultra-relativistic heavy-ion collisions*. J. Phys. G: Nucl. Part. Phys., **19**, 1705 (1993).
- [20] M. van Leeuwen for the NA49 collaboration. *Recent results on spectra and yields from NA49*. Nucl. Phys., **A715**, 161c (2003).
- [21] F. Becattini et al. *Features of particle multiplicities and strangeness production in central heavy ion collisions between 1.7A and 158A GeV/c*. Phys. Rev., **C64**, 024901 (2001).
- [22] J. Rafelski. *Strangeness production in the quark gluon plasma*. Nucl. Phys., **A418**, 215c (1984).
- [23] P. Koch, B. Müller, and J. Rafelski. *Strangeness in relativistic heavy ion collisions*. Phys. Rep., **142**, 167 (1986).
- [24] J. Kapusta and A. Mekjian. *How much strangeness production is there in ultrarelativistic nucleus-nucleus collisions?*. Phys. Rev., **D33**, 1304 (1986).
- [25] V. Manzari for the NA57 collaboration. *Hyperon yields in Pb-Pb collisions from NA57 experiment*. Nucl. Phys., **A715**, 140c (2003).
- [26] L. Riccati, M. Masera, and E. Vercellin (editors). *Quark Matter '99* (Elsevier, 1999).
- [27] T. Hallman, D. Kharzeev, J. Mitchell, and T. Ullrich (editors). *Quark Matter 2001* (Elsevier, 2002).
- [28] H. Gutbrod, J. Aichelin, and K. Werner (editors). *Quark Matter 2002* (Elsevier, 2003).
- [29] M. Gazdzicki and M. Gorenstein. *On the Early Stage of Nucleus-Nucleus Collisions*. Acta Phys. Polon., **B30**, 2705 (1999).
- [30] W. Geist et al. *Hadronic production of particles at large transverse momentum: its relevance to hadron structure, parton fragmentation and scattering*. Phys. Rep., **197**, 263 (1990).

- [31] S. Bass et al. *Microscopic Models for Ultrarelativistic Heavy Ion Collisions*. Prog. Part. Nucl. Phys., **41**, 225 (1998).
- [32] M. Bleicher et al. *Relativistic Hadron-Hadron Collisions and the Ultra-Relativistic Quantum Molecular Dynamics Model (UrQMD)*. J. Phys. G: Nucl. Part. Phys., **25**, 1859 (1999).
- [33] K. Werner. *Strings, Pomerons and the VENUS model of hadronic interactions at ultrarelativistic energies*. Phys. Rep., **232**, 87 (1993).
- [34] B. Andersson, G. Gustafson, and H. Pi. *The FRITIOF model for high energy hadronic collisions*. Z. Phys., **C57**, 1993 (485).
- [35] H. Collard, L. Elton, and R. Hofstadter. *Landolt-Börnstein, New Series, Vol. 2, Nuclear Radii* (Springer-Verlag, 1967).
- [36] B. Andersson et al. *Parton fragmentation and string dynamics*. Phys. Rep., **97**, 31 (1983).
- [37] A. Kaidalov and Y. Simonov. *Glueball spectrum and the pomeron in the Wilson loop approach*. Phys. Atom. Nucl., **63**, 1428 (2000).
- [38] A. Capella. *Baryon stopping and strangeness enhancement in the dual parton model*. J. Phys. G: Nucl. Part. Phys., **23**, 1979 (1997).
- [39] R. Hagedorn. *Statistical Thermodynamics of Strong Interactions at High Energies*. Sup. Nuovo Cimento, **3**, 147 (1965).
- [40] N. Xu for the NA44 collaboration. *Hadron distributions - Recent results from the CERN experiment NA44*. Nucl. Phys., **A610**, 175c (1996).
- [41] E. Schnedermann, J. Sollfrank, and U. Heinz. *Thermal phenomenology of hadrons from 200 A GeV S+S collisions*. Phys. Rev., **48**, 2462 (1993).
- [42] J. Rafelski and M. Danos. *The importance of the reaction volume in hadronic collisions*. Phys. Lett., **B97**, 279 (1980).
- [43] R. Hagedorn and K. Redlich. *Statistical Thermodynamics in Relativistic Particle and Ion Physics: Canonical or Grand Canonical?*. Z. Phys., **C27**, 541 (1985).
- [44] S. Hamieh, K. Redlich, and A. Tounsi. *Canonical description of strangeness enhancement from p-A to Pb-Pb collisions*. Phys. Lett., **B486**, 1 (2000).
- [45] J. Cleymans, A. Keränen, M. Marais, and E. Suhonen. *Exact baryon, strangeness, and charge conservation in hadronic gas models*. Phys. Rev., **C56**, 2747 (1997).
- [46] J. Letessier and J. Rafelski. *Importance of reaction volume in hadronic collisions: Canonical enhancement*. J. Phys. G: Nucl. Part. Phys., **28**, 1819 (2002).

- [47] A. Tounsi and K. Redlich. *Canonical constraints on particle production*. J. Phys. G: Nucl. Part. Phys., **28**, 2095 (2002).
- [48] F. Becattini and U. Heinz. *Thermal hadron production in pp and p \bar{p} collisions*. Z. Phys., **C76**, 269 (1997).
- [49] B. Kämpfer, J. Cleymans, K. Gallmeister, and S. Wheaton. *Thermal Parameters in Heavy Ion Collisions at SPS and RHIC: Centrality Dependence*. hep-ph/0204227 (2002).
- [50] J. Cleymans, B. Kämpfer, and S. Wheaton. *Towards strangeness saturation in central heavy-ion collisions at high energies*. Nucl. Phys., **A715**, 553c (2003).
- [51] P. Braun-Munzinger, J. Stachel, J. Wessels, and N. Xu. *Thermal and hadro-chemical equilibration in nucleus-nucleus collisions at the SPS*. Phys. Lett., **B365**, 1 (1996).
- [52] P. Braun-Munzinger, I. Heppe, and J. Stachel. *Chemical equilibration in Pb+Pb collisions at the SPS*. Phys. Lett., **B465**, 15 (1999).
- [53] P. Braun-Munzinger, J. Cleymans, H. Oeschler, and K. Redlich. *Maximum Relative Strangeness Content in Heavy Ion Collisions Around 30 A·GeV*. Nucl. Phys., **A697**, 902 (2002).
- [54] J. Letessier and J. Rafelski. *Chemical nonequilibrium in high-energy nuclear collisions*. J. Phys. G: Nucl. Part. Phys., **25**, 295 (1999).
- [55] http://home.cern.ch/~fokay/Press/pictures/phase_final_new.ps.
- [56] C. Greiner. *Strangeness in strongly interacting matter*. J. Phys. G: Nucl. Part. Phys., **28**, 1631 (2002).
- [57] R. Stock. *The parton to hadron phase transition observed in Pb+Pb collisions at 158 GeV per nucleon*. Phys. Lett., **B456**, 277 (1999).
- [58] J. Letessier, G. Torrieri, S. Hamieh, and J. Rafelski. *Quark-gluon plasma fireball explosion*. J. Phys. G: Nucl. Part. Phys., **27**, 427 (2001).
- [59] S. Afanasiev et al. *The NA49 large acceptance hadron detector*. Nucl. Instr. Meth., **A430**, 210 (1999).
- [60] O. Chvala. NA49 collaboration meetings
<http://www.ikf.uni-frankfurt.de/na49/collab-2001/>,
NA49 notes <http://na49-pp.web.cern.ch/NA49-pp/>.
- [61] J. Bracinik. NA49 note
<http://j.home.cern.ch/j/jurajb/public/Ondrej/trigcross.ps>.
- [62] http://na49info.cern.ch/na49/Archives/Images/results_1997/.

- [63] F. Eckhardt. Ph.D. thesis, Philipps-Universität Marburg (1996).
- [64] V. Friese. Ph.D. thesis, Philipps-Universität Marburg (1999).
- [65] F. Sikler. NA49 notes
<http://na49info.ch/na49/Physics/dEdx/notes/dedx.ps.gz>,
<http://na49info.ch/na49/Physics/dEdx/notes/landau.ps.gz>.
- [66] G. Veres. NA49 notes
<http://na49info.ch/na49/Physics/dEdx/notes/note.ps.gz>,
<http://v.home.cern.ch/v/veres/public/pp/analysis/micro/src/udst.txt>.
- [67] G. Veres. Ph.D. thesis, University of Budapest (2001).
- [68] W. Leo. *Techniques for Nuclear and Particle Physics Experiments* (Springer-Verlag, 1994).
- [69] A. Mock. Ph.D. thesis, MPI München (1997).
- [70] M. van Leeuwen. Ph.D. thesis, NIKHEF, Amsterdam (2003).
- [71] S. Afanasiev et al. *Energy Dependence of Pion and Kaon Production in Central Pb+Pb Collisions*. Phys. Rev., **C66**, 054902 (2002).
- [72] F. Sikler (NA49). Private communication.
- [73] R. Brun. *GEANT - detector description and simulation tool*. CERN Program Library Long Writeup W5013.
- [74] G. Cooper. Ph.D. thesis, Berkeley (2000).
- [75] M. Kreps. NA49 notes <http://k.home.cern.ch/k/kreps/public/corr/>.
- [76] C. Höhne for the NA49 collaboration. *System size dependence of strangeness production at 158 AGeV*. Nucl. Phys., **A715**, 474c (2003).
- [77] R. Barton. Ph.D. thesis, Birmingham (2001).
- [78] A. Mischke. Ph.D. thesis, GSI, Darmstadt (2002).
- [79] D. Drijard, H. Fischer, and T. Nakada. *Study of event mixing and its application to the extraction of resonance signals*. Nucl. Instr. and Meth. in Phys. Res., **225**, 367 (1984).
- [80] D. Drijard et al. *Production of Vector and Tensor Mesons in Proton-Proton Collisions at $\sqrt{s} = 52.5$ GeV*. Z. Phys., **C9**, 293 (1981).
- [81] T. Aziz et al. *Inclusive K^* 's and Σ^* 's Production in 360 GeV/c pp Interactions Using the European Hybrid Spectrometer*. Z. Phys., **C30**, 381 (1986).
- [82] M. Aguilar-Benitez et al. *Inclusive particle production in 400 GeV/c pp-interactions*. Z. Phys., **C50**, 405 (1991).

- [83] I. K. Yoo. Ph.D. thesis, Philipps-Universität Marburg (2001).
- [84] V. Friese and R. Lednicki. NA49 collaboration meeting, November 2002, http://www.ikf.physik.uni-frankfurt.de/na49/collab-2001/Collaborations_Meeting_11_2002/Friese/Friese.pdf.
- [85] A. Golokhvastov. *Scaling of semi-inclusive spectra of π^- mesons from pp interactions*. Z. Phys., **C26**, 469 (1984).
- [86] A. Golokhvastov. *Inclusive rapidity correlations of π^- mesons in pp interactions*. Z. Phys., **C64**, 301 (1994).
- [87] C. Markert. Ph.D. thesis, GSI, Darmstadt (2001).
- [88] J. Jackson. *Remarks on the Phenomenological Analysis of Resonances*. Il Nuovo Cimento, **34**, 1644 (1964).
- [89] D. Varga. NA49 collaboration meetings <http://www.ikf.uni-frankfurt.de/na49/collab-2001/>, NA49 notes <http://na49-pp.web.cern.ch/NA49-pp/>.
- [90] M. Basile et al. *A Detailed Study of $\langle n_{ch} \rangle$ vs. E^{had} and $m_{1,2}$ at Different $(\sqrt{s})_{pp}$ in (pp) Interactions*. Il Nuovo Cimento, **67 A**, 244 (1982).
- [91] H. Boggild et al. *Some examples of associated charged particle multiplicities in proton-proton collisions at 19 GeV/c*. Nucl. Phys., **B72**, 221 (1974).
- [92] V. Aivazyan et al. *Forward-backward multiplicity correlations in π^+p , K^+p and pp collisions at 250 GeV/c*. Z. Phys., **C42**, 533 (1989).
- [93] M. Anikina et al. *Cross-sections of inelastic interactions of neon nuclei*. Yadd. Phys., **38**, 149 (1983).
- [94] E. Abdrahmanov et al. *Interaction Cross Sections and Negative Pion Multiplicities in Nucleus-Nucleus Collisions at 4.2 GeV/c per Nukleon*. Z. Phys., **C5**, 1 (1980).
- [95] H. Heckman, D. Greiner, P. Lindstrom, and H. Shwe. *Fragmentation of ^4He , ^{12}C , ^{14}N , and ^{16}O nuclei in nuclear emulsion at 2.1 GeV/nucleon*. Phys. Rev., **C17**, 1735 (1978).
- [96] A. Bamberger et al. *Charged particle multiplicities and inelastic cross sections in high energy nuclear collisions*. Phys. Lett., **B205**, 583 (1988).
- [97] P. Barnes et al. *A measurement of cross sections for ^{16}O Al and ^{16}O Pb interactions at 60 and 200 GeV/c per nucleon*. Phys. Lett., **B206**, 146 (1988).
- [98] P. J. Karol. *Nucleus-nucleus reaction cross sections at high energies: Soft-spheres model*. Phys. Rev., **C11**, 1203 (1975).

- [99] J. Sollfrank, P. Koch, and U. Heinz. *The influence of resonance decays on the p_t spectra from heavy-ion collisions*. Phys. Lett., **B252**, 256 (1990).
- [100] C. Höhne. Diploma thesis, Universität Marburg, 1999.
- [101] S. Afanasiev et al. *Production of ϕ -mesons in $p+p$, $p+Pb$ and central $Pb+Pb$ collisions at $E_{beam}=158$ AGeV*. Phys. Lett., **B491**, 59 (2000).
- [102] P. Bevington and D. Robinson. *Data reduction and error analysis for the physical sciences* (McGraw-Hill, Inc., Second Edition, 1992).
- [103] H. Kichimi et al. *Inclusive study of strange-particle production in pp interactions at 405 GeV/c*. Phys. Rev., **D20**, 37 (1979).
- [104] J. Orear. *Universality of transverse momentum distributions in high energy physics*. Phys. Lett., **13**, 190 (1964).
- [105] A. Rossi et al. *Experimental study of the energy dependence in proton-proton inclusive reactions*. Nucl. Phys., **B84**, 269 (1975).
- [106] M. Gazdzicki and D. Röhrich. *Pion multiplicity in nuclear collisions*. Z. Phys., **C65**, 215 (1995).
- [107] H. Bialkowska (NA49). Private communication.
- [108] M. Gazdzicki and D. Röhrich. *Strangeness in nuclear collisions*. Z. Phys., **C71**, 55 (1996).
- [109] F. Sikler for the NA49 collaboration. *Hadron production in nuclear collisions from the NA49 experiment at 158 GeV/c*. A. Nucl. Phys., **A661**, 45c (1999).
- [110] T. Sammer. Ph.D. thesis, MPI München (2000).
- [111] T. Sammer. NA49 note
<http://na49info.cern.ch/cgi-bin/wwwd-util/NA49/NOTE?260>.
- [112] V. Blobel et al. *Observation of vector meson production in inclusive pp reactions*. Phys. Lett., **B48**, 73 (1974).
- [113] K. Böckmann et al. *Inclusive $K^{*\pm}(892)$ production in pp and π^+p interactions*. Nucl. Phys., **B166**, 284 (1980).
- [114] V. V. Ammosov et al. *Inclusive production of resonances in pp interactions at 69 GeV/c*. Sov. J. Nucl. Phys., **24**, 30 (1976).
- [115] D. Brick et al. *Inclusive strange-resonances production in pp , π^+p , and K^+p interactions at 147 GeV/c*. Phys. Rev., **D25**, 2248 (1982).
- [116] R. Singer et al. *$K^{*\pm}(890)$ production in 205 GeV/c pp interactions*. Nucl. Phys., **B135**, 265 (1978).

- [117] V. Blobel et al. *Test of the Zweig selection rule in ϕ -production by pp collisions*. Phys. Lett., **B59**, 88 (1975).
- [118] C. Daum et al. *Inclusive ϕ -meson production in 93 and 63 GeV hadron interactions*. Nucl. Phys., **B186**, 205 (1981).
- [119] Y. Antipov et al. *ϕ -Meson inclusive production by 70 GeV/c protons*. Phys. Lett., **B110**, 326 (1982).
- [120] H. Dijkstra et al. *High Statistics Inclusive ϕ meson production at SPS energies*. Z. Phys., **C31**, 375 (1986).
- [121] K. Anderson et al. *Inclusive μ -Pair Production at 150 GeV by π^+ Mesons and Protons*. Phys. Rev. Lett., **37**, 799 (1976).
- [122] D. Morrison. *Inclusive ϕ -Meson production - relation to J/ψ and Υ production*. CERN/EP, **79-102** (1979).
- [123] A. Mangiarotti et al. *Sub-threshold ϕ -meson yield in central $^{58}\text{Ni}+^{58}\text{Ni}$ collisions*. nucl-ex/0209012, submitted to Nucl. Phys., **A** (2002).
- [124] A. Rybicki. Ph.D. thesis, Institute of Nuclear Physics, Cracow (2002).
- [125] J. Whitmore. *Experimental results on strong interactions in the NAL hydrogen bubble chamber*. Phys. Rep., **10c**, 273 (1974).
- [126] T. Akesson et al. *Low-mass lepton-pair production in p-Be collisions at 450 GeV/c*. Z. Phys., **C68**, 47 (1995).
- [127] R. Veenhof. Ph.D. thesis, <http://rjd.home.cern.ch/rjd/Proefschrift/thesis.ps> (1993).
- [128] T. Alber et al. *Charged particle production in proton-, deuteron-, oxygen- and sulphur-nucleus collisions at 200 GeV per nucleon*. Eur. Phys. J., **C2**, 643 (1998).
- [129] J. Bächler et al. *Charged Particle Spectra in Central S+S Collisions at 200 GeV/c per Nucleon*. Phys. Rev. Lett., **72**, 1419 (1994).
- [130] K. Lee, U. Heinz, and E. Schnedermann. *Search for collective transverse flow using particle transverse momentum spectra in relativistic heavy-ion collisions*. Z. Phys., **C48**, 525 (1990).
- [131] V. Friese for the NA49 collaboration. *Strangeness from 20 AGeV to 158 AGeV*. Proceedings of Strangeness in Quark Matter, 2003, to appear in J. Phys. G: Nucl. Part. Phys.
- [132] J. Baechler et al. *Production of charged kaons in proton-nucleus and nucleus-nucleus collisions at 200 GeV/nucleon*. Z. Phys., **C58**, 367 (1993).

- [133] T. Alber et al. *Strange particle production in nuclear collisions at 200 GeV per nucleon*. Z. Phys., **C64**, 195 (1994).
- [134] I. Kraus for the NA49 collaboration. *System size dependence of strangeness production at 158 AGeV*. Proceedings of Strangeness in Quark Matter, 2003, to appear in J. Phys. G: Nucl. Part. Phys.
- [135] V. Friese for the NA49 collaboration. *Production of Strange Resonances in C+C and Pb+Pb Collisions at 158 AGeV*. Nucl. Phys., **A698**, 487c (2002).
- [136] T. Susa (NA49). Private communication, partially published in [169].
- [137] J. Bartke et al. *Neutral strange particle production in sulphur-sulphur and proton-sulphur collisions at 200 GeV/nucleon*. Z. Phys., **C48**, 191 (1990).
- [138] A. Mischke for the NA49 collaboration. *Energy Dependence of Λ and $\bar{\Lambda}$ Production at CERN-SPS Energies*. Nucl. Phys., **A715**, 453c (2003).
- [139] F. Pühlhofer (NA49). Private communication.
- [140] G. Ambrosini et al. *Impact parameter dependence of K^\pm , p , \bar{p} , d and \bar{d} production in fixed-target Pb+Pb collisions at 158 GeV/nucleon*. New Journal of Physics, **1**, 22.1 (1999).
- [141] G. Ambrosini et al. *Charged pion production in fixed-target Pb+Pb collisions at 158 GeV/nucleon*. New Journal of Physics, **1**, 23.1 (1999).
- [142] A. Dumitru, S. Bass, M. Bleicher, H. Stöcker, and W. Greiner. *Direct emission of multiple strange baryons in ultrarelativistic heavy-ion collisions from the phase boundary*. Phys. Lett., **B460**, 411 (1999).
- [143] H. Appelshäuser et al. *Hadronic expansion dynamics in central Pb+Pb collisions at 158 GeV per nucleon*. Eur. Phys. J., **C2**, 661 (1998).
- [144] T. Alber et al. *Two-pion Bose-Einstein correlations in nuclear collisions at 200 GeV per nucleon*. Z. Phys., **C66**, 77 (1995).
- [145] J. Rafelski, J. Letessier, and G. Torrieri. *Strange hadrons and their resonances: A diagnostic tool of quark-gluon plasma freeze-out dynamics*. Phys. Rev., **C64**, 054907 (2001).
- [146] P. Facchini for the STAR collaboration. *$\rho(770)^0$, $K^*(892)^0$ and $f_0(980)$ Production in Au-Au and pp Collisions at $\sqrt{s_{NN}} = 220$ GeV*. Nucl. Phys., **A715**, 462c (2003).
- [147] H. Weber, E. Bratkovskaya, W. Cassing, and H. Stöcker. *Hadronic observables at relativistic energies: Anything strange with strangeness?*. Phys. Rev., **C67**, 014904 (2003).

- [148] V. Friese (NA49). ϕ and Λ_{1520} production in the UrQMD model (2000), private communication.
- [149] M. Bleicher and J. Aichelin. *Strange resonance production: probing chemical and thermal freeze-out in relativistic heavy ion collisions*. Phys. Lett., **B530**, 81 (2002).
- [150] S. Soff et al. *Enhanced strange particle yields – signal of a phase of massless particles?*. J. Phys. G: Nucl. Part. Phys., **27**, 449 (2001).
- [151] C. Blume for the NA49 collaboration. *New Results from NA49*. Nucl. Phys., **A698**, 104c (2002).
- [152] F. Wang. *Systematics of mid-rapidity K^-/π ratio in heavy-ion collisions*. J. Phys. G: Part. Phys., **28**, 2109 (2002).
- [153] S. Kabana. *The strange border of the QCD phases*. Eur. Phys. J., **C21**, 545 (2001).
- [154] S. Kabana and P. Minkowski. *Mapping out the QCD phase transition in multiparticle production*. New Journal of Physics, **3**, 4.1 (2001).
- [155] T. Biro, H. Nielsen, and J. Knoll. *Colour rope model for extreme relativistic heavy ion collisions*. Nucl. Phys., **B245**, 449 (1984).
- [156] H. Sorge. *Flavor production in Pb(160A GeV) on Pb collisions: Effect of color ropes and hadronic rescattering*. Phys. Rev., **C52**, 3291 (1995).
- [157] H. Sorge. *Mass dependence of hadron distributions in ultrarelativistic nucleus-nucleus collisions*. Z. Phys., **C67**, 479 (1995).
- [158] S. Soff et al. *Strangeness enhancement in heavy ion collisions – evidence for quark gluon matter?*. Phys. Lett., **B471**, 89 (1999).
- [159] H. Bialkowska and W. Retyk. *Kaon and Φ production versus participants in nuclear collisions*. J. Phys. G: Nucl. Part. Phys., **27**, 397 (2001).
- [160] H. Satz. *Parton Percolation in Nuclear Collisions*. Lectures given at International School of Physics "Enrico Fermi", hep-ph/0212046 (2002).
- [161] D. Stauffer and A. Aharony. *Introduction to percolation theory* (Taylor & Francis group, Basingstoke Hauts, United Kingdom, 1991).
- [162] J. Cleymans, B. Kämpfer, P. Steinberg, and S. Wheaton. *Strangeness Saturation: Energy- and System-Size Dependence*. hep-ph/0212335 (2002).
- [163] F. Becattini and G. Pettini. *Strange quark production in a statistical effective model*. Phys. Rev., **C67**, 015205 (2003).

-
- [164] H. Appelshäuser et al. *Baryon Stopping and Charged Particle Distributions in Central Pb+Pb Collisions at 158 GeV per Nucleon*. Phys. Rev. Lett., **82**, 2471 (1999).
- [165] G. Lafferty and T. Wyatt. *Where to stick your data points: The treatment of measurements within wide bins*. CERN/PPE, **94-72** (1994).
- [166] W. Morse et al. *π^+p , K^+p , and pp topological cross sections and inclusive interactions at 100 GeV using a hybrid bubble-chamber-spark-chamber system and a tagged beam*. Phys. Rev., **D15**, 66 (1977).
- [167] T. Kafka et al. *One-, two-, and three-particle distributions in pp collisions at 205 GeV/c*. Phys. Rev., **D16**, 1261 (1977).
- [168] K. Kadija (NA49). Private communication.
- [169] T. Susa for the NA49 collaboration. *Cascade Production in $p+p$, $p+A$ and $A+A$ Interactions at 158 A·GeV*. Nucl. Phys., **A698**, 491c (2002).

Meine Mutter

*Ich hatte dir soviel zu sagen,
Ich war zu lang im fremden Land,
Und doch warst du in all den Tagen
Die, die am besten mich verstand.*

*Nun, da ich meine erste Gabe,
Die ich dir lange zugedacht,
In zagen Kinderhänden habe,
Hast Du die Augen zugemacht.*

*Doch darf ich fühlen, wie beim Lesen
Mein Schmerz sich wunderbar vergißt,
Weil dein unsäglich gütig Wesen
Mit tausend Fäden um mich ist.*

Hermann Hesse

Danke

Ein ganz herzliches Dankeschön möchte ich allen sagen, die mich in den vergangenen Jahren auf vielfältigste Art und Weise unterstützt und damit diese Arbeit ermöglicht haben. Dieser Dank gilt ganz besonders Herrn Professor Pühlhofer, seinem steten Fördern und Fordern und der starken Unterstützung in den verschiedenen Höhen und Tiefen dieser Arbeit. Insbesondere haben auch die vielen netten Geschichten aus dem Garten manches Treffen belebt. Ganz herzlich danken möchte ich auch Herrn Professor Stock für seine immerwährende und mitreißende Begeisterung für die Schwerionenphysik und die vielen heißen Diskussionen um deren Verständnis. Sein Interesse an meinem Treiben, neue Impulse und die begeisterte Aufnahme meiner Ergebnisse haben mich immer gefreut.

Das Experiment NA49 funktioniert nur durch die Zusammenarbeit von vielen Personen. A very warm thank-you to all members of NA49 for supporting and encouraging me during the last years: To Volker Friese and Jörn Putschke for sharing the office in Marburg and many helpful discussions. Special thanks to Gabor Veres and Ferenc Sikler for their work concerning dE/dx and their continuous willingness for answering all my questions; the same for Dezső Varga and the neutrons. For corrections I could use simulations and tables provided by Ondrej Chvala, Michal Kreps, Michael Mitrovski, Ferenc Sikler, and Tanja Susa. Latchezar Betev was always ready to help with NA49 or CERN software problems. Kreso Kadija kindly provided his code for the wounded nucleon model. I am very grateful to Helena Bialkowska and Kreso Kadija for cheering me up several times when having trou-

ble. Hans Gerhard Fischer and Siegfried Wenig gave me a good introduction into the physics of p+p interactions. Herbert Ströbele had the great idea of initiating the study of the system-size dependence. I would also like to thank Ingrid Kraus for providing her data on Λ -production in C+C and Si+Si collisions and Marek Gazdzicki for always being a great source for references of all kind. Representative for all others I thank Peter Seyboth as the spokesman for keeping NA49 a powerful experiment.

Gerne denke ich an die Gastaufenthalte und intensiven Rechenzeiten in Bergen zurück. Herzlichen Dank dafür an Dieter Röhrich und das BCPL sowie an die EU für ihre Unterstützung im Rahmen des „European Community – Access to Research action of the Improving Human Potential Programme“. Allen Steuerzahlern verdanke ich außerdem über das BMBF die Finanzierung der vergangenen Jahre.

Die Schwerionenphysik in Marburg ist nur eine kleine Insel umgeben insbesondere von einer stetig wachsenden Zahl an Oberflächlern. Diesen neben allem anderen ein herzliches Dankeschön dafür, dass sie mich mittags nicht haben verhungern lassen.

Mein ganz besonderer persönlicher Dank gilt meinen Freunden, der eigenen, der hinzugewonnenen und der geliehenen Familie sowie den Patenkindern für ihre Unterstützung und Zuneigung sowie insbesondere in der letzten Zeit für das kontinuierliche Verständnis andauernder Abwesenheit. Natürlich gehen meine Gedanken oft zu meiner Mutter und ich wünschte, sie könnte diese Seiten lesen. Für die vergangenen Jahre bin ich ihr so dankbar wie meinem Vater, wenngleich er diesen Dank allein entgegennehmen muss. Besonders am Herzen liegt mir ein „Lob, Dank und Anerkennung“ an meinen Lieblingsschwaben für seine Hilfe bei dieser Arbeit, mehr noch aber für das treue Leiden und Freuen an meiner Seite.

Lebenslauf

Claudia Höhne

* 13. Mai 1974 in Hüttental, jetzt Siegen

Ausbildung

10/1993 – 04/1999	Studium der Physik, Philipps-Universität Marburg
04/1999	Diplom
02/1998 – 04/1999	Diplomarbeit: ϕ -Meson-Produktion in Proton-Proton- und Proton-Kern-Stößen bei 158 GeV Strahlenergie
10/1995	Vordiplom
06/1993	Abitur
1984 – 1993	Gymnasium Stift-Keppel, Allenbach
1980 – 1984	Grundschule Allenbach

Praxis

seit 05/1999	wissenschaftlicher Mitarbeiter am Fachbereich Physik der Philipps-Universität Marburg
06/1996 – 09/1996	Sommerstudent am CERN (PS200 Experiment am LEAR)
03/1996	Praktikum am Hahn-Meitner-Institut, Berlin (Solarzellen aus Pyrit)